Phase stability, constitution and precipitation effects in Fe-Ni-Cr alloys.

WATSON, Maxine.

Available from the Sheffield Hallam University Research Archive (SHURA) at:

http://shura.shu.ac.uk/20503/

A Sheffield Hallam University thesis

This thesis is protected by copyright which belongs to the author.

The content must not be changed in any way or sold commercially in any format or medium without the formal permission of the author.

When referring to this work, full bibliographic details including the author, title, awarding institution and date of the thesis must be given.

Please visit http://shura.shu.ac.uk/20503/ and http://shura.shu.ac.uk/information.html for further details about copyright and re-use permissions.

POLYTECHNIC LIBRARY
POND STREET
SHEFFIELD S1 1WB

100310189 5
TELEPEN

26/4-20.55

Sheffield City Polytechnic Library

REFERENCE ONLY

ProQuest Number: 10701150

All rights reserved

INFORMATION TO ALL USERS
The quality of this reproduction is dependent upon the quality of the copy submitted.

In the unlikely event that the author did not send a complete manuscript
and there are missing pages, these will be noted. Also, if material had to be removed,
a note will indicate the deletion.

ProQuest 10701150

Published by ProQuest LLC (2017). Copyright of the Dissertation is held by the Author.

All rights reserved.
This work is protected against unauthorized copying under Title 17, United States Code
Microform Edition © ProQuest LLC.

ProQuest LLC.
789 East Eisenhower Parkway
P.O. Box 1346
Ann Arbor, MI 48106 – 1346

PHASE STABILITY, CONSTITUTION AND PRECIPITATION EFFECTS IN FE-NI-CR ALLOYS

Maxine Watson B.Sc.

This Thesis is submitted in partial fulfilment of the requirements for the Degree of Ph.D. of the Council for National Academic Awards.

The collaborating establishment was :-

United Kingdom Atomic Energy Authority
Atomic Energy Research Establishment HARWELL
Didcot, Oxon, OX11 ORA

The sponsoring establishment was :

Department of Metals and Materials Engineering,
Sheffield City Polytechnic,
Pond Street,
Sheffield, S1 1WB.

November 1990

SHEFFIELD
STREET
Th
669.96142
MAQ

PHASE STABILITY, CONSTITUTION AND PRECIPITATION EFFECTS IN FE-NI-CR ALLOYS

Maxine Watson B.Sc.

This Thesis is based upon an investigation carried out mainly at Sheffield City Polytechnic, but also in part at the United Kingdom Atomic Energy Establishment, Harwell, during the period October 1983 to December 1986, under the supervision of Professor F.B. Pickering of Sheffield City Polytechnic and Dr. T.M. Williams of U.K.A.E.R.E, Harwell.

The Thesis is submitted to the Council for National Academic Awards in partial fulfilment of the requirements for the Degree of Doctor of Philosophy, in October 1990. The collaborating establishment in the work reported was the United Kingdom Atomic Energy Establishment, Harwell. The candidate has not, during the period of registration for the CNAA degree of Ph.D., been a registered candidate for any other CNAA award or for any University degree. The results presented in the thesis are to the best of my knowledge, original except where reference and acknowledgement has been made to other authors. No part of this thesis has been submitted for a degree at any other University or College.

A number of courses were attended during the period of this work :

(1) "Atomic Energy" Honours topic of the BSc in Industrial Studies, October 1983-June 1984.

(2) "Corrosion Resistant and High Temperature Metals and Alloys" Advanced topic in Module 3 of the MSc in Metallurgical Process Management, February 1984-June 1984

(3) "Stainless Steels" Advanced topic in Module 3 of the MSc in Metallurgical Process Management, February 1985-June 1985.

(4) "High Strength Steels" Advanced topic in Module 3 of the MSc in Metallurgical Process Management, February 1985-June 1985.

Maxine Watson

November 1990

PHASE STABILITY, CONSTITUTION AND PRECIPITATION EFFECTS IN FE-NI-CR ALLOYS

Maxine Watson BSc

ABSTRACT

A study of the constitution, transformation and precipitation effects in ternary Fe-Cr-Ni alloys and quaternary Fe-Cr-Ni-X alloys containing Mo, Nb, Ti, and Si was carried out. A systematic approach was adopted so that the microstructural effects observed as a result of ageing the selected iron base ternary alloys could be directly compared to the quaternary alloys.

A series of ageing curves were plotted for the six ternary alloys over the temperature range 400°-900°C and for the ten quaternary alloys in the temperature range 650°-850°C. Optical and electron metallography were used to study the transformation and precipitation of intermetallic phases and carbides in the aged microstructures.

The transformation of delta ferrite to sigma phase in a duplex $(\gamma + \delta)$ ternary alloy was studied. The transformation was preceded by the precipitation of a cellular structure which formed on the δ/γ grain boundaries and consisted of $M_{23}C_6$ and new austenite. A complex transformation product, which resembled a region of immiscibility, then formed at the $\delta/(\gamma + M_{23}C_6)$ interface, this product consumed the delta ferrite grain, eventually transforming to sigma phase and new austenite.

The α' phase, more commonly referred to as 475°C embrittlement, was also observed precipitating in the delta ferrite grains in two of the iron based ternary alloys in the temperature region 400°-500°C. Overageing of the α' precipitates after 1000 hours at 500°C was accompanied by the precipitation of a rod like austenite.

The elements 2%Mo, 1%Nb, $\frac{1}{4}$%Ti and 1% and 2%Si were added to two Fe-Ni-Cr base alloys. One alloy was an austenitic (20Cr, 23Ni) and the other was a transformable alloy (18Cr, 7Ni). The quaternary element additions had no effect on the constitution of the austenitic ternary alloy. However the addition of Mo to the 18Cr, 7Ni ternary alloy caused the transformation of delta ferrite to sigma phase over ageing temperature range 650°-850°C. The addition of Si moved the constitution of the ternary alloy further into the $\gamma + \delta$ phase field, a small amount of sigma phase was observed in the 2%Si quaternary alloy on ageing at 650°C for 1000 hours.

Irradiation damage studies were performed using High Voltage Electron Microscope and Variable Energy Cyclotron. The effect of the quaternary alloying additions Mo, Si, and Nb on the void swelling behaviour of a 20Cr, 23Ni alloy were studied using 46MeV Ni^{6+} ions in the Variable Energy Cyclotron, irradiating to a total dose of 10dpa at 550°C. All additions reduced void swelling, the largest reduction was observed in the Si containing alloy. The

Insert A Thermal ageing showed the presence of $M_{23}C_6$, the amount of which increased with increasing ageing temperature. No delta ferrite was observed in these alloys.

ACKNOWLEDGEMENTS

I would like to express my gratitude to those who have assisted me with my post graduate research, culminating in this thesis.

I would like to thank the UKAEA for the provision of the CASE award that made this thesis possible. My thanks are also due to my industrial supervisor Dr. T. M. Williams of the UKAEA, Irradiation Metallurgy Group, Harwell, UKAEA.

I would also like to thank the technical staff, both at Sheffield City Polytechnic and Harwell, especially Mr. W. C. Fuller for his advice on thin foil preparation techniques.

As always, my grateful thanks are due to my family, whose love and support sustained me throughout this work and to Dr. Michael Morris who nagged at me every day until I had finished.

Above all, I would especially like to thank Professor F. B. Pickering, my internal supervisor, whose constant help, advice and encouragement has been of inestimable value.

CONTENTS

Page

1.0 INTRODUCTION 1

2.0 LITERATURE SURVEY 4

2.1 The Ternary Iron-Chromium-Nickel System 4
  2.1.1 The Experimental Determination of Phase Boundaries 5
2.2 The Iron-Chromium-Nickel Isothermal Equilibrium Diagrams 7
  2.2.1 Effects Of Alloying Elements On The Iron-Chromium-Nickel System 10
2.3 Intermetallic Phases 16
  2.3.1 Sigma Phase 16
  2.3.2 Laves Phase 18
  2.3.3 Chi Phase 20
  2.3.4 G Phase 21
  2.3.5 Eta and Gamma Prime Phases 22
2.4 Carbide Phases 23
  2.4.1 $M_{23}C_6$ 23
  2.4.2 MC 24
2.5 Transformations Occurring in Austenitic Stainless Steels 25
2.6 Transformations Occurring in Duplex Stainless Steels 32
2.7 Transformations Occurring in Martensitic Stainless Steels 38
2.8 Neutron Irradiation Damage Occurring in Fast Reactor Core Components 42
  2.8.1 Irradiation Damage Processess 45

2.9 Methods Available to Study Void Swelling 48
    2.9.1 Simulation Techniques 49
2.10 Efforts Made to Understand Void Swelling Using Simulation and Fast Neutron Techniques 51

3.0 EXPERIMENTAL METHODS 57

3.1 Ternary Alloys: Rationale 57
    3.1.1 Quaternary Alloys: Rationale 58
3.2 Manufacture of Iron Base Ternary Alloys 60
    3.2.1 Preparation for Ageing Studies 60
    3.2.2. Quaternary Alloy Manufacture 61
3.3 Optical Metallography 62
3.4 Determination of the Ageing Curves 63
3.5 Transmission Electron Microscopy 63
3.6 Sample Preparation for Irradiation in the HVEM 64
3.7 Sample Preparation for VEC Irradiation 67
3.8 Experimental Measurement of Void Swelling 70
3.9 Neutron Irradiation Studies 71

4.0 RESULTS 73

4.1 Austenitic Alloys 73
    4.1.1 Alloy A (20Cr, 23Ni) 73
    4.1.2 Alloy B (20Cr, 43Ni) 75
    4.1.3 Alloy C (30Cr, 33Ni) 76
    4.1.1 Comparison of Austenitic Alloy Results 77

4.2 Transformable and Duplex Ternary Alloys 78
  4.2.1 Alloy D (12Cr, 3Ni) 78
  4.2.2 Alloy E (18Cr, 7Ni) 80
  4.2.3 Alloy F (30Cr, 13Ni) 82
  4.2.4 Comparison of Transformable and Duplex Ternary Alloys 84

4.3 Quaternary Alloys 85
  4.3.1 Austenitic Quaternary Alloys Based on Alloy A (20Cr, 23Ni) 85
    4.3.1.1 20Cr 23Ni 2Mo 85
    4.3.1.2 20Cr 23Ni 1Nb 86
    4.3.1.3 20Cr 23Ni $\frac{1}{4}$Ti 87
    4.3.1.4 20Cr 23Ni, 1 and 2 Si 88
  4.3.2 Comparison of Austenitic Quaternary Alloy Results 89
  4.3.3 Transformable Quaternary Alloys Based on Alloy E (18Cr, 7Ni) 90
    4.3.3.1 18Cr 7Ni 2Mo 91
    4.3.3.2 18Cr 7Ni 1Nb 92
    4.3.3.3 18Cr 7Ni $\frac{1}{4}$Ti 93
    4.3.3.4 18Cr 7Ni, 1 and 2 Si 94
  4.3.4 Comparison of Transformable Quaternary Alloy Results 95
4.4 Irradiation Results 97
  4.4.1 Irradiation in the HVEM 98
  4.4.2 Irradiation in the VEC 100
  4.4.3 Thermal and Irradiation Studies on 12Cr 15Ni Base Alloys Using Fast Reactor Conditions 101
    4.4.3.1 Thermally Aged Alloys 102
    4.4.3.2 Neutron Irradiated Alloys 103

5.0 DISCUSSION OF RESULTS 105

5.1 Constitution of the Fe-Cr-Ni Alloys 105

5.1.1 The Austenitic Ternary Alloys 105

5.1.2. The Austenitic Quaternary Alloys 107

5.2 Transformation and Precipitation Effects 108

5.2.1 The Austenitic Ternary Alloys 108

5.2.2. The Austenitic Quaternary Alloys 111

5.3 Constitution of the Transformable and Duplex Ternary Alloys 114

5.3.1 Constitution of Transformable Quaternary Alloys 119

5.4 Transformation and Precipitation Effects in the Transformable and Duplex Alloys 122

5.4.1 Transformation and Precipitation Effects in the Transformable Quaternary Alloys 133

5.5 Irradiation Damage Studies 137

5.6 Neutron Irradiated Alloys 142

5.6.1 Thermally Aged for 13,000 Hours 143

5.6.2 Thermally Aged Plus Neutron Irradiated for 13,000 Hours 144

6.0 CONCLUSIONS 146

6.1 Constitution of the Fe-Cr-Ni Alloys at 1050°C 146

6.1.1 Constitution of the Fe-Cr-Ni-X Alloys at 1050°C 146

6.2 Constitution of the Fe-Cr-Ni Alloys After Ageing at 400°-900°C 147

6.2.1 Constitution of the Fe-Cr-Ni-X Alloys After Ageing at 650°-850°C 148

6.3 Transformation and Precipitation Effects Occuring in Fe-Cr-Ni Alloys After Ageing at 400°-900°C 149

6.3.1 Transformation and Precipitation Effects Occuring in Fe-Cr-Ni-X Alloys After Ageing at 650°-850°C 151

6.4 Irradiation Void Swelling 152

7.0 FURTHER WORK **154**

8.0 REFERENCES **155**

TABLES 1 to 5 **162**

FIGURES 1 to 74 **167**

1.0 INTRODUCTION

Commercial stainless steels are complex alloys often containing more than eight elements. They undergo a variety of processing conditions in order to obtain the required microstructure and properties. The corrosion resistance, mechanical properties and stability of these alloys are of utmost importance when the steels are to be used for fast breeder reactor core components. Alloys in the reactor core experience temperatures in the range 350° to 650°C whilst also under the influence of fast neutron irradiation. Under such severe service conditions irradiation induced void swelling occurs and embrittlement of the steels is possible. Both these phenomena depend largely on the composition and therefore the constitution of the alloys; also any accompanying changes in solute concentration may influence the stability of the matrix.

Although there is information available on the precipitation sequences occurring in unirradiated stainless steels, there is little data published correlating the microstructural changes observed under thermal ageing conditions with those experienced under irradiated conditions. This is especially the case where more complex ternary and quaternary alloys are concerned.

It is the aim of this work to study several high purity iron based ternary and quaternary alloys. It is important that a systematic approach be adopted so that the phase stability, constitution and precipitation sequences studied in selected iron based ternary alloys can be directly compared to the quaternary alloys, thereby seeing the effect of the fourth addition on the aforementioned properties. Also alloys whose thermal behaviour is characterised in the unirradiated condition can be compared and contrasted with that observed in the irradiated state where the added problem of void swelling occurs in austenitic alloys.

Firstly, the precipitation processes occurring in the high purity iron base ternary alloys have been investigated. Six alloys have been selected, three being fully austenitic, one duplex (austenite + ferrite) and two transformable alloys. It was proposed to study the precipitation behaviour of the inter-metallic compounds sigma phase (σ) and also α' phase more commonly referred to as 475°C embrittlement, both of which can often result from the presence of delta ferrite in these alloys. The ageing characteristics were investigated by determining the ageing curves for the ternary alloys for times of up to 1000 hours and in the temperature range 400° to 900°C. Optical and electron metallography was performed in order to determine the nature of the resulting changes in microstructure, if any.

Secondly, ten quaternary alloys have been manufactured with additions of 1% and 2% silicon, 1% niobium, 2% molybdenum and $^1/_4$% titanium being made to each of two base ternary alloys, one fully austenitic and one transformable alloy. These alloys were studied in the same manner as the iron base ternary alloys thereby enabling direct comparison to be made.

A programme of irradiation damage studies has been formulated in which it was hoped that direct comparisons could be made between the thermally aged microstructure observed in certain stainless steels with that caused by the effects of neutron irradiation. Also the direct influence of individual alloying elements on void swelling behaviour has been investigated through irradiation of the austenitic iron base quaternary alloys using Variable Energy Cyclotron (VEC) simulation techniques.

In addition the High Voltage Electron Microscope (HVEM) was used to study the irradiation void swelling of two austenitic alloys.

2.0 LITERATURE SURVEY

2.1 The Ternary Iron-Chromium-Nickel System

The iron rich corner of the Fe-Cr-Ni system forms the basis for a wide range of alloys including stainless steels. These are 'stainless' because of an addition of chromium in excess of 12 wt% which causes a protective oxide coating (Cr_2O_3) to form on the surface of the steel, which greatly improves its corrosion resistance. The Fe-Cr-Ni system has been extensively investigated at temperatures above 650°C. Four equilibrium phases have been established (1, 2, 3) and confirmed by X ray diffraction (3). These are:

(i) Austenite (γ) a face centred cubic phase based on γ - iron and face centred cubic nickel.

(ii) Alpha ferrite (α) the body centred cubic, iron-rich phase, the low temperature form of iron.

(iii) Delta ferrite (δ); this generally refers to the high chromium phase but it is also a high temperature allotrope of iron. There is no crystallographic difference between δ and α.

(iv) An intermediate phase first reported present by Bain and Griffiths (4) as B-phase a hard, brittle, non-magnetic phase subsequently designated σ phase (5), usually defined as FeCr, with a body centred tetragonal structure (6).

2.1.1 The Experimental Determination of Phase Boundaries

The determination of the phase boundaries in the Fe-Cr-Ni system has been difficult and tedious. Difficult because the methods employed to distinguish between the different phases often lead to ambiguous results and tedious because many alloys undergo very slow changes especially at lower temperatures and it is not unusual to have to heat treat for several thousands of hours before equilibrium is reached.

The most essential requirement for accurate determination of the constitution of Fe-Cr-Ni alloys is that very high purity alloys should be used as even minute levels of impurities can influence the results. Alloys are usually manufactured from high purity elements, though the purest chromium often contains high levels of nitrogen and oxygen, both known austenite formers. Therefore, degassing techniques have been employed using hydrogen (7) but recently the most reliable method of high purity alloy manufacture has utilised argon arc vacuum melting techniques. The resulting alloys are heat treated under argon usually sealed in silica tubes.

Prior cold working of the alloys has often been used in order to speed up the approach to equilibrium but this has had the disadvantage of producing extremely fine microstructures which are difficult to interpret with any certainty, even with the use of sophisticated analytical equipment.

The main techniques used for constitutional work are X-ray diffraction and optical metallography. X-ray powder diffraction using a Debye-Scherrer camera is carried out on filings of experimental alloys (8,9) that have been heat treated sealed in silica tubes under argon. By using this method it is possible to know if equilibrium has not been attained as diffuse diffraction patterns will result.

Optical microscopy employs the use of etching techniques in order to distinguish between phases. Many workers have discovered that it is extremely difficult to identify ferrite from sigma phase unambiguously (6,10,12). Dulis and Smith performed a comprehensive selection of etching experiments on nine stainless steels and reported that the only method of distinguishing between constituents was to perform a three-stage etch. Firstly, picric and hydrochloric acids in alcohol to reveal all the constituents present. Secondly, alkaline ferricyanide to stain the carbides only and thirdly, electrolytic chromic acid which attacked sigma and carbide rapidly, leaving ferrite unattacked (10). It should be noted that this etch was only successful on one of their alloys and they state that the etching behaviour of ferrite may be different when it is present in other grades of stainless steels. A technique reported by Gillman (11) involved staining sigma phase using electrolytic KOH and then staining carbide with concentrated NH_4OH. This etch was successful for steels that contained no ferrite as he found both sigma phase and ferrite gave the same response.

Hattersley et al (9) used 10N KOH solution electrolytically at 2V which was supposed to allow differentiation between sigma and ferrite, by staining sigma phase a deep yellow to bronze, ferrite pale blue and leaving austenite unaffected. Jones and Hume-Rothery (12) used this same etch and reported that it was not possible to differentiate between phases unambiguously especially when sigma and ferrite exist in a fine dispersion. They utilised a potentiostatic etching method which allows selective etching of phases at particular potentials. However, ferrite and sigma both possess the same potential and therefore cannot be distinguished if they occur in the same alloy. It is worth noting that whilst the work of Hattersley et al is in good agreement with other workers, Schulz and Merrick (13) could not reproduce their etching technique.

2.2 The Iron-Chromium-Nickel Isothermal Equilibrium Diagrams

In order to design alloys for fast reactor core applications it is necessary to have a knowledge of the Fe-Cr-Ni system. This system has been extensively investigated between 650°C and the solidus and it has been discovered that there are two general forms of the diagram.

Above 900°C as can be seen from the isothermal section at 1000°C, fig.1, there are two extensive single phase regions, chromium based delta ferrite (δ) and nickel based austenite (γ) with a two phase ($\delta + \gamma$) region between them. Both δ and γ are stable at high temperatures and the duplex region persists to the solidus.

Below 900°C the diagram becomes more complex, figs.2 and 3.

Whilst the two phase (δ + γ) region is stable down to 650°C another equilibrium phase is present, sigma phase (σ), which complicates the diagram. The small single phase σ region is bounded by two three-phase regions (γ + σ + δ) and (γ + σ + α) and three two-phase regions (γ + α), (σ + α) and (σ + δ). As temperature decreases α and σ all become more stable at lower chromium contents; this effectively reduces the compositional range over which the single austenite phase is stable and extends the (α + σ) field further towards the iron rich corner of the diagram.

Several workers have produced isothermal equilibrium diagrams spanning the temperature range 650°C to the solidus. Early research by Schafmeister and Ergang (1) and Bradley and Goldschmidt (2) established the nature of the phases occurring in the Fe-Cr-Ni system and the general outline of the phase diagram but there remained discrepancies in the definition of the phase boundaries. These early investigators used experimental alloys which contained impurities which are known to have an influence on constitution, such as silicon (1), a ferrite former, and nitrogen and oxygen (2), both austenite forming elements. The presence of these elements in extremely small amounts shifts the phase boundaries. Work performed by Rees et al (7) in 1949 on the constitution of the Fe-Cr-Ni system utilised very high purity, degassed alloys. They produced isothermal equilibrium diagrams over the temperature range 650° to 800°C which are in good agreement with present day results. Published constitutional work up to 1950 was evaluated by Andrews (14) who produced a comprehensive set of isothermal equilibrium diagrams for temperatures of 650°C up to the solidus.

Constitutional work on the ternary system below 650°C was performed by Cook and Brown (15) using high purity alloys manufactured in the same manner as Rees et al. They investigated the 550° to 800°C temperature range. Unfortunately at low temperatures such as 550°C changes in the alloys were extremely slow. Heat treatment times of up to two years did not always produce equilibrium structures, and this was manifested in the diffuse X-ray diffraction patterns they obtained. The ternary diagram they produced at 550°C is shown in fig.4.

Many workers have studied the Fe-Cr-Ni system at 650°C and upwards (1-5,7,9,12-15). The $(\gamma + \alpha + \sigma)$ triangle has been well defined (7,15) from work using high purity alloys, as are the boundaries of the two phase region $(\alpha + \gamma)$ (8,15). Cawley (16) however found that the $(\gamma + \sigma)$ and the $(\gamma + \alpha + \sigma)$ regions were stable at marginally lower chromium and higher iron contents than reported, fig.5. He also found the $(\delta + \sigma + \gamma)$ region extended to higher chromium levels as temperature decreased.

It is of great importance that the constitutional behaviour of Fe-Cr-Ni alloys below 650°C is understood especially in the case of steels used in fast reactor cores, as they remain in the 300-650°C temperature range for many years. Therefore several workers have attempted to calculate equilibrium diagrams using basic thermodynamic data. Sections have been calculated by Kaufman and Hillert et al

(17,18) down to 500°C. The techniques used to calculate these diagrams are complex but basically they involve using experimentally determined thermodynamic functions such as the free energy of formation of the phases present. Their results are in agreement with experimentally determined diagrams (8,15).

Rivilin and Raynor (19) produced a comprehensive critical review of the constitutional work available up to 1980. It presents experimentally determined isothermal equilibrium diagrams as well as calculated diagrams and compares and contrasts the various published work. Recent constitutional work by Cawley (16) is in good agreement with the results presented in the Rivilin and Raynor review (19), especially at temperatures above 800°C.

2.2.1 Effects of Alloying Elements on the Iron-Chromium-Nickel System

The alloys suitable for fast reactor core components consist of complex stainless steels made up from a large number of elements in order to give them their required mechanical, creep and corrosion

Insert B The cladding is fabricated from austenitic stainless steels such as 20% cold worked M316 and FV548, wrapper materials include solution treated and aged Nimonic PE16 and 321 austenitic stainless steel. 12%Cr martensitic alloys are now being considered due to their superior resistance to void swelling.

(17,18) down to 500°C. The techniques used to calculate these diagrams are complex but basically they involve using experimentally determined thermodynamic functions such as the free energy of formation of the phases present. Their results are in agreement with experimentally determined diagrams (8,15).

Rivilin and Raynor (19) produced a comprehensive critical review of the constitutional work available up to 1980. It presents experimentally determined isothermal equilibrium diagrams as well as calculated diagrams and compares and contrasts the various published work. Recent constitutional work by Cawley (16) is in good agreement with the results presented in the Rivilin and Raynor review (19), especially at temperatures above 800°C.

2.2.1 Effects of Alloying Elements on the Iron-Chromium-Nickel System

The alloys suitable for fast reactor core components consist of complex stainless steels made up from a large number of elements in order to give them their required mechanical, creep and corrosion resistant properties. Insert B Materials in the reactor core have to be microstructurally stable over their life time in the core where they will normally experience temperatures in the range 300° to 650°C, and occasionally higher temperatures in the hot spots. Any changes in the composition of the stainless steels directly affects their constitution and/or microstructure and it is this resultant microstructure that determines the properties of the alloys.

The behaviour of complex steels in thermal and irradiation environments cannot be understood until the behaviour of simple ternary and quaternary systems have been established as these are the basic building blocks on which alloy design depends.

Stainless steels encompass a wide range of alloy compositions and can lead to a variety of microstructures, i.e. austenitic, ferritic, martensitic and duplex ferrite-austenite. The microstructures are further complicated by the presence of intermetallic phases and carbides and in the case of austenitic steels the carbide form $M_{23}C_6$ is frequently observed.

Carbon is a common interstitial element present in stainless steels and is, along with nitrogen, an austenite forming element. It can be seen from the iron-chromium binary system, fig.6, that chromium restricts the γ-loop to the extent that above 13%Cr the binary alloys are ferritic over the whole temperature range. This ferrite is referred to as delta ferrite (δ) and the phase can exist from the melting point to room temperature. The addition of carbon to the alloy extends the γ-loop to higher chromium contents; it also widens the $(\alpha + \gamma)$ phase field. If enough carbon is added to an 18%Cr steel it can be made fully austenitic on cooling rapidly from the γ-loop region. However, the second effect of carbon is to introduce carbides into the microstructure. Carbon effectively combines with the chromium thereby depleting the matrix of both elements thus destabilising the austenite and having detrimental effects on corrosion resistance.

Lismer et al (20) have described the effect of carbon on the microstructure in terms of a shift in the $\gamma / (\gamma + \sigma)$ phase boundary to enlarge the γ phase field. Unfortunately their experimental alloys contained silicon and manganese which will have some influence on their results. Also, an isothermal treatment time of only four hours was used for temperatures down to 950°C, probably resulting in non-attainment of equilibrium.

Pryce et al (21) studied the influence of silicon on a 25%Cr 15%Ni alloy as a sigma phase former. They concluded that silicon is a powerful sigma phase forming element which is three times greater in its sigma forming capability than is chromium. They also confirmed earlier work (20) that increasing the carbon content tends to promote a wholly austenitic structure at solution treatment temperatures. Again their alloys contained manganese whose role as an austenite former is doubtful at lower temperatures.

Work was performed on a large number of alloys by Nicholson et al (8) who attempted to quantify the effects of silicon, manganese and molybdenum on the isothermal 650°C section. They reported that the effect of silicon was to displace the $\gamma/(\gamma + \sigma)$ boundary towards lower chromium contents, for all nickel contents below ~20%. They noted that the effect of silicon on the $\gamma/(\gamma + \sigma)$ boundary shift was reduced for increasing nickel contents of the alloys. The effect of manganese was uncertain although they observed that an addition of 2%

molybdenum displaced the $\gamma/(\gamma + \sigma)$ boundary by approximately 3% chromium, towards lower chromium contents.

Work by Irvine et al (22) on controlled transformation stainless steels showed the effects of several austenite and ferrite formers on a 17%Cr, 4%Ni base alloy. They produced graphs that compared the effect of various alloying elements on the constitution of a 0.1%C, 17%Cr alloy, fig.7. Nickel proved to be the most powerful of the substitutional austenite formers. The interstitial elements carbon and nitrogen are also austenite formers but can only be tolerated in small amounts due to the corrosion and welding problems incurred. Both these elements combine readily with many ferrite forming additions to produce carbides, nitrides and carbonitrides, thus decreasing the effect of the ferrite formers as these are only effective when in solid solution. Silicon was again shown to be a potent ferrite forming addition, 2% causing 16% delta ferrite to be present in the 17%Cr, 4%Ni base alloy, whilst molybdenum gave 20% delta ferrite content in the same alloy for only a 2% addition and also improved its high temperature properties, fig.7b.

Hattersley and Hume-Rothery (9) investigated the effect of 2% titanium on the constitution of certain austenitic stainless steels suitable for use in nuclear applications. They agreed with other workers that titanium stabilises both ferrite and sigma phase, thus contracting the austenite phase field, and that titanium raises the upper temperature limit of sigma phase stability. They produced chromium equivalents for titanium as determined by its effect on the boundary of the austenite field. These were 1.2 at 1050° to 1150°C where δ is the equilibrium second phase, 1.9 at 950°C where σ is the equilibrium second phase and 1.3 at 700°C where precipitation of the phase Ni_3Ti along with the sigma phase complicates the situation. When the solubility limit of titanium in austenite is exceeded the Ni_3Ti phase is formed as an equilibrium phase. The precipitation of this phase reduces the amount of nickel in the matrix thereby decreasing the extent of the austenite phase field but it also reduces the amount of titanium in solid solution thereby decreasing its effect as a ferrite former.

Binder (23) investigated 18%Cr, 8%Ni steels containing up to 3% niobium. He found niobium to be a weak ferrite former as it readily formed carbides of the type NbC and the intermetallic phase Fe_2Nb when heat treated in the 600° to 800°C temperature range.

Schultz and Merrick (13) studied the effect of various ferrite formers on the nickel rich corner of the Fe-Cr-Ni system, fig.8. Alloys containing between 24-40%Cr with 20%Fe, balance Ni, were investigated. Titanium, silicon and niobium were all found to stabilise the delta ferrite phase; they also detected the Ni_3Ti phase between 816° and 898°C in alloys containing 1.5% titanium.

Recent constitutional work by Cawley (16) using very high purity quaternary alloys has shown that at high temperatures (1050°C) silicon is a very effective delta ferrite former whilst molybdenum, niobium and titanium are less potent in their effect, by comparison, due to their tendency to form carbides and, in the case of niobium, also Laves phase. Therefore, precipitation of these carbides reduces the delta ferrite forming capabilities of the alloy additions and reduces the effect of carbon in stabilising the austenite phase. At 800°C Cawley found that silicon was a less potent sigma phase former than a ferrite former. Both molybdenum and titanium are effective sigma phase formers after the effect of carbide precipitation is taken into account. The sigma forming capabilities of niobium were small when compared with molybdenum and titanium, and Cawley did not detect the presence of Laves phase at this temperature.

Shao and Machlin (24) used the experimentally derived isothermal equilibrium diagrams for the Fe-Cr-Ni system of Cook and Brown (15) and Rees et al (7) as a basis for calculating the effects of a fourth alloying element addition on the ternary phase boundaries at 600° and 650°C. They used the thermodynamic free energy data of Kaufman et al (17) and took into account the effects of carbide precipitation to produce a series of pseudo-equilibrium diagrams for a number of commercial alloy compositions.

From their calculated diagrams it was obvious that molybdenum, titanium, silicon and niobium all stabilised sigma phase formation by enlarging the $(\gamma + \sigma)$ and $(\gamma + \alpha + \sigma)$ regions. Their calculated results compared favourably with Nicholson's (8) experimental observations.

2.3 Intermetallic Phases

Several species of intermetallic phase have been observed in commercial stainless steels (25). Most of these phases are incoherent, hard, brittle and have a tendency to precipitate on the grain boundaries and are thus detrimental to the mechanical properties of the alloy. Precipitation of these phases depletes the matrix of important solid solution elements leading to a reduction in the corrosion resistance.

Decker and Floreen have published a review (25) in which they discuss a large number of intermetallic phases that can precipitate in iron based alloys and have produced a table which shows the major types of intermetallic compounds that can occur between various elements commonly found in stainless steels, Table 1.

2.3.1 Sigma Phase

Sigma phase formation tends to occur in binary alloys containing one element from group VA or VIA of the periodic table. Fifty three examples of binary sigma phases have been reported (26).

The sigma phase which occurs in the Fe-Cr-Ni system is a very hard, brittle constituent and is renowned for its detrimental effects on the mechanical properties of stainless steels. It is particularly troublesome when alloys are exposed for long periods at high temperatures, as in nuclear applications.

Sigma phase has a tetragonal close packed crystal structure (6,27) and it exists over a wide compositional range, 25%-60%Cr, in iron chromium alloys. It can also form in chromium nickel austenites where chromium exceeds 17% (8). The phase is usually defined as FeCr but it can dissolve significant amounts of nickel and other elements. It has lattice parameters of $a_0 = 8.7995$ Å and $c_0 = 4.5442$ Å (28) although these can vary slightly depending on the amount and types of alloying element present in it.

Alloying elements modify the conditions of sigma phase formation by their effects on the precipitations kinetics or phase equilibria. Carbon and nitrogen as interstitial solid solutions affect the diffusion rate; they also form compounds which denude the matrix of chromium and therefore retard sigma formation (20,29).

Silicon, molybdenum, niobium and titanium are all ferrite formers and therefore accentuate sigma phase formation; silicon and molybdenum also extend the stability range of the sigma phase to higher temperatures when they are dissolved in it (23,30).

The sigma phase exists as a single equilibrium phase in the Fe-Cr system over the composition range 46-52% Cr, fig.6. The upper limit for its stability is 810°-820°C (15) after which it decomposes to ferrite. This boundary limit for sigma phase stability is still by no means certain as the kinetics of the transformation are sluggish.

In ternary Fe-Cr-Ni alloys the upper temperature limit for sigma formation is 925°C. The transformation rate of the sigma phase is a function of temperature and passes through a maximum. For an austenitic 25%Cr, 20%Ni steel the maximum rate is reported as being at 815°C (31). In the case of a duplex 25%Cr, 8%Ni alloy the maximum rate was observed at 730°C and the upper temperature limit of its formation at 840°C (32). Transformation rate also depends on the grain size of the alloy, and the rate of formation of sigma is enhanced by cold work due to an increase in diffusion rates (33) or by increasing the nuclei generated by cold work (34).

The sigma phase has been observed to exhibit an orientation relationship with the austenite matrix of

$$(111)_\gamma \parallel (001)_\sigma \quad ; \quad [001]_\gamma \parallel [140]_\sigma \qquad (35,36)$$

and

$$(111)_\gamma \parallel (001)_\sigma \quad ; \quad [110]_\gamma \parallel [110]_\sigma \qquad (37)$$

2.3.2 Laves Phase

The Laves phase has a hexagonal crystal structure. It is based on the chemical compositions Fe_2Nb or Fe_2Mo although it can dissolve other elements and has been given the more general formula of $(Fe, Mn, Cr, Si)_2\ (Mo, Ti, Nb)$ (38).

Silicon, niobium (39) and titanium (25) have all been observed to promote Laves formation.

Denham et al investigated the Fe_2Nb type Laves phase with a view to using it as a precipitation hardening phase in a 16%Cr, 16%Ni steel (39). Tensile testing of the alloy at 700°C produced cracking at the grain boundaries after only small elongations and it was concluded that grain boundary Fe_2Nb formation was deleterious to ductility.

Sasmal (40) observed Laves phase formation in a 316L alloy and saw that it precipitated on the grain boundaries before sigma phase precipitation began. Brown et al (41) also observed Laves phase precipitation at the ferrite grain boundaries in a 25%Cr-3%Mo-4%Ni steel stabilised with niobium and titanium, its growth being seen to be inhibited by later sigma phase precipitation.

Weiss et al (42) investigated phase instabilities in 316 alloys and found that Laves phase precipitated intragranularly as equiaxed particles or clusters of particles. They rarely saw Laves phase precipitated on the grain boundaries, although this was most probably due to $M_{23}C_6$ precipitates occupying the grain boundary sites, as these precipitate prior to Laves phase formation. Cold work appeared to accelerate the Laves phase formation, probably due to the increased diffusivity of the Laves forming elements. High carbon content delayed the appearance of Laves phase to much longer ageing times, as $M_{23}C_6$ formation was promoted.

Laves phase has been observed to have an orientation relationship with austenite.

$$(0001)_{Fe_2Nb} \parallel (111)_{\gamma} \; ; \; [1010]_{Fe_2Nb} \parallel [110]_{\gamma} (39)$$

and

$$(1113)_{Fe_2Mo} \parallel (111)_{\gamma} \; ; \; [1210]_{Fe_2Mo} \parallel [121]_{\gamma} \; (43)$$

The Fe_2Nb Laves phase has lattice parameters of a_0 = 4.831A and c_0 = 7.761Å (28) and in a 316 alloy was observed to have lattice parameters of a_0 = 4.730Å and c_0 = 7.720Å (37). The Fe_2Mo Laves phase has reported lattice parameters of a_0 = 4.730Å and c_0 = 7.740Å (28).

2.3.3 Chi Phase

The discovery of a new phase, "chi", was first reported by Andrews and Brooks (44) who observed its presence in steels containing nickel, chromium and molybdenum. Work by McMullin et al (45) on the Fe-Cr-Mo system established that chi phase was an equilibrium phase in that system.

Chi phase is observed in stainless alloys when either titanium or molybdenum is present. The phase can consist of a number of elements giving it the possibility of existing over a variety of compositions (25), even some as complex as $(Fe_{27}Ni_{18}Cr_{13})(Mo_{5.5}Ti_{4.5})$ which occurred as a massive block morphology on the grain boundaries of a 16%Cr-24%Ni-2.7%Ti-5.6%Mo steel after ageing for <10 hours at ~650°C (46).

Chi phase is believed to be a carbon dissolving compound which can behave as an intermetallic phase or as a carbide (47). The chi phase that was observed in a 316 alloy (42) precipitated on the grain boundaries and the incoherent twin boundaries, and after 100 hours of ageing at 815° it was precipitated intragranularly. It was frequently observed that chi phase particles were in close contact with the remnants of carbide particles. Both rod and massive block shapes were seen in the alloy and prior cold working accelerated the nucleation of the chi phase.

The chi phase has a body centred cubic crystal structure with a lattice parameter of $a_0 = 8.885\text{Å}$ in a 12Cr4Mo alloy (48) and with a lattice parameter of $a_0 = 8.920\text{Å}$ in Cr-Ni-Mo steels (44). It has been observed to have an orientation relationship with austenite:

$$(110) \parallel (111)_\gamma \ ; \quad [110] \parallel [011]_\gamma \qquad (42,44)$$

2.3.4 G Phase

The presence of this phase was first reported by Beattie and VerSnyder (49) who observed it in a 15Cr-20Ni alloy which contained small amounts of Mo, Ti, Si, V and Al. They found that the phase was associated with silicon, there being a direct relationship between the amount of silicon added and the abundance of G phase in the alloy. X ray diffraction showed G phase to have a face centred cubic crystal structure with a lattice parameter of 11.20Å. It has since been observed in other alloys similar to Beattie and VerSnyder's composition when either titanium or niobium are present along with 3% or more of silicon (25). It precipitates along the grain boundaries and is generally globular in its morphology. G phase exhibits the same orientation relationship as $M_{23}C_6$ in austenite:

$$(100)_{G\ phase} \parallel (100)_{\gamma} \quad ; \quad [100]_{G\ phase} \parallel [100]_{\gamma}$$

2.3.5 Eta and Gamma Prime Phases

These phases are more commonly associated with superalloys and are responsible for providing age hardening and creep resistance. The face centred cubic γ', that is the $Ni_3(Al,Ti)$ or Ni_3Al phases, has been observed in austenitic stainless steels containing 12-25%Ni with up to 18%Cr when alloyed with a few percent of aluminium or titanium either singly or in combination. In a steel free from aluminium an intermediate γ' form of Ni_3Ti precipitates before the formation of the equilibrium eta-Ni_3Ti, which is close packed hexagonal in structure (50).

The coherency of the γ' precipitate and its spherical morphology have rendered this intermetallic phase useful in superalloys and high temperature creep resisting steels, providing matrix strength due to the coherency strains associated with the precipitate inhibiting dislocation movement. However, in iron based austenitic steels the approach to equilibrium causes the replacement of the γ' transition phase by eta phase and this transition has often been associated with the deterioration in mechanical or physical properties (22). This is due to eta phase precipitating as a cellular structure on the grain boundaries at low temperatures or in a Widmanstatten form within the austenite grains. The orientation relationship within the cellular structure is

$$(0001)_{Ni_3Ti} \parallel (111)_{\gamma} \quad ; \quad [1210]_{Ni_3Ti} \parallel [011]_{\gamma} \quad (50)$$

2.4 Carbide Phases

2.4.1 $M_{23}C_6$

The carbide precipitate most commonly observed in heat treated stainless steels is of the form $M_{23}C_6$. This is basically a chromium carbide although other elements such as iron and molybdenum are known to substitute in it. $M_{23}C_6$ therefore is often reported as $(Cr,Fe,Mo)_{23}(C)_6$. It has a face centred cubic crystal structure with a lattice parameter of a_0 = 10.638 Å (28) for a $(Fe,Cr)_{23}(C)_6$ precipitate. In 316 molybdenum containing steel the lattice parameter of the $(Cr_{16},Fe_5,Mo_2)\ C_6$ precipitate was given as a_0 = 10.676 Å; the lattice parameter of $M_{23}C_6$ increases with increasing molybdenum content (42).

Several workers have studied the morphology and precipitation sequences of $M_{23}C_6$ (42,51,52,53). The carbide has been observed to precipitate successively on grain boundaries, incoherent twin boundaries, coherent twin boundaries and finally intragranularly (42,52,53). $M_{23}C_6$ has also been seen to nucleate on normal edge [110] dislocations and join together either corner to corner or face to face, according to the orientation of the dislocation. The precipitation of $M_{23}C_6$ on non-coherent twin boundaries grows out from the boundary and into the matrix by precipitating on partial [112] dislocations. $M_{23}C_6$ is almost cubic in shape and is bounded by {111} and {110} planes (53).

The $M_{23}C_6$ phase has an orientation relationship with the austenite matrix of

$$(100)_{M_{23}C_6} \quad || \quad (100)_{\gamma} \quad ; \quad [100]_{M_{23}C_6} \quad || \quad [100]_{\gamma} \qquad (52)$$

2.4.2 MC

The solubility of carbon in austenite at 1100°C is 0.1% (54), but at 700°C and below the amount of carbon that is soluble in the austenite is extremely small. The presence of nickel also increases the solubility of NbC, especially at high temperatures. Rapid quenching from high temperature produces supersaturation of carbon in the austenite at room temperature so that at service temperatures carbides will precipitate out of the matrix, thus depleting it in chromium. This causes the corrosion resistance of the alloy to be reduced. Elements such as titanium and niobium are added to the steel in order to stabilise the carbon. These additions are all ferrite and sigma phase formers and therefore austenite formers such as nickel have to be increased so as to retain an austenitic structure at room temperature. The elements added to stabilise carbon form carbides of the MC type. This effectively means that carbon is removed from solution by the precipitation of the MC, preventing chromium carbide precipitation from taking place.

Titanium and niobium carbides of the MC type have lattice parameters of $a_{0\ TiC} = 4.360\text{Å}$ and $a_{0\ NbC} = 4.470\text{Å}$ respectively. Both have face centred cubic crystal structures and have a cube on cube orientation relationship with the austenite matrix of

$$(100)_{MC} \parallel (100)_{\gamma} \quad ; \quad [100]_{MC} \parallel [100]_{\gamma}$$

These MC type carbides have been found to be useful in precipitation hardening alloys, as a fine dispersion of the carbide within the matrix can be achieved.

2.5 Transformations Occurring in Austenitic Stainless Steels

Austenitic stainless steels were essentially designed for environments where they would be expected to retain their mechanical properties after long exposures at high temperatures such as occur in fast breeder reactor cores. In such cases it is imperative that the embrittling intermetallic sigma phase does not form.

Several workers (8,34,36) have studied the formation of sigma phase from highly alloyed austenite. Nicholson et al (8) showed that, in steels containing over 17% chromium, sigma phase can precipitate directly from the austenite. They produced a diagram in which commercial stainless steel compositions are superimposed on the Fe-Cr-Ni phase diagram at 650°C, fig.9. This highlights the fact that austenitic stainless alloys are just as capable of developing the sigma phase as duplex steels and that several commercial alloys are potentially capable of precipitating sigma phase. In their 25%Cr-20%Ni alloys sigma phase was formed in the temperature range 540°-925°C; partitioning of the alloying elements present accompanying its formation. The sigma phase was found to be rich in chromium, the matrix being depleted in chromium and therefore enriched in nickel. This depletion of chromium from the matrix is detrimental to both corrosion and creep resistance.

Emmanuel (31) studied type 310 stainless steel and found that sigma phase formed directly from the austenite matrix when the alloy was held between 595°-872°C; the rate of transformation was a maximum at ~815°C and the sigma phase did not precipitate above 938°C. Prior cold working of the alloy increased the rate of sigma precipitation and also depressed the lower temperature at which the phase existed to ~550°C.

Dulis and Smith (10) also reported that cold working accelerated sigma formation and suggested that cold deformation produced more nuclei of sigma which grow after recrystallisation. Lena and Curry (34) suggested that it was recrystallisation itself which accelerated the transformation to sigma phase. They noted that the recrystallisation transformation resulted in two morphologies of the sigma phase, one being similar to pearlite with alternate plates of sigma and recrystallised austenite, while the other consisted of the sigma phase predominantly at the recrystallised grain boundaries. This later form was favoured by the rapid recrystallisation rates caused by moderate cold work prior to exposure at high temperatures or in heavily cold worked samples at moderate temperatures.

The actual mechanism of the austenite transformation to sigma phase is controversial. Firstly it must be ensured that the alloys being investigated are fully austenitic with no traces of delta ferrite present on the grain boundaries. Several workers have achieved this and have noticed that sigma phase formation is in some way connected with $M_{23}C_6$ precipitation. Goldschmidt (47) suggested that the decarburisation of $M_{23}C_6$ resulted in a topochemical transformation of the carbide to sigma phase and austenite.

Dulis and Smith's (10) investigations of a fully austenitic 17.8%Cr-12.5%Ni-2%Mo alloy reported that at 815°C the $M_{23}C_6$ precipitated on the austenite grain boundaries before the sigma phase formed on the boundaries. It was suggested by Folley in discussion of their findings (10) that the carbides could be nucleating the sigma phase.

Lismer et al (20) studied the precipitation of sigma phase from both austenitic and austenite-carbide structures in 25%Cr-15%Ni alloys at 700°-900°C and presented an hypothesis for the transformation. They suggested that as the carbide precipitates from the matrix the austenite alters its composition and becomes depleted in chromium and carbon. This will reduce the tendency for sigma to precipitate spontaneously from the austenite. Coalescence of the carbide occurs at the grain boundaries and when the critical size is attained or unknown critical conditions become favourable, the carbide breaks down to form sigma phase. As the growth of carbide is ongoing throughout the heat treatment, the tendency to form sigma phase will increase. This process continues until the increasing nickel content of the austenite secures its stability.

Further work by Pryce et al (21) performed on the same alloys confirmed that carbides were precipitated before the sigma phase and that, after long ageing times, were seen to replace the sigma phase to some extent.

Pickering (55) also reported that the precipitation of sigma phase was associated with $M_{23}C_6$ presumably by some cellular kind of reaction as a nodular type of precipitate was observed on the austenite grain boundaries.

Lewis (36) investigated the precipitation of sigma phase at 750°C from a 21%Cr-27%Ni alloy whose composition lies near the equilibrium phase boundary for sigma formation. The alloy contained titanium, aluminium and silicon and all these elements move the phase boundary in favour of sigma phase formation. He observed that the sigma phase first formed on the grain boundaries after 100 hours of ageing but did not appear within the grains until 600-700 hours of ageing time. The sigma precipitated in the form of thin plates parallel to the {111} matrix planes, the orientation relationship of Nenno et al (35) being substantiated. Lewis reported that the sigma phase was associated with TiC precipitates and he postulated a nucleation mechanism for the sigma phase. At equilibrium, when carbon is removed from solution, TiC precipitates grow by Ostwald Ripening, that is dissociation of smaller particles and growth of larger ones after diffusion of the constituent atoms preferentially along connecting dislocations. These dislocations which are pinned to the particle interfaces make ideal sites for sigma nuclei. There exists a concentration of titanium near the dislocations which may be extended to form a small region of stacking fault. A region of (111) stacking fault would form a suitable nucleus for sigma phase. The transformation of austenite to sigma phase can only occur if there is also accompanying diffusion of iron and chromium atoms.

The investigation by Blenkinsop and Nutting (56) of the precipitation of the sigma phase in an AISI 316L austenitic stainless steel set out to study the mode of nucleation and growth of sigma and examine its association with $M_{23}C_6$, in order to resolve conflicting hypotheses (10,20,47,55). They solution treated at 1100-1300°C and aged their alloys between 600°-850°C, and discovered that at 700°C sigma phase could nucleate directly on the grain boundaries in austenite and was not nucleated by the carbide. They reported that at high temperatures, above 750°C, $M_{23}C_6$ in fact nucleated first and restricted the nucleation and growth of the sigma phase. They reasoned that as both sigma phase and carbide contain essentially the same elements they are competing with each other. Extensive growth of either phase would be expected to restrict the formation of the other. They produced a schematic diagram based on their results, fig.10, showing the precipitation curves for sigma phase and $M_{23}C_6$ after solution treatment at 1300°C. Solution treating at lower temperatures, eg 1100°C shifts the sigma phase curve to higher temperatures, which allows the carbide phase to become dominant at lower temperatures.

Singal and Martin (57) suggest that high energy interfaces such as high angle grain boundaries, incoherent twin boundaries and the high energy surfaces of second phase particles, eg oxide inclusions, are required to nucleate the sigma phase. Weiss and Stickler (42) supported this view in their work on a 316 alloy, after seeing sigma phase nucleate at austenite triple points firstly and then on the grain boundaries. They state that sigma phase does not nucleate homogeneously within the matrix but always requires a high energy interface. They also reported that at 400°C and above they saw sigma phase particles which had nucleated on the grain boundary triple points with no evidence of $M_{23}C_6$ being present. However, at higher temperatures of 815°C sigma was associated with $M_{23}C_6$. The orientation relationship proposed by Nenno et al (35) was again substantiated.

In their examination of a 321 stainless steel aged for 17 years at 580°C Bentley and Leitnaker (58) reported that the majority of the sigma phase was on the grain boundaries and that sigma phase was nucleated within the austenite grains without the presence of a high energy interface, thus disagreeing with other workers (42,57). They also compared the growth of sigma phase with that of $M_{23}C_6$ and TiC, noting that the carbides bear a strong relationship with the matrix and can both nucleate easily and grow rapidly. Sigma phase on the other hand nucleates with difficulty and grows slowly.

Considering all these findings on the transformation of the austenite to the sigma phase the theory of Blenkinsop and Nutting best explains their own results and those obtained by other workers in this field. At lower temperatures sigma phase is often seen as the dominant phase, whilst at high temperatures $M_{23}C_6$ is largely dominant. There remains a large temperature region where the phases coexist and it is within this temperature range, ~750°-900°C, that diffusion reactions between the two phases are quite likely to occur.

The precipitation of sigma phase from austenite is exceedingly sluggish and may only occur after several thousands of hours of heat treatment. This is especially the case for fully austenitic steels held at lower temperatures ~500°-600°C.

2.6 Transformations Occurring in Duplex Stainless Steels

A duplex stainless steel consists of a mixture of austenite (γ) and delta ferrite (δ). The presence of as little as 1% δ in an austenitic matrix will increase the tensile strength by ~2.2MNm^{-2}. Delta ferrite also provides grain refinement of the austenite, producing additional strengthening.

Several workers have investigated the transformations occurring in duplex alloys above 600°C and have found that the sigma phase transformation occurs much more rapidly in duplex steels than in fully austenitic steels (6,20,21,55). The sigma phase formation in these alloys was found to be associated with the δ regions (6,20,55). Pickering (55) studied the formation of sigma phase in austenitic and duplex alloys based on 25%Cr-15%Ni. He observed that the sigma phase precipitated out more rapidly in the duplex alloy, the δ regions transforming to an aggregate of γ + σ which grew in from the γ/δ boundary to consume the δ grain.

Work performed by Beckitt (32) on a 25%Cr-8%Ni base alloy set out to investigate the formation of sigma phase from duplex alloys using thin foil electron microscopy. His alloys after solution treatment at 1250°C contained ~40% by volume of δ and ~60% of γ, with a very fine precipitate observed on the grain boundaries, which was assumed to be $M_{23}C_6$.

The alloys were aged at 700° and 900°C. At 700°C, after one hour, cellular $M_{23}C_6$ and γ was seen on the grain boundaries and after four hours laths of austenite were observed growing into the δ grains. The austenite laths occurred as an isolated phase within the δ regions as well as occasionally being in contact with the γ/δ grain boundaries. Large irregular precipitates of sigma phase were dispersed between the austenite laths at the grain boundaries, but no cellular structure was observed. The austenite laths that were in contact with the γ/δ boundary possessed the same orientation relationship as the austenite grain, that is the Kurdjumov and Sachs relationship

$$(111)_\delta \;||\; (110)_\gamma \quad ; \quad [110]_\delta \;||\; [111]_\gamma$$

The sigma phase was observed to form at the interface between the cellular austenite and the delta ferrite. It adopted an orientation relationship only with the austenite in which it was initially in contact. This orientation relationship is close to that proposed by Nenno et al (35).

$$(111)_\gamma \;||\; (001)_\sigma \quad ; \quad [110]_\gamma \;||\; [110]_\sigma$$

After 25 hours ageing the majority of the remaining delta ferrite had transformed to a coarse sigma/austenite aggregate.

The ageing behaviour at 900°C was similar to that at 700°C in the early stages. The $M_{23}C_6$ had grown into the δ grain as small plates with areas of new austenite between the plates forming a cellular structure. This $M_{23}C_6$ adopted an orientation relationship with the austenite grain which it was in contact with, namely,

$$(100)_{M_{23}C_6} \,||\, (100)_\gamma \;; \qquad [100]_{M_{23}C_6} \,||\, [100]_\gamma$$

the new austenite again having the same relationship as the austenite grain. After ageing for greater than four hours the amount of new austenite in the cellular precipitate increased. No transformation to sigma phase took place.

Grain boundaries have previously been seen to be preferred sites for the precipitation of $M_{23}C_6$ (51,52). Beckitt suggested that the γ/δ boundary was favourable for $M_{23}C_6$ nucleation as it is the junction between chromium rich δ and carbon rich γ. The orientation relationship he quoted between $M_{23}C_6$ and the austenite in which it nucleated is in agreement with that found in fully austenitic alloys by other workers (51,52,53).

Beckitt (32) observed that the formation of sigma phase was confined to the prior delta ferrite regions; this again has been reported by others (6,7,20,55). He produced a C curve for sigma formation showing the maximum rate occurring between 700-750°C, fig.11, which compares favourably with the C curves produced by Blenkinsop et al (56) for a fully austenitic alloy, fig.10, and with Shortsleeve et al (59) for sigma formation from a fully ferritic alloy, fig.12.

As well as the possibility of sigma phase precipitation occurring in duplex alloys there is another phenomena which adversely affects mechanical properties. This is the precipitation of a very fine coherent chromium rich phase α', more commonly referred to as 475°C embrittlement as it is observed when heat treating steels in the temperature range 450°-550°C. The α' phase precipitates only from the delta ferrite phase (60-63). Prior to 1951 the observed embrittlement at 475°C was attributed to sigma phase formation. However Heger (64) suggested that the embrittlement was a precipitation hardening reaction caused by the formation of a transition phase occurring before the equilibrium transformation to sigma phase. This transition phase was coherent with the matrix, the coherency strains being responsible for 475°C embrittlement, and as the transition phase dissolved in favour of the equilibrium sigma phase formation an overageing response would result.

Fisher et al (65) extracted this transition phase and identified it as having a body centred cubic structure with a lattice parameter of $a_0 = 2.878$Å, which contained 85%Cr and 15%Fe. Both workers (64,65) decided that the chromium rich α' precipitate was metastable and would dissolve to provide chromium atoms for the formation of the equilibrium sigma phase. They stated that the formation of the precipitate was hard to explain. The Fe-Cr phase diagram indicated that ferrite and sigma should be stable in their

27%Cr equilibriated alloy but on exposure at 475°C the alloy preferred to separate into iron rich and chromium rich ferrites.

Williams and Paxton (66) published a partial phase diagram of the Fe-Cr system showing the miscibility gap implied by Fisher et al. They reported that the 475°C embrittlement was a precipitation hardening phenomenon and that the precipitate was a result of the miscibility gap in the Fe-Cr system. This miscibility gap is connected by a eutectoid reaction at 520°C to the region where sigma phase is stable, fig.13.

The precipitation of the chromium rich α' phase has been reported to occur by spinodal decomposition at high chromium contents, or by nucleation and growth at lower chromium contents (62,63,66,67) and the phase occurs as fine spherical zones that at high temperatures develop into discs on {100} ferrite planes. The embrittling phenomenon becomes more pronounced with increasing chromium content, the maximum effect being observed at 40wt%Cr (60).

It is now widely accepted that 475°C embrittlement is caused by the α' precipitate which forms because of the miscibility gap in the Fe-Cr system (60,70). There is evidence to suggest that a nucleation and growth mechanism is operative, hardness versus time curves having shown that there is an incubation time before hardening begins (63). The slow growth rate of the α' precipitate and hence the extremely slow overageing reaction has been explained by Lagneborg (67) who suggested that the α' particles grow by coalescence and therefore the hardness of the alloys will remain constant for long ageing times. Ludwigson et al claim to have overaged the α', in a 16%Cr alloy which was held at 482°C for 10,000 hours (68).

It has been reported that carbon and nitrogen increase the embrittlement (62,63) but the effects of these elements are confusing as they both undergo precipitation reactions themselves. 475°C embrittlement can be distinguished from embrittlement caused by carbide and nitride precipitation as it can occur even after tempering. Courtnall et al (62) showed that carbon, nitrogen, titanium, niobium and molybdenum all increase the rate of age hardening caused by the α' precipitate.

Solomon et al (69) have studied the 475°C embrittlement of both duplex and ferritic alloys using Mossbauer spectroscopy and transmission electron microscopy and have produced a Fe-Cr-Ni ternary phase diagram using their results augmented by computer calculated data. They have assumed that sigma phase formation does not occur and they state that the boundaries (γ + α' + α) region are open to question, fig.14.

Southwick et al (70) studied the decomposition of delta ferrite to austenite in a 26%Cr-5%Ni steel. They found that the decomposition took place via two mechanisms, firstly nucleation and growth in the high temperature range 650°-1200°C and secondly by an athermal martensitic process in the low temperature range 300°-650°C. In the 400°-600°C range α' precipitates formed after only 5 seconds.

They noticed that precipitation of α' occurred throughout the ferrite grains but precipitate free zones were observed around the ferrite grain boundaries. On prolonged ageing the α' dissolved in the ferrite, the disappearance of the precipitate being accompanied by the precipitation of rod like austenite.

The precipitate free zones in this alloy suggest that the α' phase precipitates by a nucleation and growth process as has been postulated by other workers (60 63,67,70) and not by spinodal decomposition which has also been suggested (69).

2.7 Transformations Occurring in Martensitic Stainless Steels

Martensitic stainless steels contain between 12-17%Cr, 0-4%Ni and 0.1-1.0%C. They are often alloyed with elements such as titanium, niobium, molybdenum, aluminium and copper to produce the required strength and tempering resistance. The steels are austenitic at solution treatment temperatures such as 1050°C, although they may contain small proportions of delta ferrite, which depends upon their composition. The austenite transforms to martensite on cooling from solution treatment temperatures, the high hardenability of the steels ensuring that martensite is formed even at very slow cooling rates. It is essential that delta ferrite is not formed in these alloys as it decreases the maximum available strength. The steels are usually tempered to give the best combination of strength, ductility and toughness, therefore it is important that the M_s temperature of the alloys is not excessively low or large amounts of retained austenite will be produced. The Ac_1 temperature also should not be depressed too far as this will limit the maximum tempering temperature that can be used (71).

Almost all alloying elements except for cobalt depress the M_s temperature for martensitic steels and both the M_s and M_f temperatures are known to be generally linear functions of composition (72). The factors governing the alloy content in 12%Cr steels have been given by Irvine et al (73) who carried out a comprehensive study of the physical metallurgy of 12%Cr steels. They reported that there were two temperature ranges in which it was advantageous to temper the steels to give good mechanical properties. These were 250°-300°C and 600°-700°C. Undesirable mechanical properties were produced when the steels were tempered in the range 450°-500°C. After 10 hours ageing at 450°C the maximum hardness had been reached and overageing took place. A fine precipitate was observed in the matrix at 450°C and 500°C and the original Fe_3C precipitate was seen to be dissolving during the formation of the fine matrix precipitate.

It has been clarified by Pickering (74) that the fine plate-like precipitate formed in 12%Cr steels is Cr_7C_3. This precipitate can be nucleated separately as well as undergoing an in situ transformation from the Fe_3C particles, where the Cr_7C_3 takes the place of the dissolving Fe_3C precipitates.

As well as the Cr_7C_3 precipitation occurring in the 12%Cr steels another phase is also observed; this is the M_2X precipitate which in

12-17%Cr steels is based on $Cr_2(CN)$ (75). This M_2X phase is hexagonal and it can dissolve large amounts of many alloying elements and thereby causes extra secondary hardening. Increasing the nitrogen content or adding alloying elements such as molybdenum, stabilises the M_2X precipitate and in 12%Cr-Ni-Mo steels the major secondary hardening precipitate is the M_2X (73). At the higher tempering temperatures, closer to the A_1 temperature, the $Cr_{23}C_6$ based carbide is often precipitated and at the same time the Cr_7C_3 or M_2X dissolves.

Two martensitic phases have been identified in Fe-Cr-Ni steels; α' martensite which is ferromagnetic and has a body-centred cubic crystal structure in relatively low carbon austenitic alloys and ε-martensite, which is non-magnetic and has a close packed hexagonal structure. The ε is often found in association with the α' martensite. The transformation sequence favoured by several workers is austenite→epsilon→alpha prime martensite; this transformation is accompanied by a volume contraction and expansion of ~1.1 and 2.5% respectively (76). The ε and α' martensite are metastable phases and revert to the γ phase on heating. There is general agreement that the reversion of ε commences on heating to ~150°C and is complete at ~400°C (77). The reversion of α' to γ occurs progressively with increasing temperature above ~500°C and the temperature at which it occurs is nickel dependent.

α' - martensite forms as laths on the $\{111\}\gamma$ habit planes. The laths within a packet are separated by low angle boundaries. ε

martensite is essentially composed of stacking faults on every alternate $\{111\}_\gamma$ plane and occurs when the stacking fault energy of an alloy approaches zero. Therefore, in alloys where solute additions decrease the stacking fault energy of austenite, the energy for the austenite to ε transformation will be reduced to that below the austenite to α' martensite transformation and thus metastable ε is formed.

The compositions of the austenitic alloys determine the extent of the α' martensite formed during quenching. Several empirical equations have been derived relating the $M_s\alpha'$ temperature to the elemental compositions:

$$M_s\ \alpha'{}^\circ C = 1305-(61.1Ni)-(41.7Cr)-(33.3Mn)-(27.8Si)-1667(C+N)$$

after Eichelman and Hull (78).

$$M_s\ \alpha'{}^\circ C = 502-810(C)-1230(N)-13(Mn)-30(Ni)-12(Cr)-54(Si)-46(Mo)$$

after Pickering (72)

Comparatively little work has been devoted specifically to investigations of compositional effects on ε martensite formation. However it has been reported (77) that the phase was not formed in alloys quenched to room temperature or -196°C if the combined nickel plus chromium content was less than 24-28wt%.

2.8 Neutron Irradiation Damage Occurring in Fast Reactor Core Components

The fast breeder reactor (FBR) is fuelled with a mixture of plutonium and uranium oxides clad in stainless steel and made up into very compact hexagonal fuel element assemblies. It relies upon the nuclear fission of plutonium and uranium -235 atoms in an intense flux of high energy, (or fast), neutrons produced in a highly compact core without any moderator. Having established the fast chain reaction in a compact core of this kind, it is also possible to make use of the very intense neutron radiation emanating from the edge of the core. By using a blanket of depleted uranium, mostly uranium-238 waste product from enrichment plants it is possible to convert a substantial quantity of the material to plutonium by neutron capture. It is in fact possible to produce more plutonium in the blanket region than is being consumed in the core region and it is this process which is known as breeding.

The type of FBR at the most advanced stage of development is the Liquid Metal-cooled FBR (LMFBR). The liquid metal used to provide very efficient heat transfer from a compact high power reactor core is sodium or Na-K solutions. The reactor core is suspended in a large pool of sodium together with primary pumps and intermediate heat exchangers. Sodium is pumped from the pool to the bottom of the core and the sodium emerging from the top of the core flows down through a straight-tube intermediate heat exchanger and back to the pool. The intermediate heat exchanger heats a secondary flow of sodium which is passed to a steam generating plant. The low pressure of the sodium coolant circuits is considered to be a safety feature once the techniques of handling hot sodium have been mastered.

Constant efforts are being made to improve reactor efficiency; this can be achieved by increasing the burn up of the fuel. At the present time 10% of burn up is achieved but 15% is aimed for by improving the fuel design. For 1% of burn up of fuel the reactor core components receive a neutron irradiation dose of approximately 10 displacements per atom (dpa). This means that the expected lifetime dose for a FBR core component is conceivably in the range of 100 to 150 dpa.

The LMFBR cores experience fast neutron irradiation to higher doses than other types of reactor and therefore it has very special materials requirements. The austenitic stainless steels used in the reactor core have to satisfy not only the mechanical stresses imposed but must also have excellent corrosion resistance and the ability to withstand fast neutron irradiation. Unfortunately, fast neutron irradiation coupled with the reactor core temperatures experienced cause a phenomena known as void swelling in austenitic stainless steels. Void swelling manifests itself in the outward growth of the reactor core components which means that there are great problems in designing the reactor fuel assembly where fine engineering tolerances are essential.

The major core components consist of the fuel cladding, the supporting grid structure for the fuel elements and the hexagonal wrapper which encompasses all these. Designing the core assembly is made more difficult due to the swelling problem. Even if the whole core were made out of the same alloy it would not all swell evenly due to the irradiation dose and temperature variations across the components.

In the case of the hexagonal wrappers, bowing can occur due to the different doses received between the faces on the wrapper. Some compensation can be made by rotating the wrapper and therefore evening out the dose received by the faces.

Materials selection problems can be highlighted by the fact that if the internal grid assembly alloy swells more than the wrapper then this will cause the grid to expand and force the wrapper to do likewise - the wrapper could then twist, or even worse perforate. If the grid alloy swells less than that of the wrapper then the sodium coolant will take the easiest path through the gap between the grid and wrapper. Therefore inefficient cooling of the fuel pins will result and as a consequence reactor efficiency will decrease. In the case of the fuel cladding, as it is very thin it is assumed that the same dose is received across the pin diameter; however there is a temperature difference along the pin and thermal stresses as well as swelling are a problem. The fuel pins can elongate as well as bow, not only restricting the flow of the sodium coolant between the pins but also causing the pins to come against stops and to buckle. This could cause the pins to fail and allow the oxide fuel to come into contact with the coolant.

Associated with the problems of void swelling is solute fluxing which could decrease the stability of the matrix phases and result in embrittlement or even enhanced growth. From these few considerations of the design problems it can be seen that it would be ideal if the austenitic alloys used in the core components did not swell at all, but remained in the incubation period before the onset of void swelling.

2.8.1 Irradiation Damage Processes

There is no precise mechanism known for the nucleation and growth of voids during irradiation although there are known damage sequences which occur (79,80). Components in the reactor core are subject to fast neutron irradiation; these fast neutrons penetrate the alloy lattice. Being a neutral particle, the neutron ignores the many atoms in its path as it speeds through the lattice. Eventually it loses energy and can no longer avoid the atoms in its path and so a direct collision occurs. This is called the primary knock-on (pko) as the neutron knocks the atom out of its original lattice site. The positively charged atom is displaced from its site with some considerable force and it travels through the lattice but, as it is repelled by the other atoms along its path, it quickly loses its energy and collides with another atom, which is knocked out of its site to collide with another, etc, etc. This is a secondary knock-on effect, commonly referred to as a collision cascade. From this it can be seen that most of the observed damage by a neutron entering an alloy is at the end of the neutron's path.

The direct result, therefore, of irradiation is to create Frenkel, or point, defects. These are interstitial atoms and vacancies created by an atom being knocked out of its site. These point defects can recombine and the atoms fall back into the vacant sites. However, if interstitial atoms diffuse away before recombining this can leave a two dimensional vacancy cluster, i.e. a dislocation loop which serves only to increase the dislocation density of the alloy, and no swelling occurs. This is very much the behaviour observed when the alloy is held at up to one third of its melting temperature ($0.3T_m$) where swelling is limited due to recombination of defects.

At higher temperatures $\sim 0.5T_m$, both glide and climb of dislocations can take place because there is more energy available and diffusion rates are enhanced. Although interstitials and vacancies are created in equal numbers they are not annihilated equally. Defects can migrate to grain boundaries and precipitate interfaces etc. These sinks are neutral. However, due to the large elastic strains associated with interstitial atoms these defects are absorbed at dislocations therefore creating biassed sinks. As interstitials are preferentially absorbed, this leaves a surfeit of vacancies which can migrate to vacancy clusters.

The actual method of void nucleation from these clusters is not well understood. In earlier work (81) concerned with the production of transmutation gases during irradiation it was suggested that the coalescence of two gas atoms would produce a 'bubble'. 'Bubble' implies that the interfacial energy created by the formation of the bubble is balanced by the gas pressure inside it. However, there is insufficient gas created to equilibriate the observed voidage seen in steels. It has been shown experimentally that in an outgassed, face centred cubic, high purity metal no voidage occurs, whereas in the same material implanted with helium, voids were produced on irradiation (82). It can be seen that residual gases and transmutation gases play an important role in the nucleation of voids.

At temperatures within the void swelling range the swelling process appears to consist of two separate but related stages, that of void incubation/nucleation and that of void growth. Both these stages are governed by the same criteria but, although most published work is concerned with void swelling, it is the incubation period before the onset of voiding which is the most important factor. If the incubation period can be extended so that it lasts the lifetime of the component then void swelling would cease to be a problem in the design of reactor cores.

The factors governing the incubation period are the irradiation dose and temperature experienced in the reactor, the amount of residual gas present and also that produced as a result of irradiation, the initial dislocation density of the alloy and any other metallurgical factors that are responsible for point defect trapping. It is difficult to draw the line where the incubation/nucleation period ends and void growth begins due to the fact that it is very difficult experimentally to measure the incubation period.

2.9 Methods Available to Study Void Swelling

There are three methods of investigation that can be used in order to study the mechanism and effects of void swelling. Insert C

Firstly, offcuts of actual reactor core components can be studied. From these it will be possible to see the extent of damage that has occurred to the alloy after its lifetime in the reactor. Unfortunately not much information can be gained from these components as the metallurgical prehistory is unlikely to be known, the reactor temperature will have varied and the actual temperature of the component will not have been monitored.

Secondly, it is possible to place specially selected and prepared specimens into experimental reactors. In this way the full metallurgical history of the alloy will be known and the temperature of the specimen can be accurately monitored. Experiments may be performed isothermally or with pre-determined temperature changes; the displacement dose the alloy receives is also carefully controlled. This method is an extremely comprehensive one, its only drawback being that results are obtained after a matter of years of testing so it is not a method that can be used for immediate problem solving.

The third technique is to use simulation experiments. The results of these can never be as good as the second method since the irradiation damage is not caused by neutrons but by charged particles. However, several advantages can be gained, such as good temperature and dose control, the ability to generate high dose rates and the techniques lend themselves to quick response to new ideas.

2.9.1 Simulation Techniques

Some of the published literature on irradiation damage studies stems from experiments performed using simulation techniques Insert D This is understandable for reasons mentioned in the last section. Extensive work has been performed at UKAEA Harwell on reactor core materials using charged particle experiments (83). This has helped to provide an even better understanding of the advantages and limitations of these techniques.

One of the first methods employed was the use of a high voltage electron microscope (HVEM) in which one million volts are used to generate energetic electrons which will displace atoms within a thin foil of material. In the HVEM the electrons produce uniform damage through the area of the foil that is being subjected to the electron beam, the surface layers do not produce any voidage because the foil surfaces act as sinks for the generated defects. A major advantage of the HVEM is that temperature remains constant for the duration of the testing, and doses as high as 80 dpa can be generated within a day. A disadvantage with the technique is that only a very small portion of material can be irradiated, of the order of Angstroms in diameter. The damage created resembles only the primary knock-on stage of irradiation, no collision cascades are seen and therefore the results must be interpreted with this in mind. The onset of void nucleation is also very difficult to determine, the observations made being only as accurate as the resolution of the microscope.

Another method of charged particle simulation is by the use of a variable energy cyclotron (VEC) which is basically an ion accelerator. This can produce and accelerate various ions which bombard a target made out of the test material. It is also possible to test in the presence of helium (generated by α particle irradiation) to further simulate neutron damage. The irradiation dose can be built up over a period of days to a high level, although, because of target changes etc., temperature cycling does then occur.

Several charged particles species have been used to study irradiation damage. It is better to avoid using bombarding ions which will substantially alter the composition of the alloy being bombarded. Therefore for stainless steels, iron, chromium or nickel ions could be used. It is necessary that the ion should penetrate to at least a few thousand angstroms to eliminate surface effects and this is achieved by selecting a high enough accelerating energy so as to give sufficient penetration.

The use of charged particles to produce voids in stainless steel was first demonstrated by Nelson and Maizey (84) who used 100KeV protons and carbon atoms. Protons are often considered ideal particles because of their mass similarity to neutrons, but unfortunately the dose rate is excessively slow and there are problems with hydrogen generation. Carbon atoms have also been used (85) but this increases the amount of carbon in the damage layer and confuses results as void swelling is critically dependent on constitution and therefore composition.

Nelson et al (83) reviewed the use of accelerators to simulate fast neutron induced voidage and highlighted the differences between this technique and actual neutron damage. The fundamental difference between fast neutron and charged particle irradiation lies in the elastic scattering cross section because, whereas neutrons have a cross section of about 10^{-24}cm^2, the cross section for charged particle collisions can be in excess of six orders of magnitude greater. Damage caused by fast neutrons is uniform throughout the specimen, whereas the interaction of a beam of charged particles with a solid can only result in damage to a depth roughly equal to the particles range in the solid, and in the case of the HVEM damage is limited to an even smaller area.

2.10 Efforts Made to Understand Void Swelling Using Simulations and Fast Neutron Techniques.

Austenitic alloys have been chosen as reference fuel cladding and sub-assembly wrapper material in the UK and in other FBR systems (86). The formation of voids in austenitic alloys subjected to fast neutron irradiation was first reported by Cawthorne and Fulton (87) and this discovery has now been extensively studied (88,89).

Void swelling is dependent on the nickel and chromium contents of the stainless alloys as these are the primary determinants of its phase constitution (90-96). It has been suggested that (90) single phase austenite has better resistance to void swelling than two phase ($\gamma + \delta$) or ($\gamma + \sigma$) and three phase ($\gamma + \alpha + \sigma$) alloys. The formation of second phases e.g. ferrite and sigma phase have been demonstrated to have a large effect on void swelling (94-96) The stability of the austenite matrix depends on the amount of Ni present and high Ni steels are better than low Ni steels for resisting void swelling (87-90). Simulation experiments using 46 MeV Ni^{6+} ions have shown that a 18%Cr, 12%Ni alloy swells less than a 18%Cr, 8%Ni alloy both in the solution treated and cold worked conditions (77).

Efforts have been made by many workers to understand void formation and swelling in austenitic alloys with a view to increasing the incubation period and also reducing void swelling in alloys. Actual reactor core materials, eg 316 stainless steel, have been investigated by several workers using different ion bombardment techniques, as well as fast neutrons, and it is difficult to compare data obtained by these different techniques and impossible to do so where there is a variation in the alloy compositions. A review of the use of ion accelerators to simulate neutron damage has been produced which highlights some of the problems (83).

The shortcomings of comparing HVEM data with 'in reactor' swelling data have been mentioned in a previous section, but the problem is highlighted from experiments using alloy FV548 (97), as HVEM irradiation produces point defects only as Frenkel pairs rather than collision cascades which are produced as a result of fast neutron irradiation. This means that it is also difficult to compare HVEM data with VEC obtained data (98).

Johnson et al (99) compared 5 MeV Ni^+ ion irradiated, with fast neutron irradiated 316 and 304 alloys and found that maximum void swelling occurred at more than 100°C higher temperatures in the ion irradiated specimens than in the neutron irradiated specimens. However, there was good agreement between the magnitude of the voids produced, the void density and the size of the voids, if the alloys were compared in their maximum void swelling state.

General trends in void swelling behaviour are apparent. Cold working an austenitic alloy prior to irradiation increases its resistance to void swelling which has been shown using ion irradiation techniques where bombardment of an 18Cr-8Ni-Ti cold worked alloy with 20 MeVC^{++} ions showed reduced void swelling compared with the solution treated condition (98). This was also observed with a 316 alloy using the same technique (100), and when it was subjected to fast neutron irradiation (101). It is now generally agreed that void swelling is delayed in cold worked austenitic alloys. Cold working increases the initial dislocation density of the alloys, which can then act as defect sinks.

It has already been stated that the ability of an alloy to resist void swelling depends on its composition and therefore its constitution and other alloying elements as well as nickel influence this. Carbon has proved effective in reducing void swelling (83,102,103,), its effect being more pronounced at low temperatures (104-106). Williams has observed that void swelling decreased with increasing soluble carbon content up to doses of 40 dpa in a 316 alloy irradiated with 46 MeV Ni^{6+} ions (107). The effect of soluble carbon on void swelling is complicated by the formation of carbides, which precipitate during the alloys life in the reactor, as these may have additional effects on the void swelling characteristics.

Appleby et al (108) have examined the role of precipitates in neutron irradiated steels and state that they can inhibit void formation and swelling if closely spaced and present in an extremely fine distribution throughout the matrix, as they provide sites for the mutual annihilation of vacancies and interstitials.

Silicon has a major role in reducing void swelling which has been demonstrated in simulation experiments (90,95,109) and fast neutron irradiated tests (110-112) in austenitic alloys. Silicon is thought to decrease void nucleation as, when silicon atoms are in solution, they act as trapping sites for the irradiation induced point defects thereby extending the incubation period. Above 0.5% Si the effect is diminished as Ni and Si rich precipitates form, thus depleting the matrix of both elements, which causes the alloy to swell at higher rates (112). Simulation experiments with 46 MeV Ni^{6+} ions on 12Cr, 15Ni alloys showed that additions of silicon between 0.5 and 1.46 wt% decreased void swelling.

The Ni_3Si phase has been reported as being present in neutron irradiated steels (113-115). Williams and Titchmarsh observed the precipitation of a nickel-niobium silicide (G-phase) and a silicon rich phase with a diamond cubic M_6C structure in a neutron irradiated niobium stabilised austenitic steel (114,115). The two silicon rich phases were precipitated at point defect sinks at temperatures up to ~560°C. The G-phase was the predominant silicon rich phase in the 850°C aged condition (113) whilst the M_6C phase was dominant in specimens irradiated after solution treatment at 1150°C (115). These observations led to the belief that the nature of the phase formed depended on the soluble carbon present (115). In the aged condition where carbon was low, the carbon free silicon rich G-phase was favoured, whilst a silicon rich carbide was formed in the solution treated specimens which had a high initial soluble carbon content. Investigations of the solute fluxing behaviour further (114), led to the conclusion that, as the precipitation of Ni_3Si and G-phase depleted the matrix of nickel, the formation of Cr, Fe, Nb and Mo rich precipitates increased the matrix nickel content and therefore great care must be taken when interpreting void swelling behaviour in terms of irradiation induced changes in matrix composition.

There is evidence that Ni_3Si and G-phase are only observed in austenitic steel specimens containing normal silicon levels (~0.5wt%) and irradiated with neutrons at temperatures up to ~560°C (112,113) whilst the same phases may be observed at significantly higher temperatures after irradiation with heavy ions at a dose rate ~10^3 times greater (113,116). Thus, whilst simulation studies of irradiation-induced precipitation phenomena using heavy ion accelerators are feasible, and of great potential value, account should always be taken of dose rate effects when the results of such studies are interpreted.

Lee et al (117) have also observed G-phase and a silicon rich carbide in fast neutron irradiated austenitic steels (117) and they have concluded (118) that fast neutron irradiation does not produce any completely new phase, but, due to irradiation induced segregation and enhanced diffusion rates, several major changes in phase relationships occur during irradiation. Phases from remote regions of the phase diagram appear unexpectedly and the compositions of phases are altered by the incorporation of Ni or Si in them. Several phases develop at lower temperatures than they normally occur at during neutron irradiation, ie irradiation induced G-phase and γ' phase.

3.0 EXPERIMENTAL METHODS

3.1 Ternary Alloys: Rationale

Six very high purity ternary alloys were selected. These consisted of:

(a) three fully austenitic iron base alloys with nominal compositions of 20Cr-23Ni (A), 20Cr-43Ni (B), and 30Cr-33Ni (C), the balance being iron. Their full chemical compositions are given in Table 2.

These are all stable austenitic alloys in the 1050°C solution treated condition, their compositions lying well within the austenite phase field, fig.1. Examining the isothermal equilibrium section at the lower temperature of 650°C, fig.3, shows that whilst alloy B would remain in the austenite phase field, alloys A and C both lie close to phase boundaries. A is in the $(\gamma + \sigma)$ field and C is in the $(\gamma + \sigma + \delta)$ field. It is possible to assume therefore that both these alloys could precipitate a second phase if they were held for long periods of time at about 650°C, and alloy B may also destabilise.

(b) three iron base transformable and duplex alloys with nominal compositions of 12Cr-3Ni (D), 18Cr-7Ni (E) and 30Cr-13Ni (F) were selected, their chemical compositions are given in Table 2.

Alloy D lies just inside the austenite region at 1050°C according to the phase diagram, fig.1. However, the phase boundaries at the edge of the diagram are only projected boundaries and therefore alloy D could lie just within the (δ + γ) field. This would mean that the structure at low temperature could consist of martensite with small islands of delta ferrite. The austenite transforms to martensite on cooling as the Ms temperature for this alloy is above room temperature. The ageing behaviour of the 12%Cr steels is of great interest as these alloys are being considered for use as wrappers in the fast breeder reactor core, due to their void swelling resistance coupled with their good strength.

Alloy E again lies just inside the austenite phase boundary at solution treatment temperatures, fig.1. This alloy at 650°C however lies on the triple point of the (γ) + (γ + σ) + (γ + α) + (α + γ + σ) boundaries. The transformation behaviour of this alloy is likely to be complex, as any of the three phases could form in it. This alloy is particularly interesting as its composition is very close to the 18Cr-8Ni steels which are in wide commercial use.

Alloy F lies in the delta ferrite + austenite phase field at temperatures above 1000°C, but at 650°C it lies in the (γ + σ) region. It should be possible to study the transformation of the duplex (γ + δ) structure to a sigma phase and austenite aggregate in this alloy.

3.1.1 Quaternary Alloys: Rationale

The two iron base ternary alloys that have been chosen to form the basis of the quaternary alloys are:

(i) Alloy A, 20Cr-23Ni balance iron. This is a fully austenitic alloy after solution treatment at 1050°C and its composition is near to the commercially used 20Cr-25Ni stainless steel. A preliminary study of the ageing characteristic of this alloy at temperatures between 400°-900°C showed it to have in general little hardening response. At 650°C, however, the composition lies close to the $(\gamma)/(\gamma + \sigma)$ phase boundary, so the direct effects of a fourth element addition on the constitutional behaviour of this alloy can be examined.

(ii) Alloy E, 18Cr-7Ni balance iron. This is a transformable alloy its solution treated microstructure consists of austenite which has partially transformed to martensite plus a small amount of delta ferrite. Its base composition is deficient in nickel as compared with its commercial counterpart, the 18Cr-8Ni series of alloys. The effect of a single alloy addition on the phase constitution of this steel and the effect of the quaternary additions on the transformation behaviour are being examined.

The quaternary addition elements are 2%Mo, 1%Nb, ¼%Ti and 1-2%Si; the chemical compositions of all the quaternary alloys can be seen in Table 3.

Temperatures of 650°C, 750°C and 850°C were selected to study the precipitation sequences occurring in the quaternary alloys. These can be directly compared and contrasted with the precipitation behaviour of the ternary alloys at the same temperatures and times of ageing.

3.2 Manufacture of Iron Base Ternary Alloys

The iron base ternary alloys on which ageing studies were performed were received in the form of 3mm thick cold rolled strip. They had been manufactured previously (16) at the University of Sheffield. 750g casts were made as ingots, 25mm diameter and ~15cm long. The surfaces were cleaned by turning and they were then milled into 19mm square sections, the millings being saved for analysis. The milled bars were then hot rolled at 1100°C using two passes, then reheated and given two further passes to achieve a final thickness of 6mm. The bars were then cold rolled to 3mm thick strip, again using two passes.

3.2.1 Preparation for Ageing Studies

As the resulting strip contained edge cracks it was necessary to grind them off before further cold rolling could take place. The strip was cut transversely to give a section ~10mm wide, 3mm thick and ~20mm long. These were ground on all sides and faces, all sharp edges being rounded off. This was considered a necessary precaution to prevent further cracking. The sections were then cold rolled down to 0.5mm thick strip. The strip was then cut into 2.5cm long pieces, cleaned to remove any traces of oil and sealed in silica tubes which contained a pressure of one third atmospheres of argon. The strip was solution treated at 1050°C for a period of 30 minutes, the silica tubes being broken open during quenching. The specimens were then resealed in silica tubes for ageing studies.

Ageing was carried out for times of 10,20,50,100,200,500 and 1000 hours at temperatures of 400°-900°C at 50°C intervals.

3.2.2 Quaternary Alloy Manufacture

Off cuts and turnings of the high purity iron base ternary alloys were used to make the quaternary alloys. An existing argon arc button melter was used, which was capable of producing 50g of material by melting on a cruciform hearth. This hearth allows the buttons to be remelted several times, so as to ensure homogeneity. Only a slight modification was needed to be made to the hearth, due to the fact that the shape of the cross was worn and the material refused to run into the channel. Therefore, the button emerged from melting as a rounded lozenge shape rather than a bar. By putting negative and positive gradients on the channels, fig.15, the alloy was encouraged to flow and overcome surface tension forces to give a more acceptably shaped bar and to encourage mixing.

It was possible to adjust the vacuum and argon flushing apparatus to give one third of an atmosphere of argon passing continually through the chamber during melting. This served to reduce the partial pressures of nitrogen and carbon monoxide and therefore the final nitrogen and carbon content of the steels, which was essential to retain the high purity of the quaternary alloys.

The alloys that were manufactured are listed in Table 3. Drillings were taken from the buttons, and these were used for chemical analysis. The surfaces of the buttons were ground to remove any surface defects. Homogenisation was carried out by sealing the alloys in silica phials under one third atmosphere partial pressure of argon and soaking for 24 hours at 1150°C. The buttons were then cold rolled down to 0.5mm thick strip. The strip was sectioned into 2.5cm by 1cm lengths and sealed in silica phials prior to solution treatment at 1050°C for 30 minutes.

3.3 Optical Metallography

Optical metallography was used to investigate any microstructural changes resulting from ageing. Small sections were cut from the alloys and mounted in bakelite. The specimens were ground on silicon carbide papers and then polished to a $\frac{1}{4}$ micron diamond surface finish.

To reveal the aged microstructure several etching techniques were employed, such as KOH electrolytically (9), aqua regia and glyceregia, Schaftmeisters and Marbles reagents. Of these KOH gave the best results but this was not as effective as electrolytic oxalic acid used at 8 volts, as the staining effect produced by the KOH tended to be uneven and it was difficult to obtain repeatable results. Oxalic acid etching has been used by several workers as it is a good general etch for revealing the microstructure (15,20,21,16,68). It is especially good for revealing austenite/ferrite, and austenite/sigma boundaries. Longer etching times are required to reveal ferrite/ferrite and austenite/austenite boundaries but etching for long periods of time can produce etch pitting.

The austenitic alloys were etched in 10% oxalic acid at 8 volts for 15 seconds. Alloy A (20Cr,23Ni) proved particularly difficult to etch and was liable to etch pitting. The duplex/transformable alloys were all etched at 4 volts, alloy F (30Cr,13Ni) for 10 seconds, alloy E (18Cr,7Ni) for 30 seconds and alloy D (12Cr,2Ni), which was particularly resistant took up to a minute before the structure was revealed.

Photomicrographs were taken of representative areas of all the specimens using a Reichert MeF optical microscope.

3.4 Determination of the Ageing Curves

Due to the small specimen thickness, hardness testing was carried out using a Tukon microhardness tester. This was calibrated to give comparable results to a 136° diamond pyramid number (DPN) on a standard Vickers macro hardness tester, using 0.5kg and 1kg loads.

A load of 0.7kg was selected for hardness testing as this gave an indentation of the most convenient size for accurate measurement. Five tests were performed on each specimen, these being averaged to give the final result. Isothermal age hardening curves were prepared from these results

3.5 Transmission Electron Microscopy

Transmission electron microscopy was used to investigate the precipitation sequences occurring in the ternary alloys. Using this technique the morphology and nucleation sites of precipitating phases were investigated. The phases present were identified by using selected area diffraction techniques coupled with energy dispersive X-ray analysis. The transmission electron microscope (TEM) was a Jeol 100 CX fitted with an EDAX analysis unit.

To prepare thin foil specimens the alloy strip was secured to a brass backing plate and 3mm diameter discs spark machined out, using a brass electrode. These discs were then placed in a recessed jig and lapped down to 200 µm thick, on silicon carbide paper.

The discs were profiled and polished to perforation in a Struers Tenupol. The polishing solution was 6% perchloric acid in glacial acetic acid, used at room temperature with a current of 1.6mA. The discs were washed thoroughly in methanol and dried on filter paper. The specimens were inserted into the TEM using a uniaxial tilt stage. To identify the phases present in the specimens, diffraction patterns were obtained and analysed using standard methods as defined by Andrews et al (28).

3.6 Sample Preparation for Irradiation in the HVEM

To assess the relative void swelling in the austenitic alloys it was necessary to prepare thin foils of the materials. This was done by spark machining 3mm diameter discs out of solution treated strip, and lapping both sides of each disc until a thickness of 150 µm was reached. The discs were then electropolished using a Struers Tenupol and 6% perchloric acid in acetic acid at room temperature, at a current of 1.6m amps. These discs were stored in methanol and taken to Harwell to be irradiated in the high voltage electron microscope.

Temperatures of 500°C and 600°C were chosen for irradiation so as to give a good compromise between foil thickness and intervoid spacing.

An area of the foil must be selected that lies well within a grain so that vacancies would have to diffuse through the material rather than just to the grain boundaries. It was also important to choose an area of sufficient thickness because the foil surfaces act as sinks for the point defects and result in a void free layer at both top and bottom of the foil. It is necessary that this void free layer is less than one third of the intervoid spacing. Complying with these criteria should ensure that the area irradiated will contain sufficient voids, without too many overlapping voids being imaged in the HVEM. The electron beam was conditioned and stabilised at 1.1 MeV before testing began at 1 MeV. Before inserting the foil into the column, the bias was set at 1 and condenser 1 set at 7. The beam was focused using condenser 2 and the total beam current maximised by using the beam shift controls. This was recorded. The 80μm diffraction aperture was inserted to enable the centre beam current to be measured and this was maximised using the bright field tilt controls. The screen was then tilted to the normal operating position, the aperture was removed and I_0, the screen current, was measured.

The foil was inserted and the central perforation located. The specimen was brought up to temperature by using a small molybdenum wound furnace which is an integral part of the irradiation specimen stage.

When the temperature was stabilised, a suitable dislocation free area was located and I, the current passing through the area, was measured.

These measurements are necessary as foil thickness (FT) is related to I and I_0 by:

$$FT = f\ (I/I_0)$$

The I/I_0 ratio is not the same for different alloys, but previous experience had shown that for stainless steels a ratio of 0.008 to 0.01 is needed, which will give an area of sufficient thickness where there will not be too much void image overlap.

The HVEM is calibrated to give a constant relationship between the centre beam current and the dose rate:

$$\text{Dose rate } (\text{dpa.min}^{-1}) = 0.036 \times \text{centre beam current } (\times 10^{-9}\text{A}).$$

The dose rate usually approximates to 0.5 dpa.min^{-1} .

Irradiation began when the beam was focused onto the area selected. At intervals corresponding to ~10dpa, the test was stopped by defocusing the beam and a through focus series of micrographs were taken. This series of images was necessary as the voids are difficult to resolve and therefore to focus upon. It has been established that whilst the beam is defocused negligible irradiation damage is occurring. The time was recorded as soon as the testing was stopped and therefore a series of micrographs were produced that represent the void growth rate up to ~60dpa, when the testing was terminated.

In order to determine the void layer thickness, stereographic pairs were used. These were obtained by stopping testing after voiding had been established, taking micrographs of the area and then tilting the specimen to another zone where the image is recorded again. This provides two micrographs between which the angle of tilt is known and the void layer thickness can be measured by using a stereotable.

The prints of the micrographs of the irradiated area were enlarged by up to x6 in order to facilitate the counting and measuring of the voids. It was necessary only to count the voids that were within a central region in which the dose rate was approximately constant. A graph of control area versus total magnification, fig.16, was available from previous calibration experiments to enable this to be done.

3.7 Sample Preparation for VEC Irradiation

The extent of irradiation damage generated in the VEC specimens differs from that in the HVEM specimens. In the HVEM only an extremely small region of irradiation damage is created, i.e. the order of a few angstroms confined to one localised area. In the VEC however, a damage layer is produced approximately at 3μm depth from the target face. This is due to the fact that the 46 MeV Ni^{6+} ions that are used to create the damage have an average path length in the material of the order of 3μm. The ions are monochromatic and therefore produce a virtual mono-layer of damage within the discs. As this layer is so thin it would be impossible to locate it using standard TEM preparation techniques. Therefore the target is rocked during bombardment to increase the thickness of the damage layer so that it occurs between 2.5 to 3 μm depth from the target face.

Up to twelve 3mm disc specimens are able to be irradiated at the same time in the VEC, as this is the limit of the target size used. A temperature of 550°C was chosen as this is well within the known void swelling range for austenitic alloys. The specimens were irradiated to 10 dpa, this dose being able to be generated without any temperature cycling occurring as it can be built up over 6 hours. Also, by choosing such a relatively low dose it was possible to study the early stages of the irradiation damage process.

To make a target for the VEC it is necessary to spark machine 3mm diameter discs. These are then engraved on the reverse side with an identification mark. They are lapped down to 200μm thick using 1200 grit silicon carbide paper. A fine layer of nickel is electroplated onto the specimens, followed by copper which is built up around the discs to form a solid block.

The target was then vibrapolished, using a gamma alumina slurry, until all the disc faces were polished to a high lustre. The target was then placed in the VEC, brought up to temperature and bombarded with 46 MeV Ni^{6+} ions to the required dose.

The irradiated discs were released from the target block by dissolving away the copper in a nitric acid solution. The discs were then cleaned, dried and fixed to stainless steel stubs.

The technique used for locating the damaged layer is specialised and exacting. As the layer occurs between 2.5-3μm from the target face of the disc, a method of measuring to that depth is required. By knowing that the relationship between diagonal length and depth of a 136° pyramid microhardness indentation is 7:1, it is possible to polish away the surface of the disc down to the required depth.

A load of 200g was chosen in order to give a microhardness indentation of 42μm diagonal length and therefore equal to 6μm in depth. An indentation was placed on the face of each disc, one quarter of the distance in from the edge.

As locating the damage layer can be a 'hit and miss' affair, one specimen at a time is taken through a set preparation sequence. It is then examined using the TEM to see if the damage layer is present. If the layer has not been located then a different initial depth is chosen each time, with separate specimens, until it is located. Once the exact distance of the layer from the face is known, all the specimens can be prepared in the same manner, usually with a high degree of success.

After being microhardness indented, one specimen was vibrapolished down to remove approximately 2.7μm. The irradiated face was then stopped off using Lacomit. The reverse side of the disc was then dished elecrolytically using 20% nitric acid in methanol solution with a current of 70 mA at room temperature. The disc was then polished to perforation using 10% perchloric acid in methanol at 0.18A, the temperature being reduced to -40°C. The disc was soaked in acetone to remove the Lacomit. It was then cleaned in methanol and dried.

Examination of the foils at this stage was hampered as the Lacomit formed a very persistant film on the surface of the disc and impeded the passage of the electron beam through the thin area of the foils. In order to remove this film the discs were cleaned using an ion-beam thinner. Only short periods of time ~15 minutes were required to do this.

Transmission electron microscopy was used to investigate the effects of the irradiation damage. A series of electron micrographs were taken from which it was possible to characterise the void swelling behaviour of the alloy, the thickness of the foil being measured from stereo pairs.

3.8 Experimental Measurement of Void Swelling

The extent of void swelling occurring in the alloys subjected to irradiation in the HVEM or VEC is measured in the same manner.

Measurements are taken from the enlarged photomicrographs of the damaged regions. The number of voids present in a known volume are counted to give a value termed the void number density N_v. The volume of the voids is determined by measuring them in three directions across their diameter d_v, and assuming they are spherical, the mean void diameter $\bar{d}_v$ can be calculated. This is expressed as the diameter $\bar{d}_v$, of a void of mean volume:

$$\bar{d}_v = \frac{1}{N_v} \sum_{i=1}^{N_v} d_v^{3} \; {}^{1/3}$$

The void volume is then found from

$$v = \frac{\bar{d}_v^{\,3}}{6M}$$

where v is mean volume of the voids

M is total magnification of print

$\bar{d}_v$ is mean diameter of the voids

3.9 Neutron Irradiation Studies

A series of specimens were available through Dr T M Williams of Harwell, which provide a comparison between the effects of thermal ageing and neutron irradiation. The alloys are of the same base composition, 12Cr 15Ni, but differ in their silicon content. The full analysis of the alloys can be seen in Table 5.

One series of four alloys has been solution treated and thermally aged for 13000 hours sealed in silica tubes at temperatures of 435°, 505°, 575° and 645°C. The second series of alloys has been irradiated up to 20 dpa in the experimental fast reactor EBR II at the same temperatures.

Optical metallography was carried out on the 13000 hour aged series. The specimens were mounted in bakelite, ground and polished to a ¼ μm diamond finish. They were then etched to reveal their microstructure using Schafmeisters reagent (100HCl:100H_2O:10HNO_3).

Transmission electron microscopy was then carried out in order to characterise the aged microstructure and investigate any metallurgical changes that may have occurred as a result of ageing.

4.0 RESULTS

4.1 Austenitic Ternary Alloys

The three ternary alloys, 20Cr 23Ni, 20Cr 43Ni and 30Cr 33Ni were all solution treated for 30 minutes at 1050°C. Their resulting microstructures were examined using optical and electron metallography and were all found to be fully austenitic, The alloys were then aged for times up to 1000 hours in the temperature range 400°-900°C.

Before discussing the ageing characteristics and microstructural changes, it is worthwhile noting that the solution treated hardness values for the fully austenitic materials particularly exhibited a slightly lower hardness than specimens which had been aged for the shortest time of 10 hours, especially at the lower ageing temperatures. This difference decreased with increasing ageing temperatures and it is suggested that it may well be due to internal stresses produced in the small specimens by rapid quenching from solution treatment temperatures. This effect is shown by the broken lines on the age hardening curves.

4.1.1 Alloy A (20Cr, 23Ni)

The ageing curves produced for this alloy are shown in fig.17. It is apparent that the 20Cr, 23Ni alloy exhibited no major trends in its ageing behaviour. No age hardening took place between 400°C and 500°C, but electron metallography revealed the presence of internal stress, shown as slip traces and microtwinning which was responsible for the increase in hardness observed between that obtained after solution treatment and the value recorded after 10 hours ageing between 400°C and 500°C, fig.18.

Between 550°C and 750°C there was very slight age hardening at the longer ageing times, and this seemed to be rather more rapid with increasing ageing temperature. No age hardening occurred at temperatures of 800°C, 850°C and 900°C.

The microstructural examination of alloy A (20Cr, 23Ni) using optical metallography did not reveal conclusively the presence of any second phases. However, the samples aged between 650°C and 750°C had a much quicker etching response than at the other temperatures with a thickening of the grain boundaries being evident, fig.19.

Transmission electron microscopy of the specimens was carried out and the TTP diagram in fig.20 plotted from the results. No precipitation was observed between 400°C and 500°C or between 800°C and 900°C. This confirms the results obtained from the ageing curves and supports the optical metallography. However, transmission electron microscopy of specimens aged in the 550° to 750°C temperature range revealed the presence of a second phase on the grain boundaries, after 200 hours at 550° and 600°C and after 10 hours at 650°, 700° and 750°C. This second phase precipitate was identified in all cases by electron diffraction and EDX techniques as chromium carbide, $M_{23}C_6$.

In all cases the carbides were observed only on grain boundaries, growing as discrete precipitates, fig.21. Only a small amount of precipitation was present in this alloy, even after 1000 hours ageing at 750°C when a slight age hardening response was observed. However, the quantity of precipitates was seen to increase with increasing ageing temperature.

At no stage was either ferrite or sigma phase observed and the published equilibrium diagrams confirm that these phases would not be present at any temperature above ~600°C, below which precipitation, if any, would be extremely slow.

4.1.2 Alloy B (20Cr, 43Ni)

The ageing curves for this alloy are shown in fig.22. There was no evidence of age hardening in this alloy at the lower temperatures of 400°C-600°C or at the higher temperatures of 800°C-900°C and only a slight response between 650°-750°C. Optical metallography of the specimens did not reveal the presence of a second phase, but there was a more intense etching response in the specimens aged at 650° and 700°C, especially at the longer ageing times, fig.23. Transmission electron microscopy was performed on this alloy and carbide precipitates of the $Cr_{23}C_6$ type were identified using electron diffraction and EDX techniques. The precipitation of carbide was first observed after 1000 hours at 500°C, where it was very fine and therefore difficult to resolve. No $Cr_{23}C_6$ was observed at 850°C and 900°C. Therefore the slight age hardening response at 650-750°C was attributed to $Cr_{23}C_6$ precipitation, fig.24. The TTP diagram for $Cr_{23}C_6$ in this alloy is shown in fig.20, and it can be seen that whilst the temperature range of precipitation was slightly wider than for alloy A(20Cr,23Ni), the nose of the C curve occurred at the same temperature i.e. 700°C.

4.1.3 Alloy C (30Cr, 33Ni)

The age hardening curves produced for alloy C (30Cr, 33Ni) show no age hardening at 400°C, fig.25. This was confirmed by optical and electron metallography which revealed the lack of precipitation. Between 450° and 600°C there was a slight age hardening reaction which was greatest at an ageing temperature of 500°-550°C. This age hardening is attributed to the presence of grain boundary $Cr_{23}C_6$ which was observed by electron metallography and identified using electron diffraction and EDX techniques. The carbides were observed only at the longer ageing times and were confined to the grain boundaries where they occurred as discrete precipitates, fig.26. This ageing effect seemed to accelerate with increasing ageing temperature up to 600°C, but at 600°C there was a small decrease in the age hardening response. A second age hardening seemed to be occurring at ageing temperatures of 650°-900°C, which was somewhat more rapid. Optical metallography revealed the presence of a second phase on the grain boundaries in the 650° and 700°C, fig.27, aged specimens, with intragranular precipitation being evident in the 750° to 900°C aged specimens, especially after ageing for more than 100 hours, fig.28. These two different morphologies of precipitate are apparently related to the second of the ageing reactions, which was the more intense as might be expected from precipitates occurring within the grains.

Electron metallography revealed that $Cr_{23}C_6$ was present on the grain boundaries in the specimens aged at 650°C to 850°C but no carbide precipitation was evident in the 900°C aged specimens.

However both inter-and intragranular precipitation was also observed after 100 hours at 650°C and after 10 hours in the 700°-900°C aged specimens. This intragranular precipitate had a cubic/lath like morphology, fig.29, and was identified as delta ferrite. The TTP curves for this alloy were plotted and are shown in fig.30. These correspond well with the ageing curves and the optical metallography.

4.1.4 Comparison of Austenitic Alloy Results

Alloy A (20Cr,23Ni) and Alloy B (20Cr,43Ni) exhibited very similar ageing characteristics in that there was no observed age hardening at the lower or the higher aged temperatures and very little at the intermediate temperatures of 650°-750°C. This slight age hardening was due to $Cr_{23}C_6$ precipitation on the grain boundaries in the alloys. The $Cr_{23}C_6$ precipitates were very finely distributed and always discrete. Maximum precipitation was observed to occur around 700°/750°C, fig.20.

Transformation to delta ferrite or sigma phase did not occur at any temperature or time during ageing in either alloy A (20Cr, 23Ni) or alloy B (20Cr, 43Ni) and these findings are in agreement with published ternary phase diagrams.

In the case of alloy C (30Cr, 33Ni) $Cr_{23}C_6$ was precipitated in the same manner as in alloys A and B. However this alloy did not remain a stable austenitic alloy as delta ferrite was precipitated above 650°C. This corresponds well with the observed age hardening response in this alloy at 650°-900°C, as the delta ferrite was present intragranularly. This transformation of γ → δ is predicted by the published equilibrium diagrams which show that above 650°C alloy C (30Cr, 33Ni) lies just within the (γ + δ) region on the diagram, figs. 3 and 5.

4.2 Transformable and Duplex Ternary Alloys

The three alloys were all solution treated at 1050°C for 30 minutes and aged in the temperature range 400°-900°C for periods of up to 1000 hours. It should be noted that alloy D (12Cr, 3Ni) consisted of austenite with some transformation to martensite, whilst alloy E (18Cr, 7Ni) was mainly austenitic with small islands of delta ferrite being present - the austenite undergoing some transformation to martensite. Alloy F (30Cr, 13Ni) was a duplex austenite and delta ferrite alloy after solution treatment at 1050°C.

4.2.1 Alloy D (12Cr, 3Ni)

In the solution treated condition, the hardness was ~240HV and the structure comprised austenite which had partially transformed on cooling to martensite. The ageing curves are shown in fig.31. Ageing at 400°C caused marked hardening which is believed to be due to ageing causing a conditioning of the austenite, perhaps by clustering effects, which then allows more martensite to be formed during cooling from the ageing temperature. This caused an increase in hardness. It should be noted that the hardness, once the specimen has been conditioned at 400°C, shows no effect of time at 400°C.

Ageing at 450°C caused some tempering of the martensite after short times, and only a slight increase in hardness after longer times in excess of 20 hours. It seems that less conditioning of the austenite, to allow further to transform to martensite on cooling occurs at this temperature.

Ageing between 500°C and 600°C simply caused tempering of the martensite. Because of its very low carbon content, this tempering effect in the martensite can be readily explained by an annealing out of the dislocations in the martensite laths. This was also evident from the optical micrograph sequence shown in fig.32 where at 600°C tempered martensite can be observed. The hardness curves obtained during ageing at 650°C and 700°C indicated that an initial tempering reaction had taken place followed by an increase in hardness which was very marked at 700°C. The hardening effect following the tempering was due to the A_1 temperature being exceeded at 650° and 700°C so that partial reaustenitisation occurred and on subsequent cooling to room temperature this reformed austenite partially (or wholly) transformed to martensite with the observed hardening effect.

Ageing from 750°C up to the maximum temperature of 900°C produced an initial hardening response, fig.31, which was simply due to the considerable reaustenitisation and a transformation of that new austenite to martensite during cooling from the ageing temperature.

An interesting feature of the ageing curves at 750°-850°C was the decrease in hardness which occurred at longer ageing times. This was due to a greater amount of austenite being formed during reaustenitisation at the longer times, especially at the higher ageing temperatures. On cooling a partial transformation to martensite occurred leaving a greater amount of retained austenite present in the resulting microstructure, fig.33. This would produce the observed decrease in the hardness.

A small amount of the chromium carbide $Cr_{23}C_6$ was observed precipitating on lath boundaries in the 750°C and 800°C aged specimens. The precipitation was extremely fine and difficult to resolve. However, this precipitation would contribute to the reaustenitising reaction, the partitioning of elements causing the austenite to have increased stability and therefore resisting the transformation to martensite and accentuating the decrease in hardness at the longer ageing times, fig.31 and 34. In contrast at 900°C no $Cr_{23}C_6$ was observed, and there was no decrease in hardness associated with there being any increase in austenite present.

4.2.2 Alloy E (18Cr, 7Ni)

This alloy exhibited a most complex series of hardness and microstructural changes during ageing. Alloy E was in the austenite plus delta ferrite region of the ternary phase diagram at the solution treatment temperature of 1050°C. However the austenite was partially unstable and transformation to martensite plus a small amount of delta ferrite constitutes the resulting solution treated microstructure, fig.35. The M_s temperature for this alloy was 101°C according to Eichelman et al (78) or 61°C according to Pickering (71) and so some retained austenite was present due to the M_f temperature being below room temperature.

At the lower ageing temperatures of 400°C and 450°C, fig.36, there was a pronounced hardening observed due to precipitation of α' in the delta ferrite and due to conditioning of the austenite, which in this case probably was also associated with withdrawal of chromium which resulted in more martensite being formed on cooling from the ageing temperature. Ageing at 500°C showed a rapid increase in hardness because conditioning of the austenite led to more martensite being formed on cooling and this may be augmented by α' precipitation, fig.37(b), although 500°C is at the upper limit for such precipitation. At the longer times however, the hardness progressively decreased due, it is suggested, to progressive tempering of the original pre-existing martensite. This explanation correlates well with the progressive softening which occurred at 550°C and 600°C, which can be attributed to tempering of pre-existing martensite and an increase in the amount of retained austenite as the A_s is exceeded, and the lack of α' precipitation, fig.37.

Ageing at 650°-850°C produced an increase in hardness which was only small at the lower temperatures in this range, the amount of hardening increasing slightly with increasing ageing temperature up to 850°C. Due to the high percentage of nickel in this alloy (7%) the A_s temperature was much reduced which limits the upper temperature at which tempering can be carried out without reaustenitization. At 650°C and above therefore virtually complete reaustenitization of the matrix occurred which led to a combination of retained austenite and untempered martensite in the resulting aged microstructure. In addition finely distributed $Cr_{23}C_6$ was also seen to precipitate in this temperature range of 650°-800°C, fig.38. This precipitation further complicated the transformations, as carbon and chromium were withdrawn from the austenite, raising the M_s temperature so that on subsequent quenching from the ageing temperature the transformation of the alloy matrix from austenite to martensite was further enhanced. In addition to this matrix transformation, delta ferrite was present as discrete islands in this alloy. At low temperatures, 400°-600°C, there was no observable change in the amount of delta-ferrite present, but at the higher temperatures, 650°-850°C, the amount of delta ferrite present increased with increasing temperature and increasing ageing times, fig.39.

At 900°C, which is above the temperature for $Cr_{23}C_6$ formation, the hardness first increased and then decreased with longer times. This may well be due to the change in the proportion of delta ferrite present at 900°C as compared with the 1050°C solution treated condition, as equilibrium was approached.

4.2.3 Alloy F (30Cr, 13Ni)

After solution treatment at 1050°C the resulting microstructure contained about 50% delta ferrite in an austenite matrix. This alloy exhibited some age hardening response at all temperatures in the range 400°-850°C, but not at 900°C, fig.40.

At 400°-500°C pronounced age hardening occurred more rapidly with increasing ageing temperature. This was due to α' precipitation which occurred in the ferrite phase. The α' precipitation was impossible to resolve by optical microscopy, although there was an increased etching response. Transmission electron microscopy was used in order to resolve the precipitates. The slight decrease in hardness observed at the longer ageing times at 400°-500°C is due to the over ageing of the α' precipitates, fig.41.

In the temperature range 550°-850°C a different but still intense age hardening effect occurred as can be seen by the much slower ageing response at 550°C compared with 500°C. The optical microstructure showed that a transformation was occurring in the delta ferrite, fig.42. Transmission electron microscopy was performed on the aged specimens in order to determine the nature of the transformations or precipitations.

At the low temperature of 400°C the microstructure consisted of austenite/delta ferrite grains only, fig.43. The delta ferrite grains appeared much darker than the austenite grains due to the increased dislocation density associated with the precipitation of α'. At 450°C, after only 10 hours $Cr_{23}C_6$ precipitation was evident on the delta ferrite/austenite grain boundaries. This precipitation was in the form of a cellular, or aggregate structure of $Cr_{23}C_6$ with austenite, and in some cases completely surrounded the delta grains, fig.43. This cellular precipitation thickened with increasing ageing time, fig.43, and grew into the delta ferrite grains.

At 550°C the $Cr_{23}C_6/\gamma$ aggregate could be observed bowing out from the nucleating boundaries and into the delta ferrite grains. Precipitation of the $Cr_{23}C_6/\gamma$ cellular structure proceeded until 200h when sigma phase formation began to take place. This corresponds well with the ageing response at 550°C, where only slight age hardening was observed up until 200 hours. The sigma phase was observed to nucleate at the $Cr_{23}C_6/\gamma$ aggregate, delta ferrite boundary, fig.44. Sigma phase was present after only 10 hours at 600°C-850°C, and after longer ageing times the matrix consisted solely of austenite and sigma phase, the delta ferrite being entirely consumed, fig.45. This agrees with published phase diagrams which show alloy F (30Cr, 13Ni) to lie in the austenite/sigma phase field, figs.3 and 5.

At 900°C no age hardening was observed, the microstructure remaining duplex, austenite/delta ferrite. This was expected as 900°C is above the maximum temperature at which sigma phase is formed in Fe-Cr-Ni alloys.

4.2.4 Comparison of Transformable and Duplex Ternary Alloys

Alloys D (12Cr, 3Ni) and E (18Cr, 7Ni) both undergo a transformation of the austenite to martensite, their respective M_s temperatures being ~240°C and ~60°C (71). Therefore, there are similarities in their ageing behaviour. Both alloys undergo a tempering reaction in the temperature range 500/600°C, both experience reaustenitization to some degree at the higher ageing temperatures starting at ~650°C. The chromium carbide $Cr_{23}C_6$ precipitates in both alloys in the temperature range 650°-800°C.

In addition, alloy E (18Cr, 7Ni) contains delta ferrite islands as does alloy F (30Cr, 13Ni). Alloy E however did not transform to sigma phase after 1000 hours ageing at any temperature, but alloy F (30Cr, 13Ni) underwent a transformation of delta ferrite to sigma and austenite at temperatures between 550°C and 850°C.

The constitution of these alloys at ageing temperatures between 440°-900°C agrees well with published equilibrium diagrams.

At low temperatures of 400°-500°C, hardening was experienced in alloys E (18Cr 7Ni) and F (30Cr 13Ni) due to precipitation of α' (475° embrittlement) in the delta ferrite.

4.3 Quaternary Alloys

4.3.1 Austenitic Quaternary Alloys based on Alloy A(20Cr, 23Ni)

To the high purity base ternary alloy A (20Cr,23Ni) additions of either 2% Mo, 1% Nb, $^{1}/_{4}$% Ti and 1 or 2% Si were made. These alloys were all fully austenitic after solution treating at 1050°C for 30 minutes. The quaternary alloys were all aged at 650°, 750° and 850°C for times up to 1000 hours.

4.3.1.1 20Cr 23Ni 2Mo

The addition of 2% Mo caused a significant increase in the solution treated hardness compared with the ternary base alloy. A relatively slight age hardening occurred at 650° and 850°C, fig.46, but overageing had taken place after 1000 hours. At 750°C, however, there was no observable age hardening effect, which is undoubtably due to the very low carbon content which results in 750°C being close to, if not above the carbide solvus. Despite the absence of age hardening at 750°C, optical microscopy did indicate the presence of a few grain boundary precipitates, fig.47, which were by no means continuous and it is concluded that they were insufficient to produce any hardening effect. The precipitates where identified using E.D.X. and electron diffraction techniques as a Mo bearing $M_{23}C_6$ type carbide.

4.3.1.2 20Cr 23Ni 1Nb

The presence of 1% Nb raised the solution treated hardness compared with the ternary base alloy and the alloy contained some undissolved NbC particles, which were very small and occurred intragranularly. Ageing at 650°C produced similar effects to those observed in the 2% Mo alloy, ie a slight hardening and overageing after 1000 hours, fig.48. The optical microstructure indicated some grain boundary precipitates and also some precipitation within the grains at the longer times. The increase in intragranular precipitation was probably responsible for the slight ageing hardening effect observed.

Ageing at 750°C also showed some age hardening after 100/200 hours and overageing at longer times. Optical microscopy indicated a quite heavy matrix precipitation after 200 hours which correlated with the hardening effect, fig.48. After 1000 hours the matrix and grain boundary precipitates had coarsened significantly which correlates with the observed overageing effect, fig.49.

At 850°C a small progressive hardening was observed. This occurred as the time increased up to 100/200 hours and overageing took place after longer times. The optical and electron microstructures were similar to those obtained after ageing at 750°C in that a matrix precipitate formed progressively with increasing ageing time, figs.49 and 50. This correlated with the observed changes in hardness.

A large number of the precipitates were examined using E.D.X. and electron diffraction techniques and most were found to be NbC, their precipitates having a cube-on-cube orientation relationship with the austenite. Although Laves phase Fe_2Nb was not positively identified its formation in this alloy cannot be ruled out.

4.3.1.3 20Cr 23Ni $^{1}/_{4}$Ti

There was a slight increase in the solution treated hardness of this quaternary alloy but no significant age hardening was evident, fig.51. Optical metallography revealed the presence of a grain boundary precipitate after 500 hours at 650°C and 750°C and after 200 hours at 850°C. These precipitates were also observed in the T.E.M. and were identified as TiC. The precipitates overaged after the longest ageing times, but at no stage during ageing were they capable of producing hardening, being small, discrete and largely confined to the grain boundaries, fig.52.

4.3.1.4 20Cr 23Ni, 1 and 2% Si

The addition of both 1% and 2% silicon caused the solution treated hardness of these alloys to be increased and this was greatest for the 2% addition, due to increased solid solution hardening. Si is a well known solid solution hardening element in austenitic steels.

In the 1% Si alloy there was no observable age hardening at 650°, 750° or 850°C, fig.53. However, the optical microstructures showed an etching effect at the grain boundaries and twin boundaries, which at short times was simply a grain boundary grooving effect. At 750°C, after longer times, widely dispersed precipitates were observed in the grain and twin boundaries, fig.54, but these were in small amounts and confined to the boundaries so that the absence of hardening can be readily understood. At 650° and 850°C similar structures were observed, but there was no observed precipitation on the twin boundaries. The ageing characteristics of the 2% silicon alloy were very similar to those of the 1% silicon alloy, fig.55, no age hardening being observed. Optical microscopy showed virtually identical structures to those seen in the 1% Si alloy but a few matrix precipitates were observed in the overaged condition and there was considerable coarsening of the grain boundary precipitates after longer ageing times, fig.56.

The 1% and 2% silicon alloys were examined using transmission electron microscopy and the precipitates identified as $M_{23}C_6$. It is well known that Si decreases the solubility of carbon in austen ite and will therefore promote the formation of carbides. This would account for the observed increase in carbide precipitation in the 2% Si alloy compared to the 1% Si alloy and also the presence of $M_{23}C_6$ in the 650°C aged specimens.

The intragranular $M_{23}C_6$ was observed to precipitate on dislocations within the grains in the 2% Si alloy whilst coarse carbides were seen on the grain boundaries. The amount of matrix precipitation was very small and unlikely to produce an observable age hardening effect, fig.57.

4.3.2 Comparison of Austenitic Quaternary Alloy Results

All the fourth element additions made to the 20Cr 23Ni base alloy produced an increase in the solution treated hardness of the alloy due to solid solution hardening effects. There was no significant age hardening effects observed in the austenitic quaternary alloys, only slight age hardening was seen in the Mo and Nb containing alloys after 200/500 hours. This effect was nullified after 1000 hours when overageing was present in all cases.

Although the quaternary additions of 2% Mo, 1% Nb, $^1/_4$% Ti and 1-2% Si are all known ferrite formers no delta ferrite was observed, neither was there any evidence of sigma phase precipitation in these alloys. The precipitation observed in the Mo bearing alloy was due to carbide formation, no Chi phase precipitation was evident. However, in the Nb containing alloy, especially at the higher ageing temperature the possibility of Laves phase formation cannot be ruled out.

The Si containing quaternary alloys precipitated $M_{23}C_6$ type carbides in much larger quantity than in the Mo containing alloy. The maximum amount of precipitation, in both cases, was seen at 750°C which is close to the nose on the precipitation C-curve, fig.20, for alloy A (20Cr, 23Ni), the base ternary alloy. Although most of the precipitates identified in the Si containing quaternary alloy were $Cr_{23}C_6$, some of the precipitates were identified as Si bearing $M_{23}C_6$. It is therefore possible that G phase was being produced in these alloys. G phase is an analogue of $M_{23}C_6$ and the two are not easily distinguished.

The Nb and Ti quaternary alloys precipitated NbC and TiC, respectively. The amount of precipitation being observed to increase with increasing temperature, but the precipitation was small due to the relatively low carbon contents of the alloys.

4.3.3 Transformable Quaternary Alloys Based On Alloy E(18Cr, 7Ni)

Additions of either 2% Mo, 1% Nb, $^1/_4$% Ti and 1 or 2% Si were made to alloy E (18Cr, 7Ni). These quaternary alloys were all solution treated at 1050°C for 30 minutes, and then aged at 650°C, 750°C and 850°C for times up to 1000 hours.

All the alloys showed extremely complex microstructures and age hardening behaviour. The alloy on which they are based, 18Cr, 7Ni, lies in the austenite plus delta ferrite region of the ternary phase diagram, fig.1 at the solution treatment temperature but the austenite is partially unstable and therefore some transformation to martensite occurs on cooling.

4.3.3.1 18Cr 7Ni 2Mo

The microstructure of this alloy after solution treatment consisted of austenite and approximately 35% delta ferrite, the austenite having partially transformed to martensite. The age hardening effects, fig.58, were similar in nature to those obtained for the 18Cr 7Ni ternary alloy but there was a greater increase in hardness. At all the ageing temperatures of 650°, 750° and 850°C a fine precipitation of a Mo bearing $M_{23}C_6$ type carbide was seen. There was also a marked increase in the amount of delta ferrite present, the microstructure becoming increasingly coarser with increasing temperature and time, fig.59. To further complicate the microstructure there was a transformation of delta ferrite to sigma phase at the longer ageing times.

At 650°C there was no change in hardness up to 100 hours, and this was similar to the ternary alloy. Thereafter the hardness increased up to 1000 hours due to an increase in the amount of delta ferrite present, the gradual transformation to sigma phase, and the precipitation of the fine Mo bearing $M_{23}C_6$ type carbide. At 750° and 850°C the hardness increased after 10 hours and continued to increase, although there was slight overageing observed after 1000 hours in the 850°C specimens, fig.58.

As has already been mentioned in section 4.2.2, the microstructure of alloy E undergoes complex transformations in its ternary form, where it lies in the $\gamma + \delta$ phase field. The addition of Mo causes the additional transformation of delta ferrite to sigma phase after ageing at 650°, 750° and 850°C, therefore the alloy will lie in the $\delta + \gamma + \sigma$ phase field. The amount of sigma phase as well as the amount of delta ferrite was seen to increase with increasing temperature and ageing time. As in this 7% nickel alloy the A_s temperature was below 650°C there will be virtually complete reaustenitization of the matrix leading to a combination of retained austenite and untempered martensite. Chromium was withdrawn from the austenite as the amount of delta ferrite/sigma phase and carbide precipitated, thus raising the M_s temperature and therefore enhancing the transformation to martensite on cooling from ageing temperatures above the A_s.

4.3.3.2 18Cr 7Ni 1Nb

Again the solution treated condition consisted of an austenite matrix which had partially transformed to martensite with small delta ferrite islands and a fine dispersion of undissolved NbC particles.

Ageing at 650°C showed no change in hardness, fig.60, and the microstructure did not materially alter, although during ageing any martensite would have reverted to austenite and then reformed on cooling to room temperature.

At 750°C there was also little change in hardness, but indications of precipitation were observed in the microstructures, fig.61. The longer ageing times produced less martensite in the alloy on cooling, which would reduce the overall hardness of the alloy. However, precipitation hardening was occurring simultaneously and so little change in the overall hardness of the alloy resulted.

Age hardening occurred up to 100 hours at 850°C, fig.60, and at longer times progressive and rapid overageing took place. Some precipitation had clearly occurred but again it seems that there was less martensite formed after cooling after longer ageing times. This could account for the much lower hardness values obtained after ageing for 500 and 1000 hours.

Transmission electron metallography showed that at both 750°C and 850°C after longer ageing times $M_{23}C_6$ type carbide as well as NbC was present in the microstructure.

4.3.3.3 18Cr 7Ni $^1/_4$Ti

The solution treated microstructure of this alloy consisted largely of austenite, there being only a small amount of transformation to martensite and no delta ferrite. Unfortunately, this alloy fell short of its specification on Ti, having only 0.015% Ti instead of 0.25%. Coupled with this the nickel concentration was too high, the alloy having 8.21% rather than 7% nickel. Hence the alloy was relatively stable with respect to martensite formation.

There was no age hardening observed in this alloy, fig.62, indeed there was a decrease in the solution treated hardness due to the smaller amount of martensite in the structure. There was little change in the microstructure during ageing except for a few grain boundary precipitates of $M_{23}C_6$ which were small, discrete, and unlikely to cause hardening, fig.63.

4.3.3.4 18Cr 7Ni with 1% or 2% Si

(a) 1% Si

The 1% Si alloy exhibited a solution treated microstructure of very small islands of delta ferrite finely dispersed in a matrix of austenite which again had partially transformed to martensite. During ageing at 650°, 750° and 850°C very marked hardening occurred, fig.64.

At 650°C major hardening commenced after 50 hours, reaching a maximum after 200 hours. Thereafter overageing did not occur. Precipitation was evident in the optical microstructures, fig.65, which was identified using electron diffraction and E.D.X techniques as $M_{23}C_6$. A small amount of sigma phase was also present but this however would not account for the great increase in hardness observed of >100 Hv. There was an increase in the amount of martensite present as ageing time increased which suggests that the precipitation, by withdrawing solute from the austenite, has raised the M_s appreciably. It is this increased martensite content which has resulted in the increase in hardness, thus explaining the fact that no overageing had taken place after longer times.

Similarly, marked hardening also occurred at 750°C and 850°C and generally similar microstructural changes were observed. However, there was evidence, particularly at the longer ageing times that the matrix was in the $(\gamma + \alpha)$ region, there being interlocking laths of both phases present, fig 65. This was probably due to an increase in the A_s temperature by silicon and by partitioning effects accompanying precipitation along with the approach to equilibrium at these higher ageing temperatures.

(b) 2% Si

The solution treated structure again contained delta ferrite and austenite which had transformed partially to martensite. Again marked hardening took place at 650°, 750° and 850°C, fig.66, similar to that observed for the 1% silicon alloy. Ageing at 650°C gave microstructures which showed the increase in martensite content with increasing ageing time consequent upon the increase in the M_s as precipitation occurred. Ageing at 750°C and 850°C also indicated structures typical of those occurring within the two phase ($\gamma + \alpha$) region similar to these in the 1% Si alloy. It is worth noting that the addition of 1% silicon to the 18% Cr 7% Ni base ternary alloy gave a 1000h aged hardness at 650° and 750°C which was 40Hv more than for the pure base ternary alloy, and in the 2% silicon quaternary alloy this increase was greater than 60Hv. In both alloys at 850°C the hardness change was less marked.

4.3.4 Comparison of Transformable Quaternary Alloy Results

The four quaternary additions of Mo, Si, Ti and Nb are all known ferrite formers, although the effects of Nb and Ti are difficult to assess as they also combine with and remove austenitizing elements i.e. carbon and nitrogen, from solution.

In the base ternary alloy (18Cr,7Ni) ageing at 650°, 750° and 850°C yielded a microstructure which consisted of delta ferrite islands in a matrix of retained austenite and untempered martensite, along with a finely dispersed precipitation of $M_{23}C_6$. The amount of delta ferrite present in the microstructure was seen to increase with increasing temperature and ageing time. In the Mo bearing quaternary alloy there was an even greater increase in the amount of delta ferrite both after solution treatment and after ageing. The addition of Mo had also caused a transformation of delta ferrite to sigma phase by moving the alloy into the $\gamma + \delta + \sigma$ region of the phase diagram at all three ageing temperatures, figs.1 and 2.

In contrast the addition of silicon to the base ternary alloy showed only a small increase in the amount of delta ferrite present after solution treatment, the amount of delta ferrite being seen to increase with increasing ageing temperature and time. Only a very small amount of sigma phase was observed after ageing at 650°C for 1000 hours. This was expected as the 18Cr 7Ni base ternary alloy lies very close to the corner of the 3 phase $(\gamma + \alpha + \sigma)$ phase field, fig.3. However, at 750°C and 850°C the effect of both 1 and 2% silicon additions had served to move the quaternary alloys into the $(\gamma + \alpha)$ phase field after ageing. $M_{23}C_6$ was also precipitated in these alloys at all three ageing temperatures.

The Nb containing quaternary alloys contained a fine dispersion of NbC after solution treatment and also precipitated a small amount of $M_{23}C_6$ after ageing at all three temperatures but otherwise remained similar to the base ternary alloy.

By far the greatest amount of $M_{23}C_6$ precipitated was in the silicon quaternary alloys. Less was seen in the Mo alloy as transformation to sigma phase would have caused competition for chromium and in the Nb alloy the carbon would have been largely tied up in the NbC precipitates. Again, as in the austenitic quaternary alloys based on 20Cr, 23Ni, the maximum amount of $M_{23}C_6$ precipitated was seen in the 750°C aged specimens.

4.4 Irradiation Results

The presence of voids within the microstructure occurs as a direct result of irradiation damage in austenitic stainless steels which are held in the temperature range 300°C to 700°C. Using simulated irradiation experiments in the HVEM and VEC, an assessment of the void swelling behaviour of an alloy can be made.

Two alloys, A (20Cr, 23Ni) and C (30Cr, 33Ni), were subjected to irradiation damage by electrons in the HVEM and their relative void swelling characteristics evaluated.

Alloy A (20Cr, 23Ni), the pure ternary alloy and the five quaternary alloys based on alloy A with 2% Mo, 1% Nb, ¼% Ti or 1 and 2% Si were assembled into targets and irradiated in the VEC. From this series of experiments the effect of the fourth element addition on the void swelling behaviour of alloy A (20Cr, 23Ni) was evaluated, but under VEC conditions rather than the less realistic HVEM conditions.

4.4.1 Irradiation in the HVEM

The HVEM produces irradiation damage by means of electrons at 1 MeV bombarding the surface of the thin foil of the alloy. The damage produced is localised to the area impinged on by the electron beam. Voids occur after an initial incubation period during which dislocation build up is observed, fig.68. The measurements taken from the photomicrographs of the damaged region give the thickness of the void layer t_v, the volume of the voids V and the number density of the voids N_v. The total volume of voids, T_v, in a given volume is calculated by $T_v = N_v \times V$.

In these calculations it is important that the void layer thickness is measured accurately from stereomicrographs because irradiation in the HVEM produces a void free layer at the surfaces of the thin foil specimens. This is due to the surfaces acting as sinks for the point defects. The thickness of the layer containing voids, t_v is given by:

$$t_v = t_m + \tfrac{1}{2}\,\bar{d}_v$$

where d_v is the mean void diameter

t_m is the measured thickness of the layer containing the voids.

It is necessary to add the $\frac{1}{2}\,d_v$ term as the voids cut the surface of the void containing layer. To count only the voids within a known volume, a circle is drawn on the micrographs, the number of voids within this circle being counted and their diameters measured. The control volume is found from:

$$V = \frac{\pi (D)^2}{4 \times M} \times t_v$$

where D is the circle diameter

M is the total magnification

t_v is the void layer thickness

By knowing the total volume of voids T_v in the control volume V, a value of relative void swelling can be found from

$$\frac{(V - \Delta Tv)}{V}$$

The relative percentage void swelling versus irradiation dose for alloy A (20Cr, 23Ni) irradiated at 500°C and for alloy C (30Cr, 33Ni) irradiated at 500°C and 600°C is shown in fig.69. Both alloys were irradiated at a dose rate of approximately 0.5 dpa per minute and the experiments were terminated when the void density became so great as to cause extensive overlapping of the voids seen in the electron microscope image. Excessive overlapping of the voids makes them difficult to count and measure acccurately.

In both alloys, voids were nucleated after an initial incubation dose had been reached. The voids grew in size as shown in figs.68, 70 and 71.

Alloy A at 500°C swelled at a slower rate than alloy C at the same temperature. Alloy C swelled much faster at 600°C than at 500°C as shown in fig.62.

By extrapolating back to zero swelling, an incubation dose can be found for the alloys. The incubation dose for alloy A (20Cr, 23Ni) irradiated at 500°C was 1 dpa, for alloy C (30Cr, 33Ni) at 500°C was 6 dpa and at 600°C, 3 dpa.

From the micrographs, figs.68 and 70, it was apparent that although alloy A (20Cr, 23Ni) at 500°C nucleated far more voids than alloy C (30Cr, 33Ni) at the same test temperature, the voids in alloy A grew more slowly, fig.71.

4.4.2 Irradiation in the VEC

Alloy A (20Cr, 23Ni), the pure ternary alloy, and the five quaternary alloys based on alloy A with 2% Mo, 1%Nb ¼% Ti or 1 and 2% Si were irradiated in the VEC using 46 MeV Ni^{6+} ions. A temperature of 550°C was used and the alloys were irradiated up to a dose of 10 dpa. This dose was achieved in a one day experiment, therefore no temperature cycling of the specimens occurred. 10 dpa is a relatively low dose; fast reactor core components would be expected to receive ~120 dpa in their lifetime in the reactor. However, in order to study the effect of the fourth element on the incubation period for void swelling as well as the growth of voids, a low dose was necessary.

The technique used for calculating the void number density N_v, and void layer thickness t_v was basically the same as that used for the HVEM swelling measurements. The VEC irradiated specimens, however, were prepared in such a way that there was no void free surface layer (section 3.7), so that any voids seen to cut the surface of the foils were counted as half voids.

The VEC irradiation results are presented in Table 4. Very little reduction in relative void swelling was observed for additions of 1% Nb and 1% Si. However, additions of 2% Si and 2% Mo showed a large reduction in the relative void swelling compared with the base ternary alloy A (20Cr, 23Ni). Although the addition of 2% Mo reduced swelling it had little effect on the void number density, N_v, a marginal increase being observed. Mean void diameter, however, was seen to decrease. The 2% silicon addition reduced N_v considerably, although the void volume increased, fig.72. 1% Nb and 1% Si additions were also observed slightly to reduce N_v.

There was no result available for the ¼% Ti specimen due to the void layer not being correctly located during the preparation of the specimens.

4.4.3 Thermal and Irradiation Studies on 12Cr, 15Ni Base Alloys Using Fast Reactor Conditions.

This series of alloys was based on the composition 12Cr, 15Ni (Table 5), the basic difference being in the silicon content which varied from 0.14 to 1.42%.

The first series of alloys was thermally aged for 13,000 hours at temperatures of 435°, 505°, 575° and 645°C, whilst a second series of identical alloys was neutron irradiated during holding for 13,000 hours at the same temperatures inside the experimental fast reactor, EBRII.

4.4.3.1 Thermally Aged Alloys

The first series of alloys, N1-N4, were examined by optical and electron microscopy to investigate the effects of thermal ageing. Optical metallography revealed that a second phase had precipitated on the grain and twin boundaries in the specimens aged at 645°C. At the lower temperatures, however, there was little evidence of precipitation, fig.73. The amount of precipitation was observed to increase with increasing silicon content. This was evident from optical microscopy, fig.73, but was further substantiated by transmission electron microscopy of thin foil specimens taken from the alloys, fig.74.

Alloy N1 had the lowest silicon content of 0.14% and showed negligible precipitation even at the 645°C ageing temperature, only a very small amount of second phase being observed on the occasional grain boundary.

Alloy N2 (0.49% Si) was similar to N1 in this respect but contained a larger amount of grain boundary precipitate at the higher temperatures of 575° and 645°C and the start of intragranular precipitation on dislocations within the microstructure.

A small amount of grain boundary precipitate was observed in alloys N3 (0.95% Si) and N4 (1.42% Si) at 435°C and 500°C, whilst at 575°C and 645°C there was a greater amount of grain boundary and intragranular precipitation. Needle like and cubic precipitates were seen intragranularly at 645°, fig.74, there being a larger proportion in alloy N4 than in N3. The precipitates were mainly located on dislocations within the austenite grains and attached to each other, corner to corner, fig.74.

All four alloys possessed an austenite matrix which was stable with respect to sigma phase or ferrite formation after 13,000 hours at these temperaures. Electron diffraction and E.D.X of the grain boundary and intragranular precipitates showed them to be chromium carbide of the type $M_{23}C_6$.

4.4.3.2 Neutron Irradiated Alloys

Due to the highly radioactive nature of these specimens they were examined at Harwell by T M Williams et al (119), their results are reported here. The response of the alloys to irradiation varied with temperature and silicon content. The N1 (0.14% Si) alloy remained mostly austenitic at all irradiation temperatures and contained void populations typical of austenitic steels. The alloys containing higher silicon levels exhibited much lower void swelling and a progressive increase in the formation of silicon rich precipitates with an associated decrease in the stability of the austenite. Transformation to ferrite occurred in the higher silicon alloys N2-N4, the extent of the transformation increasing with increasing silicon content.

At the higher irradiation temperatures of 575°C and 645°C the transformation was confined to regions near the grain boundaries. The silicon remained in solution in silicon rich intragranular regions, and chromium rich, nickel depleted regions remained austenitic. However, at lower temperatures (435°C and 505°C) transformation often extended throughout the grains. Silicon rich precipitates were formed in silicon rich regions and the chromium rich regions transformed to ferrite. The scale of this transformation became increasingly fine with decreasing irradiation temperature.

The transformation was a consequence of extensive irradiation induced solute redistribution. Nickel and silicon segregate to, and chromium and iron are depleted from grain boundaries. In addition intragranular regions separate into nickel and silicon rich, and chromium and iron depleted, and chromium and iron rich, nickel and silicon depleted zones.

5.0 DISCUSSION OF RESULTS

5.1 Constitution of the Fe-Cr-Ni Alloys

5.1.1 The Austenitic Ternary Alloys

The following alloys, A (20Cr, 23Ni), B (20Cr, 43Ni) and C (30Cr, 33Ni), were fully austenitic at the solution treatment temperature of 1050°C. The published equilibrium diagrams indicated that these alloys would lie in the austenite phase field, fig.1. This was found to be the case after solution treating at 1050°C for 30 minutes. The published equilibrium diagrams were used to predict the constitution of these alloys in the temperature range 400°-900°C. However, as shown in section 2.2 phase equilibrium diagrams for Fe-Cr-Ni ternary alloys have only been determined down to temperatures of 650°C with a reasonable degree of accuracy (7,16,19). Cook and Brown (15) studied the constitution of Fe-Cr-Ni alloys in the temperature range 550°-800°C and produced an equilibrium diagram representative of their results, fig.4, but the diffuse X-ray diffraction lines obtained for many of the alloys they studied indicated that even after long periods of ageing, equilibrium conditions had not been obtained. Information on the constitution of Fe-Cr-Ni alloys below 550°C is not available but calculated equilibrium diagrams (17) have been produced. The calculated Fe-Cr-Ni ternary diagram for 475°C is shown in fig.14.

From the published equilibrium diagrams alloy A (20Cr, 23Ni) was predicted to lie in the austenite phase field from 1050°C down to 700°C. At 650°C the diagrams as presented in the critical review of Rivilin and Raynor (19) indicate this alloy should lie in the sigma and austenite field. The diagram produced by Cawley (16), however, shows alloy A remaining in the austenite field at 650°C, although it is close to the $\gamma/\gamma + \sigma$ boundary, fig.5. Cook and Brown's isothermal equilibrium diagram for 550°C, fig.4, indicates that the alloy A will lie in the austenite and sigma phase field.

Microstructural examination of alloy A (20Cr, 23Ni), aged for up to 1000 hours in the temperature range 400°-900°C has shown that it remains in the austenite phase field. Ageing for up to 1000 hours as in this work may not be long enough for equilibrium to be attained especially at the lower temperatures.

Alloy B (20Cr, 43Ni) also remained fully austenitic after ageing between 400°-900°C for up to 1000 hours and the published equilibrium diagrams all agree that this alloy should lie in the austenite phase field in this temperature range.

Alloy C (30Cr, 33Ni) lies in the austenite phase field at the solution treatment temperature of 1050°C, but between 900°C and 550°C the published equilibrium diagrams show that it should lie in the austenite and delta ferrite phase field. Ageing alloy C between 650°-900°C produced an age hardening response, fig.25, and optical and transmission electron microscopy confirmed an austenite and delta ferrite micro-structure. This was especially evident after the longer ageing times and at higher ageing temperatures as shown by the typical micrographs in figs.28 and 29. The lath-like delta ferrite phase was observed precipitating in the austenite grains as well as on the grain boundaries. The delta ferrite identification was confirmed by electron diffraction and dark field microscopy. At the lower ageing temperatures of 600°C down to 400°C, alloy C remained austenitic after 1000 hours ageing. It is possible that after much longer ageing times this alloy may transform to give an austenite and delta ferrite microstructure as was observed by Cook and Brown (15) who aged their alloy for 12,672 hours at 550°C. The temperature dependence of the kinetics of the approach to equilibrium are therefore very important.

5.1.2 The Austenitic Quaternary Alloys

Quaternary alloy additions of 2% Mo, 1% Nb, ¼% Ti, 1% and 2% Si were made to the base ternary Fe-Cr-Ni alloy A (20Cr, 23Ni). The chemical compositions of the five quaternary alloys are shown in Table 3. All the quaternary addition elements investigated in this work were known to stabilise both delta ferrite and sigma phase in the temperature range 650°-850°C (8, 13, 14, 16, 23). All the elements, after the effects of carbide precipitation have been taken into account, are known to expand the $(\gamma + \alpha)$ and $(\gamma + \alpha + \sigma)$ phase fields of the Fe-Cr-Ni ternary diagram, shifting the $\gamma/\gamma + \sigma$ boundary towards lower chromium contents.

Alloy A (20Cr, 23Ni) lies in the austenite phase field after solution treating at 1050°C and retained a fully austenitic matrix on subsequent ageing at 650°C, 750°C and 850°C for up to 1000 hours. However, from the equilibrium diagrams figs.1, 2, 4 and 5, it can be observed that as ageing temperatures decrease, the composition of alloy A moves nearer to the $\gamma/\gamma + \sigma$ phase boundary.

The five quaternary alloys based on alloy A (20Cr, 23Ni) all were observed to have fully austenitic microstructures after solution treating at 1050°C for 30 minutes. All five additions produced a small amount of solid solution hardening, figs.46, 48, 51, 53 and 55 and a slight age hardening response was observed in the Mo, Nb and Si containing alloys which could be attributed to the small amount of carbide precipitation which was observed both by optical and transmission electron metallography. There was no evidence of transformation to delta ferrite or sigma phase taking place on ageing these quaternary alloys, all five alloys remaining austenitic on ageing at 650°, 750° and 850° for up to 1000 hours.

5.2 Transformation and Precipitation Effects

5.2.1 Austenitic Ternary Alloys

All three austenitic ternary Fe-Cr-Ni alloys showed a slight hardness increase when ageing in the 650°-750°C temperature range, figs.17, 22, and 25, which corresponded with the presence of a grain boundary phase, evident in the optical micrographs at these temperatures. The grain boundary precipitate was identified as the chromium carbide $Cr_{23}C_6$. As all three alloys have a very low carbon content, only a small amount of carbide would be produced and hence the hardening response would be small, as indeed was observed. The $Cr_{23}C_6$ carbides were located solely on the grain boundaries as small discrete precipitates which had the

$$(100)_{M_{23}C_6} \,||\, (100)_{\gamma} \;:\; \langle 100\rangle_{M_{23}C_6} \,||\, \langle 100\rangle_{\gamma}$$

orientation relationship with the austenite matrix which has been observed by several workers. The nose of the TTP curves for these alloys occurred at ~700°/750°C, figs.20 and 30. $Cr_{23}C_6$ is known to be a dominant phase in this temperature range (56) but was, however, present over a larger temperature range of 550°C-800°C in alloys B (20Cr, 43Ni) and C (30Cr, 33Ni) as opposed to 600°C-750°C in alloy A (20Cr, 23Ni). This was due to the larger amount of nickel present in alloys B and C. Nickel is known to reduce the solubility of carbon as $M_{23}C_6$ in austenite, especially at the higher temperatures. This will produce a greater supersaturation of carbon in the austenite after quenching from solution treatment temperatures so that upon ageing carbide precipitation will take place more readily.

As well as $Cr_{23}C_6$ precipitation, delta ferrite was also observed in alloy C (30Cr, 33Ni) in the temperature range 650°-900°C. The delta ferrite was observed in the optical micrographs both as inter and intragranular particles, fig.28. TEM studies showed the delta ferrite was precipitating as laths in the austenite grains with islands of delta ferrite being observed at the grain boundaries, especially at triple points, fig.29. Delta ferrite was observed in alloy C after 10 hours at 800°-900°C, 20 hours at 750°C, 50 hours at 700°C and after 100 hours at 650°C. It was not observed after 1000 hours at 400°-600°C, fig.29.

Cook and Brown (15) and Rees et al (7) aged a low carbon 33Cr, 33Ni ternary alloy in the temperature range 550°-800°C. This alloy was very similar to alloy C (30Cr, 33Ni), although their alloy contained more chromium. Rees et al (7) observed fine particles of delta ferrite precipitating within the original austenite matrix after ageing for 4,000 hours at 650°C, and the precipitation of delta ferrite was considerably coarser in the 800°C aged alloy. The delta ferrite observed precipitating in alloy C (30Cr, 33Ni) was also seen to coarsen with increasing ageing temperature and time, figs.28 and 29. There was no delta ferrite precipitation present in alloy C after 1000 hours at 550°C although Cook and Brown (15) observed very fine particles of delta ferrite in their 33Cr, 33Ni alloy after ageing at 550°C for 12,672 hours. It is probable that the 1000 hours ageing of alloy C in this work was not sufficiently long for equilibrium conditions within alloy C to be obtained and that the possibility of delta ferrite formation occurring in this alloy at temperatures of 550°C and below cannot be ruled out.

No transformation to sigma phase was detected in alloy C (30Cr, 33Ni), nor by Cook and Brown and Rees et al in their alloys, even though their alloys contained more chromium and were therefore more likely to form sigma phase. The compositions of all these alloys places them in close proximity to the $\gamma + \delta + \sigma/\gamma + \delta$ phase boundary, but the 30Cr, 33Ni composition appears to be stable with respect to sigma formation, remaining in the $\gamma + \delta$ field.

5.2.2 Austenitic Quaternary Alloys Based on Alloy A (20Cr, 23Ni)

The quaternary addition elements Mo, Nb, Si and Ti all increased the solution treated hardness of alloy A (20Cr, 23Ni). Mo and Nb both produced a slight age hardening response in this alloy, figs.46 and 48, but the additions of 1% and 2% Si and ¼% Ti did not produce any significant hardening reaction, figs.51, 53 and 55.

Molybdenum and silicon have been observed by several workers (8, 22, 26) to be strong ferrite and sigma phase promoting elements in Fe-Cr-Ni alloys, both having the effect of displacing the $\gamma + \sigma/\gamma$ phase boundary to lower chromium contents. Titanium and niobium are regarded as less potent stabilizers of ferrite and sigma phases due to their ability rapidly to form stable carbides of the MX type.

After solution treatment at 1050°C all the five quaternary alloys remained fully austenitic although the composition of alloy A (20Cr, 23Ni) does place it close to the $\delta + \gamma/\gamma$ boundary, fig.1. Subsequent ageing of the alloys at 650°, 750° and 850°C did not cause a transformation to delta ferrite or sigma phase even though published equilibrium diagrams, figs. 2, 3 and 5, do indicate that alloy A (20Cr, 23Ni) lies close to the $(\gamma + \sigma)/\gamma$ phase boundary.

It is not inconceivable that sigma phase could form in the five quaternary alloys as the ageing time of 1000 hours may be insufficient to allow transformation to sigma phase which is well known to be extremely slow in fully austenitic alloys. The effect of all the quaternary additions as sigma stabilising elements will have also been reduced as carbide precipitation was seen to occur in all five alloys, thus withdrawing sigma forming solute from solution.

In the 2% Mo quaternary alloy a molybdenum bearing $M_{23}C_6$ type carbide was precipitated on the grain boundaries, the Mo being detected by EDX analysis. This was a maximum at 750°C. In the 1% and 2% silicon quaternary alloys $M_{23}C_6$ was again observed precipitating on grain and twin boundaries. Silicon was also associated with the $M_{23}C_6$ carbide and the occurrence of G-phase in the alloy cannot be totally ruled out as G-phase is analogous to $M_{23}C_6$ and the two phases are extremely difficult to distinguish by electron diffraction from one another. But as shown in figs.54 and 56 the particles were coarser than normally associated with $M_{23}C_6$ and may therefore be G-phase. It was expected that $M_{23}C_6$ would be present in these quaternary alloys as the pure ternary alloy A (20Cr, 23Ni) precipitated the $Cr_{23}C_6$ on ageing at 650°, 750° and 850°C. The TTP curve for this alloy is shown in fig.20, where the nose of the precipitation C-curve was seen to occur at ~700°/750°C.

In the niobium containing alloy a fine precipitation was observed after solution treating at 1050°C for 30 minutes. The solution treatment temperature of 1050°C was found to be not high enough to dissolve all the NbC carbides. Subsequent ageing of the 20Cr 23Ni 1Nb alloy at 650°, 750° and 850°C caused the precipitates to coarsen, along with the occurrence of further intragranular precipitation. Overageing of the matrix precipitates was observed after longer times, fig.50. No transformation to delta ferrite or sigma phase occurred in this alloy, the effectiveness of niobium as a ferrite and sigma stabiliser being reduced due to its removal from solid solution by the formation of carbides and possibly Laves phase. The carbon content of this alloy was very low and the amount of precipitation observed, although very fine, cannot all be attributed to carbide formation.

Laves phase, Fe_2Nb, is known to be a high temperature phase, several workers having observed it to form at temperatures ~700°/800°C and above, in Fe-Cr-Ni alloys (16, 25, 39). The morphology of the very small, finely distributed precipitates present after ageing the niobium quaternary alloy closely resembled the precipitation observed by Denham and Silcock (39) in their 16Cr 16Ni alloy. They reported that Laves phase precipitated on the grain boundaries before precipitating within the austenite grains. On ageing at 700° and 800°C the grain boundary Laves phase was seen to grow and protrude into the austenite grains whilst the intragranular Laves phase formed small hexagonal particles. Large grain boundary precipitates and hexagonal, smaller precipitates where observed in the aged microstructure of the 20Cr 23Ni 1Nb quaternary alloy, fig.50. It is most probable that Laves phase and NbC precipitates were both present after solution treating the alloy at 1050°C as the NbC solvus was calculated as being ~1120°C. Subsequent ageing of the Nb containing quaternary alloy coarsened the existing precipitation with new intragranular precipitation also being formed. It was not possible to detect unequivocably the presence of the Laves phase as electron diffraction of the very small precipitates present in the thin foil specimens produced complex multi-oriented diffraction patterns, mostly corresponding to the NbC d-spacings. Removal of the precipitates by extraction replica techniques also proved unsuccessful, the precipitates being extremely difficult to extract.

The precipitation of TiC occurred in the ¼Ti quaternary alloy upon ageing at 650°, 750° and 850°C. The amount of observed precipitation was very small and produced no detectable age hardening responses, fig.51. The titanium carbides were seen precipitating on the grain boundaries and twin boundaries, fig.52, the amount of precipitation increasing with increasing ageing temperature and time. At the highest ageing temperature of 850°C the small TiC precipitates were also seen to be nucleating on dislocations within the austenite grains, fig.52.

5.3 Constitution of the Transformable and Duplex Ternary Alloys

The three iron based ternary alloys that were investigated were alloy D (12Cr, 3Ni),alloy E (18Cr, 7Ni) and alloy F (30Cr, 13Ni). Consulting the Fe-Cr-Ni equilibrium diagram, fig.1, shows the expected constitution of the alloys at the solution treatment temperature of 1050°C. Alloy D (12Cr, 3Ni) should lie in the austenite phase field, although it is close to the $\gamma/\delta + \gamma$ boundary. The solution treated microstructure of alloy D (12Cr, 3Ni) consisted of austenite which was unstable and transformed, in part, to martensite on cooling. The low solution treated hardness of 236 DPN confirms that the alloy had not wholly transformed to martensite and also reflects the very low carbon content. There was no delta ferrite present in this alloy after solution treating.

Alloy E (18Cr, 7Ni) contained 5% delta ferrite which was in the form of small islands in the austenite/martensite matrix. The solution treated constitution of alloy E (18Cr, 7Ni) was predicted, from the ternary equilibrium diagram, fig.1, to lie close to the $\gamma/\gamma + \delta$ phase boundary and so the alloy should consist of austenite and a small percentage of delta ferrite, which indeed was the case. Again the austenite phase had partially transformed to martensite on cooling from 1050°C, the M_f temperature for this alloy being calculated (72,78) to be below room temperature.

The composition of the duplex alloy F (30Cr, 13Ni) at 1050°C places the alloy well within the $\gamma + \delta$ phase field, fig.1. The solution treated microstructure of the alloy showed that it consisted of ~ 40% delta ferrite in a stable austenite matrix. The equilibrium diagram provided an accurate predic tion of the constitution of these three alloys at solution treatment temperatures.

Ageing alloy D (12Cr, 3Ni) in the temperature range 400°-900°C for times up to 1000 hours did not produce any transformation to ferrite in this alloy, although the equilibrium diagrams for 550°C, fig.4, 650°C, figs.3 and 5, and 800°C, fig.2, all predict that alloy D should lie in the $(\gamma + \alpha)$ phase field. Irvine et al (22) observed that the addition of nickel to a 12%Cr, 0.1%C steel was particularly effective in retarding the transformation to delta ferrite, which is generally regarded as being very slow in 12% Cr low carbon steels. At 700°C, 1% nickel proved sufficient to prevent transformation after prolonged ageing of 10,000 hours. In alloy D (12Cr, 3Ni) there was a much larger addition of 3.6% Ni, Table 2. This relatively large percentage of nickel when added to a low carbon 12%Cr alloy markedly reduced both the M_s and A_s temperatures and thus with the M_f temperature depressed to below room temperature not all of the austenite will transform to martensite on cooling. The addition of 3.6% nickel also prevented the transformation to ferrite taking place when ageing alloy D (12Cr, 3Ni) at the lower temperatures of 400°-550°C.

Rees et al (7) are accredited with defining the $\alpha + \gamma/\gamma$ boundary at 800°C, fig.2 and Cook and Brown at 650°C (15, 19). However, neither of these two groups of workers investigated the 12Cr 3Ni alloy composition. The nearest composition studied was a 17%Cr 3%Ni alloy which proved to be fully ferritic after solution treatment, but precipitated austenite after ageing at 650°C and 800°C. Both Rees et al (7) and Cook and Brown (15) fixed the triple point and extrapolated the $\alpha + \gamma/\gamma$ boundary to the composition of the boundary in the simple iron-nickel binary system.

The constitution of alloy E (18Cr, 7Ni) was predicted from the published equilibrium diagrams to lie on the $\gamma/\gamma + \delta$ boundary. A small amount of delta ferrite was observed in the microstructure after solution treating at 1050°C; this was as predicted. The amount of delta ferrite present in the alloy was observed to increase with increasing ageing temperature and time. At the lower ageing temperatures of 650°C and below Cawley (16) suggested that sigma phase might be present in this alloy and if so, then the 18Cr, 7Ni composition would be situated at the corner of the four phase fields γ, $(\delta + \gamma)$, $(\gamma + \alpha + \sigma)$ and $(\sigma + \gamma)$ at 650°C. Rees et al and Cook and Brown (7, 15) place the junction of these four phase fields at the composition 18Cr, 8Ni, for both 650°C and 550°C respectively, but their alloys were aged for considerably longer times than the 1000 hours duration used in this work. Both groups of workers claimed to have observed sigma phase in their 18Cr, 8Ni alloys, which they examined solely by optical metallography. It is extremely difficult to distinguish between sigma phase and ferrite when these phases are observed optically and as they did not carry out any electron microscopy, it cannot be conclusively claimed that the sigma phase was present. No sigma phase was observed either optically or during the T.E.M. study of alloy E (18Cr, 7Ni), in this work, at any of the ageing temperatures investigated. There was also no significant increase in hardness of the alloy which would indicate the presence of sigma phase. The small increase in hardness of alloy E (18Cr, 7Ni) observed after ageing at 650°C and 700°C corresponded to the precipitation of $Cr_{23}C_6$ and the reaustenitisation of the martensite present in the solution treated microstructure, which formed new untempered martensite on cooling from the ageing temperatures. The large proportion of nickel present in alloy E, i.e. 7%, markedly reduced the A_s temperature to ~650°C, above which reaustenitisation will occur.

At the lower ageing temperatures of 450°C a significant increase in hardness of alloy E (18Cr, 7Ni) was apparent. A new phase was observed precipitating inside the delta ferrite islands. This was identified as the α' phase, fig.41, more commonly referred to as 475°C embrittlement. This was in agreement with the calculated equilibrium diagram of Kaufman et al, fig.14, which places this 18Cr, 7Ni alloy in the (γ + α + α') phase field at 475°C.

Alloy F (30Cr, 13Ni) whose solution treated microstructure consisted of γ + δ, also precipitated the α' phase in the ferrite grains. The precipitate could be clearly resolved after ageing at 400°, 450° and 500°C. Again the equilibrium diagram as proposed by Kaufman et al indicated that alloy F would lie centrally in the (γ + α + α') phase field at 475°C, fig.14. 550°C is generally regarded as being the upper temperature limit for α' formation and after ageing alloy F (30Cr, 13Ni) at 550°C for 1,000 hours no α' phase was observed, fig.45. However, after 200 hours ageing time at 500°C, sigma phase was seen precipitating at the delta ferrite/ austenite boundaries. After 1000 hours at 550°C the microstructure of alloy F (30Cr, 13Ni) consisted of austenite and sigma phase, the delta ferrite having completely transformed, fig.45. Alloy F (30Cr, 13Ni) was predicted to lie in the $(\gamma + \sigma)$ phase field at 550°C, fig.4, 650°C, figs.3 and 5, and 800°C, fig.2, and indeed the alloy's microstructure did consist of $\gamma + \sigma$ phases in the temperature range 550°-850°C. At 900°C, which is the upper limit for sigma phase precipitation, alloy F (30Cr, 13Ni) consisted of a $\gamma + \delta$ structure with no σ phase. Also there was no change in the hardness of the alloy, fig.40, indicating that precipitation had not occurred.

5.3.1 Constitution of Transformable Quaternary Alloys

Alloy E (18Cr, 7Ni) formed the base Fe-Cr-Ni ternary alloy to which the five quaternary additions of 2% Mo, 1% Nb, ¼% Ti, 1% and 2% Si were made. The chemical compositions of the five quaternary alloys are shown in Table 3.

The microstructure of Alloy E, after solution treatment at 1050°C, consisted largely of austenite some proportion of which had transformed to martensite on cooling. It also contained a small proportion of delta ferrite. The ageing behaviour of alloy E (18Cr, 7Ni) was complex. Ageing was carried out at 650°C, 750°C and 850°C and an increase in the proportion of delta ferrite resulted with increasing ageing temperature and time.

Also, due to the high nickel content of 7%, the A_s temperature was depressed and above 650°C reaustenitisation commenced with the subsequent transformation of that austenite to untempered martensite on cooling from the ageing temperature.

The composition of alloy E (18Cr, 7Ni) places it just within the $(\gamma + \delta)$ phase field in the temperature range 1050°C - 650°C, although it lies very close to the junction of four phase fields γ, $(\alpha + \gamma)$, $(\gamma + \alpha + \sigma)$ and $(\sigma + \gamma)$. The addition of the quaternary elements Mo, Nb, Ti and Si would be expected to affect the constitution of the base ternary alloy E over the temperature range studied as all these elements are known ferrite and sigma phase promoters.

The addition of 2% Mo to alloy E (18Cr, 7Ni) caused a greater proportion of delta ferrite to be present in the quaternary alloy after solution treating at 1050°C, 35% delta ferrite as compared to only 5% in the base ternary alloy. Irvine et al (22) demonstrated the potent delta ferrite forming capabilities of Mo by adding 2% Mo to their 17Cr, 4Ni alloy, where a 20% increase in the delta ferrite content of the alloy resulted. The present observation is generally in confirmation of the indications of Irvine et al (22).

Ageing the Mo quaternary alloy at 650°, 750° and 850°C produced an increase in the amount of delta ferrite with increasing ageing temperature and time, fig.59. Sigma phase was also seen precipitating at the longer ageing times, fig.59. The addition of 2% Mo to alloy E (18Cr, 7Ni) caused the constitution of alloy E to change from consisting of $\gamma + \delta$ to $\gamma + \delta + \sigma$ in the temperature range 650°C-850°C when aged for 1000 hours or less. The $\gamma/\gamma + \sigma$ phase boundary therefore has been shifted to lower chromium contents. Mo has been shown to be a potent sigma phase stabilising element (8, 16), Nicholson et al (8) demonstrated that an addition of 2% Mo would displace the $\gamma/\gamma + \sigma$ boundary by ~3% chromium, towards lower chromium contents at 650°C which agrees well with this work.

Silicon, which is also reported to be a potent delta ferrite former (16) especially at solution treatment temperatures, was added to the base ternary alloy E (18Cr, 7Ni). The silicon additions of 1% and 2% only marginally increased the amount of delta ferrite present in the quaternary alloy after solution treatment, although upon ageing at 650°C, 750° and 850°C the amount of delta ferrite was seen to increase with increasing ageing temperature and time. Ageing at 850°C and 750°C moved the alloy further into the $(\gamma + \alpha)$ phase field, and upon ageing at 650°C for 1000 hours a very small amount of sigma phase was detected in both the 1% Si and 2% Si quaternary alloys.

It was not possible effectively to study the effect of Ti or Nb quaternary additions on the constitution of alloy E. The $\frac{1}{4}$% Ti containing alloy fell short of its specification, having only 0.015% Ti present. This coupled with a higher nickel content of 8.21% served to place the alloy in the austenite region of the phase diagram both at solution treatment temperatures and upon ageing at 650°, 750° and 850°C. The solution treated microstructure of the 1% Nb containing alloy resembled that of the base ternary alloy E (18Cr, 7Ni). It consisted of an austenitic matrix which had partially transformed to martensite on cooling along with a few, discrete, delta ferrite islands. It also contained a fine dispersion of NbC precipitates and therefore the effect of niobium on the constitution of alloy E (18Cr, 7Ni) was negated, as much Nb had been taken out of solution. Ageing of the 1% Nb quaternary alloy at 650°, 750° and 850°C did not affect the constitution of alloy E and it remained in the $(\gamma + \delta)$ phase field.

Niobium and titanium are both known to be ferrite and sigma phase stabilisers (9, 16, 13, 23) although their effect is often reported as being 'weak' due to their ability to form carbides of the MX type and other intermetallic phases i.e. Ni_3Ti and Fe_2 Nb.

5.4 Transformation and Precipitation Effects in the Transformable and Duplex Alloys

The transformation and precipitation effects which occurred in alloy D (12Cr, 3Ni), alloy E (18Cr, 7Ni) and alloy F (30Cr, 13Ni) were initially observed by the changes in hardness, as seen in the series of ageing curves, figs.31, 36 and 40.

Optical metallography revealed the presence of new phases forming in the alloys which were further investigated using transmission electron microscopy.

In both alloys D (12Cr, 3Ni) and E (18Cr, 7Ni) there was a transformation of the austenite matrix, on cooling from the solution treatment temperature of 1050°C, forming martensite. It is well known that in the leaner Fe-Cr-Ni alloys, the austenite phase is unstable at low temperatures and that it transforms - martensitically. This martensite differs from that found in carbon or alloy steels as the carbon content is extremely low. Therefore the low carbon martensite formed in these two Fe-Ni-Cr alloys D and E was not as hard and brittle as the martensite that is found in plain carbon steels - although the nature of the martensite transformation is essentially the same.

Both alloy D (12Cr, 3Ni) and E (18Cr, 7Ni) contained a high percentage of nickel and thus the M_s, M_f and A_s temperatures are markedly depressed. Both alloys have their calculated M_f temperatures below room temperature and so a proportion of retained austenite was present in their solution treated microstructures. In the case of alloy E (18Cr, 7Ni) a small proportion of delta ferrite was also present after solution treatment. On ageing alloys D (12Cr, 3Ni) and E (18Cr, 7Ni) in the temperature range 400°-900°C some similarities in their ageing behaviour were observed.

At 400°C an increase in hardness was observed in both alloys, figs.31 and 36. In alloy D (12Cr, 3Ni) this was due to conditioning of the austenite by carbide precipitation which allowed more martensite to form on cooling from the ageing temperature. Once conditioned, after 10 hours at 400°C the hardness of alloy D (12Cr, 3Ni) showed very little variation with time up to the maximum ageing time of 1000 hours, fig.31.

In alloy E (18Cr, 7Ni) there was also some conditioning of the retained austenite and therefore further transformation to martensite on cooling from 400°C. Superimposed upon this increased hardening was the effect of the α' precipitation observed in the delta ferrite grains, fig.37, and therefore an even higher hardness value was obtained, fig.36. The α' phase was also responsible for the increase in hardness observed in alloy F (30Cr, 13Ni) at the lower ageing temperatures of 400°-500°C. Both alloys E and F exhibited an increase in hardness after 10 hours at 500°C, followed by a steady decrease in hardness up to 1000 hours.

The phenomenon of 475°C embrittlement has been investigated by many workers (60 - 70) who have observed the very fine, coherent, chromium rich α' phase precipitating in the delta ferrite grains in Fe-Ni-Cr alloys. It is generally agreed that at lower chromium contents 475° embrittlement is caused by a precipitation hardening and overageing reaction, and the results of this work would lend support to this. The extremely fine α' precipitates are shown in the delta ferrite grains in alloy F (30Cr, 13Ni) after 10 hours ageing at 500°C, fig.41. The precipitates could only be resolved at high magnifications in the TEM at 50,000 times, fig.41. There was also a fine precipitation of $Cr_{23}C_6$ observed on the grain boundaries in this alloy. After 1000 hours at 500°C the hardness curves indicated that overageing

of the α' precipitate had taken place, fig.40. The TEM micrographs show that the α' precipitate had indeed coarsened and a lath-like austenite phase had also formed within the delta ferrite grains, fig.41. The $Cr_{23}C_6$ precipitation on the grain boundaries had also increased and was seen to be growing in a cellular manner into the delta ferrite grains, fig 41.

The withdrawal of chromium both into the $Cr_{23}C_6$ and the α' precipitate was a contributing factor to the transformation to austenite which occurred within the delta ferrite grains. At high magnification, as seen in the TEM, this lath-like austenite was almost martensitic in appearance, fig 41.

Southwick and Honeycombe (70) studied the decomposition of delta ferrite to austenite in a 26Cr, 5Ni alloy. At low temperatures 300°-650°C they observed that α' precipitated very quickly - after only 5 seconds in the 400°-600°C temperature range and that on prolonged ageing the α' phase dissolved in the ferrite grains, the disappearance of the α' being accompanied by the precipitation of lath-like austenite. The precipitation observed in alloy F (30Cr, 13Ni) was similar in nature to that observed by Southwick and Honeycombe (70) - however, the precipitate free zone they observed adjacent to the grain boundaries was not clearly evident in either alloy E (18Cr, 7Ni) or F (30Cr, 13Ni). The α' precipitate was not observed in the alloys at the 550°C ageing temperature, this temperature is above the limit of α' formation in Fe-Cr-Ni alloys containing less than 50% chromium, fig.13.

Ageing alloy D (12Cr, 3Ni) and alloy E (18Cr, 7Ni) in the temperature range 500°-700°C produced tempering of the martensite present, the ageing curves showing the characteristic decrease in hardness, figs.31 and 36. The presence of nickel in both alloys served to lower the A_s temperature and reaustenitisation of the matrix commenced at 650°C. The 650°C and 700°C ageing curves for both alloy D (12Cr, 3Ni) and alloy E (18Cr, 7Ni) are shown in figs.31 and 36 respectively. The initial annealing out of the dislocations in the martensite was indicated by the small decrease in hardness of the alloys at the shorter ageing times. Prolonged ageing produced some austenite which on cooling produced a heavily dislocated martensite and hence a subsequent increase in the hardness. At the ageing temperatures of 750°and 850°C, the transformation to austenite proceeded rapidly. The amount of new austenite formed in the alloys increased with increasing ageing temperature and time. On quenching the alloys from these ageing temperatures some of the newly formed austenite transformed to martensite, but as the ageing temperature and time increased more retained austenite was present in the resulting aged microstructures.

In alloy D (12Cr, 3Ni) this behaviour was very pronounced, fig.31. In addition to the reaustenisation occurring a small amount of $Cr_{23}C_6$ was also observed precipitating on the lath boundaries at 750° and 800°C. This precipitation was extremely fine and therefore difficult to resolve, fig.34. The $Cr_{23}C_6$ contributed to the reaustenitisation reaction by partitioning of elements leading to the increased stability of the newly formed austenite and therefore decreasing the amount of martensite formed on quenching from the ageing temperatures. At 900°C there was no $Cr_{23}C_6$ precipitation; the hardness of alloy D (12Cr, 3Ni) remained constant on ageing for 10 to 1000 hours. The amount of austenite and transformed martensite remained the same, equilibrium conditions being apparently obtained.

Although there are similarities in the ageing behaviours exhibited by alloy D (12Cr, 3Ni) and alloy E (18Cr, 7Ni), the transformations occurring in alloy E are somewhat more complex. The reaustenitisation which occurred between 650°-900°C in alloy E was more marked. More retained austenite was present in the aged microstructures after the shorter ageing times and there was less of a tendency for transformation to martensite to occur. The delta ferrite phase was also present in alloy E (18Cr, 7Ni) and the amount of delta ferrite was observed to increase with increasing ageing temperature and ageing time. The partitioning of chromium to the delta ferrite phase would increase the stability of the austenite phase, as would the precipitation of $Cr_{23}C_6$, the chromium partitioning more than offsetting that of carbon which was also observed precipitating in alloy E between 650°C and 850°C. The $Cr_{23}C_6$ precipitates were observed on the lath boundaries and again, as seen in alloy D, the precipitation was very fine, fig.38. This is not surprising as the carbon content of both alloys was very low. At 900°C the hardness of alloy E first increased then gradually decreased with longer ageing times. There was less delta ferrite present at this ageing temperature than at 850°C. There was a change in the amount of delta ferrite present at 900°C as equilibrium conditions were approached and the hardness of the alloy approached that of the solution treated value.

The ageing behaviour of alloy E (18Cr, 7Ni) between 650°C and 850°C, which showed a moderate increase in hardness, demonstrates a balance between the effects of increasing delta ferrite content, the precipitation of $Cr_{23}C_6$, and the reaustenitisation of the matrix accompanied by subsequent transformation of the newly formed austenite in some part to martensite. It is interesting to note that no sigma phase precipitation occurred in this alloy although there was delta ferrite present. The ageing study performed on alloy E (18Cr, 7Ni) would indicate that the alloy remains in the $(\gamma + \delta)$ region of the phase diagram. However, because the nature of the sigma phase transformation is notoriously sluggish, eventual sigma phase precipitation in this alloy cannot be ruled out.

The transformation to sigma phase was studied in alloy F (30Cr, 13Ni). The published equilibrium diagrams, fig.1, indicated that alloy F would lie in the $(\gamma + \delta)$ field at 1050°C and at 800°C and 650°C, figs.2 and 5, the composition of alloy F (30Cr, 13Ni) placed it in the ($\gamma + \sigma$) region of the Fe-Cr-Ni ternary phase diagram. Alloy F exhibited a degree of age hardening at temperatures of 400°-850°C, but not at 900°C as this was above the temperature limit for sigma phase formation. As previously discussed, alloy F was susceptible to 475°C embrittlement, caused by α' precipitation occurring in the delta ferrite phase between 400°-500°C, figs.40-43. At 550-850°C a transformation to sigma phase occurred in alloy F. The transformation was rapid at the higher ageing temperatures of 800°-850°C. A large amount of sigma phase was present in alloy F after only 10 hours, which corresponded well with the observed increase in hardness of the alloy, fig.40, at 600°-850°C. However, at 550°C the transformation was slower, allowing the progress of the transformation to be observed. After ageing for both 10 and 100 hours at 550°C, alloy F (30Cr, 13Ni) consisted of austenite, delta ferrite and a cellular precipitation of $Cr_{23}C_6$ which was situated on the delta ferrite/austenite interfaces, fig.44. This cellular form of precipitation of $Cr_{23}C_6$ has been observed by a number of workers (16, 32, 53, 55). $Cr_{23}C_6$ was also precipitated on the γ/γ grain boundaries but as discrete precipitates, fig.43. Sigma phase was detected in the 200 hour, 550°C aged alloy. Fig.44 shows the delta ferrite grains undergoing transformation. This corresponded with the age hardening curve, fig.40, where only slight hardening was observed until 200 hours, followed by a rapid increase in hardness up to 1000 hours.

Sigma phase is a very hard, brittle intermetallic phase which has been responsible for many catastrophic failures occurring in stainless steels

Insert E
↓ The transformation to sigma phase

Insert E at room temperature after embrittlement at higher temperatures . However, for this reason no failures have been observed in stainless steels used in fast breeder reactors.

completed. The transformation occurs considerably more rapidly in duplex ($\delta + \gamma$) alloys which is not surprising as it is the delta ferrite phase itself, to which chromium is partitioned, which undergoes transformation (6, 20, 21, 32, 36, 55). Cold working prior to ageing has been seen to accelerate sigma formation (10, 34). Sigma phase has also been observed associated with and in some cases precipitating on carbides and other intermetallic phase (20, 21, 32, 36). In duplex ($\delta + \gamma$) alloys the maximum rate of sigma phase precipitation is generally agreed to occur at ~ 700°-750°C, which corresponds with the maximum precipitation temperature range for $Cr_{23}C_6$. It is not surprising that several workers have concluded that the sigma phase transformation is in some way connected with the precipitation of $Cr_{23}C_6$ as both phases, whilst precipitating over the same temperature range, are essentially in competition with each other for chromium.

The transformation to sigma phase was observed in alloy F (30Cr, 13 Ni), and was associated with the carbide $Cr_{23}C_6$. After only 10 hours, even in this very low carbon alloy, $Cr_{23}C_6$ was observed precipitating in a cellular manner along with new austenite, the cellular transformed region bowing out into the delta ferrite grains. The precipitates were a little coarser after 100 hours of ageing but otherwise the microstructure was similar to that observed after 10 hour ageing. After ageing for 200 hours at 550°C the delta ferrite grains could be observed in a state of partial transformation, fig.44. A complex and to a large extent unresolvable structure was formed at the delta ferrite/austenite and cellular carbide boundary. This structure grew inwards consuming the whole of the delta ferrite grain. This complex transformation product, fig.44, resembled a region of immiscibility, possibly associated with a spinodal decomposition giving areas of high and low chromium contents, which subsequently forms sigma and new austenite. Dislocation networks were observed in the transforming delta ferrite grains, most likely as a result of the strains produced during the transformation. Moiré fringes were observed around the γ particles indicating some degree of coherence of the precipitate with the matrix. These γ particles themselves precipitate sigma which then coalesces leaving a sigma phase grain in place of the delta ferrite grain, but with some new austenite which can form as laths, often observed protruding into the sigma grain, fig.44. This resultant sigma phase was heavily faulted due to the sigma forming within δ which contains dislocations, and because it comprises many particles of coalesced sigma. After 1000 hours ageing at 550°C the microstructure of alloy F (30Cr, 13 Ni) consisted of austenite and sigma phase, the sigma being surrounded by necklaces of new austenite and $Cr_{23}C_6$ cellular precipitation, fig.44.

Several mechanisms for the transformation of delta ferrite to sigma phase have been postulated. There is now general agreement upon some aspects involved in the transformation to sigma phase. It is accepted that a cellular precipitation always precedes the transformation of delta ferrite to sigma phase as was indeed observed in the present work. The new austenite/$Cr_{23}C_3$ cellular precipitate always forms on the δ/γ interfaces and the new austenite always has the same orientation relationship with the prior austenite grains and the:

$$(100)_{Cr_{23}C_6} \parallel (100)_{\gamma}; \quad \langle 100\rangle_{Cr_{23}C_6} \parallel \langle 100\rangle_{\gamma}$$

orientation relationship exists between the $Cr_{23}C_6$ and the new austenite. Several workers (16, 53, 55) have reported that sigma phase begins to form as rods, accompanied by new austenite formation, giving a lamellar structure that begins to grow out from the interface between the cellular $Cr_{23}C_6$/new austenite and into the delta ferrite grains before final decomposition of the remainder of the delta ferrite to sigma phase and new austenite. This was not observed in this work. What was apparent was that after the formation of the cellular $Cr_{23}C_6$/new austenite precipitation, which bowed out into the delta ferrite grains, the remainder of the delta ferrite grains broke down into two phases, sigma and austenite. The transformation best resembled a spinodal type of reaction, fig.44.

5.4.1 Transformation and Precipitation Effects in the Transformable Quaternary Alloys

The ageing behaviour of alloy E (18Cr, 7Ni) on which the five quaternary transformable alloys are based, has been previously discussed in section 5.3. The composition of alloy E (18Cr, 7Ni) places it in the $(\gamma + \delta)$ phase field at 1050°C and also at the ageing temperatures 650°-850°C, although it lies close to the corner of four phase fields γ, $(\alpha + \gamma)$, $(\gamma + \alpha + \sigma)$, $(\sigma + \gamma)$. At 650°C and above reaustenitisation takes place causing untempered martensite and retained austenite to be present in the aged microstructure. The amount of delta ferrite present in the alloy was also seen to increase with increasing ageing temperature and time. Furthermore, the precipitation of $Cr_{23}C_6$ also occurred in this alloy, the maximum rate being observed at 700°-750°C. The addition of ferrite forming elements Mo, Si, Nb and Ti could have a number of effects on the microstructure of alloy E (18Cr, 7Ni). They would be expected to produce a greater proportion of delta ferrite in both the solution treated and aged microstructures and to stabilise the sigma phase in the 650°-850°C temperature range.

Of the four quaternary addition elements Mo and Si are known to be the stronger ferrite forming elements. The effects of Nb and Ti are reduced due to their strong ability to form carbides/nitrides of the MX type. In the case of the niobium containing quaternary alloy, the cubic carbide NbC was present as a finely divided intragranular precipitate after solution treating at 1050°C. It is not, however, inconceivable that a proportion of the high temperature Laves phase (Fe_2Nb) could also have been present, although no positive identification of the phase was made during TEM studies. A small amount of $M_{23}C_6$ was observed after ageing the 1% Nb quaternary alloy at 750° and 850°C along with coarsening of the precipitates which were present after solution treatment. As the quaternary alloys only contain a very small amount of carbon, 0.007%, the 1% Nb addition should have easily formed carbides with all the available carbon; however, $M_{23}C_6$ was also precipitated in this alloy suggesting that a proportion of the 1% Nb additions may have been incorporated in another phase - most likely Fe_2Nb, thus leaving some carbon free to form $M_{23}C_6$. Niobium is a strong carbide forming element and along with titanium is used commercially to stabilise a range of commercial stainless steel, preventing the formation of $M_{23}C_6$ taking place on the grain boundaries and so reducing the alloys susceptibility to intergranular corrosion.

Although the titanium quaternary alloy fell short of its specification, a very small amount of TiC was observed on ageing at 650°, 750° and 850°C, again accompanied by a small amount of $Cr_{23}C_6$ precipitation. The amount of precipitation was so small as to cause no age hardening response in the alloy. The increased amount of nickel present in the Ti transformable quaternary alloy produced a greater proportion of austenite in the solution treated and aged microstructures.

$M_{23}C_6$ was also observed precipitating in the Mo and Si quaternary alloys after ageing at 650°, 750° and 850°C. Only a very small amount of Mo bearing $Cr_{23}C_6$ was observed in the 2% Mo quaternary alloy, which was expected as there would be competition for chromium with the sigma phase which formed in the alloy. The greatest amount of $Cr_{23}C_6$ precipitation was observed in the 2% silicon quaternary alloy. Silicon was also dissolved in the carbide and it is not inconceivable that G-phase formation was taking place. $Cr_{23}C_6$ has been reported as being analogous to G-phase. It was not possible to distinguish between the two phases using electron diffraction techniques. Silicon is also known to lower the solubility of carbon in austenite thereby promoting precipitation.

The relatively large amount of precipitation in the 2% Si quaternary alloy resulted in a shift in the martensite transformation range leading to a greater amount of austenite being present on ageing the alloy at 750° and 850°C. This transformed to untempered martensite on cooling which produced a corresponding increase in the hardness of the quaternary alloy as compared with the base ternary alloy E (18Cr, 7Ni).

It is interesting to note that sigma phase was observed in the 1% and 2% silicon quaternary alloys after ageing at 650°C for 1000 hours. The amount of sigma phase produced was extremely small and could not be observed optically, but was detected during the TEM study. At 750°C and 850°C no sigma phase precipitation was observed. It is likely that $Cr_{23}C_6$

precipitation, which is at a maximum in this temperature range, could slow down sigma phase precipitation due to competition for chromium. Also the depletion of chromium from the matrix would serve to push the alloy further into the (γ + α) phase field. The microstructure of the 750°C and 850°C aged silicon quaternary alloys consisted of interlocking laths of γ + α, which is due to $M_{23}C_6$ precipitation at martensite lath boundaries during ageing which then nucleate for austenite thus forming an austenite lath between two tempered martensite laths, fig.67. This type of structure is not unusual in alloys which have become partially austenitised when starting from a martensite structure (c.f. 9% Ni steels).

The addition of 2% molybdenum to the base ternary alloy E (18Cr, 7Ni) however, was observed to promote sigma phase formation in the 650°-850°C ageing temperature range. This placed the 2% Mo quaternary alloy in the (γ + δ + σ) phase field, moving the γ / γ + α boundary to lower chromium contents. The increased amount of delta ferrite that was present after solution treatment gave rise to increased nucleation sites for sigma formation. It is known to precipitate on the γ/δ boundaries very rapidly in duplex alloys.

These observations of the effect of the quaternary additions on the base ternary alloys agree very well with Cawley's work (16). He observed that silicon, although a potent delta ferrite former at 1050°C, had markedly less effect as a sigma former at 800°C. Molybdenum, however, was an even stronger ferrite former than silicon at 1050°C and at 800°C was a potent sigma phase former. These results suggest that Mo shifts the four phase field intersection to lower Cr contents, but that Si moves the same intersection towards the Fe rich corner or to lower Ni contents. It is known that Ni_3Si is a stable phase, which could explain the effect of Si, but in the present work no evidence for Ni_3Si formation has been obtained. However, it may be speculated that the effects of Mo and Si, which appear so different in terms of the shift of phase boundaries could be due to mutual clustering of elements in the austenite matrix.

5.5 Irradiation Damage Studies

There are obvious advantages to be gained from simulating irradiation damage in austenitic alloys by use of electron or charged particle techniques. However, the nature of the irradiating medium must be borne in mind when interpreting the irradiation damage results. The major advantage to be gained from using simulation techniques is that results can be obtained in a matter of days, unlike neutron irradiation damage studies which require years before any information can be gained. The two main simulation techniques which were used were the HVEM and the VEC; both have their limitations with regard to comparing the results with actual neutron irradiation damage.

In the HVEM irradiation damage is produced in an alloy by a focused beam of accelerated electrons. These electrons possess an energy of 1MeV and are capable of displacing one atom from its lattice site per electron. Irradiation damage caused by fast neutrons, however, is much more severe. The neutron unlike the electron has a relatively large mass and low elastic scattering cross section. The neutron generates high energy primary knock ons (pko) when the first atom is displaced from its lattice site leading to a collision cascade where relatively large vacancy rich areas collapse to form vacancy clusters and the large number of interstitial atoms created form a network of dislocations. However, an advantage of using the HVEM is that it was possible to observe the irradiation damage process whilst it was occurring. A large dose level of ~ 80 dpa can easily be attained in a day, unlike the maximum ~ 25 dpa per year for neutron irradiation at the centre of the core in a fast breeder reactor, and valuable information about the void swelling characteristics of alloys can be gained if the HVEM results are interpreted taking into consideration the limitations of the technique.

The two alloys on which HVEM irradiations were performed were alloy A (20Cr, 23Ni) and alloy C (30Cr, 33Ni). Both alloys were fully austenitic and would therefore be likely to exhibit void swelling when held in the temperature range ~ 350°-700°C. Voids will grow only if the temperature is high enough for vacancy diffusion to occur.

The effect of temperature on void swelling can be observed in fig.69. The rate of swelling of alloy C (30Cr, 33Ni) during irradiation at 600°C was twice as fast as that at 500°C. It was expected that at higher temperatures the swelling rate would increase as void growth depends on the diffusion of vacancies and this is a thermally dependent process. Raising the temperature towards the upper limit of 700°C (above which the vacancy clusters become unstable) would increase vacancy diffusion and so enhance the rate of void swelling.

The constitution, and therefore the composition of the matrix, is known to have a dominating influence on the void swelling behaviour of austenitic alloys (79) . Alloy A (20Cr, 23Ni) was observed to have a much slower void swelling rate than alloy C (30Cr, 33Ni) when irradiated in the HVEM at the same temperature of 550°C.

Void swelling depends critically on the nickel content of the Fe-Cr-Ni base alloys (79) and has been observed to increase with increasing concentration of chromium and chromium equivalent elements. Swelling has also been seen to be dependent on the stability of the alloy. Maximum void swelling rates are observed when the composition of an alloy places it in the three phase field with minimum swelling rates being obtained from single phase alloys. Alloy A (20Cr, 23Ni) has a more stable single phase austenitic structure at 550°C than alloy C (30Cr, 33Ni) which lies in the two phase ($\gamma + \delta$) phase field. It is therefore to be expected that the more stable austenitic alloy should exhibit a lower percentage of void swelling.

The programme of irradiation damage studies using the VEC irradiation was designed to show the direct effect of a fourth element addition on the void swelling behaviour of alloy A (20Cr, 23Ni). The elements added to alloy A were 2% Mo, 1% Nb, ¼% Ti or 1 and 2% Si. No results were obtained from the Ti alloy due to the voided layer not being located. The quaternary alloys were irradiated in the VEC with 46 MeV Ni^{6+} ions at 550°C, up to a dose of 10 dpa. This dose was achieved in one day so no temperature cycling of the specimens occurred. 10 dpa is a relatively low dose as fast reactor core components would be expected to receive ~ 120 dpa during their lifetime in the reactor. At this low dose the direct effect of the fourth element addition on void nucleation, number, density and void size could be assessed as coalescence of the voids had not taken place.

The 1% Nb addition caused a slight reduction in the number of voids present in the alloy, Table 4, although the size of the voids was larger than that generated in the pure ternary alloy A. This resulted in only a very small overall reduction in void swelling being observed.

The addition of 2% Mo produced an increase in the number of voids present after irradiating for 10 dpa, although these voids were very much smaller in size, fig.72, and therefore, a large reduction in the percentage void swelling was obtained. An even greater reduction in void swelling was produced by the addition of 2% Si. This was as a result of far less voids being produced, although, on average, these voids were larger than those produced in alloy A. The presence of 1% Si in alloy A, slightly reduced the void number density whilst marginally increasing void size and therefore, producing only a very slight decrease in void swelling.

The incubation period before the onset of void swelling occurred at doses lower than 10 dpa in all the alloys examined. Several authors make the assumption that small voids indicate that the growth of the voids is slow and therefore they assume that the nucleation of voids must also take place slowly (88); this is not necessarily the case. The presence of fewer voids in the matrix was caused by the addition of 2% Si to alloy A, suggesting that silicon has a direct effect on nucleation. However, the addition of 2% Mo did not affect the nucleation of the voids; a larger number were present in the alloy although they were considerably smaller. The molybdenum addition served to either considerably slow down the growth of voids or to delay the onset of nucleation by increasing the incubation period, or indeed influencing both of these mechanisms.

The reasons why solute elements affect the void swelling of austenitic alloys is not fully understood. It is widely accepted that solute atoms affect the defect trapping capability of the matrix and silicon is known to trap interstitials because of the small size of the silicon atom (89) providing extra volume for the interstitials. This trapping enhances the recombination and annihilation of the point defects as the interstitials cannot escape from the vacancy rich areas. The result of this will be to reduce the number of vacancies available for void growth and therefore swelling will be reduced. This mechanism of solute trapping is only effective whilst the solute is in solid solution in the matrix. Likewise, with the molybdenum atom whose very large atomic size produces a compressively strained lattice which, again provides preferential sites for vacancies. Whilst this theory may explain the observed slow growth of the voids in the molybdenum containing alloy, the voids in the silicon alloy were very much larger therefore substantial growth of voids had taken place whilst the number nucleated was very much reduced.

5.6 Neutron Irradiated Alloys

The two series of alloys based on the 12Cr, 15Ni composition, (alloys N1 - N4, see Table 5), with additions of silicon allow a comparison to be made between the thermally aged microstructures and the neutron irradiated microstructures. The thermally aged specimens were examined using optical and transmission electron microscopy in order to assess their phase stability and the nature of any precipitation occurring after ageing for 13,000 hours. The neutron irradiated alloys were examined at Harwell, using a transmission electron microscope fitted with EDX analysis.

5.6.1 Thermally Aged for 13,000 Hours

The composition 12Cr, 15Ni lies in the austenite phase field at 550°C (15) and 650°C (19). Although the N series of alloys contained silicon (Table 5), which is a known ferrite and sigma former, the matrix remained austenitic after ageing at 13,000 hours at 435°, 505°, 575° and 645°C.

The presence of $M_{23}C_6$, the high chromium containing carbide, was observed precipitating in the manner described by Lewis et al (52) and Beckitt et al (53). The cube corner to cube corner precipitation occurs on dislocations which are formed during quenching from the solution treatment temperatures, fig.74. The grain boundary precipitation of $M_{23}C_6$ was seen to consist of separate precipitates as opposed to a continuous grain boundary network, fig.74. Lewis and Hattersley (52) also observed this discontinuous precipitation and concluded that it occurred because of the initial rapid rate of decrease in the volume free energy associated with the enhanced diffusion of the solute atoms along the migrating boundary.

Beckitt and Clark (53) studied the shape and mechanism of formation of $M_{23}C_6$ in austenite. They suggested that $M_{23}C_6$ particles have a tendency to be cubic in shape and are bounded by {111} and {110} planes. The $M_{23}C_6$ precipitated in the 12Cr, 15Ni experimental alloys adopted a cubic shape when observed growing within the austenite grains.

The precipitation of $M_{23}C_6$ was also seen to increase with both increasing temperature and silicon content, figs.73 and 74. At higher temperatures there is enhanced thermal diffusion of chromium and carbon, so an increase in the amount of precipitate present in the alloys was expected. $M_{23}C_6$ has been suggested as being a dominant phase in austenitic alloys between 650°-750°C, higher temperatures favouring its formation.

Silicon is known to lower the solubility of carbon in austenite and will therefore promote carbide formation by increasing the degree of supersaturation. Also it is possible that a small amount of G-phase, a ternary silicide based on nickel and silicon, could be precipitating in these alloys, its formation being associated with $M_{23}C_6$ (47).

Recent work by Williams et al, 1987, has however, produced evidence for the presence of some ferrite.

5.6.2 Thermally Aged Plus Neutron Irradiated for 13,000 Hours

T M Williams et al (119) examined the fast neutron irradiated N series alloys (12Cr, 15Ni) which contained 0.14% - 1.42% Si. The alloys had been irradiated at temperatures in the range 435°-645°C. Increasing silicon content was again observed to reduce void swelling, although a transformation to ferrite occurred in alloys N2 - N4 where the transformation was seen to increase with increasing silicon content. The microstructural instability of these alloys was a consequence of solute redistribution. As there was no evidence found for segregation in the thermally aged, unirradiated alloys, in this work the mechanisms which lead to solute redistribution and microstructural instability were (whilst being irradiation driven) enhanced by the presence of silicon. Although the mechanism for why this should be the case is not understood, the results of Williams et al (119) suggest that silicon significantly accelerated the separation of the intragranular regions into nickel-rich and nickel depleted zones.

6.0 CONCLUSIONS

6.1 Constitution of the Fe-Cr-Ni Alloys at 1050°C

(i) The constitution of the three ternary austenitic alloys and the three transformable and duplex ternary alloys, after solution treatment at 1050°C, was in agreement with published equilibrium diagrams (19).

(ii) At 1050°C the microstructure of alloy D (12Cr, 3Ni) consisted of austenite, whilst alloy E (18Cr, 7Ni) consisted of austenite and delta ferrite. In both alloys the austenite phase was unstable and partial transformation to martensite resulted on cooling, the M_f temperatures for these alloys being below room temperature.

6.1.1 Constitution of Fe-Cr-Ni-X Alloys at 1050°C

(i) Quaternary alloy additions of 2%Mo, 1%Nb, ¼%Ti and 1% and 2%Si were made to the base ternary alloy A (20Cr,23Ni). Although the constitution of the austenitic base ternary alloy at 1050°C is close to the austenite/delta ferrite boundary, the addition of these four known ferrite forming elements was not sufficient to alter the constitution of alloy A (20Cr,23Ni). All five quaternary alloys retained a fully austenitic microstructure on cooling from 1050°C.

(ii) Alloy E (18Cr, 7Ni) formed the base Fe-Cr-Ni ternary alloy to which the five quaternary additions of 2%Mo, 1%Nb, ¼%Ti, 1% and 2%Si were made. The addition of 2%Mo and 1% and 2%Si caused a greater proportion of delta ferrite to be present in the quaternary alloys after solution treating at 1050°C. This confirms the findings of Irvine et al (22) and Cawley (16).

6.2 Constitution of the Fe-Cr-Ni Alloys after Ageing at 400°-900°C

(i) The constitution of alloy B (20Cr, 43Ni) and alloy C (30Cr, 33Ni) in the temperature range 400°-900°C was in good agreement with the published equilibrium diagrams (7,15,16,19).

(ii) Alloy A (20Cr, 23Ni) was predicted to lie in the austenite + sigma phase field at temperatures below 650°C (7,15,16,19). Alloy A remained fully austenitic over the ageing temperature range; no sigma phase was formed. However, the kinetics of the sigma transformation are notoriously slow and equilibrium conditions may not have been attained in this alloy especially at the lower ageing temperatures.

(iii) The phase equilibrium diagrams for 550°, 650° and 800°C (7,15,16,19) predict alloy D (12Cr, 3Ni) to lie in the austenite + delta ferrite phase field. No delta ferrite was formed in this alloy over the ageing range studied in this work.

(iv) The aged microstructure of alloy E (18Cr, 7Ni) consisted of austenite and delta ferrite. Several workers place alloy E near to, if not at the corner of the four phase fields (γ), ($\gamma + \sigma$), ($\gamma + \alpha + \sigma$) and ($\gamma + \alpha$) at 650°C and below. However no sigma phase was formed in this alloy despite the presence of delta ferrite.

(v) The constitution of alloy F was as predicted from the published equilibrium diagrams (7,15,16,19). Sigma phase was formed in the alloy over the 550°-850°C temperature range with α' observed precipitating in the delta ferrite between 400°-500°C which is in agreement with the calculated equilibrium diagram of Kaufman et al (17) which placed this alloy in the $\gamma + \alpha + \alpha'$ field at 475°C.

6.2.1 Constitution of the Fe-Cr-Ni-X Alloys After Ageing at 650°-850°C

(i) The five quaternary alloy additions did not affect the constitution of the base ternary alloy A (20Cr, 23Ni) which remained austenitic throughout the ageing temperature range.

(ii) The addition of 2%Mo to the base ternary alloy E (18Cr, 7Ni) moved the constitution of this alloy into the $\gamma + \delta + \sigma$ phase field in the temperature range 650°-850°C.

(iii) Silicon which is known to be a potent delta ferrite former pushed alloy E further into the $\gamma + \delta$ region at 750° and 850°C.

At 650°C a very small amount of sigma phase was present therefore placing alloy E in the $\alpha + \gamma + \sigma$ field. This is in good agreement with Cawley's work (16).

6.3 Transformation and Precipitation Effects Occurring in Fe-Cr-Ni Alloys Aged Between 400°-900°C

(i) The carbide $M_{23}C_6$ was precipitated in all six ternary alloys. As the carbon content of the alloys was very low there was only a small amount of precipitation observed. The maximum rate of precipitation was seen at 700°/750°C which is in agreement with other workers. The carbide was observed to have the

$$(100)_{M_{23}C_6} \quad || \quad (100)_\gamma \quad : \quad \langle 100\rangle_{M_{23}C_6} \quad || \quad \langle 100\rangle_\gamma$$

orientation relationship with the austenite matrix. $M_{23}C_6$ precipitated as discrete particles on the grain and twin boundaries in the austenitic ternary alloys A, B and C. However in alloys D and E the $M_{23}C_6$ precipitated on lath boundaries and was extremely fine. In alloy F, the duplex $\gamma + \delta$ alloy, $M_{23}C_6$ precipitated in a cellular manner on the γ/δ boundaries. It was accompanied by new austenite formation and was observed growing into the delta ferrite grains.

(ii) Delta ferrite was observed precipitating in alloy C (30Cr, 33Ni) both inter and intragranularly at temperatures above 650°C. The delta ferrite precipitated as laths within the austenite and as islands on the grain boundaries especially at triple points. The amount of delta ferrite precipitated from the austenite was observed to increase with increasing time and ageing temperature.

(iii) The chromium rich α' precipitate, which gives rise to the 475°C embrittlement phenomenon, was observed in the delta ferrite grains in alloys E and F in the 400°-500°C temperature range. The α' precipitates grew with increasing ageing temperature and time. Overageing of the α' precipitates occurred in alloy F after 1000 hours at 500°C and was accompanied by the formation of a rod like austenite. These observations were of a similar nature to those studied by Southwick and Honeycombe (70).

(iv) Ageing the duplex ($\gamma + \delta$) alloy F (30Cr, 13Ni) in the temperature range 550°-850°C produced a transformation of the delta ferrite phase which formed sigma phase and new austenite. This transformation was preceded by a cellular precipitation of $Cr_{23}C_6$ and new austenite which formed on the γ/δ grain boundaries. After 200 hours at 550°C the delta ferrite grains were observed in a state of partial transformation. A complex and to some extent unresolvable structure formed at the delta ferrite/cellular carbide + austenite interface. This structure grew inwards and consumed the whole of the delta ferrite grains. This complex transformation product resembled a region of immiscibility, possibly associated with a spinodal decomposition, giving areas of high and low chromium contents, which subsequently forms sigma phase and new austenite.

6.3.1 Transformations and Precipitation Effects Occurring in Fe-Cr-Ni-X Alloys After Ageing at 650°-850°C

(i) The carbide $M_{23}C_6$ was precipitated in all the quaternary alloys on ageing between 650°-850°C. The Nb and Ti quaternary alloys also precipitated NbC and TiC respectively. In the Nb containing alloys the possibility of Laves phase formation, especially at the higher ageing temperatures cannot be ruled out.

(ii) In both the 1% and 2% silicon containing transformable quaternary alloys based on alloy E (18Cr, 7Ni) a small amount of sigma phase was observed after ageing at 650°C for 1000 hours. No sigma phase was observed in the 750° and 850°C aged specimens. Silicon moves the four phase field intersection towards the Fe rich corner of the equilibrium diagram i.e. to lower Ni contents. The precipitation of $Cr_{23}C_6$, which is at a maximum in this temperature range also slows down sigma phase precipitation due to competition for chromium.

(iii) The addition of 2% molybdenum to alloy E moved the $\gamma/(\gamma + \alpha)$ boundary to lower chromium contents increasing the amount of delta ferrite formed after solution treatment and promoting sigma phase precipitation in the 650°-850°C ageing temperature range. There was no chi phase precipitation observed in this alloy nor in the quaternary alloy based on alloy A.

6.4 Irradiation Void Swelling

(i) The effect of increasing temperature on the void swelling rate was demonstrated during HVEM irradiation. A temperature increase of 100°C doubled the rate of void swelling in alloy C (30Cr, 33Ni)

(ii) Alloy A (20Cr, 23Ni) was observed to have a much slower void swelling rate than alloy C (30Cr, 33Ni) when irradiated in the HVEM at the same temperature of 500°C.

(iii) The 1% Nb addition made to alloy A (20Cr, 23Ni) produced only a very small reduction in the void swelling rate of alloy A after irradiating under VEC conditions at a temperature of 550°C and a total dose of 10 dpa. There was a slight decrease in the number of the voids produced but this was accompanied by an increase in the overall size of the voids.

(iv) The addition of 2% Mo produced an increase in the number of voids present after irradiating in the VEC for 10 dpa at 550°C, these voids were very much smaller in size and therefore a large reduction in the percentage void swelling of alloy A was obtained.

(v) The greatest reduction in the void swelling of alloy A was caused by the 2% Si addition . Considerably fewer voids were produced although, on average, these voids were larger than those produced in alloy A after irradiating in the VEC with 46 MeV Ni^{6+} ions at 550°C for a total dose of 10 dpa.

(vi) A series of iron based 12Cr, 15Ni alloys containing additions of 0.14%-1.42% Si were thermally aged for 13,000 hours at 435°, 505°, 575° and 645°C. The alloys remained austenitic, there was no transformation to ferrite or sigma phase. The carbide $M_{23}C_6$ was precipitated in these alloys, the amount of precipitation was observed to increase with increasing ageing temperature and Si content.

(v) The microstructures of the thermally aged 12Cr, 15Ni alloys were compared to an identical series of alloys which had undergone fast neutron irradiation. Irradiation induced void swelling was observed to decrease with increasing Si content. Transformation to ferrite also occurred in these alloys, the extent of this transformation increased with increasing Si content and temperature. This microstructural instability was irradiation driven, enhanced by the presence of silicon. It is suggested that the separation of intergranular regions into nickel-rich and nickel depleted zones is significantly accelerated by the presence of silicon.

7.0 FURTHER WORK

The constitution, phase transformations and precipitation effects in Fe-Cr-Ni alloys is a wide research field. Consequently the areas requiring further investigation are correspondingly wide.

The constitution of Fe-Cr-Ni alloys above 650°C has been studied by several workers and isothermal equilibrium diagrams
Insert F
determined.↓ However, below 600°C only computer calculated diagrams

Insert F Further ageing beyond 1000 hours is needed to obtain a better approach to equilibrium especially at lower temperatures.

boundaries, especially for the detrimental sigma and α' phases. Also, the effect of alloying additions on the Fe-Cr-Ni ternary is not fully understood. More work is needed in this area to enable the design of new stainless steels which have known phase stabilities especially at elevated temperatures.

Further work is also needed to determine the kinetics of phase transformations and precipitation in Fe-Cr-Ni alloys. Time-Temperature-Precipitation diagrams have not been determined for the majority of stainless steels.

In this work it was demonstrated that elements such as Si and Mo reduced the void swelling of austenitic Fe-Cr-Ni alloys. The reasons for this reduction in swelling are not fully understood. Further work should address not only the effect on void swelling of single element additions but the synergistic effects that may occur when a combination of elements are added to austenitic alloys.

REFERENCES

1. Schafmeister, P. and Ergang, R. Arch. Eisenh., 1938-39, 12, 459-463.
2. Bradley, A.J. and Goldschmidt, H., JISI, 2, 1941, p273.
3. Jenkins, C.M.M. et al, JISI, 136, 1937, p187.
4. Bain, E.G. and Griffiths, W.E., Am. Inst. Min. Met. and Pet. Engs, vol.75, 1927, p166-210.
5. Jette, E.R. and Foote, F., Metals and Alloys, 7, 1936, p207-210.
6. Bergman, B.G. and Shoemaker, D.P., Acta. Crysta. 7, 1954, p857.
7. Rees, W.P., Burns, B.D., and Cook, A.J., JISI, July 1949, p325.
8. Nicholson, M.E., Samans, C.H. and Shortsleeve, F.J., Trans ASM 44, 1952, p601-620.
9. Hattersley, B. and Hume-Rothery, W., JISI, July 1966, p683-701.
10. Dulis, E.J. and Smith, G.V., ASTM STP 110, 1950, p3-37.
11. Gilman, J.J., Trans ASM 44, 1952, p589-601.
12. Jones, J.D. and Hume-Rothery, W., JISI, Jan. 1966, p1-7.
13. Schultz, J.W. and Merrick, M.F., Met. Trans., 3, Sept. 1972, p2479-2483.
14. Andrews, K.W., 'The System Iron-Chromium-Nickel', United Steel Companies Report, 1950.
15. Cook, A.J. and Brown, B.R., JISI, Aug. 1952, p345-353.
16. Cawley, J., Phd Thesis, Sheffield City Polytechnic, 1982.

17. Kaufman, L. et al., 'Computer Calculations of Phase Diagrams, Academic Press, New York, 1970.

18. Hillert, M. 'Hardenability Concepts with Applications to Steels', Eds. Doane and Kirkaldy, Met. Soc. of AIME, 1978, p5.

19. Rivilin, V.G. and Raynor, G.V., International Metals Reviews 248, 1980, No.1, p21.

20. Lismer, R.E., Pryce, L. and Andrews, K.W., JISI, May 1952, p42-58.

21. Pryce, L., Hughes, H and Andrews, K.W., JISI, Nov. 1956, p289-301.

22. Irvine, K.J., Llewellyn, D.T. and Pickering, F.B., JISI, July 1959, p218-238.

23. Binder, W.O., ASTM STP 110, 1950, p146-164.

24. Shao, J. and Machlin, E.S., Met. Trans. 10A, May 1979, p585-590.

25. Decker, R.F. and Floreen, S., 'Precipitation from Substitutinal Iron Base Austenitic and Martensitic Solid Solutions', Pub. AIME 1965, p69-139.

26. Hall, E.O and Algie, S.H., Met. Review 104, 1966, p61-69.

27. Yakel, H.L., Acta Crysta. B39, 1983, p20-33.

28. Andrews, K.W., Dyson, D.J. and Keown, S.'Interpretation of Electron Diffraction Patterns', Hilger and Watts, 1967.

29. Gow, J.T. and Harder, O.E., Trans. ASM, Dec 30, 1942, p855-935.

30. Franks, R., Binder, W.O. and Bishop, C.R. 'Physical Properties and Corrosion Resistance of Austenitic Stainless Steels', Trans. ASM 29, 1941, p35-85.

31. Emmanuel, G.M. ASTM STP 110, 1950, p82-99.

32. Beckitt, F.R., JISI, May 1969, p632-638.

33. Talbot, A.M. and Furman, D.E., Trans. ASM 45, 1953, p429-443.

34. Lena, A.J. and Curry, W.E., Trans. ASM 47, 1955, p193.

35. Nenno et al., 1962, Trans. Jap. Inst. Metal, 3, p82

36. Lewis, M.H., Acta. Met. 14, Nov. 1966, p1421-1428.

37. Mansfield, J., Ed. 'Convergent Beam Diffraction of Alloy Phases', Pub. Adam Hilgar, Bristol and Boston, 1984.

38. Sullivan, C.P. et al, ASM Technical Report C.70-9.1, 1970. p1-33.

39. Denham, A.W. and Silcock, J.M., JISI, 1969, 207, p585-592.

40. Sasmal, B. 'Solid to Solid Transformations', Pittsburgh, 10-14., Aug. 1981, The Met. Soc. AIME.

41. Brown, E.L. et al., Metall. Trans. 14A, May 1983, p791-800.

42. Weiss, B. and Stickler, R., Met. Trans. 3A. April 1972, p851-866.

43. Nutting, J. and Parsons, P.D., BISRA Rep. MG/E/93/65, 1965.

44. Andrews, K.W. and Brooks P.E., Metal Treat. and Drop Forging, July 1951, p301-311.

45. McMullin, J.G. et al. Trans ASM 46, 1954, p799-811.

46. Beattie, H.Jnr. and Hagel, W.C., Trans. AIME, 221, 1961.

47. Goldschmidt, H.J., 'Interstitial Alloys', Butterworth, London. 1967.

48. Versnyder, F.L. and Beattie, H.Jnr. Trans.ASM 47, 1955, p211.

49. Beattie, H.J. and Versnyder, F.L., Nature, 178, 1956, p208.

50 Pickering F.B., Heat Treatment '73, Metals Society, 1975, pp1-11.

51. Hattersley, B. and Lewis, M.H., Phil. Mag, 10, 1964, p1075-1079.

52. Lewis, M.H. and Hattersley, B., Acta Met. 13, Nov. 1965, p.1159-1168.

53. Beckitt, F.R. and Clarke, B.R., Acta Meta. 15, 1967, p113-129.

54. Tuma, M. et al., Arch. Eisen., 41, No.10, 1976, p983-988.

55. Pickering, F.B., JISI, Spec. Rep. No.64, 1959, p118-127.

56. Blenkinsop, P.A. and Nutting, J. JISI, Sep 1967, p953-958.

57. Singal L.M. and Martin J.W., JISI, 1969, 207, p1382.

58. Bentley, J. and Leitnaker, J.M. 'The Metal Science of Stainless Steels' Met.Soc. AIME Conf. Proc. Denver Colorado, March 1978.

59. Shortsleeve, F.J. and Nicolson, M.E., Trans ASM 43, 1951, p142-159.

60. Williams, R.O. and Paxton, H.W., JISI, March 1957, p358-374.

61. Blackburn M.J. and Nutting, J., JISI, July 1964, p610-613.

62. Courtnall, M. and Pickering, F.B. Metal Science, Aug 1976, p273-276.

63. Grobner, P.J. and Steigerwald, R.F., J Metals, July 1977, p17-23.

64. Heger, J.J., Metal Progress, August 1951, p55-61.

65. Fisher, R.M., Dulis, E.J. and Carroll, K.J., Trans AIME, May 1953, Journal of Metals, p690-695.

66. Williams, R.O., AIME, 212, 1958, p358.

67. Lagneborg, R., Trans ASM 1967, 60, p67-78.

68. Ludwigson D.C. and Link H.S., ASTM STP 369, 1965, p299-311.

69. Solomon, H.D., and Levinson L.M. Acta Met., 26, 1976, p429-442.

70. Southwick, P.D. and Honeycombe, R.W.K., Metal Science July 1980, p253-261.

71. Pickering, F.B. 'Physical Metallurgy and The Design of Steels', Pub. Applied Science Publishers Ltd., 1978.

72. Pickering, F.B., Mi Con 78, ASTM STP 672, 1979, p263-293.

73. Irvine, K.J., Crowe, D.J. and Pickering, F.B. JISI, Aug 1960, p386.

74. Pickering, F.B. 4th Int. Conf. on Electron Microscopy, Berlin, 10-17 Sept. 1958, p668-670.

75. Andrews, K.W. and Hughes, H., JISI, 1959, 194, p304.

76. Bowkett, M.W., Harries, D.R. AERE Harwell Report 9093, April 1978.

77. Bowkett, M.W. Harries, D.R. and Williams, T.M. Proc. Conf. Ajaccio, Corsica, June 4-8, 1979, p1-8.

78. Eichelman, G.M.Jr. and Hull, F.C., Trans ASM 45, 1953, p77-103.

79. Harries, D.R. Nucl. Energy 17, Oct., 1978, No4, p301-311.

80. Mayer, R.M. et al., J.Nucl. Mat. 95, Oct. 1980, p44-107.

81. Greenwood, G.W. et al., J.Nucl. Mat. 14, 1959, p305-324.

82. Glowinski, L.D. et al. J.Nucl. Mat. 61, 1976, p22.

83. Nelson, R.S. et al. J.Nucl. Mat. 37, 1970, p1-12.

84. Nelson, R.S. and Mazey, D.J. Sym. of Radiation Damage in Reactor Mat. Int. A.E. Agency, Vienna, 1969, p157-163.

85. Nelson, R.S. AERE Report R.6151 Harwell 1969.

86. Conf. Proc. Int. Conf. Scottsdale Arizona, June 1977.

87. Cawthorne, C. et al. Nature, 216, 1967, p575-576.

88. Proc. Int. Conf. 'Radiation Induced Voids in Metals', Albany, U.S.A. 1971.

89. Proc. BNES Conf. 'Voids Formed by Irradiation of Reactor Material', Reading 1971.

90. Harries, D.R. AERE Report R.7934, Harwell 1975.

91. Johnston, W.G. Int. Conf. Scottsdale, Arizona, June 1977, p421-431.

92. Harries, D.R. ibid. p 27-40

93. Harries D.R. Consultants Symposium, The Physics of Irradiation Produced Voids. Sept. 1974, p 287-298.

94. Johnston, W.G.J. Nucl. Mat. 54, 1974, p24-40.

95. Johnston, W.G. Proc. ASM Mat. Sci. Seminar, Cincinnati, Nov. 1975, p429.

96. Bates J.F. et al Int. Conf. Scottsdale, Arizona, June 1977, p625-645.

97. Williams, T.M. J.Nucl. Mats. 64, 1977, p183-185.

98. Williams, T.M. Rad. Effects 17, 1973, p49-55.

99. Johnston, W.G. et al. ASTM STP 529. 1973, p213.

100. Williams, T.M. British Nucl. Energy Conf, March 1971.

101. Brager, HR and Garner, F. J.Nucl. Mats. 57, 1975, p103-118.

102. Decker, R.F. et al., Am.Inst.Min.Metal. Pet.Eng. Conf.Proc. 28, 1965, p69.

103. Bullough, R. et al. Proc. BNES Conf., Reading 1971, p79.

104. Makin, M.J. et al., Int. Conf. Scottsdale, Arizona, June 1977.

105. Bramman, J.I. et al., Proc. BNES Conf., Reading 1971, p27-33.

106. Bagley, K.Q. et al. ibid. p1-26.

107. Williams, T.M., J.Nucl. Mats 88 1980, p217-225.

108. Appleby, W.K. and Wolf, U.E. ASTM STP 529, 1973, p122-136.

109. Bloom, E.E. et al. Scripta Met., 10, 1976, p303.

110. Silvester, G. et al J.Nucl. Mats 57, 1975, p125-135.

111. Garner, F.A. ASTM STP, 725, 1981, p165-189.

112. Cawthorne, C. and Brown, C. J.Nucl. Mats, 66, 1977, p201-202.

113. Williams, T.M. et al. J.Nucl. Mats, 82, 1979, p199.

114. Williams, T.M. et al. J.Nucl. Mats, 98, 1981, p223-226.

115. Williams, T.M. et al. J.Nucl. Mats, 87, 1979, p398.

116. Mazey, D.J., Harries, D.R. and Hudson, J.A., Proc.Int.Conf - Irradiation Behaviour of Metallic Materials for Fast Reactor Core Components, Ajaccio, Corsica, 1979, p61.

117. Lee, E.M. et al. Microstructural Science 7, 1979, p403.

118. Lee, E.M. et al. Proc. TMS/AIME Symp. Pittsburgh, 1980.

119. Williams, T.M. et al. AERE Report No R12492 Harwell, 1987.

TABLE 1 (after Decker et al (25))

THE OCCURRENCE OF INTERMETALLIC PHASES BETWEEN ALLOY ELEMENTS COMMONLY FOUND IN AUSTENITIC STAINLESS STEELS

A

B	Ti	Zr	Hf	V	Nb	Ta	Cr	Mo	W
Mn	Sigma B_2A Chi	B_2A Chi	B_2A Chi	Sigma BA Chi	B_2A Chi	B_2A Chi	Sigma Chi	Sigma Chi	Chi
Fe	B_2A BA Chi	B_2A	B_2A	Sigma BA Chi	Sigma B_2A	B_2A	Sigma	Sigma B_2A Chi Mu	B_2A Mu
Co	B_2A BA G	B_2A BA G	B_2A BA G	Sigma B_3A Chi	B_2A G	B_2A G	Sigma	Sigma B_3A Mu	B_3A Mu
Ni	B_3A BA G	G	G	Sigma B_3A Chi G	B_3A Mu G	B_3A Mu G	Sigma	B_3A	

TABLE 2 : ALLOY COMPOSITIONS - IRON BASED TERNARYS

Alloy Type	Nominal Composition			Chemical Analysis		
	Fe wt%	Cr wt%	Ni wt%	Fe wt%	Cr wt%	Ni wt%
A	57	20	23	56.63	20.10	23.27
B	37	20	43	38.35	20.15	41.05
C	37	30	33	37.71	30.21	32.08
D	85	12	3	84.14	12.26	3.60
E	75	18	7	74.73	18.16	7.11
F	57	30	13	56.11	32.25	13.64

C = 0.007 wt%

N_2 = 0.004 wt%

O_2 = 0.400 wt%

TABLE 3 : QUATERNARY ALLOY COMPOSITIONS

Element / Alloy	Cr	Ni	Mo	Nb	Ti	Si
A 2Mo	18.8	23.8	1.74	\	\	\
A 1Nb	19.8	21.7	\	1.15	\	\
A ¼Ti	20.7	21.4	\	\	0.37	\
A Si	21.8	22.0	\	\	\	1.03
A 2Si	19.8	23.7	\	\	\	1.73
E 2Mo	17.9	7.0	1.64	\	\	\
E 1Nb	17.8	7.9	\	1.22	\	\
E ¼Ti	18.0	8.21	\	\	0.015	\
E1Si	20.40	7.7	\	\	\	0.99
E2Si	18.3	7.7	\	\	\	1.42

C = < 0.007 wt%

N = < 0.008 wt%

Table 4: V.E.C. Irradiation Results for 10dpa at 550°C

Specimen	Number Density cm^3	Average Void Volume cm^3	% Relative Void Swelling
A(20Cr 23Ni)	1.68×10^{15}	1.59×10^{-18}	0.267%
A + 1% Nb	9.1×10^{14}	2.73×10^{-18}	0.248%
A + 2% Mo	2.0×10^{15}	4.01×10^{-19}	0.080%
A + 1% Si	1.26×10^{15}	1.88×10^{-18}	0.237%
A + 2% Si	6.67×10^{13}	9.94×10^{-18}	0.066%

TABLE 5 : NEUTRON IRRADIATED ALLOYS

	Cr	Ni	C	Mn	Si	Mo	Ti	V
A N1	12.1	15.0	0.054	1.00	0.14	<0.02	<0.02	<0.02
C N2	11.8	15.1	0.047	0.98	0.49	"	"	"
E N3	11.9	15.2	0.052	1.03	0.95	"	"	"
G N4	11.8	15.1	0.061	0.99	1.42	"	"	"

Figure 1. The 1000°C isothermal section of the Fe-Ni-Cr system after Rivilin V.G. and Raynor G.V. (19).

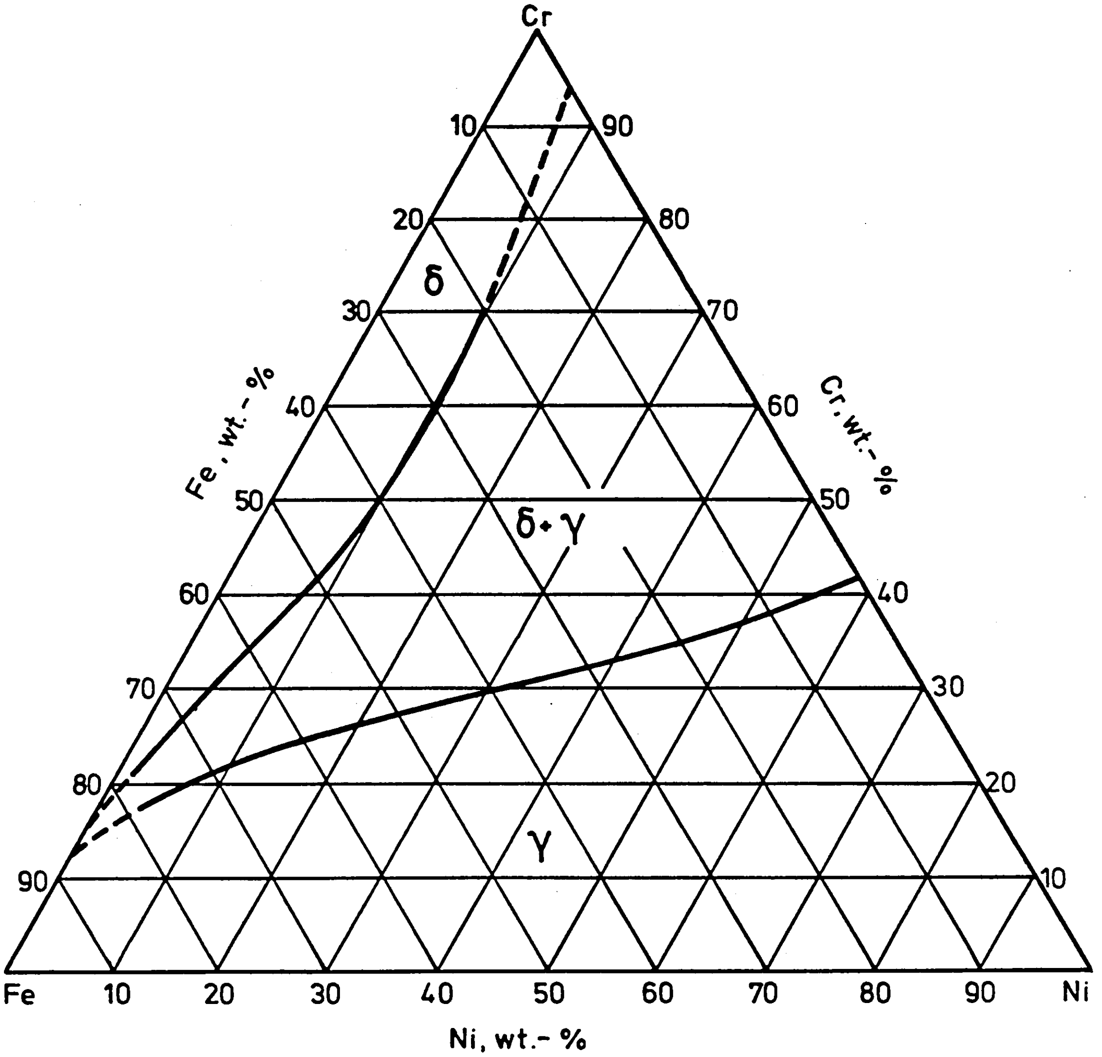
Cr
Fe
Ni
Fe, wt.-%
Cr, wt.-%
Ni, wt.-%
10
20
30
40
50
60
70
80
90
δ
δ+γ
γ

Figure 2. The 800°C isothermal section of the Fe-Ni-Cr system, after Rivilin G.V. and Raynor V.G. (19).

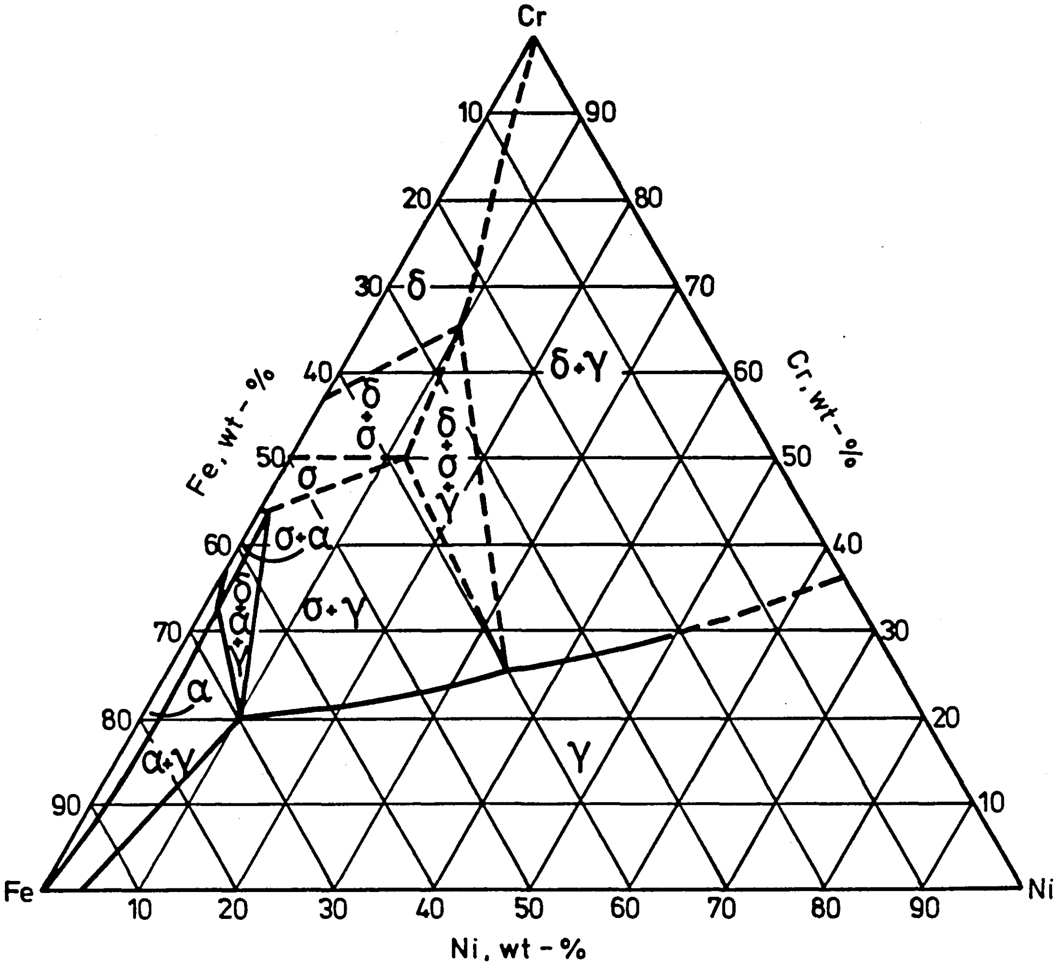
Cr
Fe
Ni
Fe, wt - %
Cr, wt - %
Ni, wt - %
10
20
30
40
50
60
70
80
90
δ
δ+γ
δ+σ
δ+σ+γ
σ
σ+α
σ+γ
σ+α+γ
α
α+γ
γ

Figure 3. The 650°C isothermal section of the Fe-Ni-Cr after Rivilin V.G. and Raynor G.V. (19).

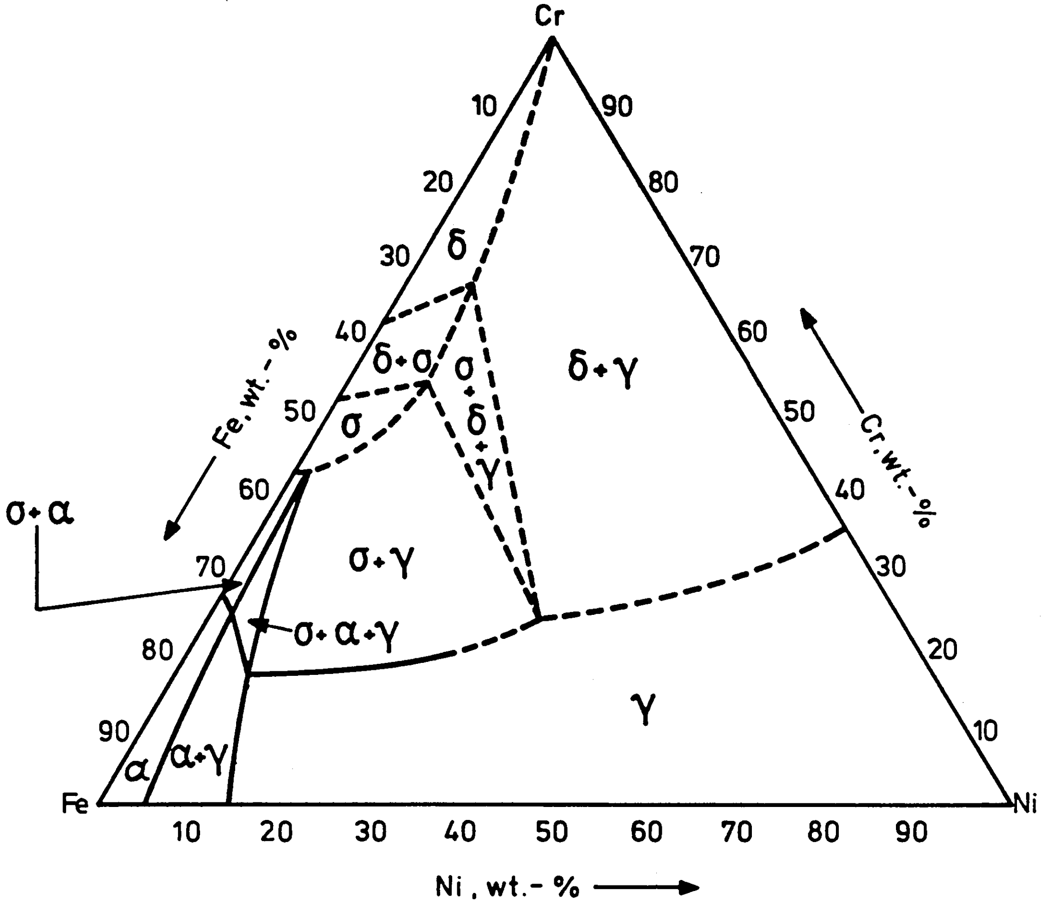
Cr
Fe
Ni
Fe, wt.- %
Cr, wt.-%
Ni, wt.- %
10
20
30
40
50
60
70
80
90
δ
δ+σ
σ
σ+δ+γ
δ+γ
σ+γ
σ+α
σ+α+γ
γ
α
α+γ

Figure 4. The Fe-rich corner of the 800°C isothermal section as derived by Cook A.J. and Brown B.R. (15)

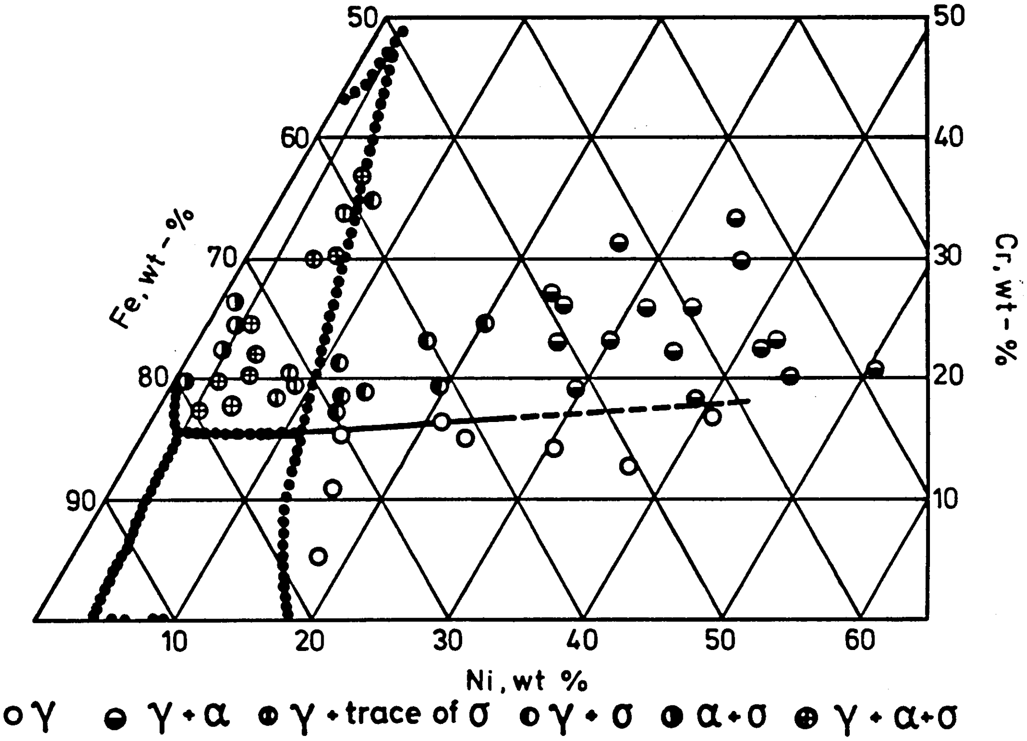
50
60
70
80
90
Fe, wt - %
50
40
30
20
10
Cr, wt - %
10
20
30
40
50
60
Ni, wt %
○ γ
⊖ γ + α
⦶ γ + trace of σ
◐ γ + σ
◑ α + σ
⊕ γ + α + σ

Figure 5. The 650°C isothermal section of the Fe-Ni-Cr system after Cawley J. (16).

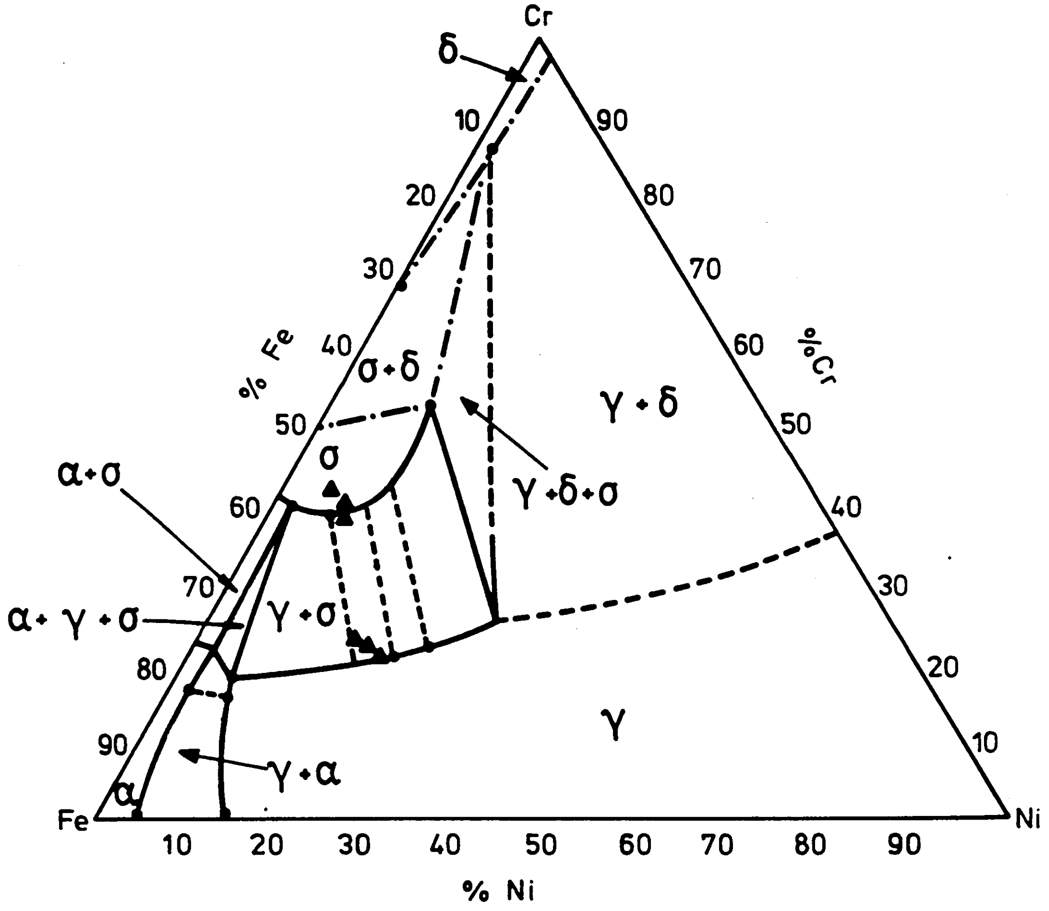
Cr
δ
% Fe
%Cr
σ+δ
γ+δ
σ
γ+δ+σ
α+σ
γ+σ
α+γ+σ
γ
γ+α
α
Fe
Ni
% Ni

Figure 6. The Fe-Cr binary system after Rivilin V.G. and Raynor G.V. (19).

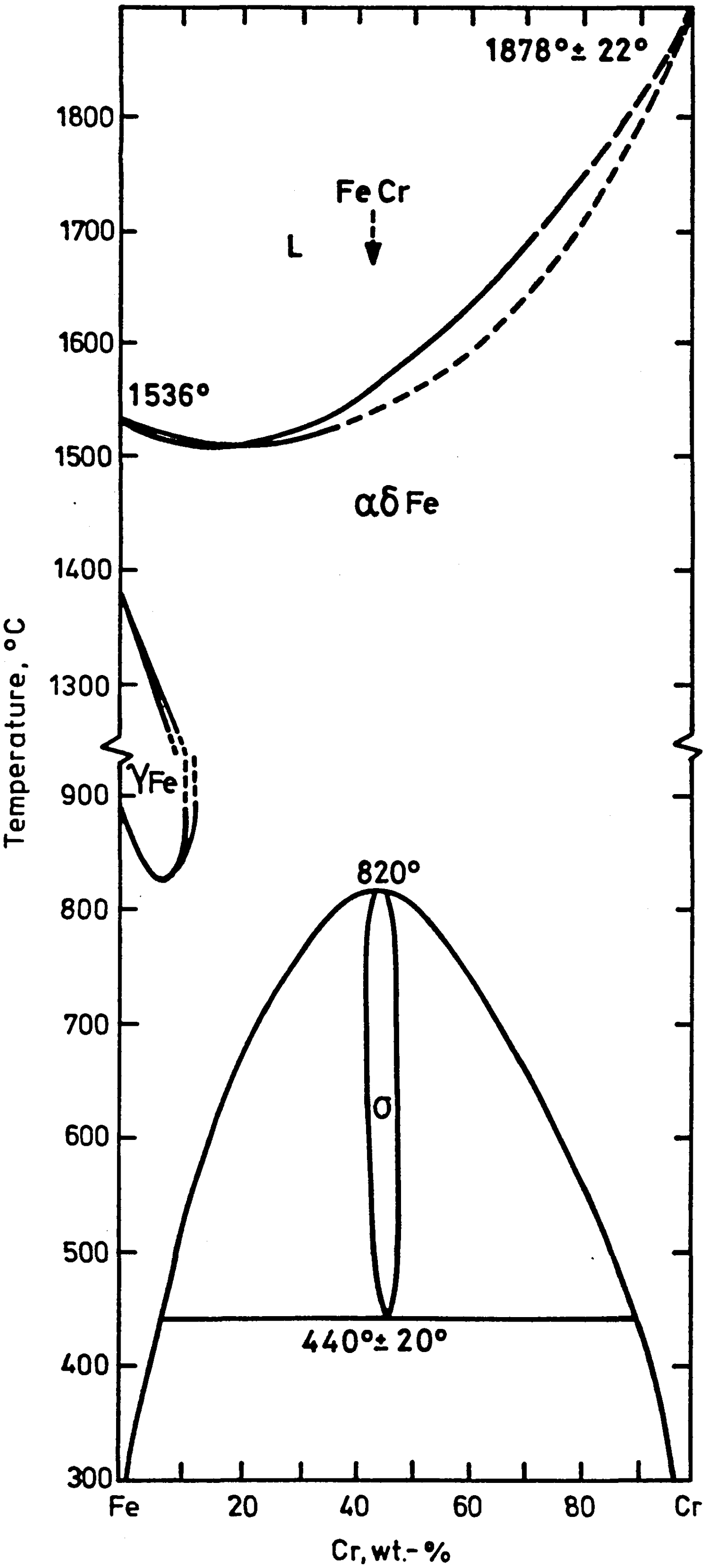

1878°± 22°
Fe Cr
L
1536°
αδ Fe
γFe
820°
σ
440°± 20°
Temperature, °C
1800
1700
1600
1500
1400
1300
900
800
700
600
500
400
300
Fe
20
40
60
80
Cr
Cr, wt.- %

Figure 7(a). The effect of alloying elements on the delta ferrite content of a 17Cr,0.1C steel, solution treated at 1050°C, after Irvine K.J. et al (22).

Figure 7(b). The effect of alloying additions on the delta ferrite content of a 17Cr,4Ni,0.1C steel, solution treated at 1050°C, after Irvine K.J. et al (22).

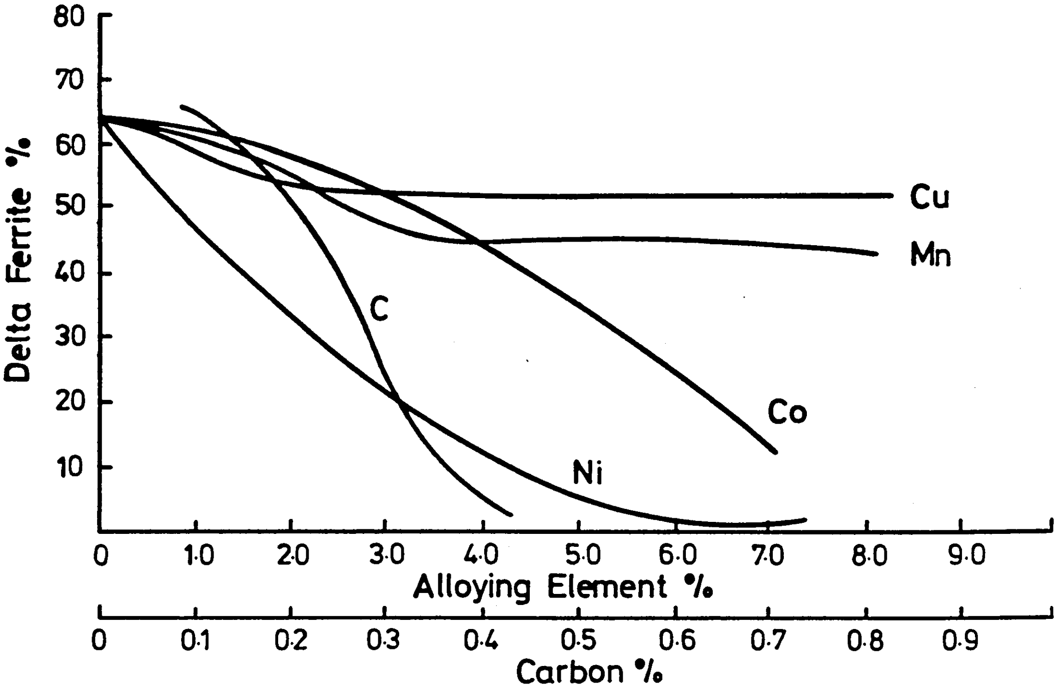

80
70
60
50
40
30
20
10
Delta Ferrite %
Cu
Mn
C
Co
Ni
0
1·0
2·0
3·0
4·0
5·0
6·0
7·0
8·0
9·0
Alloying Element %
0
0·1
0·2
0·3
0·4
0·5
0·6
0·7
0·8
0·9
Carbon %

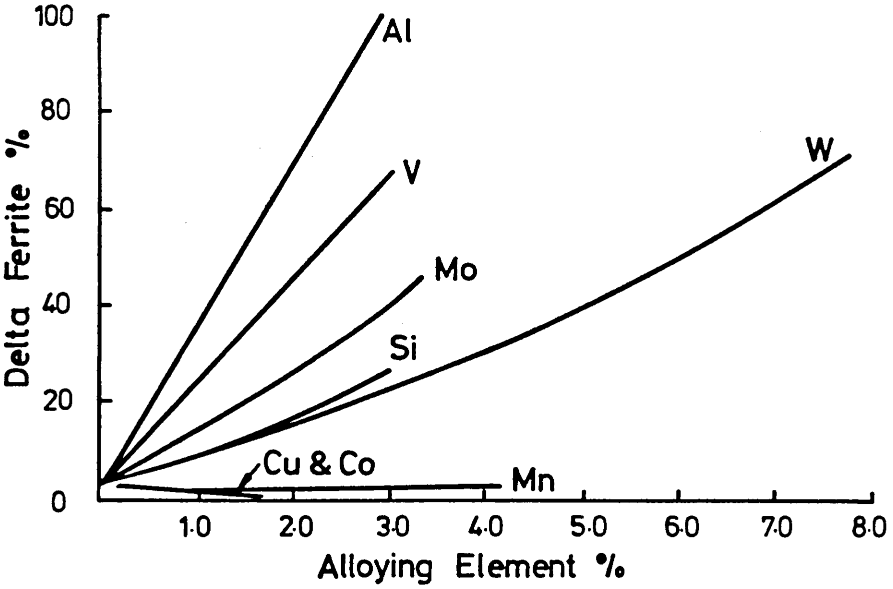

100
80
60
40
20
0
Delta Ferrite %
Al
V
Mo
Si
W
Cu & Co
Mn
1·0
2·0
3·0
4·0
5·0
6·0
7·0
8·0
Alloying Element %

Figure 8a. The effect of titanium on the $\gamma / \gamma + \delta$ phase boundary for alloys containing up to 20% Fe, after Shultz J.W. and Merrick H.F. (13).

Figure 8b. The effect of aluminium, silicon and niobium on the $\gamma / \gamma + \delta$ phase boundary for alloys containing 20% Fe, after Shultz J.W. and Merrick H.F. (13).

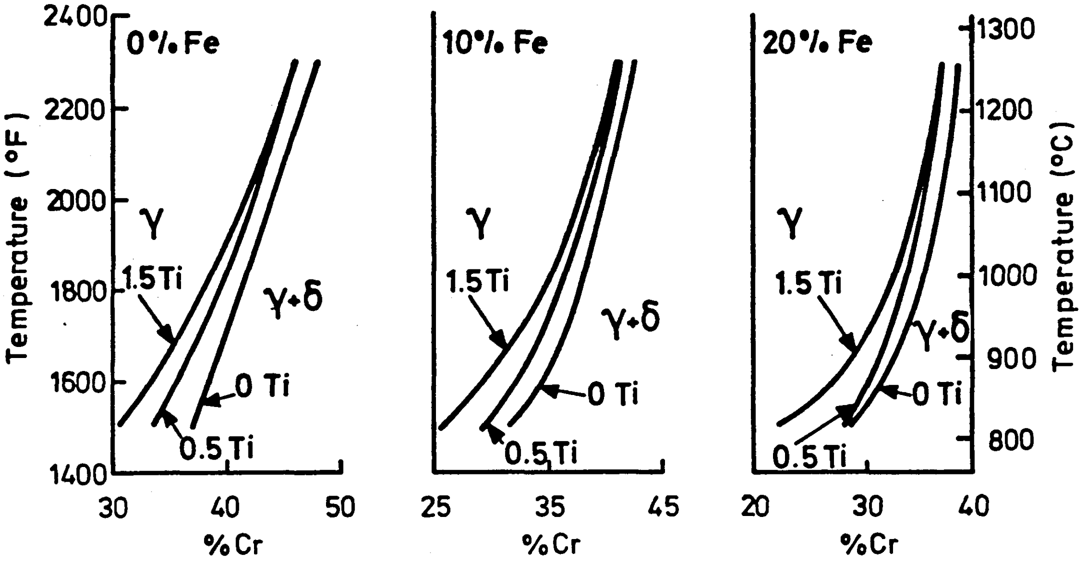
0% Fe
10% Fe
20% Fe
Temperature (°F)
Temperature (°C)
2400
2200
2000
1800
1600
1400
1300
1200
1100
1000
900
800
γ
γ+δ
1.5Ti
0.5 Ti
0 Ti
1.5 Ti
30
40
50
25
35
45
20
%Cr

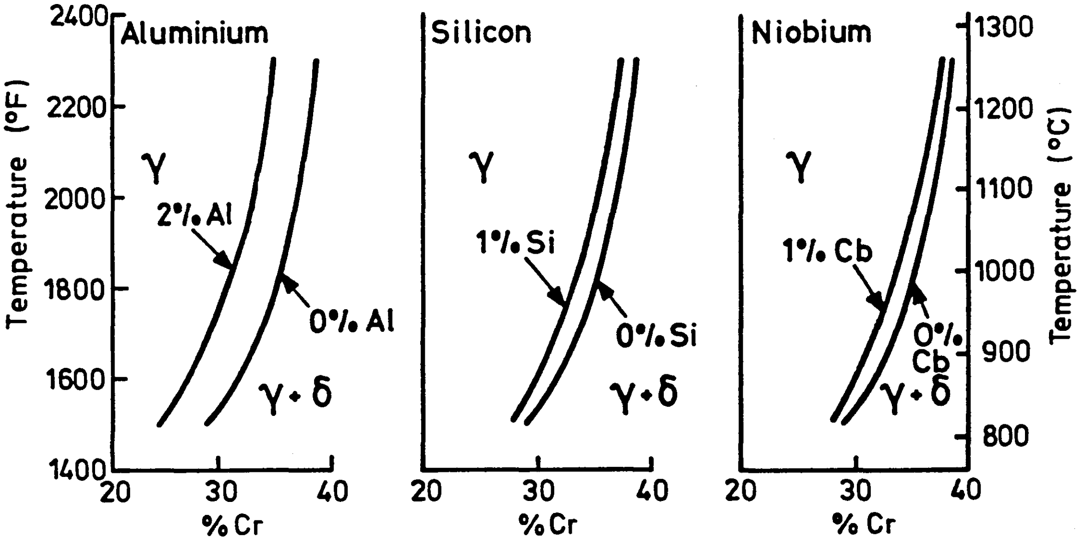
Aluminium
Silicon
Niobium
Temperature (°F)
Temperature (°C)
2400
2200
2000
1800
1600
1400
1300
1200
1100
1000
900
800
γ
γ+δ
2% Al
0% Al
1% Si
0% Si
1% Cb
0% Cb
20
30
40
% Cr

Figure 9. The relative locations of some of the important AISI stainless steel compositions with respect to the limits of the sigma phase regions at 650°C as drawn from the data of Nicholson M.E. et al (solid lines) and from the data of Schafmeister and Ergang (1) (dashed lines). The regions of uncertainty in placing the lines have not been indicated. After Nicholson M.E. et al (8).

	%Cr	%Ni	AISI Spec. No.
A	16-18	6-8	301
B	17-19	8-10	302,303
C	18-20	8-11	304
D	19-21	10-11	308
E	22-24	12-15	309
F	24-26	19-22	310
G	17-19	8-11	321
H	17-19	9-12	347

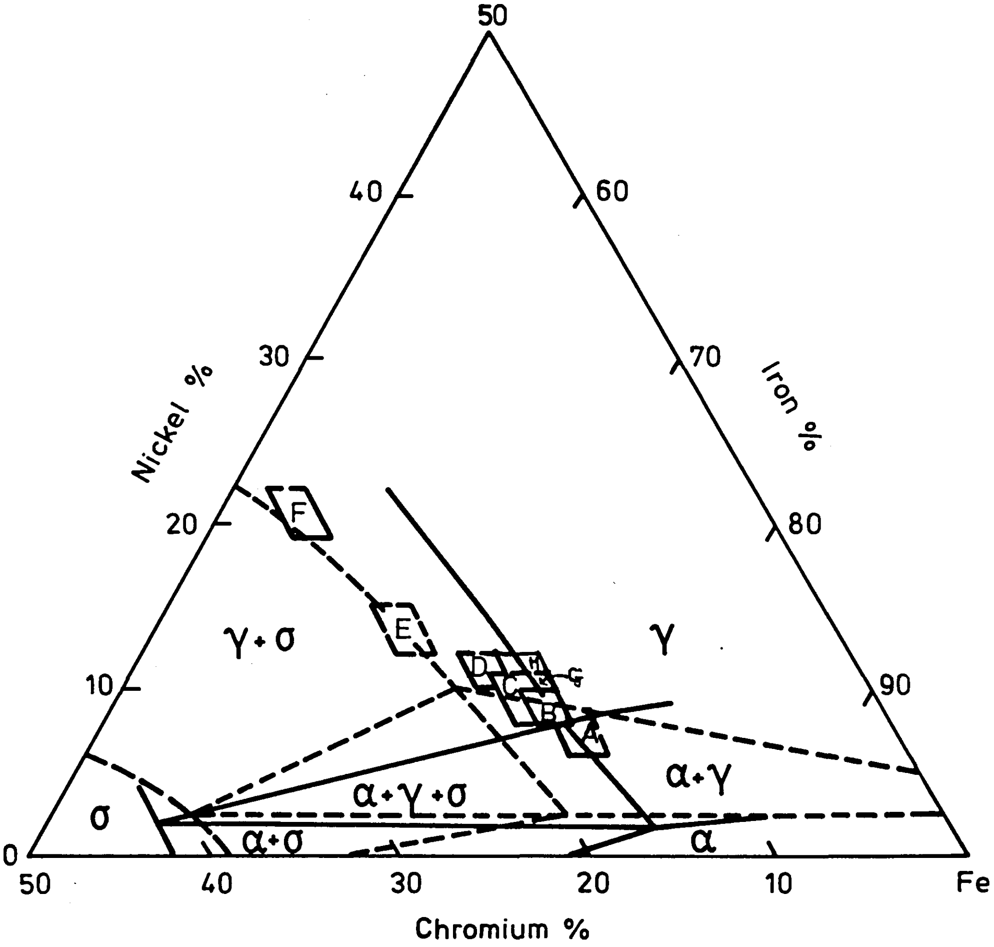
50
40
30
20
10
0
60
70
80
90
Nickel %
Iron %
50
40
30
20
10
Fe
Chromium %
F
E
D
H
G
C
B
A
γ + σ
γ
σ
α + γ + σ
α + γ
α + σ
α

Figure 10. Schematic representation of relative positions of curves showing influence of ageing temperature upon time to initiate precipitation of sigma and carbide phases after an initial solution treatment at 1300°C. Below 700°C and above 800°C, sigma is the dominant phase; between 700°C and 800°C carbide is the dominant phase. After Blenkinsop P.A. and Nutting J. (56).

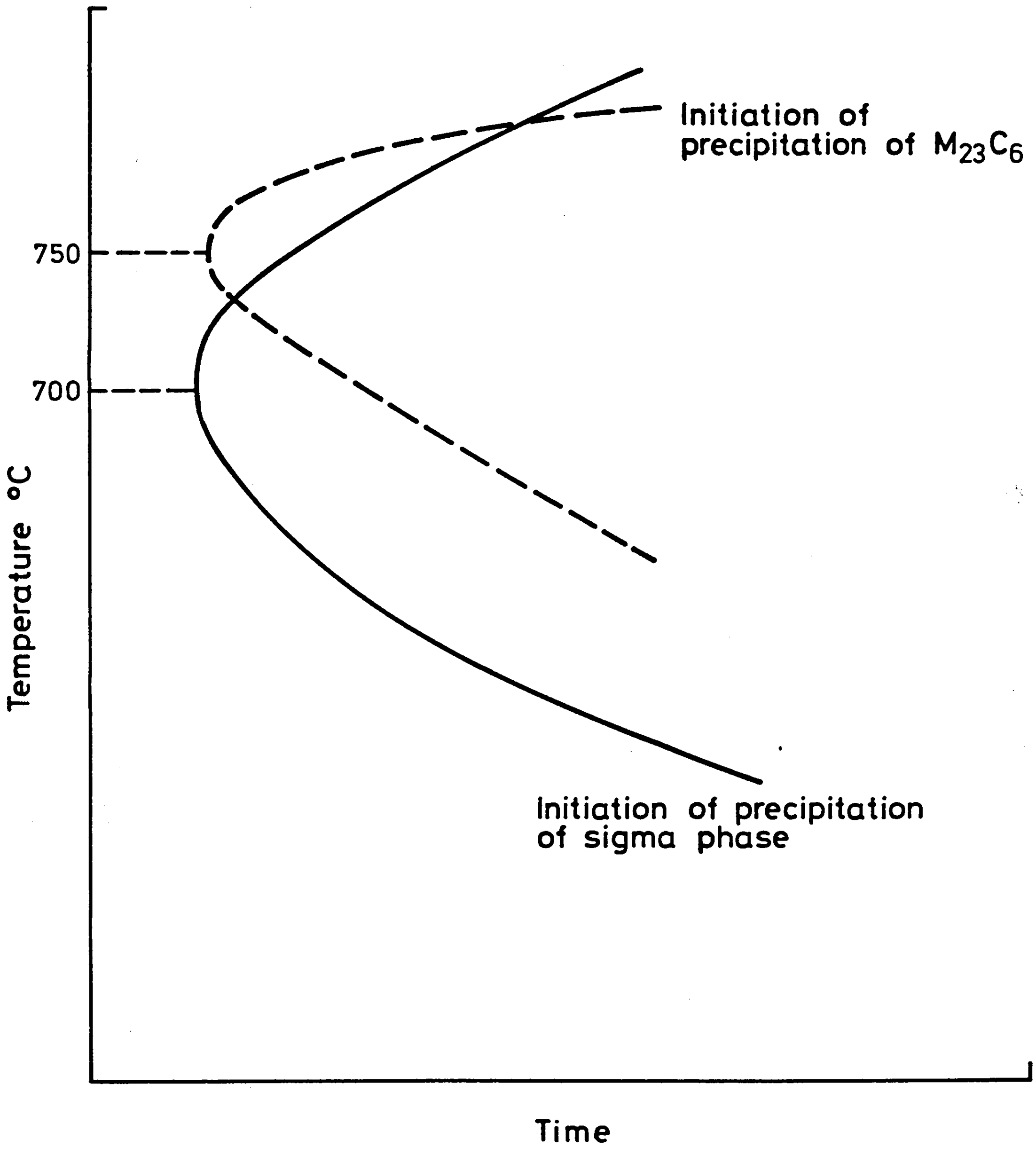
Initiation of precipitation of $M_{23}C_6$
750
700
Temperature °C
Initiation of precipitation of sigma phase
Time

Figure 11. C-curve for the formation of sigma phase in duplex alloys after Beckitt F.R. (32).

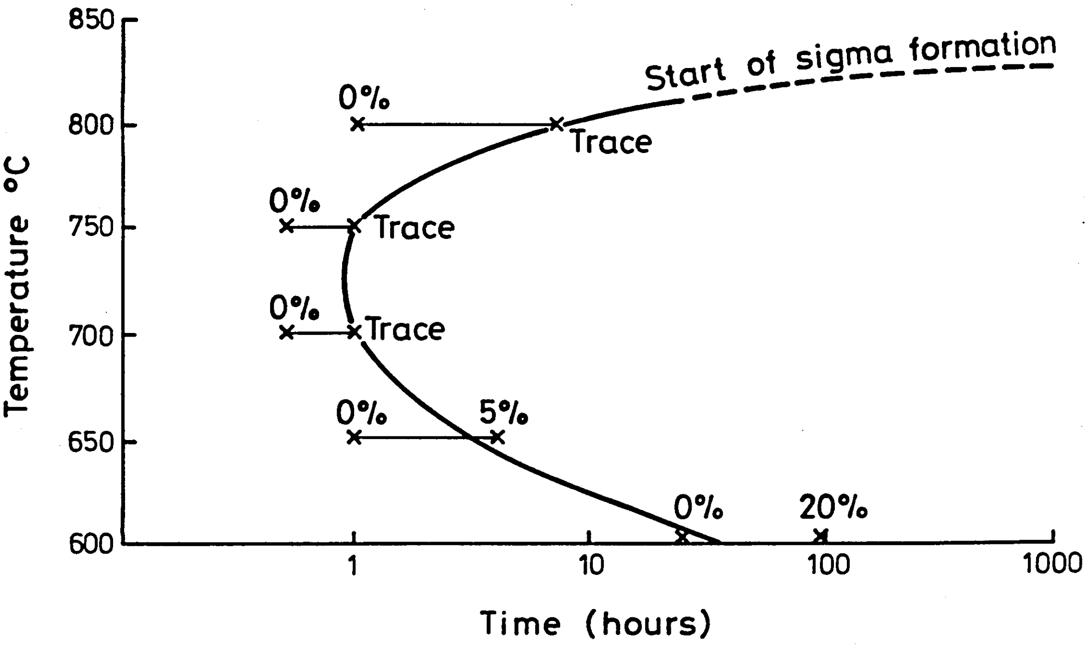
Start of sigma formation
Temperature °C
850
800
750
700
650
600
1
10
100
1000
Time (hours)
0%
Trace
0%
Trace
0%
Trace
0%
5%
0%
20%

Figure 12. Time-temperature-transformation curves of the ferrite to ferrite plus sigma transformation in the 24, 31 and 33% chromium alloys after Shortsleeve F.J. and Nicholson M.E. (59).

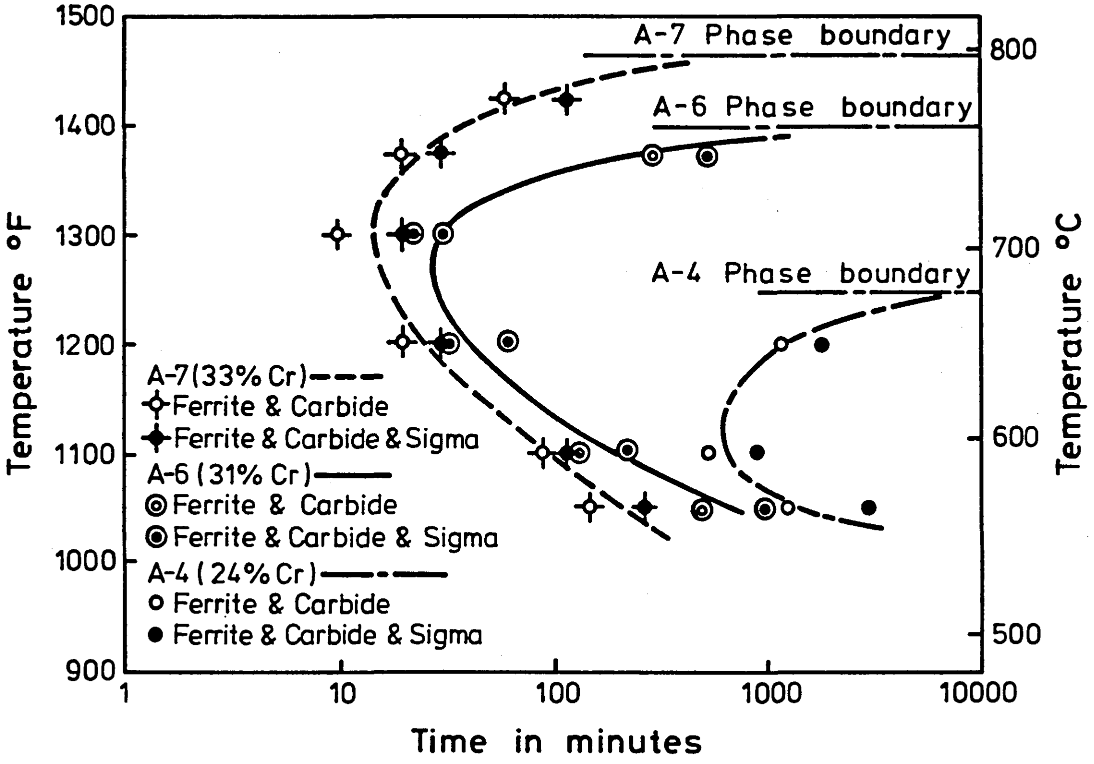
A-7 Phase boundary
A-6 Phase boundary
A-4 Phase boundary
A-7(33% Cr)
Ferrite & Carbide
Ferrite & Carbide & Sigma
A-6 (31% Cr)
Ferrite & Carbide
Ferrite & Carbide & Sigma
A-4 (24% Cr)
Ferrite & Carbide
Ferrite & Carbide & Sigma
Temperature °F
1500
1400
1300
1200
1100
1000
900
Temperature °C
800
700
600
500
1
10
100
1000
10000
Time in minutes

Figure 13. The phase diagram of the Fe-Cr system according to Williams R.O. (66).

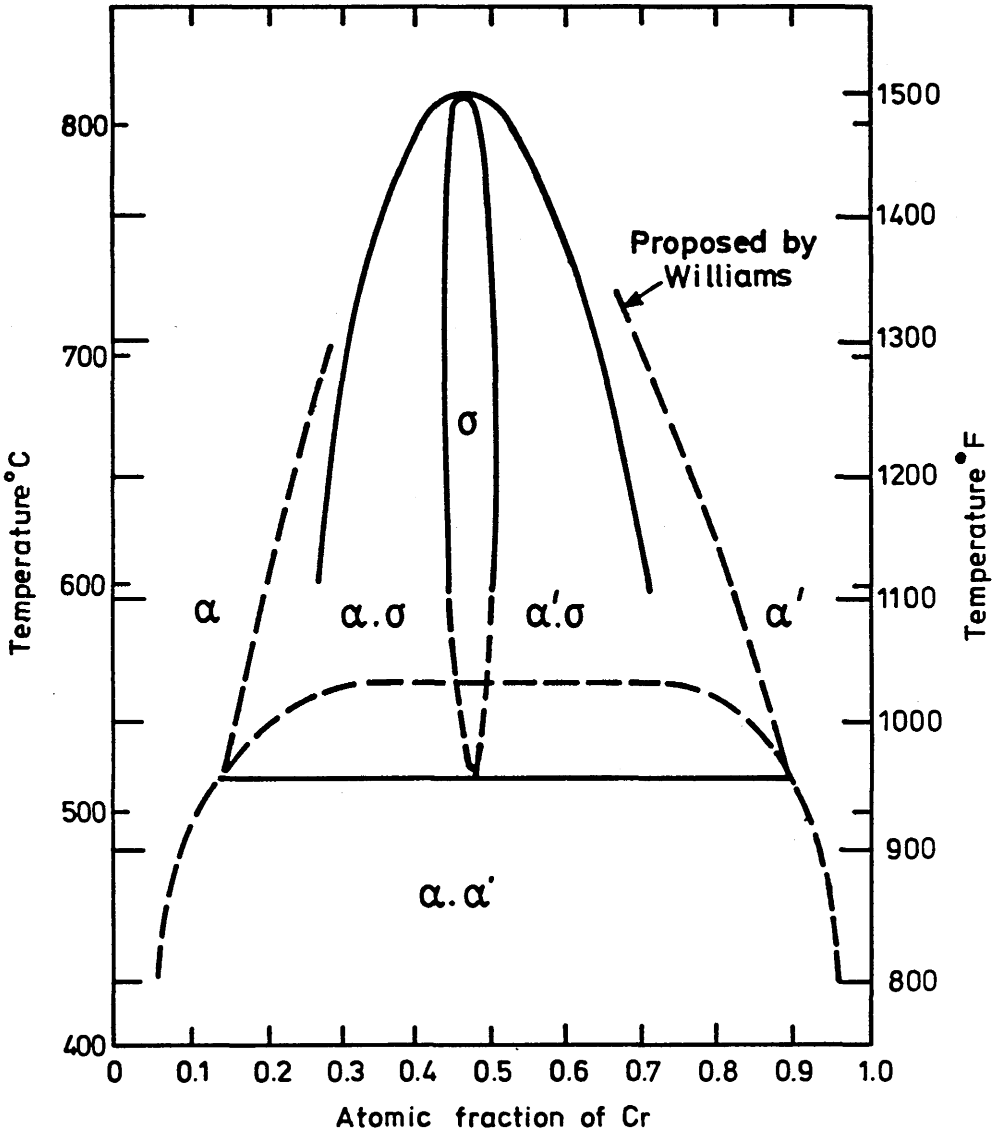
Proposed by
Williams
σ
α
α.σ
α'σ
α'
α.α'
Temperature °C
800
700
600
500
400
Temperature °F
1500
1400
1300
1200
1100
1000
900
800
0
0.1
0.2
0.3
0.4
0.5
0.6
0.7
0.8
0.9
1.0
Atomic fraction of Cr

Figure 14. The 475°C phase diagram as constucted from thermodynamic data by Solomon H.D. and Levinson L.M. (69).

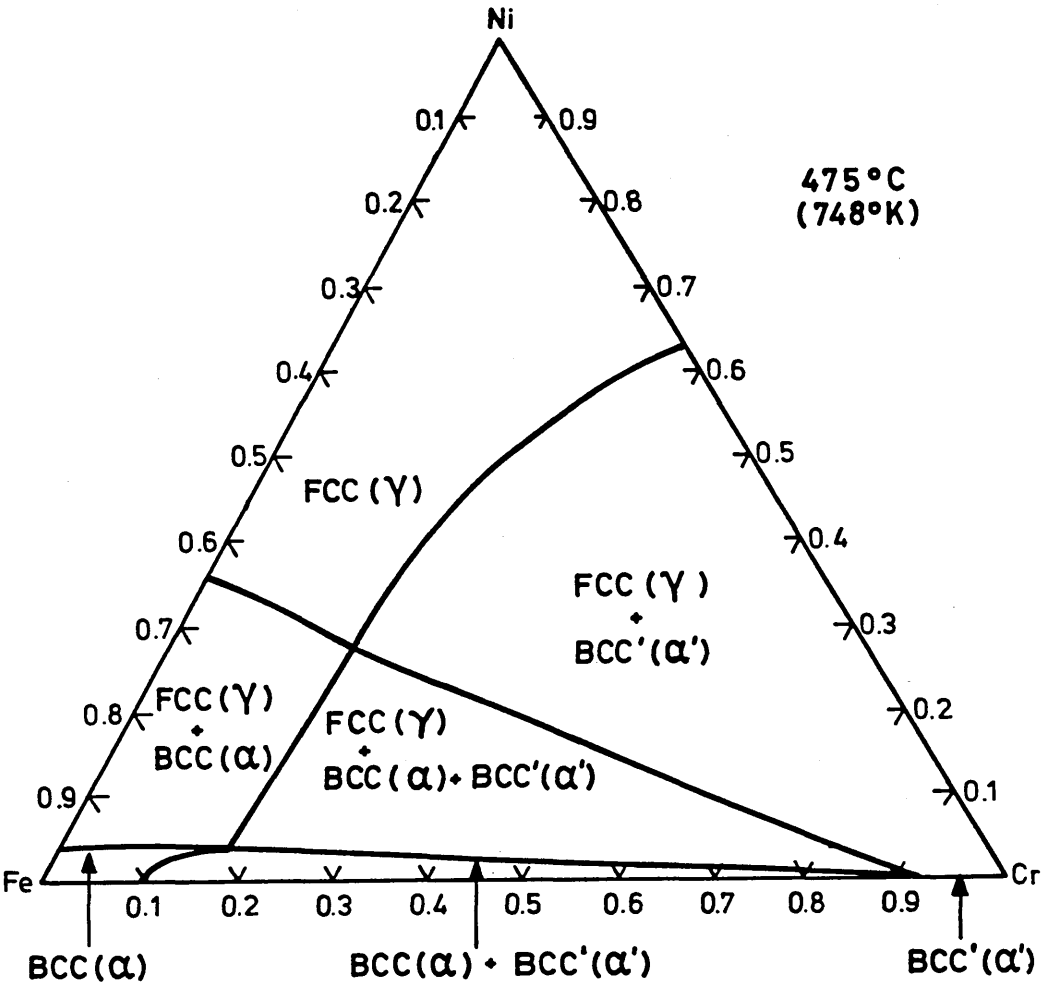
Ni
0.1
0.2
0.3
0.4
0.5
0.6
0.7
0.8
0.9
0.9
0.8
0.7
0.6
0.5
0.4
0.3
0.2
0.1
475 °C
(748°K)
FCC (γ)
FCC (γ) + BCC'(α')
FCC(γ) + BCC(α)
FCC(γ) + BCC(α) + BCC'(α')
Fe
Cr
0.1
0.2
0.3
0.4
0.5
0.6
0.7
0.8
0.9
BCC(α)
BCC(α) + BCC'(α')
BCC'(α')

Figure 15(a). The former hearth of the small scale vacuum arc furnace used for manufacturing the high purity alloys.

Figure 15(b). The modifications which had to be carried out to the former hearth in order to be able to manufacture button melts of the high purity alloys used in this work.

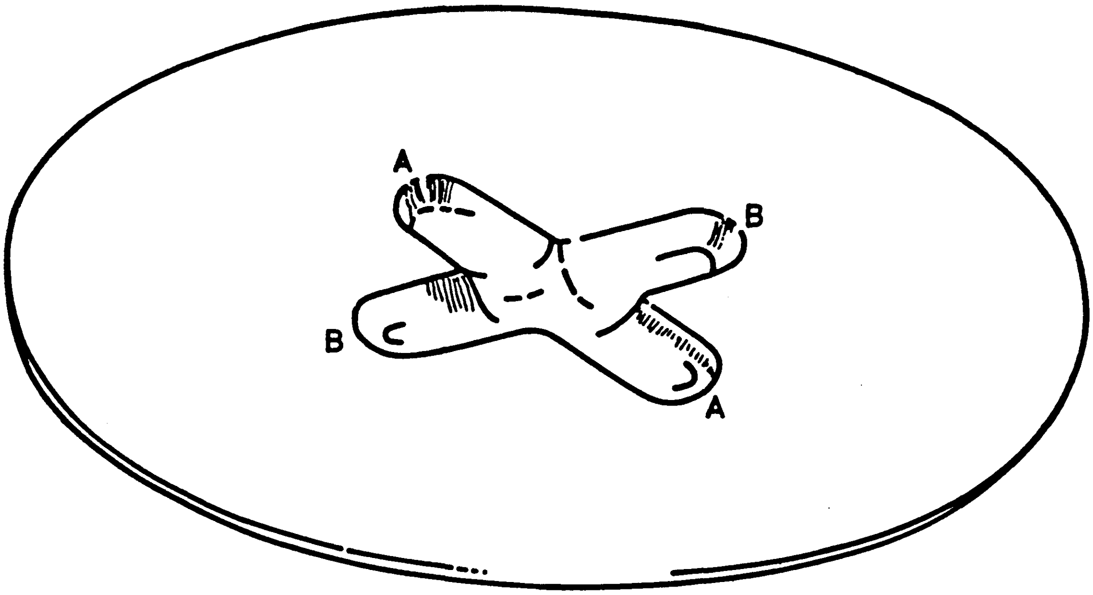

Modifications to hearth

Cross-section channel A

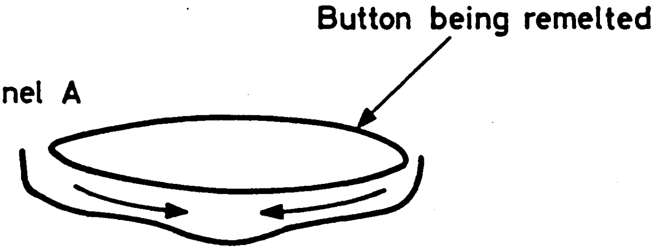
Button being remelted

Cross-section channel B

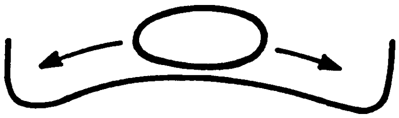

Figure 16. Graph of circle diameter versus the total magnification on prints and was available from previous HVEM work carried out at Harwell. This enabled the area in which the dose rate was constant to be calculated so that only voids within that control area would be measured.

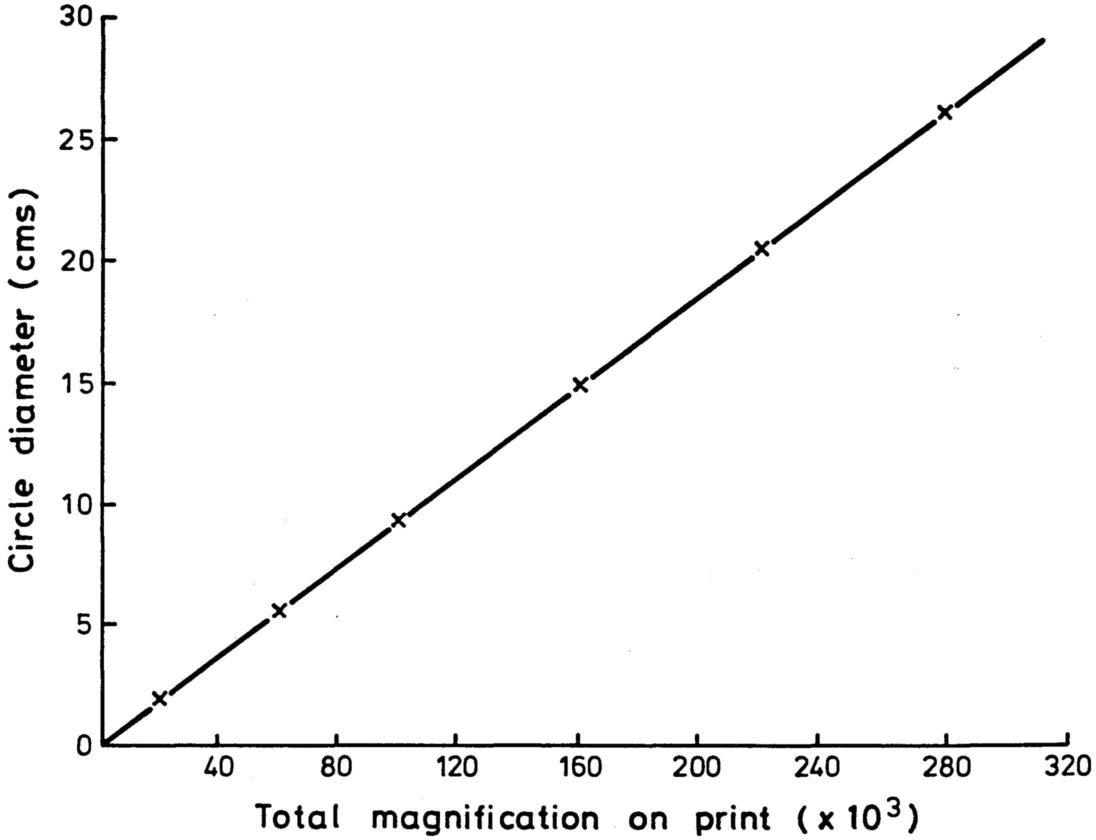
30
25
20
15
10
5
0
Circle diameter (cms)
40
80
120
160
200
240
280
320
Total magnification on print (x 10^3)

Figure 17. Hardness versus time curves for alloy A(20Cr,23Ni) solution treated at 1050°C for 0.5 hours followed by ageing at temperatures in the range 400°C-900°C for times of 10-1000 hours.

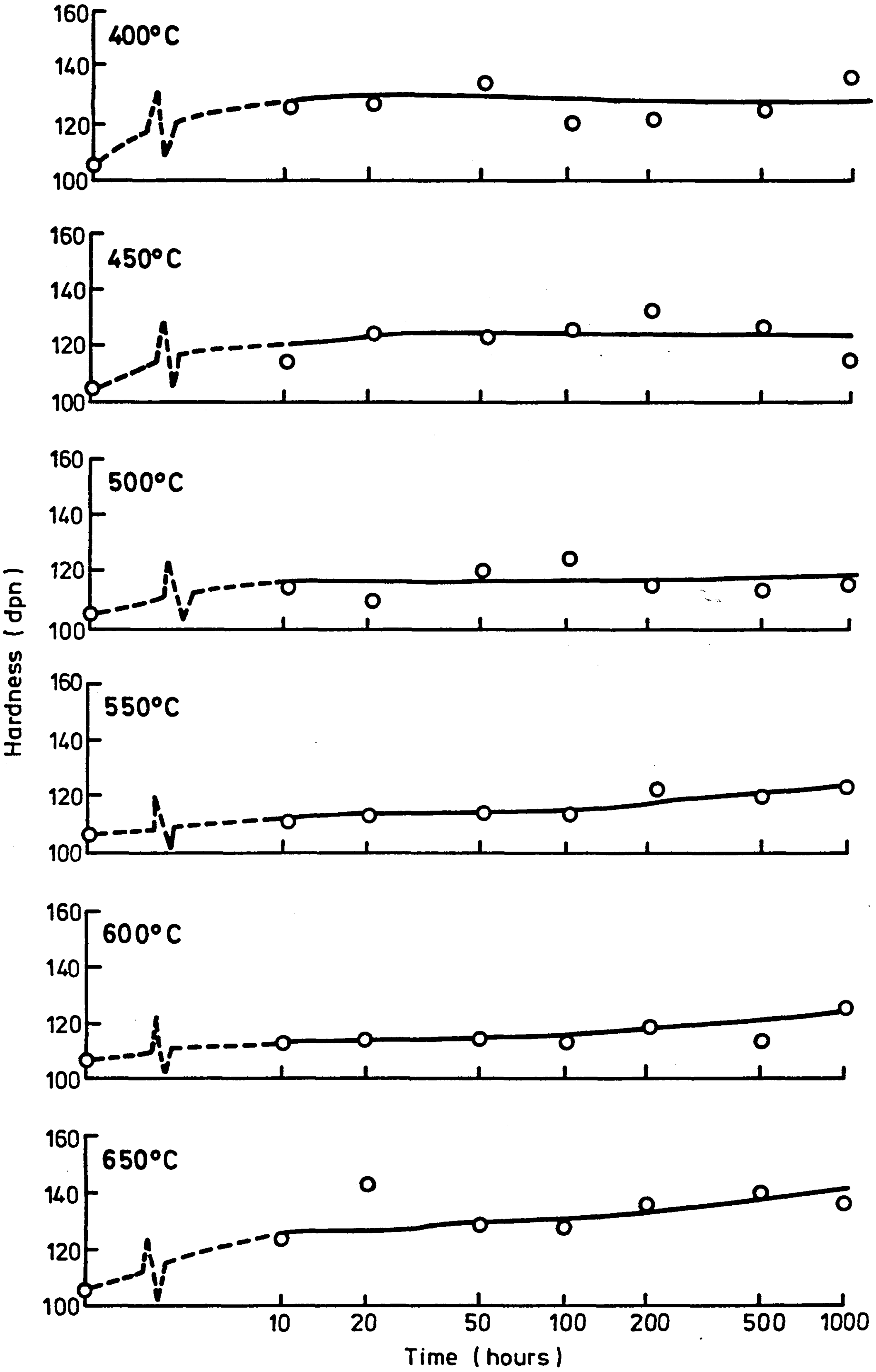
160
140
120
100
400°C
450°C
500°C
550°C
600°C
650°C
Hardness (dpn)
10
20
50
100
200
500
1000
Time (hours)

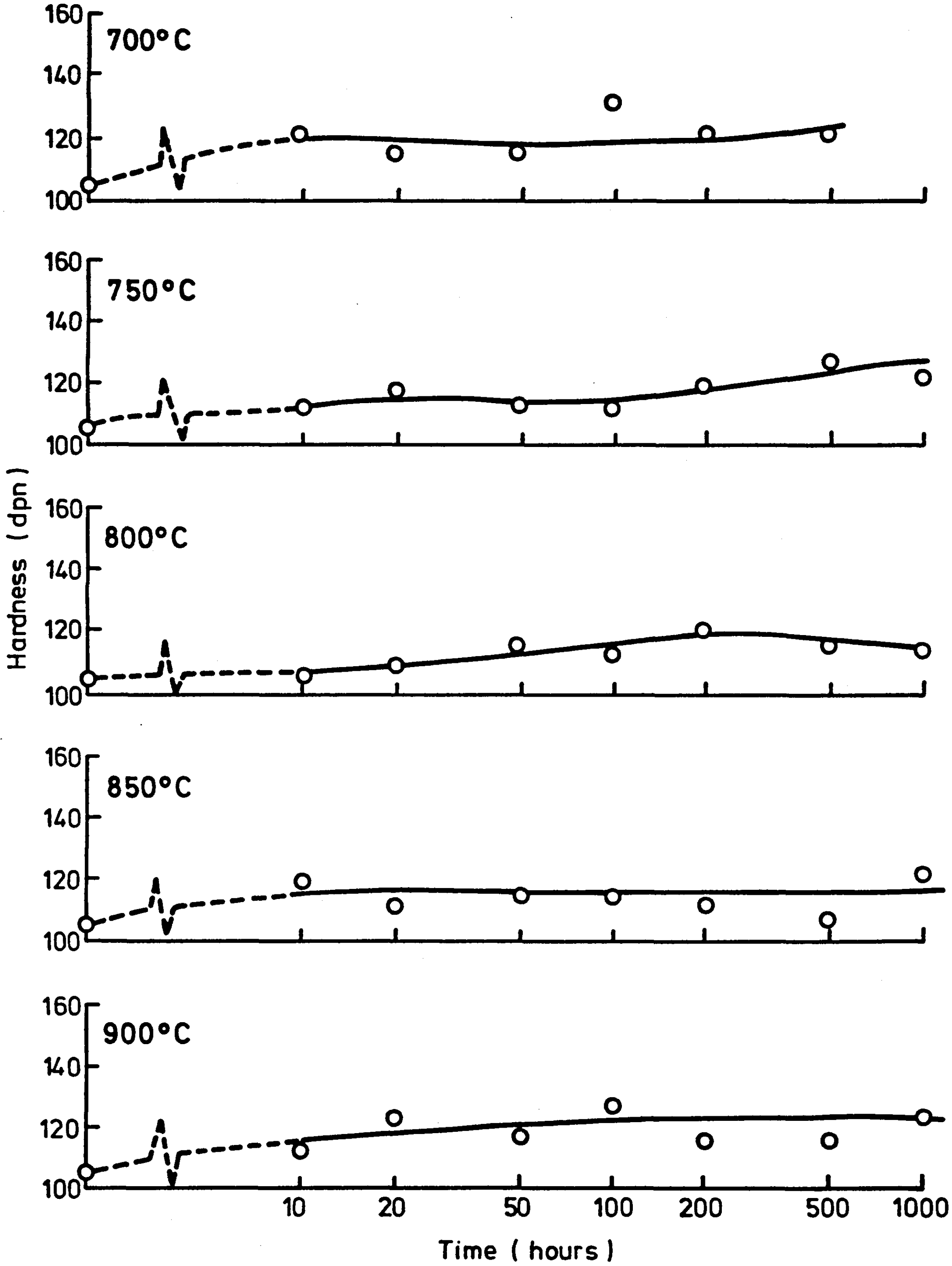
160
140
120
100
700°C
750°C
800°C
850°C
900°C
Hardness (dpn)
10
20
50
100
200
500
1000
Time (hours)

Figure 18. Transmission electron micrographs of microtwinning in alloy A(20Cr,23Ni) after solution treatment at 1050°C followed by ageing at 450°C for 200 hours (a) and at 500°C for 1000 hours (b).

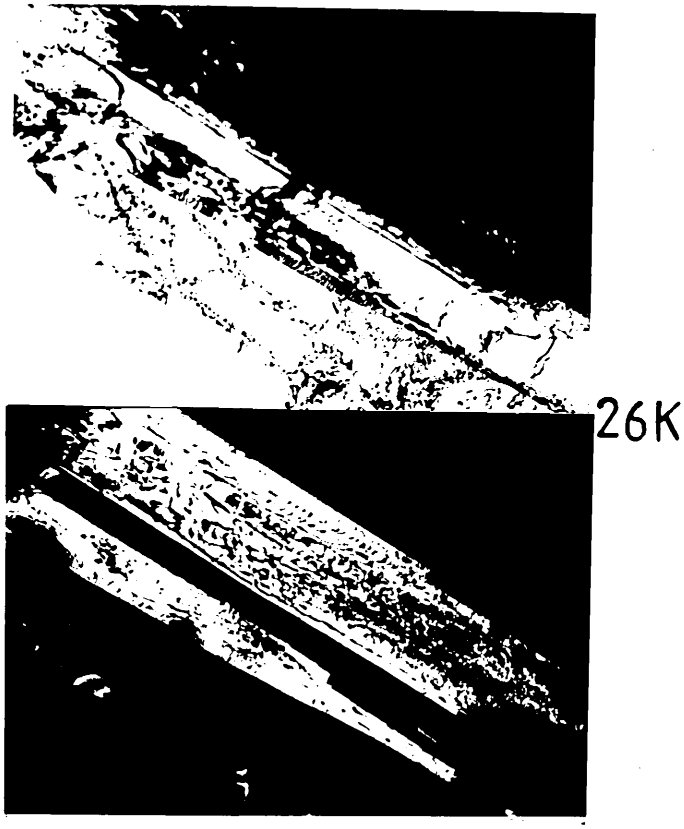

a

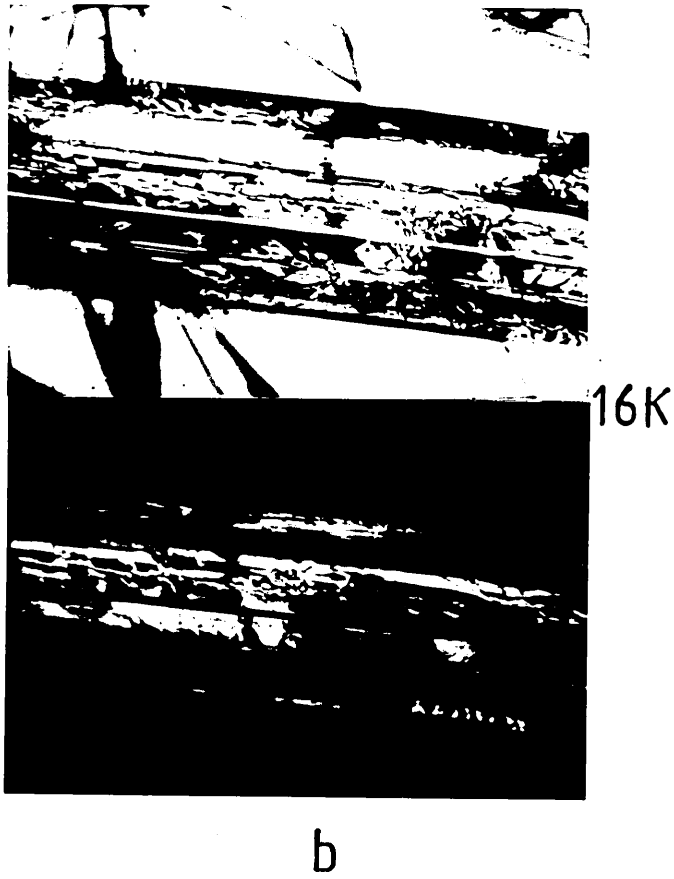

b

Figure 19. Optical micrographs at x100 of alloy A(20Cr,23Ni), solution treated at 1050°C followed by ageing at 650°C for (a) 10 hours, (b) 50 hours, (c) 200 hours and (d) 1000 hours. The alloy was electrolytically etched in 10% oxalic acid.

a

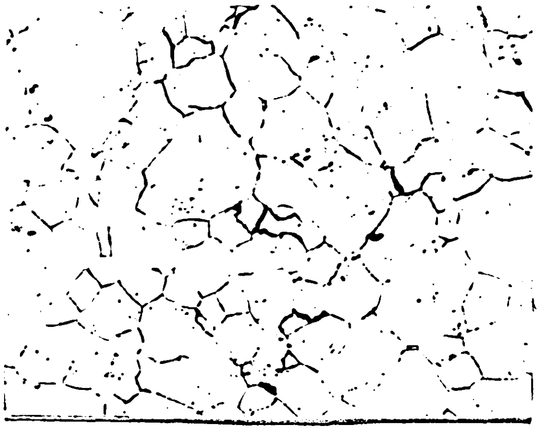

b

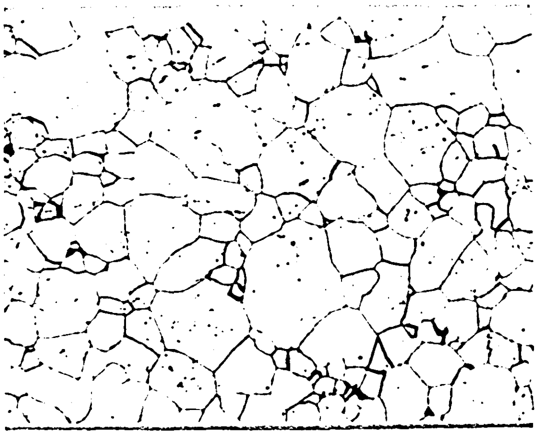

c

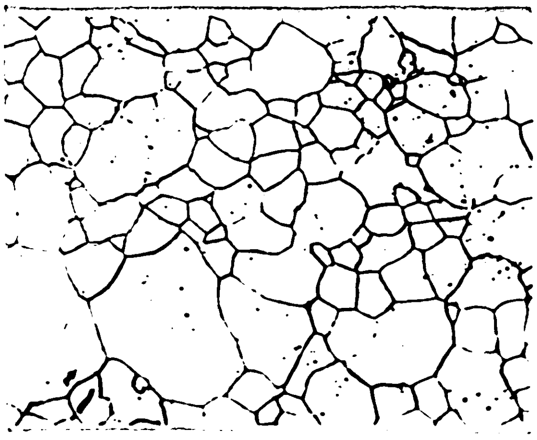

d

Figure 20. Time-Temperature-Precipitation diagrams for alloys A(20Cr,23Ni) and B(20Cr,43Ni), showing the onset of the precipitation of $Cr_{23}C_6$.

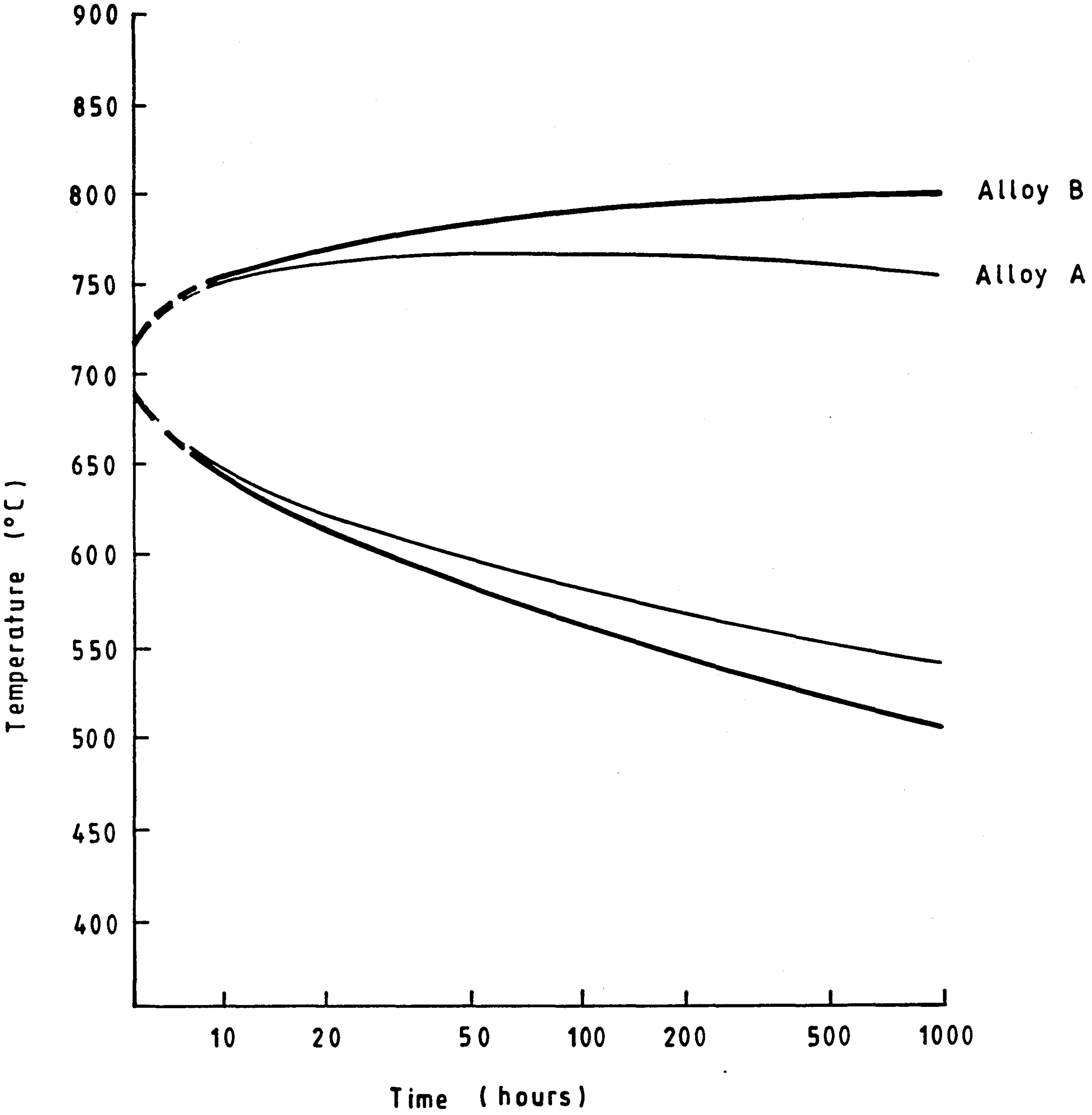
900
850
800
750
700
650
600
550
500
450
400
Temperature (°C)
10
20
50
100
200
500
1000
Time (hours)
Alloy B
Alloy A

Figure 21. Transmission electron micrographs of alloy A(20Cr,23Ni), solution treated at 1050°C followed by ageing at (a) 550°C for 1000 hours, (b) 650°C for 100 hours and (c) 700°C for 100 hours. The small precipitates that were observed on the grain boudaries in alloy A were identified as $Cr_{23}C_6$.

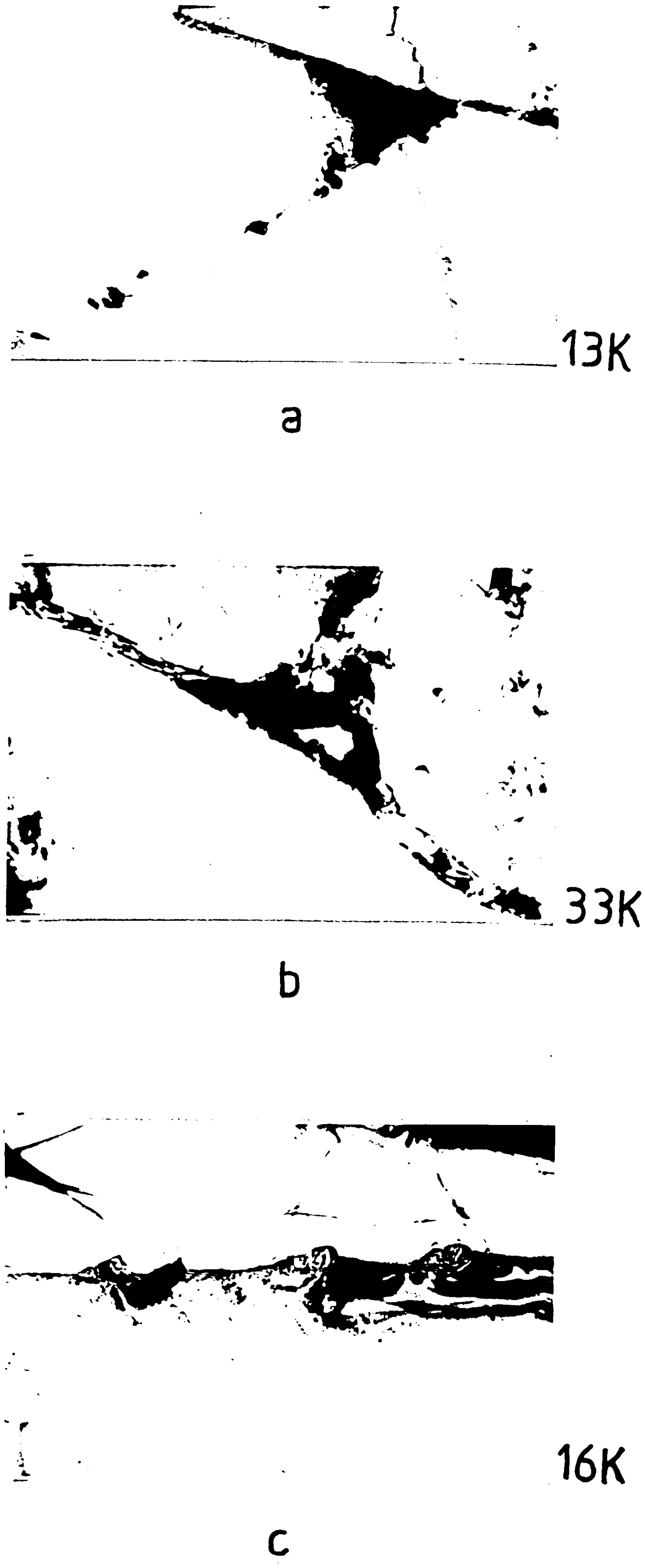
13K
a
33K
b
16K
c

Figure 22. Hardness versus time curves for alloy B (20Cr,43Ni) solution treated for 0.5 hours at 1050°C then aged at temperatures in the range 400°C-900°C for times of 10-1000 hours.

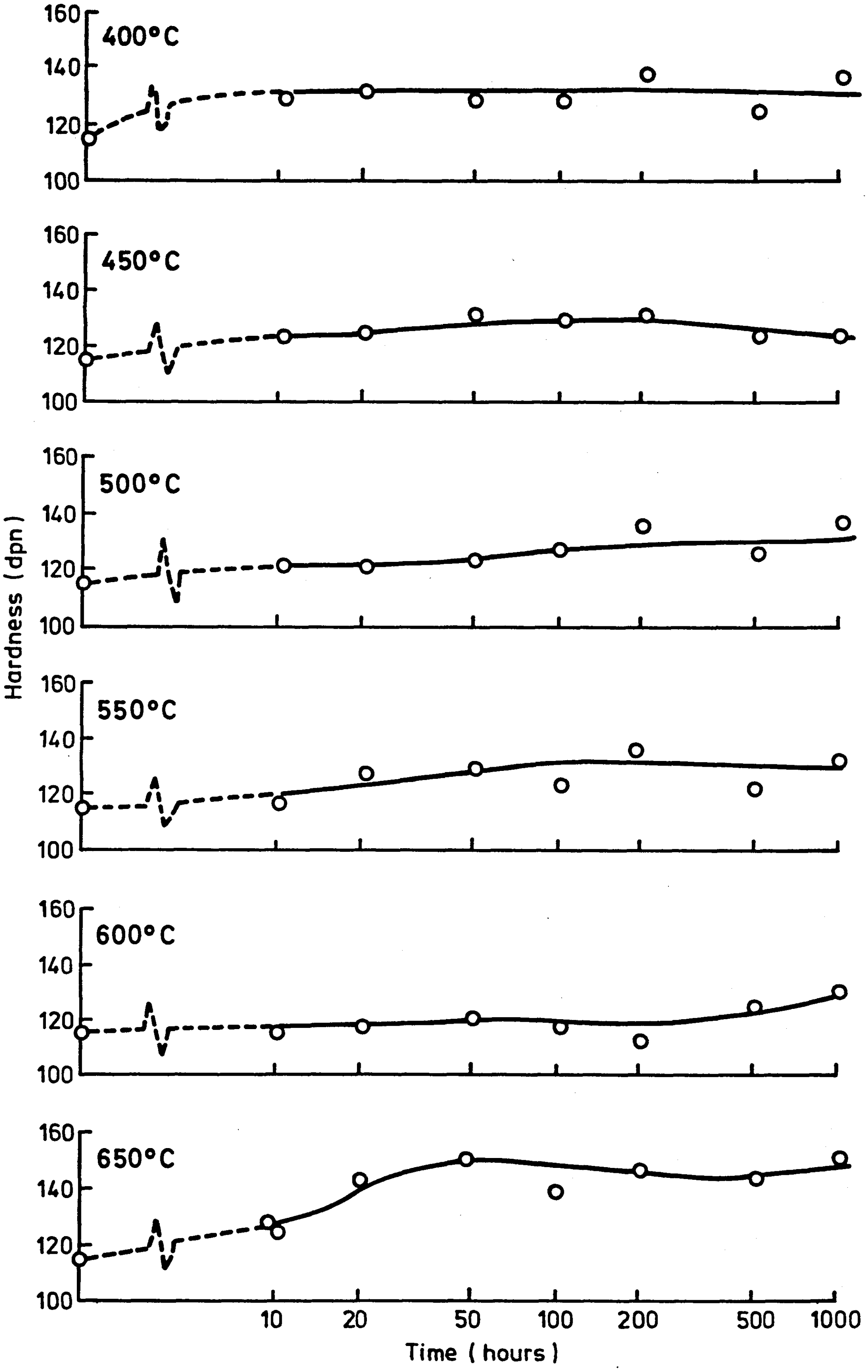

400°C
450°C
500°C
550°C
600°C
650°C
160
140
120
100
Hardness (dpn)
10
20
50
100
200
500
1000
Time (hours)

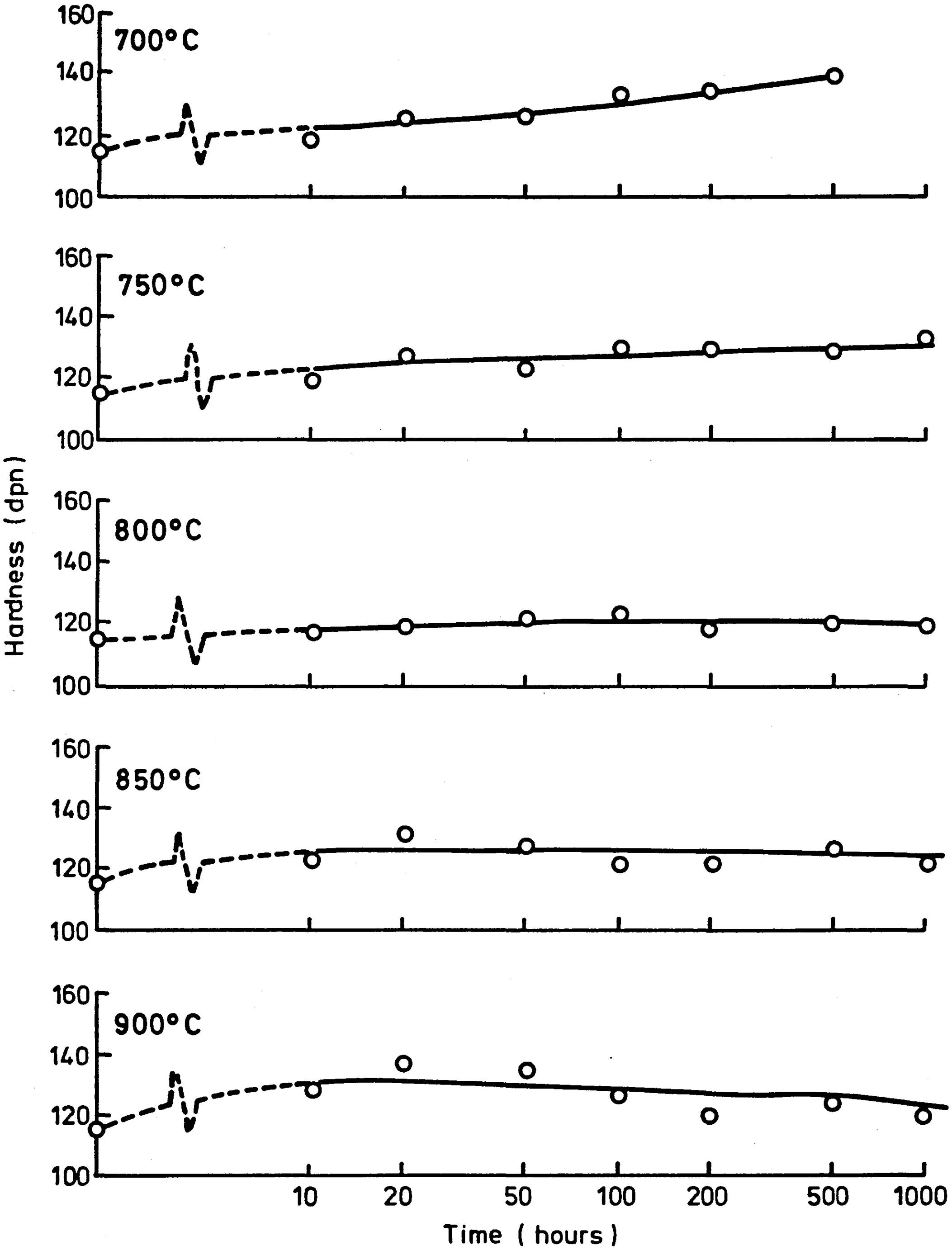

160
140
120
100
700°C
750°C
800°C
850°C
900°C
Hardness (dpn)
10
20
50
100
200
500
1000
Time (hours)

Figure 23. Optical micrographs taken at x100 of alloy B(20Cr,43Ni) after solution treating at 1050°C for 30 minutes followed by ageing at (a) 650°C for 50, 500 and 1000 hours and (b) 750°C for 50, 500 and 1000 hours. Electrolytically etched in 10% oxalic acid.

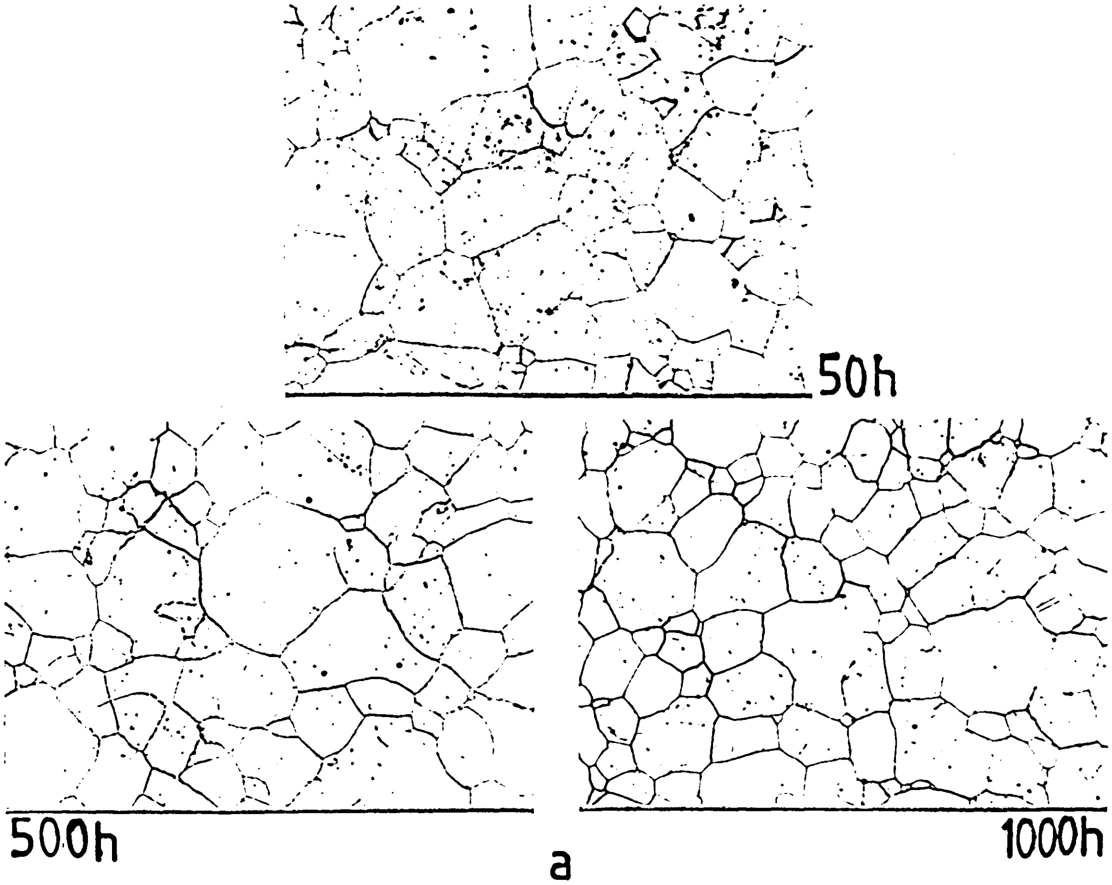
50h
500h
1000h

a

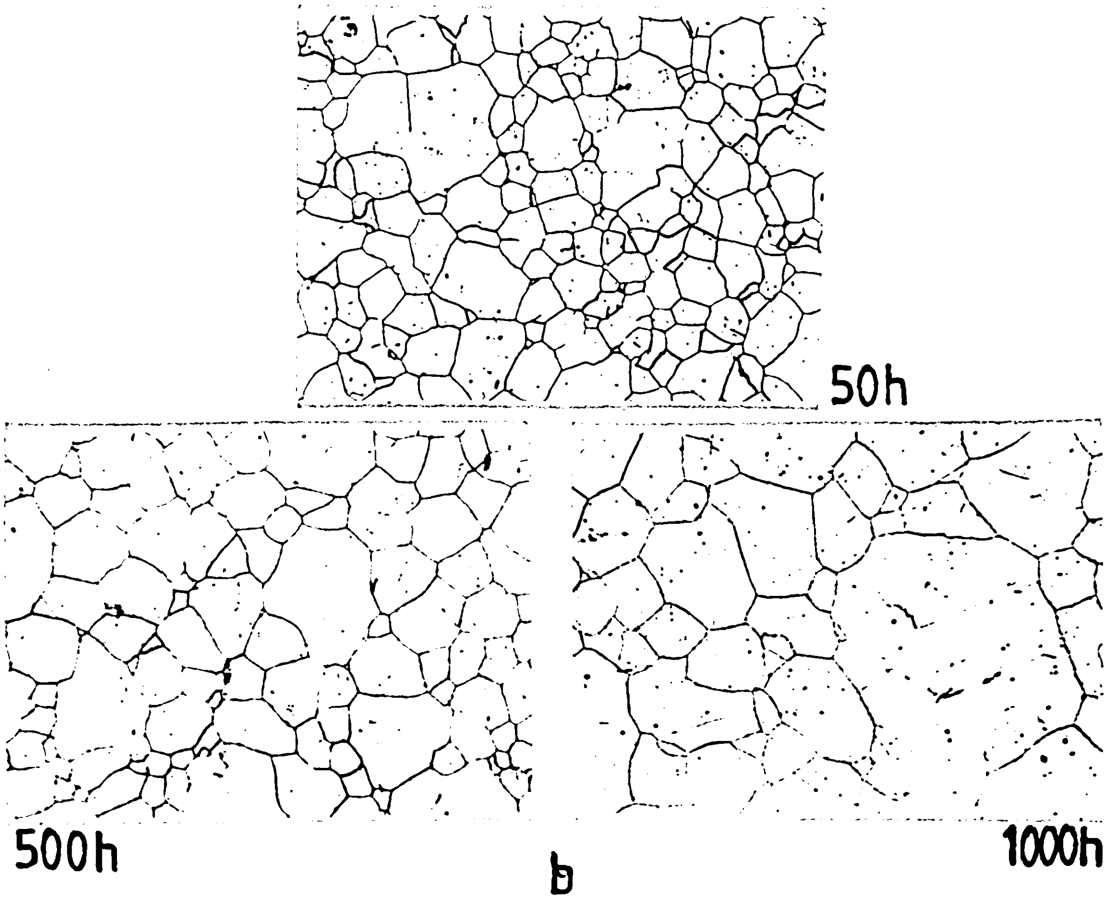
50h
500h
1000h

b

Figure 24. Transmission electron micrographs of alloy B(20Cr,43Ni) after solution treating for 0.5 hours at 1050°C followed by ageing at 700°C for 500 hours. The small, discrete precipitates that were observed on the grain boundaries in this alloy were confirmed by electron diffraction and EDX to be $Cr_{23}C_6$.

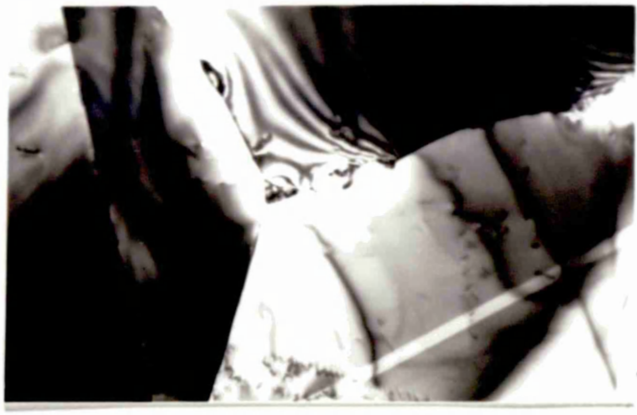
10K

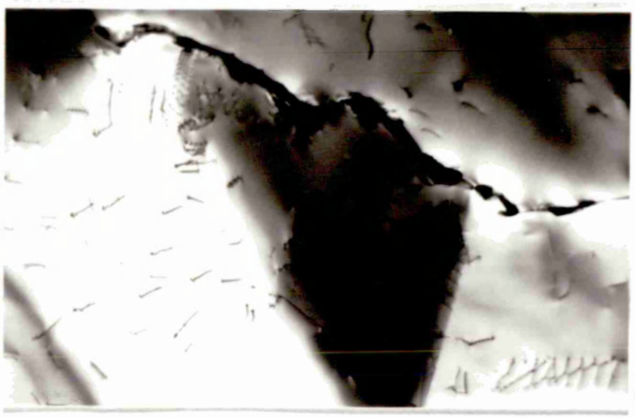
8,3K

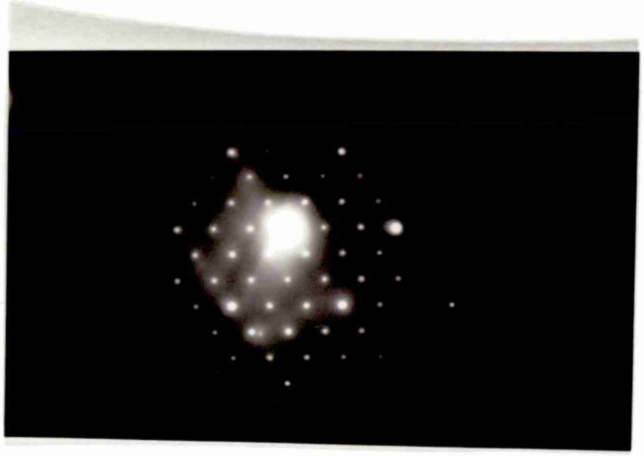

Figure 25. Hardness versus time curves for alloy C(30Cr,33Ni), solution treated for 0.5 hours at 1050°C then aged at temperatures in the range 400°C-900°C for times up of 10-1000 hours.

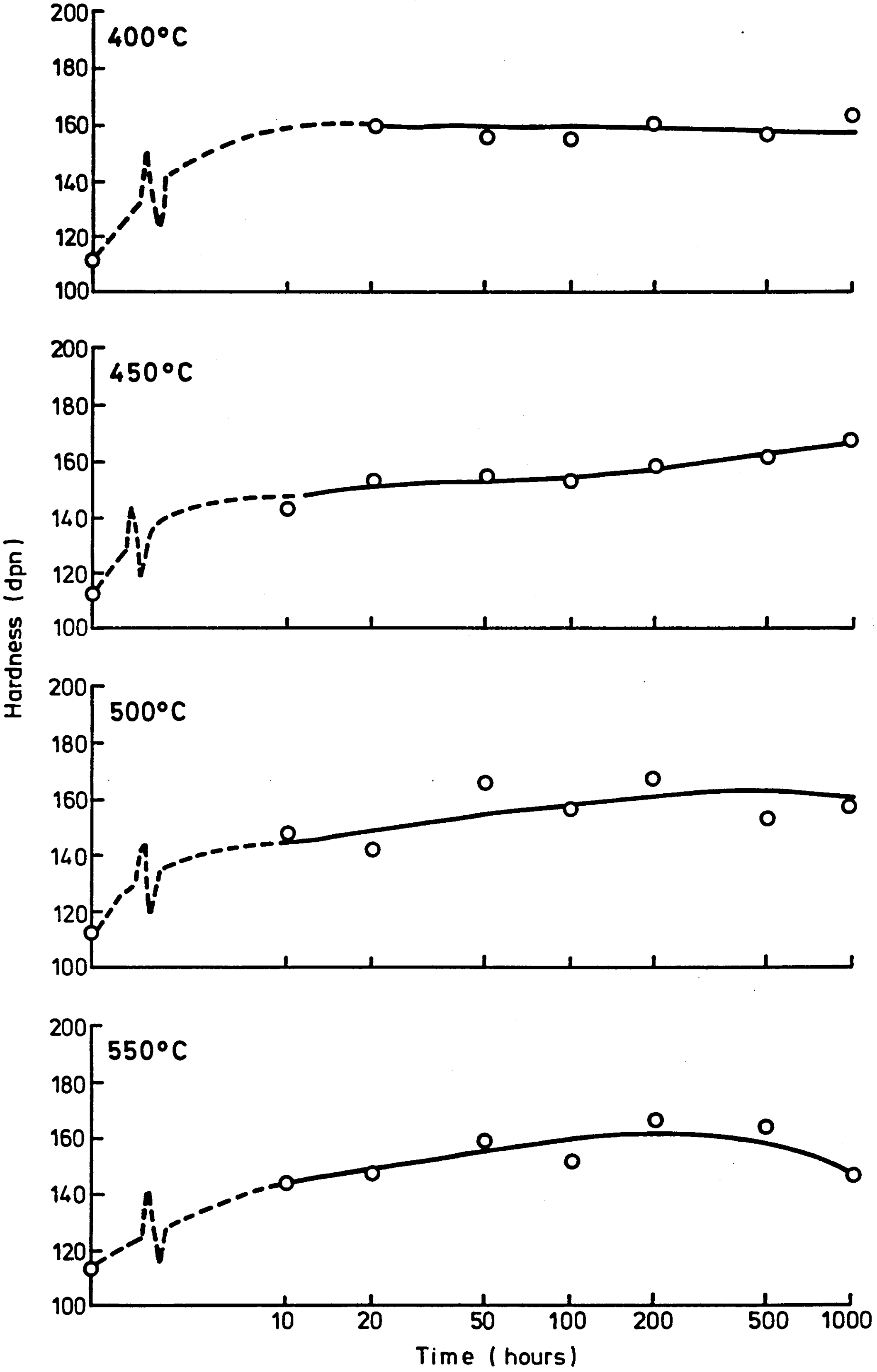
400°C
450°C
500°C
550°C
Hardness (dpn)
200
180
160
140
120
100
10
20
50
100
200
500
1000
Time (hours)

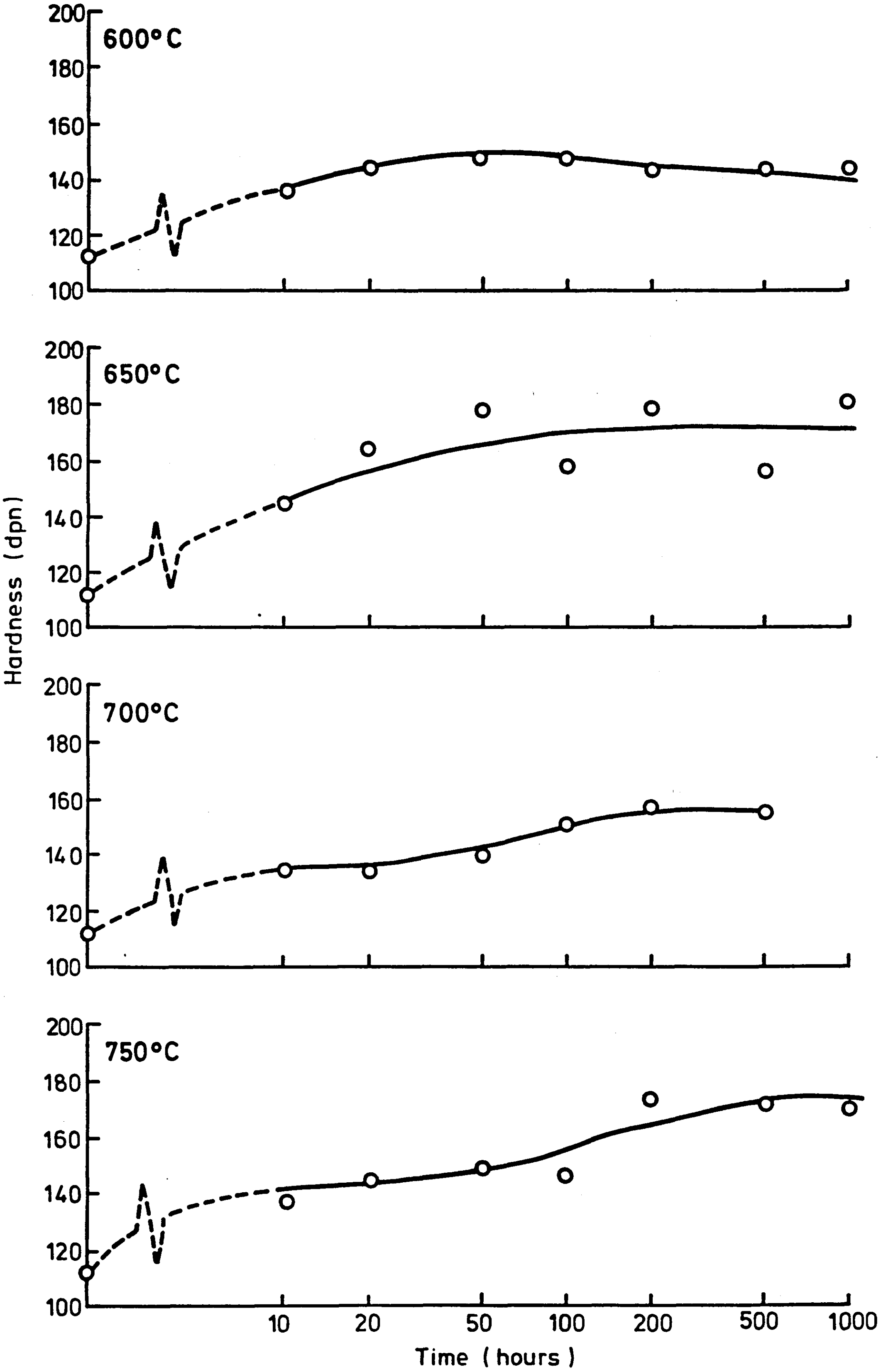
600°C
650°C
700°C
750°C
Hardness (dpn)
200
180
160
140
120
100
10
20
50
100
200
500
1000
Time (hours)

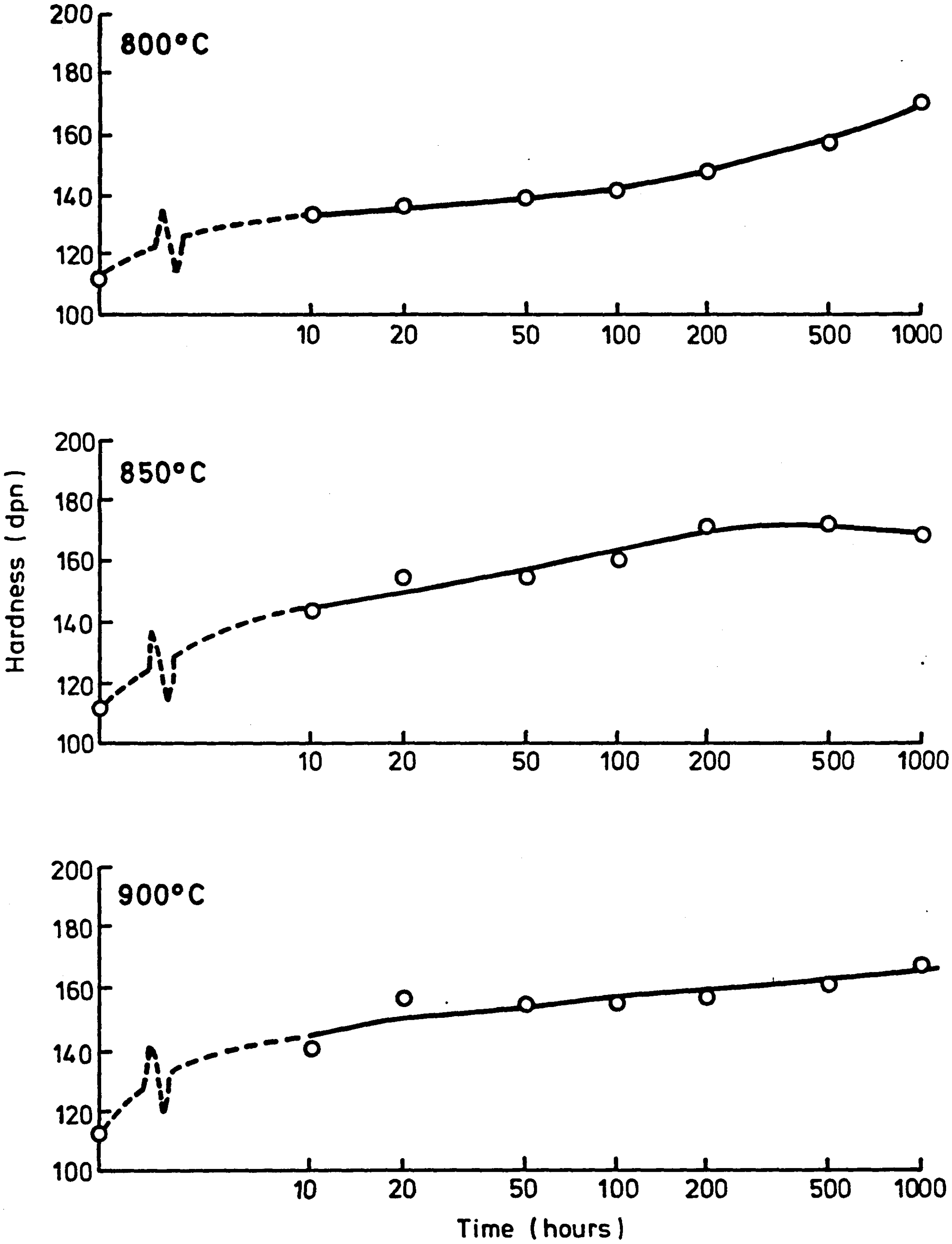
800°C
850°C
900°C
Hardness (dpn)
Time (hours)
200
180
160
140
120
100
10
20
50
100
200
500
1000

Figure 26. Transmission electron micrographs of alloy C(30Cr,33Ni) solution treated at 1050°C for 0.5 hours then aged at (a) 450°C for 1000 hours, (b) 500°C for 1000 hours and (c) 600°C for 1000 hours. The discrete precipitates which were seen on the grain boundaries were identified as $Cr_{23}C_6$.

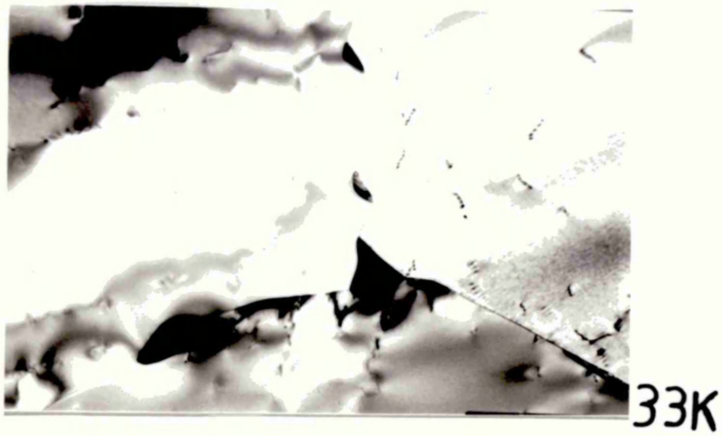

a

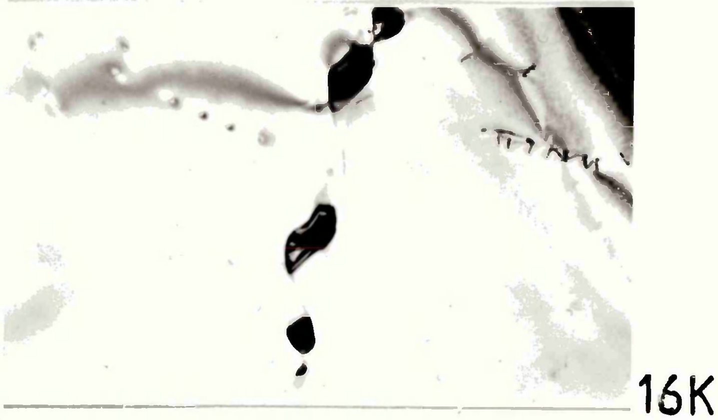

b

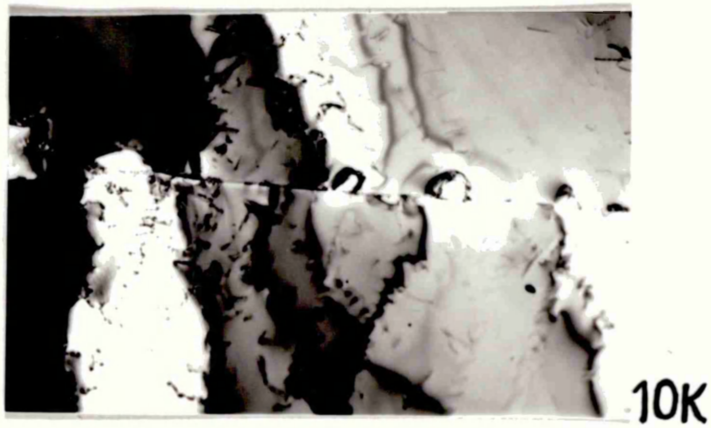

c

Figure 27. Two series of optical micrographs at x100 of alloy C(30Cr,33Ni), electrolytically etched using 10% oxalic acid. Column (a) shows the microstructure of alloy C after ageing at 650°C for 10, 100, 500 and 1000 hours, colunm (b) shows the 700°C aged microstructures after 10, 100, 500 and 1000 hours. Alloy C was solution treated at 1050°C for 0.5 hours prior to ageing.

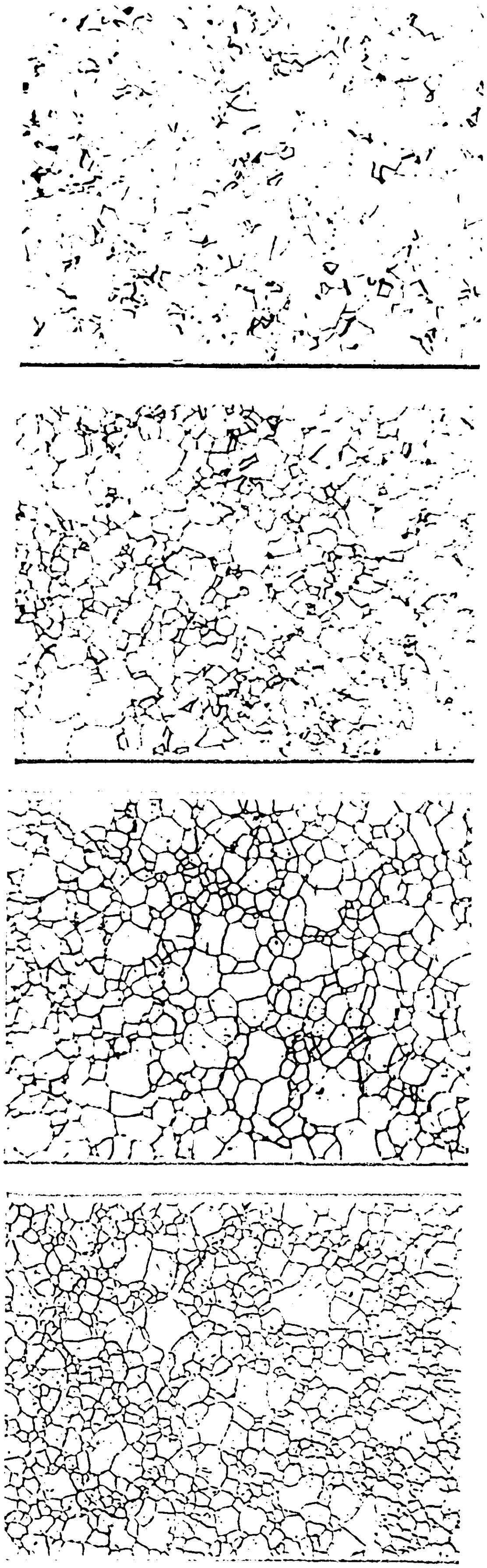

a

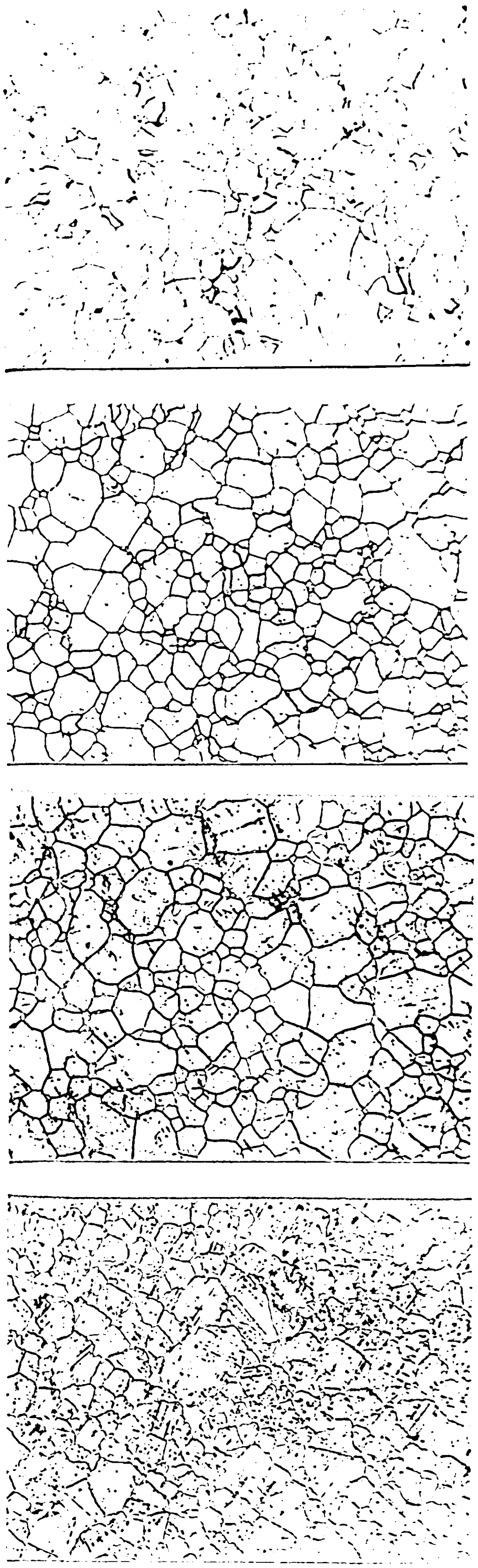

b

Figure 28. Optical micrographs at x100 of alloy C(30Cr,33Ni) which was solution treated at 1050°C prior to ageing at (a) 750°C and (b) 850°C. The alloy was electrolytically etched in 10% oxalic acid to reveal the microstruture. Intragranular precipitation of delta ferrite was evident after ageing for more than 100 hours at temperatures in the range 750°C-900°C.

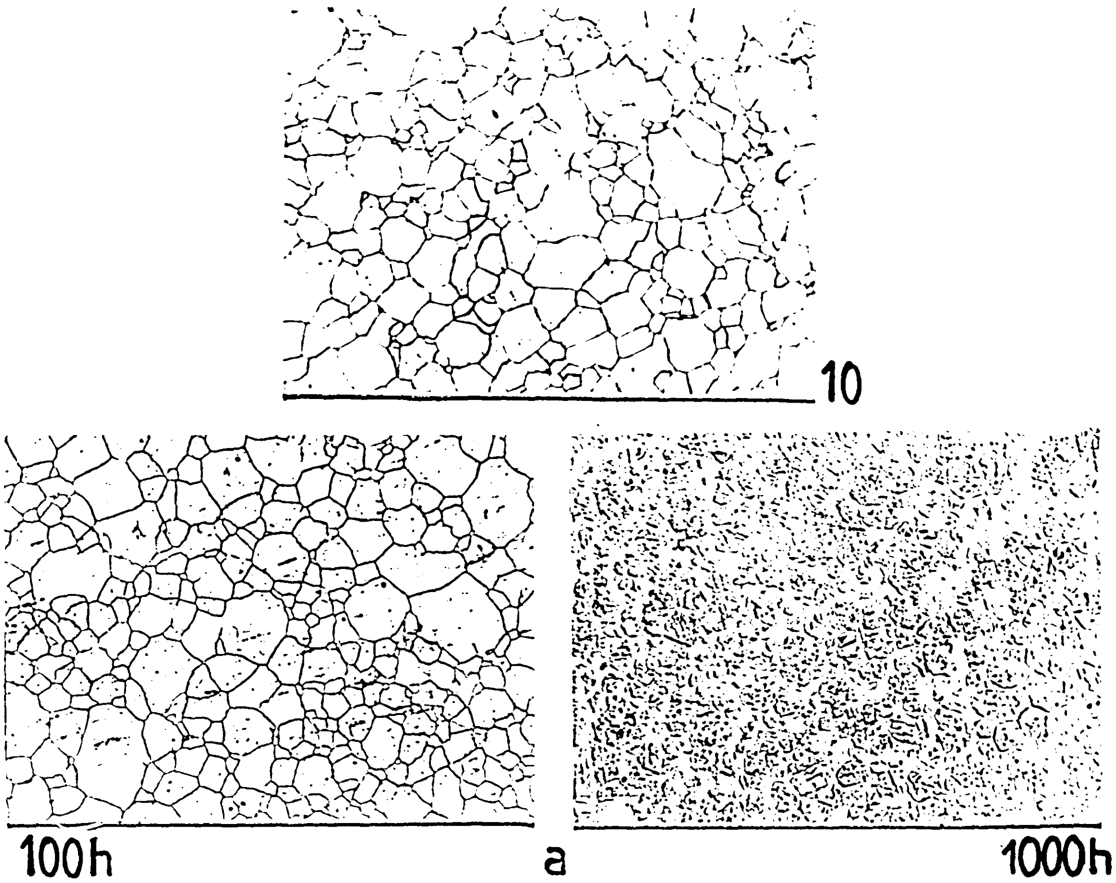
10
100h
1000h

a

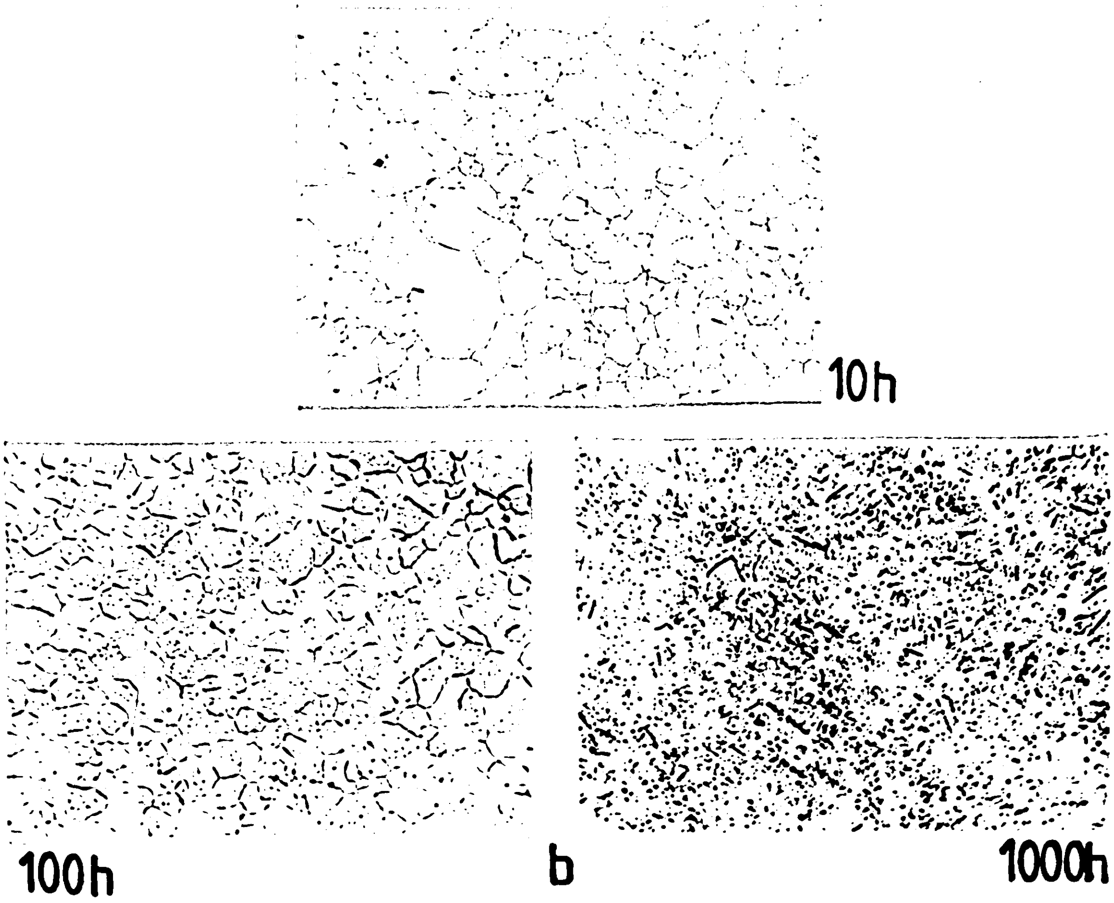
10h
100h
1000h

b

Figure 29. Transmission electron micrographs of alloy C(30Cr,33Ni), which was solution treated at 1050°C prior to ageing.

(a) shows delta ferrite precipitating both intra- and intergranularly in alloy C after ageing for 1000 hours at 650°C.

(b) shows bright field and dark field images of delta ferrite precipitating in alloy C after ageing for 1000 hours at 750°C.

(c) shows the nature of the delta ferrite precipitation as observed in the 1000 hours, 850°C aged alloy.

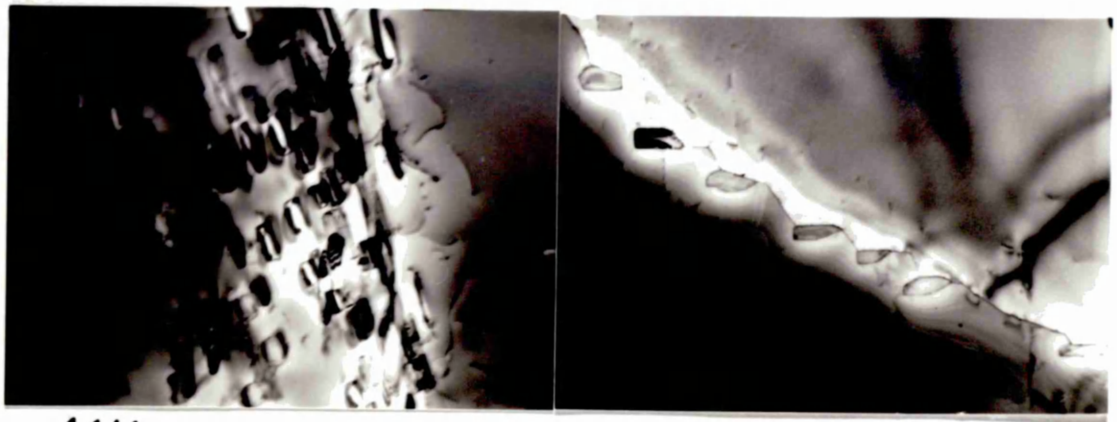

a

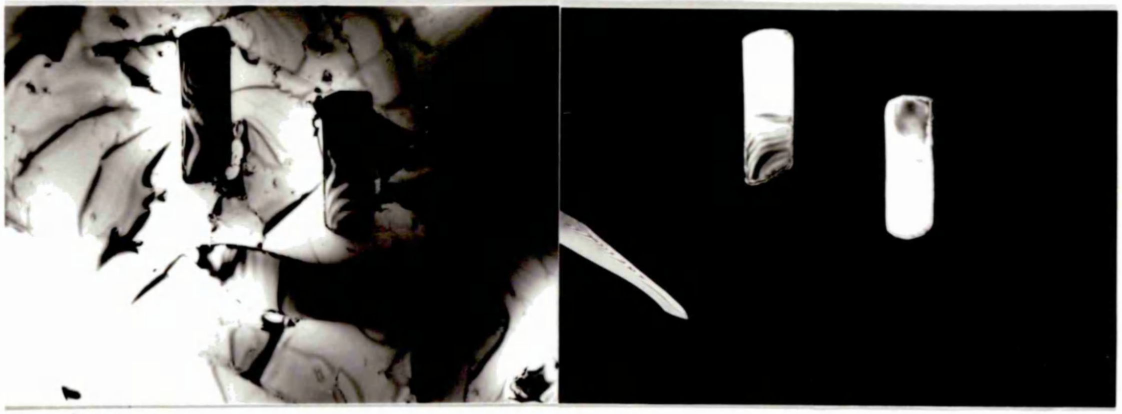

b

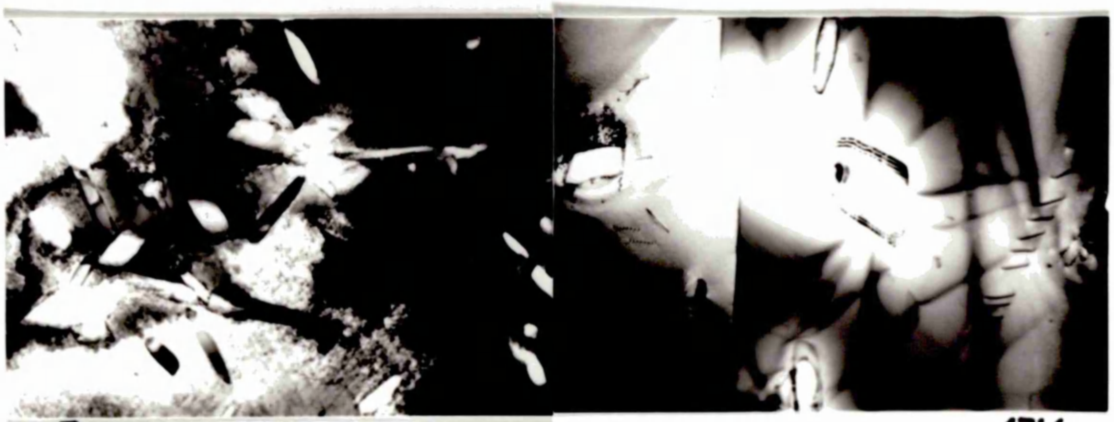

c

Figure 30. Time-Temperature-Precipitation diagram for alloy C(30Cr,33Ni). The fine line represents the first observation of $Cr_{23}C_6$ precipitating in this alloy, the bold line represents the precipitation of delta ferrite in alloy C.

Figure 30. Time-Temperature-Precipitation diagram for alloy C(30Cr,33Ni). The fine line represents the first observation of $Cr_{23}C_6$ precipitating in this alloy, the bold line represents the precipitation of delta ferrite in alloy C.

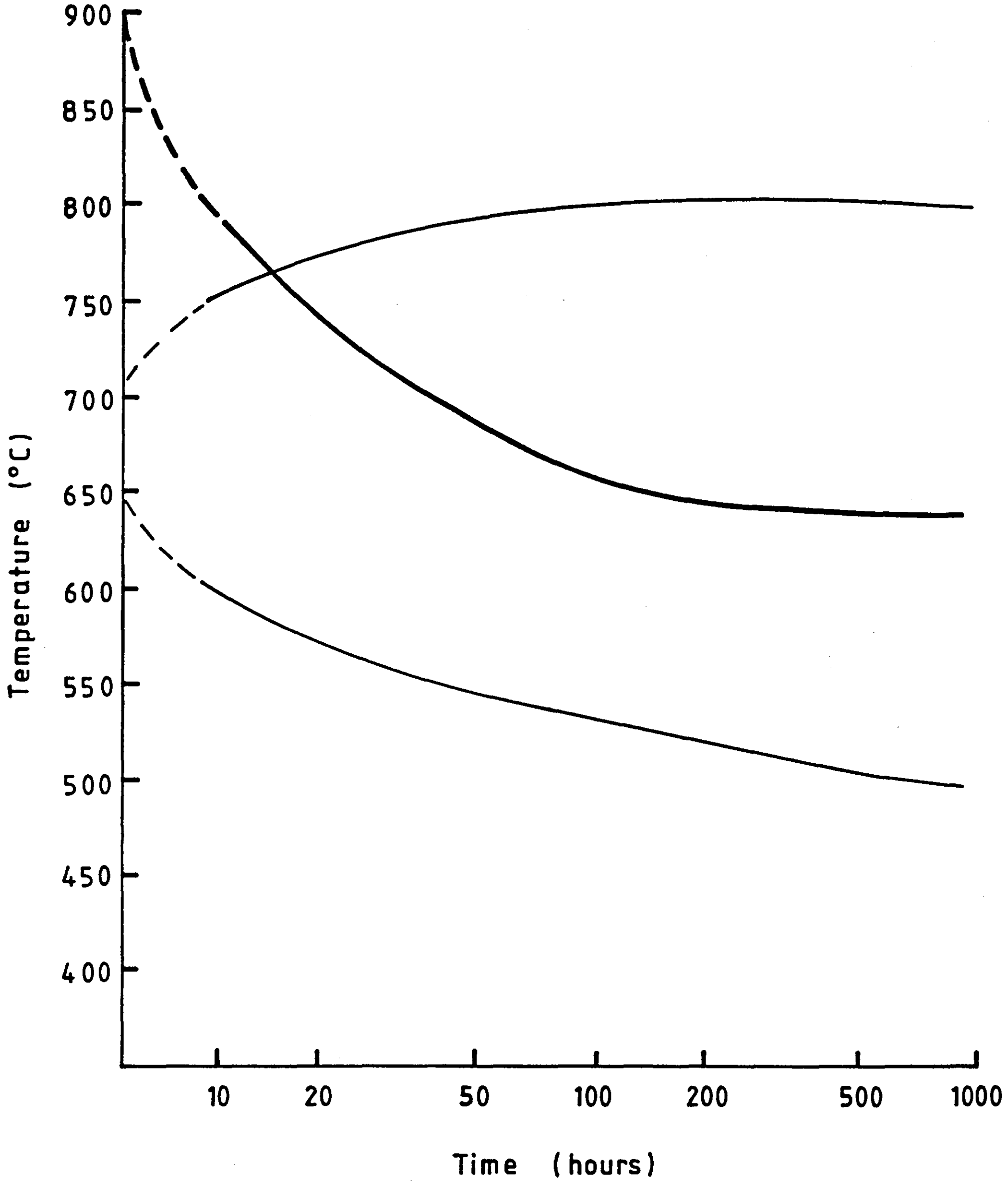
900
850
800
750
700
650
600
550
500
450
400
Temperature (°C)
10
20
50
100
200
500
1000
Time (hours)

Figure 31. Hardness versus time curves for alloy D(12Cr,3Ni), solution treated for 0.5 hours at 1050°C then aged at temperatures in the range 400°C-900°C for times of 10-1000 hours.

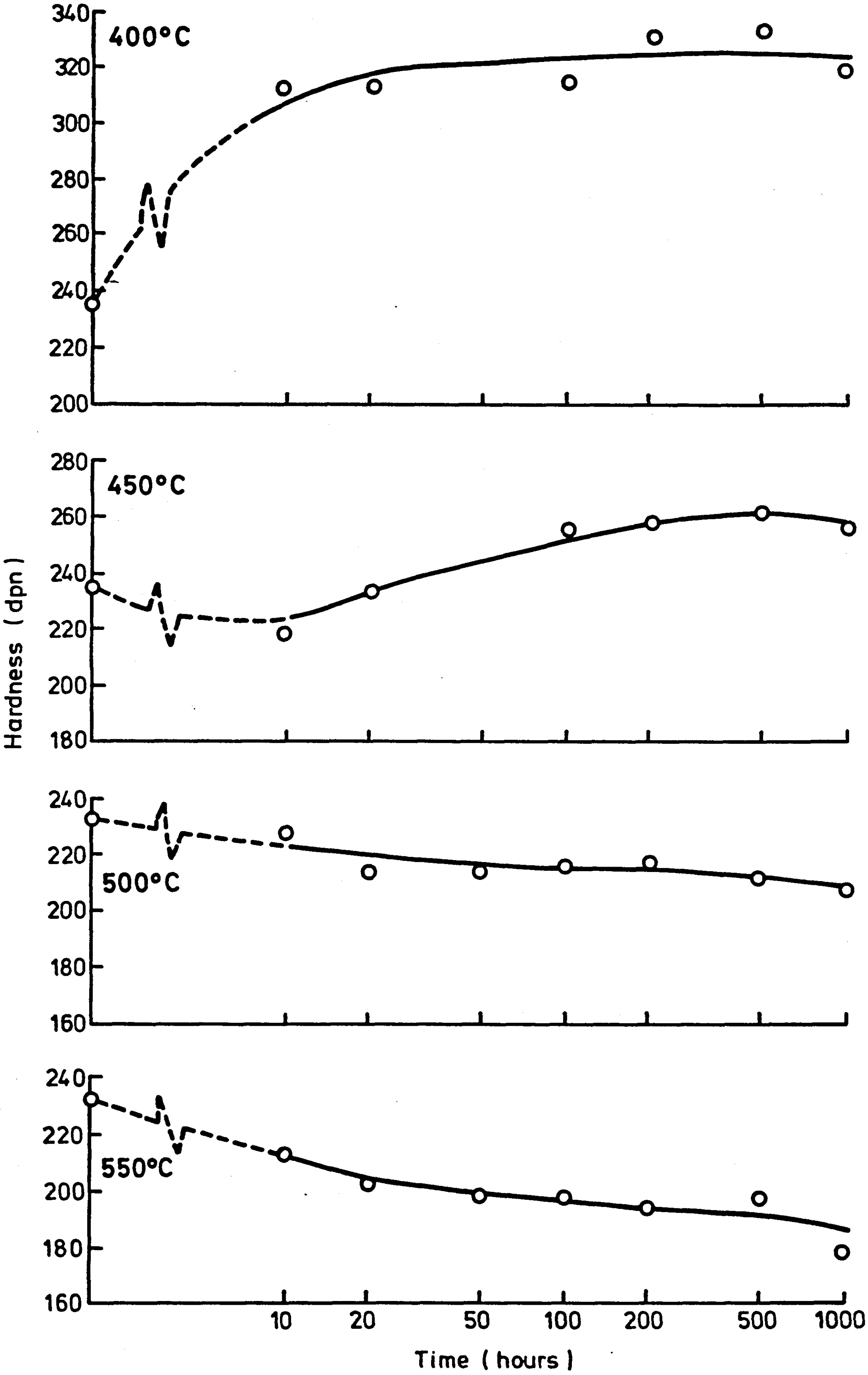

400°C
450°C
500°C
550°C
340
320
300
280
260
240
220
200
180
160
Hardness (dpn)
10
20
50
100
200
500
1000
Time (hours)

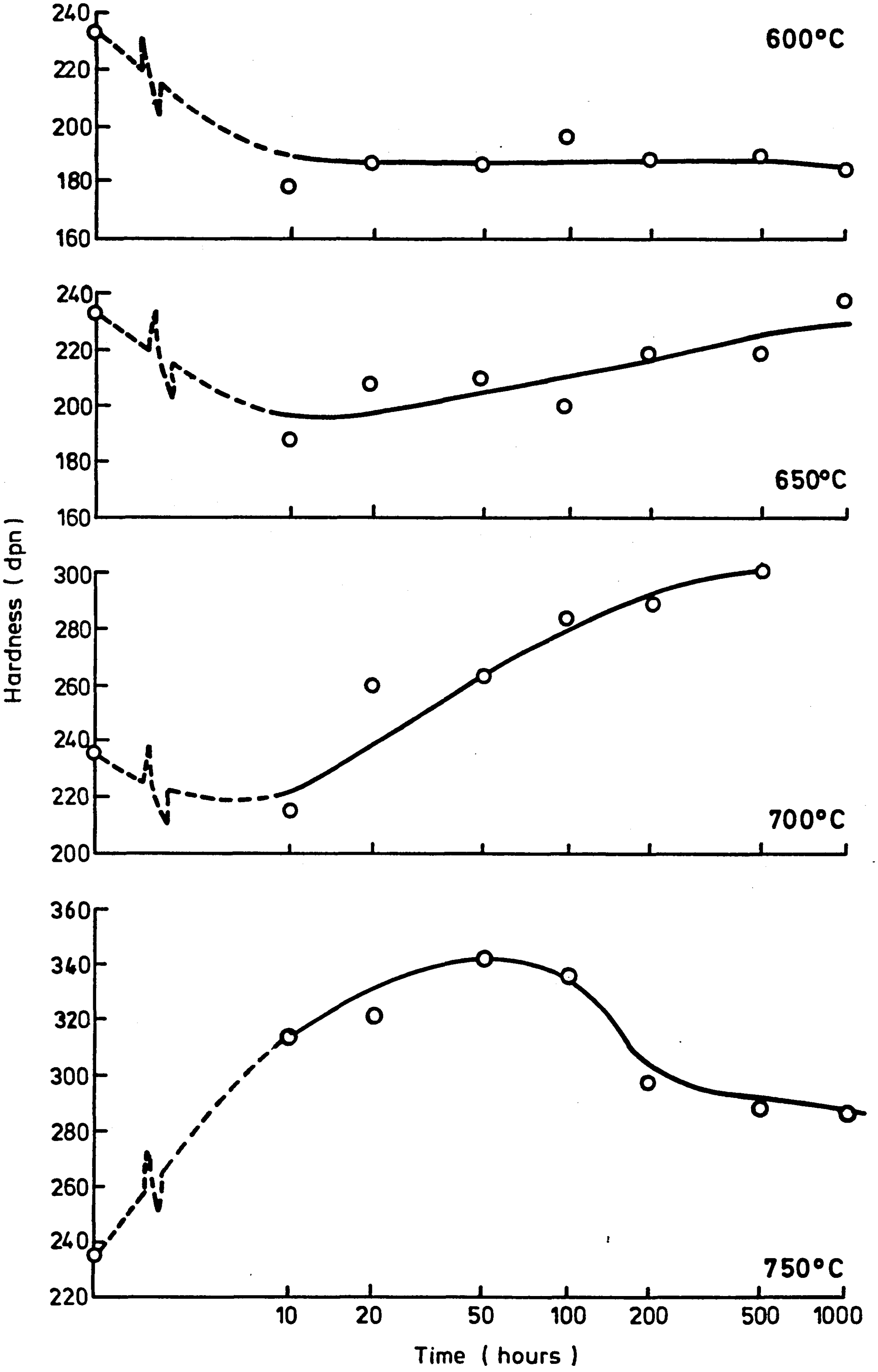
600°C
650°C
700°C
750°C
Hardness (dpn)
Time (hours)
240
220
200
180
160
300
280
260
360
340
320
10
20
50
100
200
500
1000

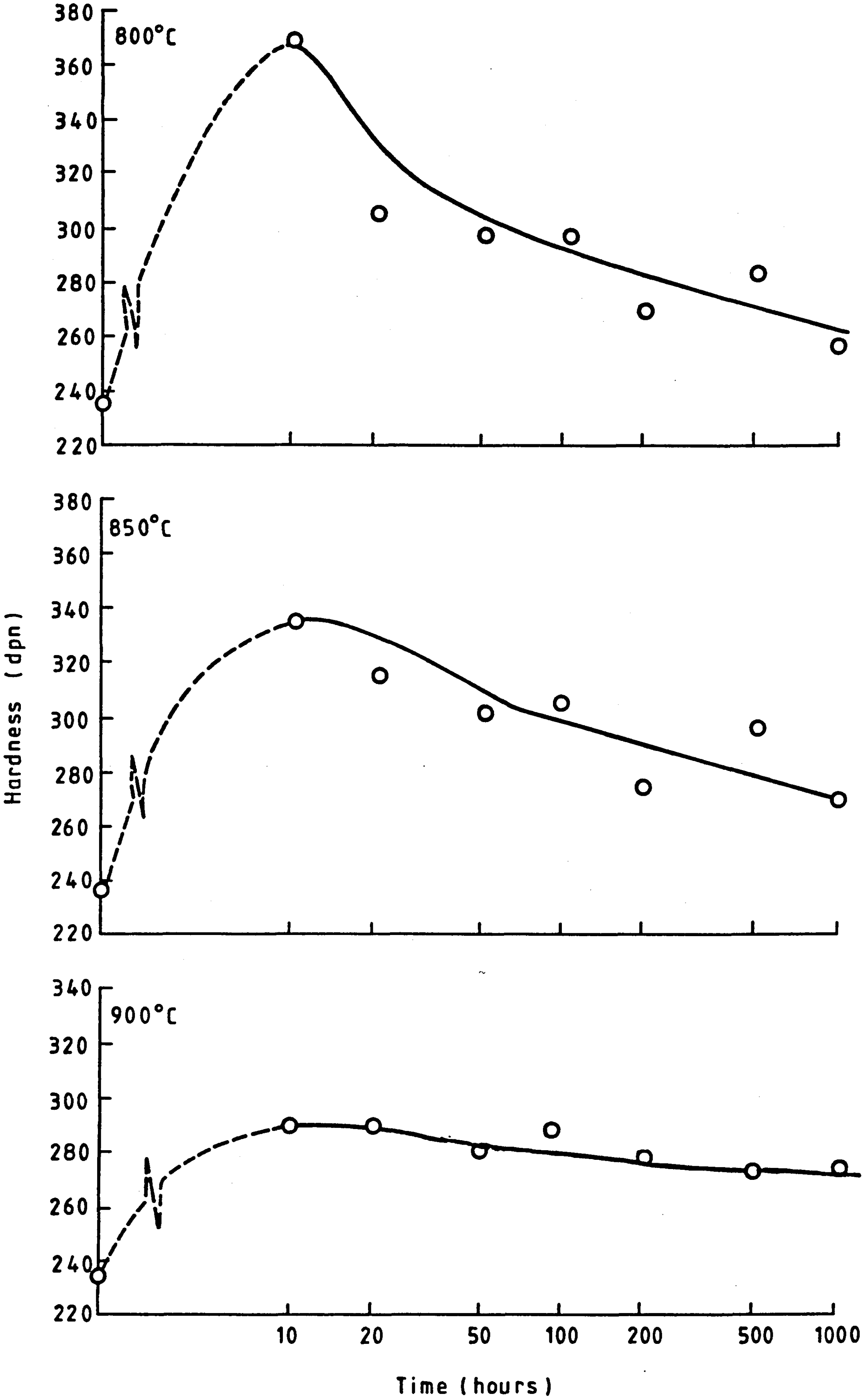
380
360
340
320
300
280
260
240
220
800°C
850°C
340
320
300
280
260
240
220
900°C
Hardness (dpn)
10
20
50
100
200
500
1000
Time (hours)

Figure 32. Optical micrographs taken at x200 of alloy D which was solution treated at 1050°C prior to ageing at 600°C. A tempered martensitic structure was obtained upon ageing. Alloy D was electrolytically etched in 10% oxalic acid.

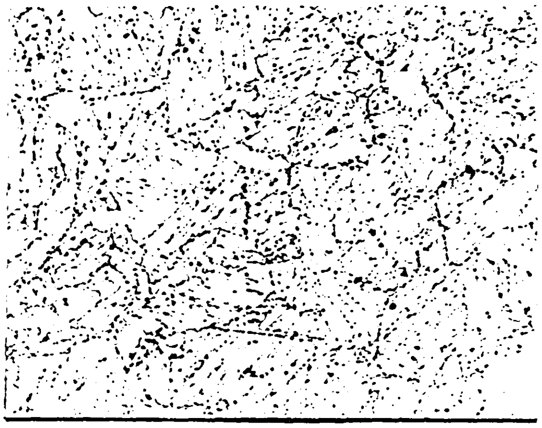
20 h

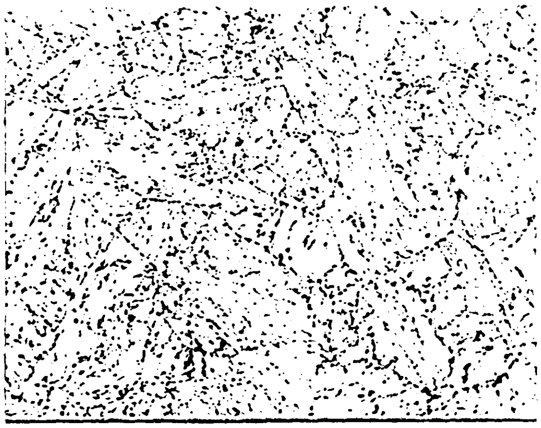
50h

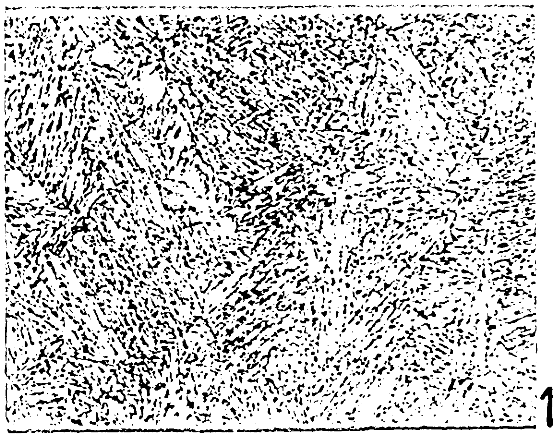
100h

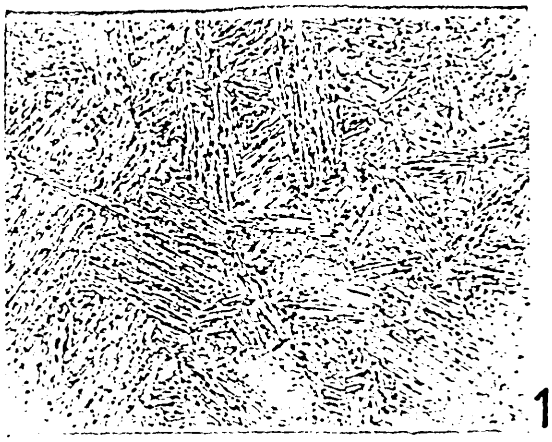
1000h

Figure 33. Alloy D(12Cr,3Ni) was solution treated at 1050C prior to ageing at 750°C. Above-650°C the A_s temperature was exceeded and therefore the alloy contained retained austenite on cooling to room temperature. The transmission electron micrographs taken from the 750°C, 1000 hours aged alloy show this retained austenitic structure.

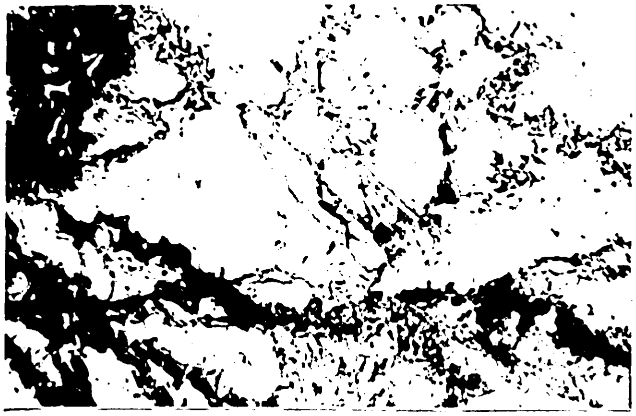

26K

26K

Figure 34. Very fine precipitation of $Cr_{23}C_6$ present in alloy D(12Cr,3Ni) after solution treating at 1050°C for 0.5 hours and ageing at 750°C for 1000 hours.

(a) shows the bright field image.

(b) shows the dark field image.

(c) shows the electron diffraction pattern obtained.

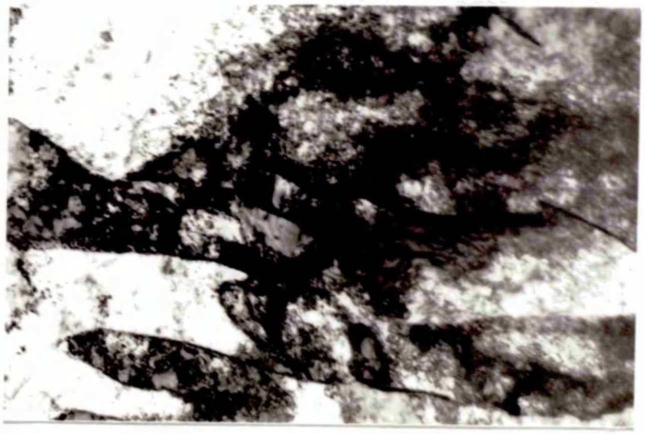

16K

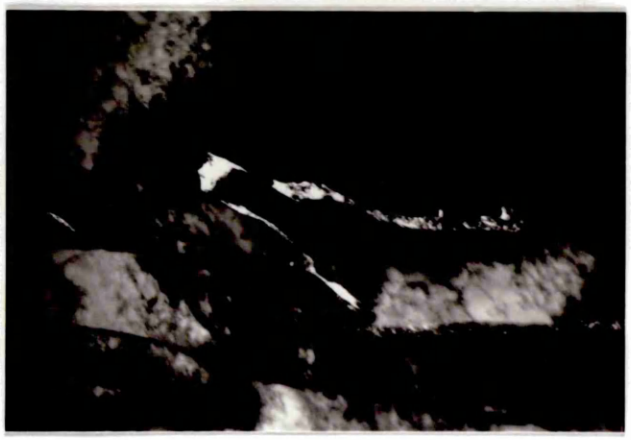

16K

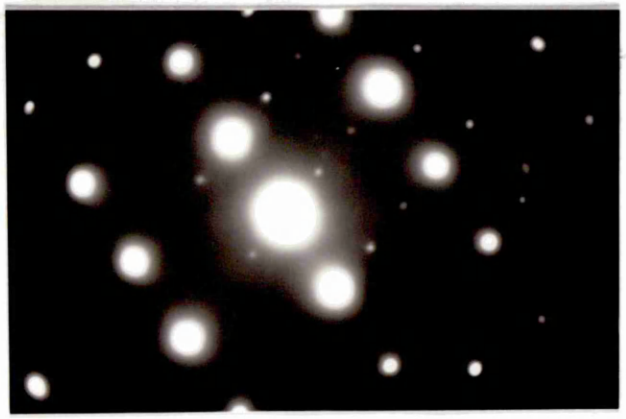

Figure 35. Transmission electron micrographs of alloy E after solution treating at 1050C for 0.5 hours. The islands of second phase that were present in the alloy were identified as being delta ferrite.

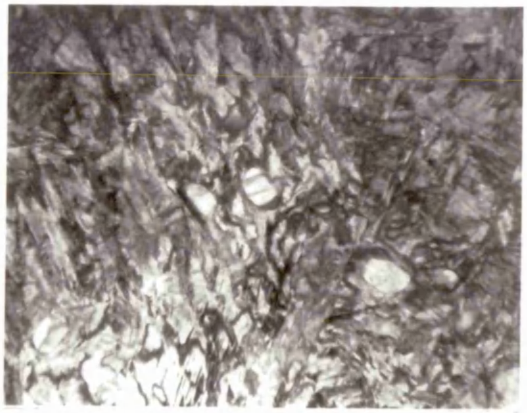

2.6K

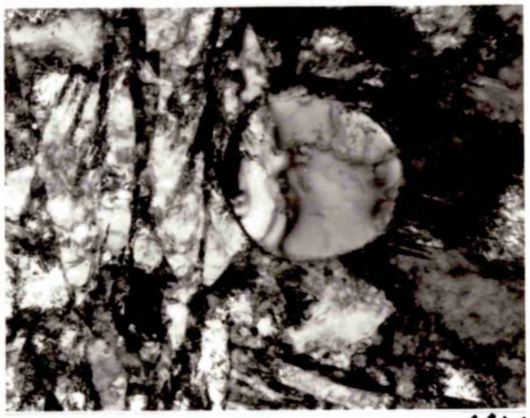

16K

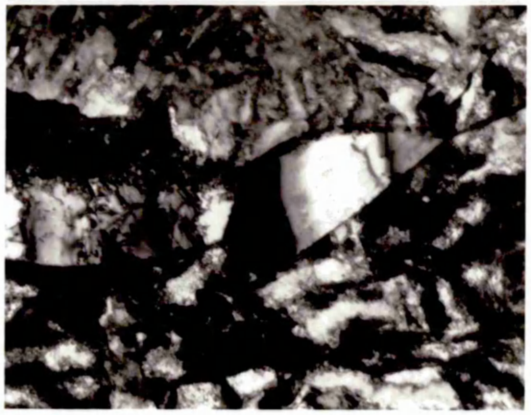

10K

10K

Figure 36. Hardness versus time curves for alloy E(18Cr,7Ni), solution treated for 0.5 hours at 1050°C then aged at temperatures in the range 400°C-900°C for times of 10-1000 hours.

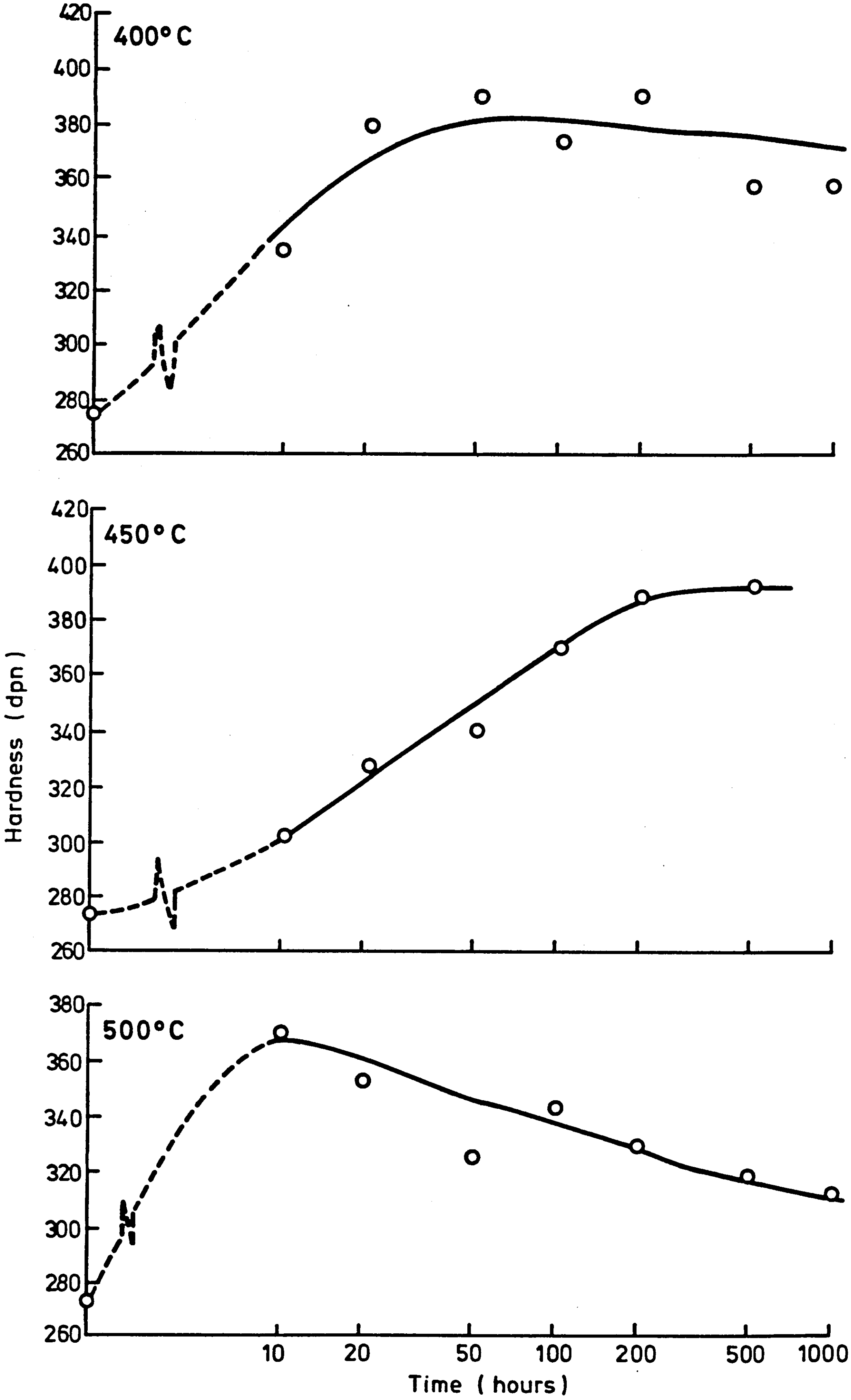
400° C
450° C
500° C
Hardness (dpn)
420
400
380
360
340
320
300
280
260
10
20
50
100
200
500
1000
Time (hours)

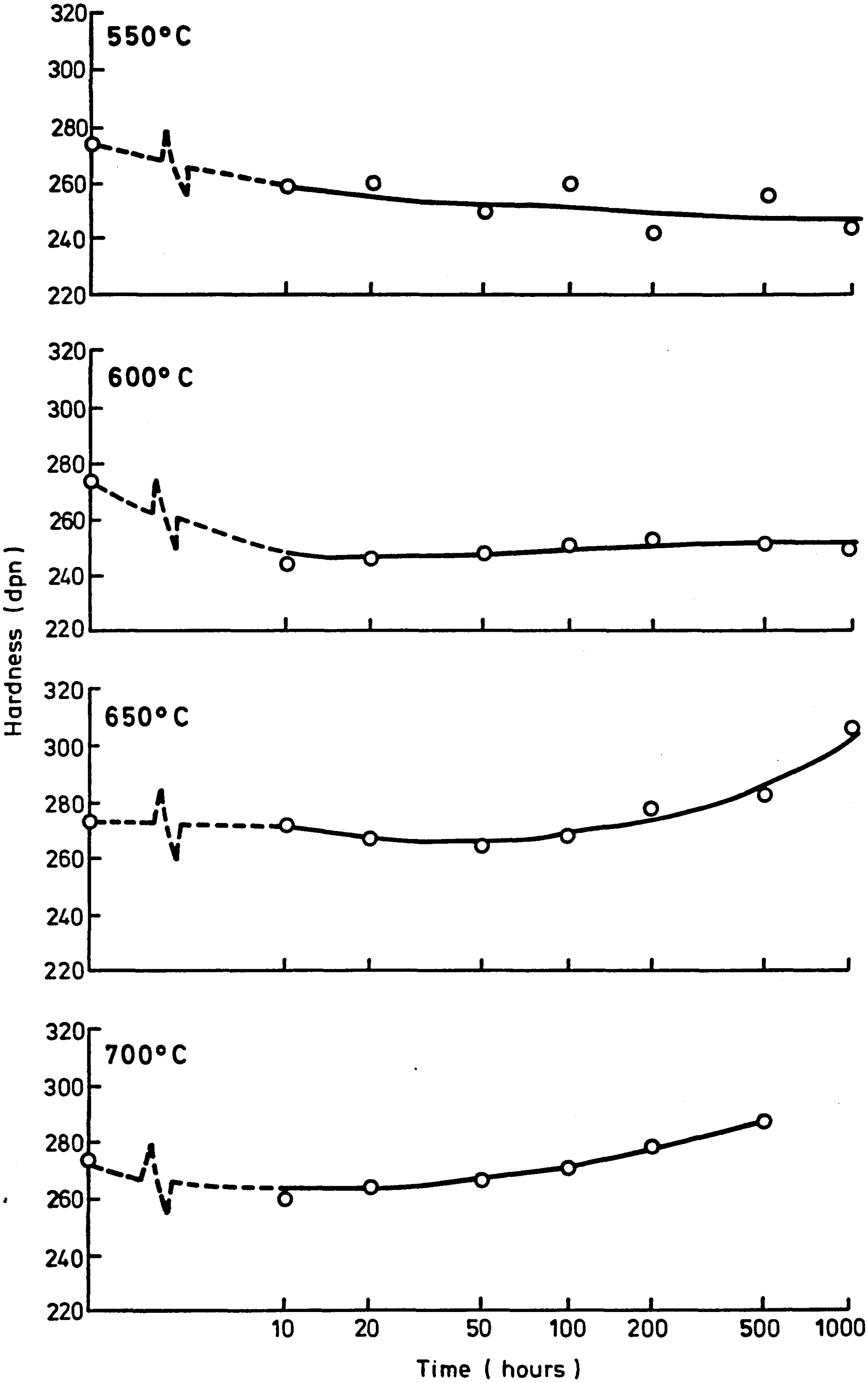
550°C
600°C
650°C
700°C
320
300
280
260
240
220
Hardness (dpn)
10
20
50
100
200
500
1000
Time (hours)

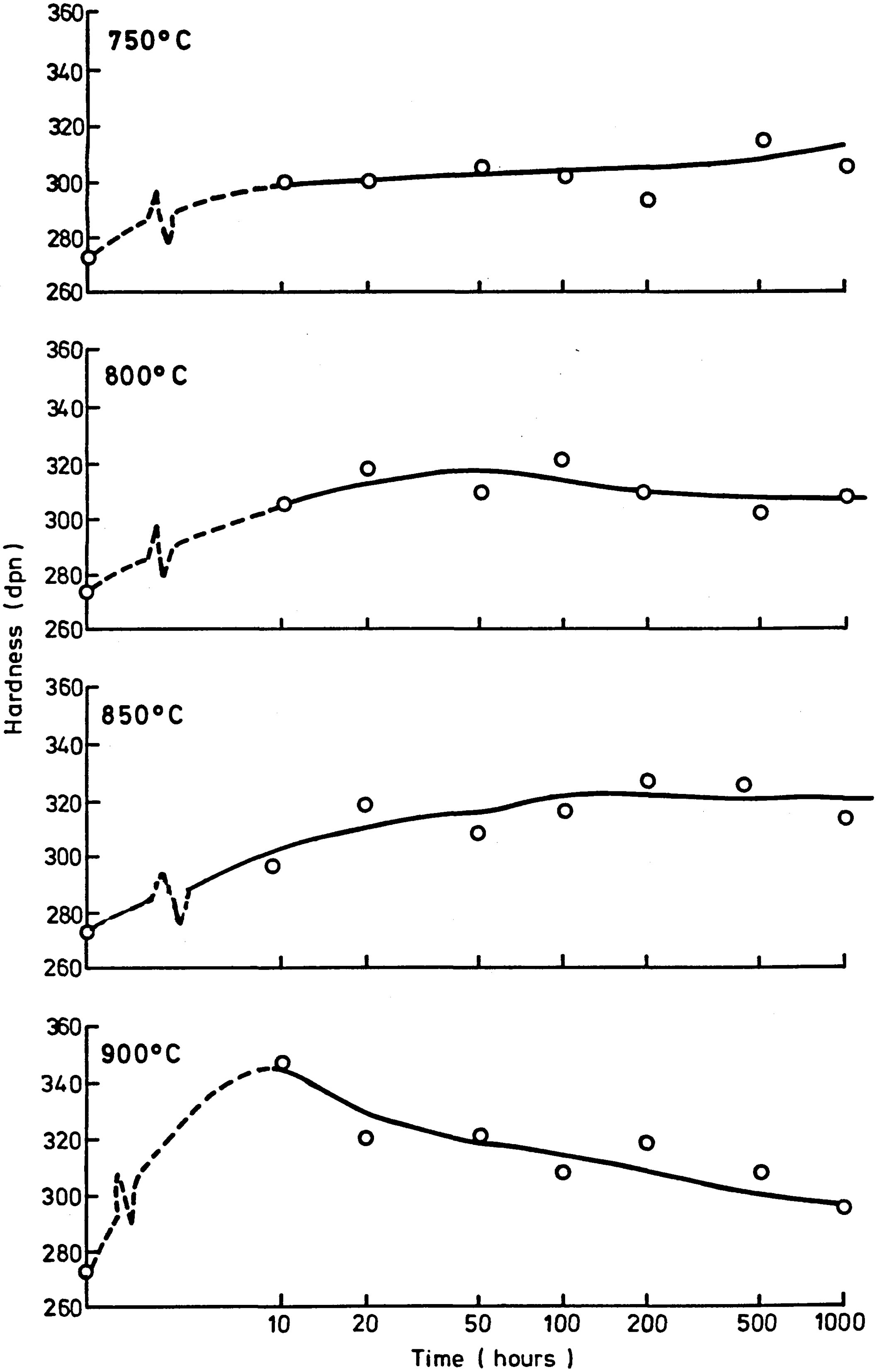

750° C
800° C
850° C
900° C
Hardness (dpn)
360
340
320
300
280
260
10
20
50
100
200
500
1000
Time (hours)

Figure 37. Transmission electron micrographs of alloy E(18Cr,7Ni), solution treated at 1050°C for 0.5 hours then aged at the following temperatures and times:-

(a) 500°C for 10 hours.

(b) 500°C for 1000 hours.

(c) 600°C for 1000 hours.

Delta ferrite was present as large islands within the matrix. The hardness of alloy E was observed to decrease with increasing ageing time as progressive tempering of the martensite phase took place.

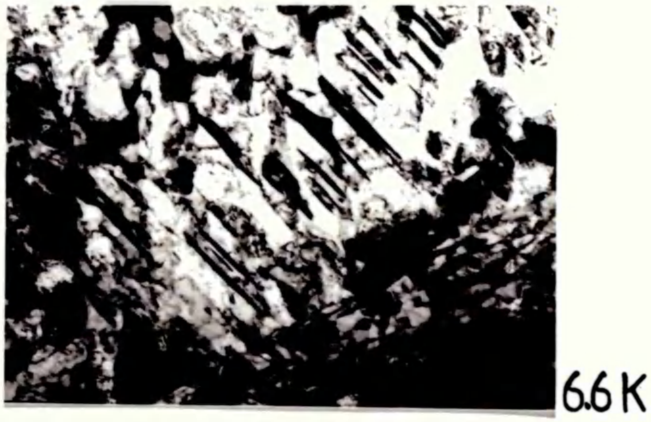

a

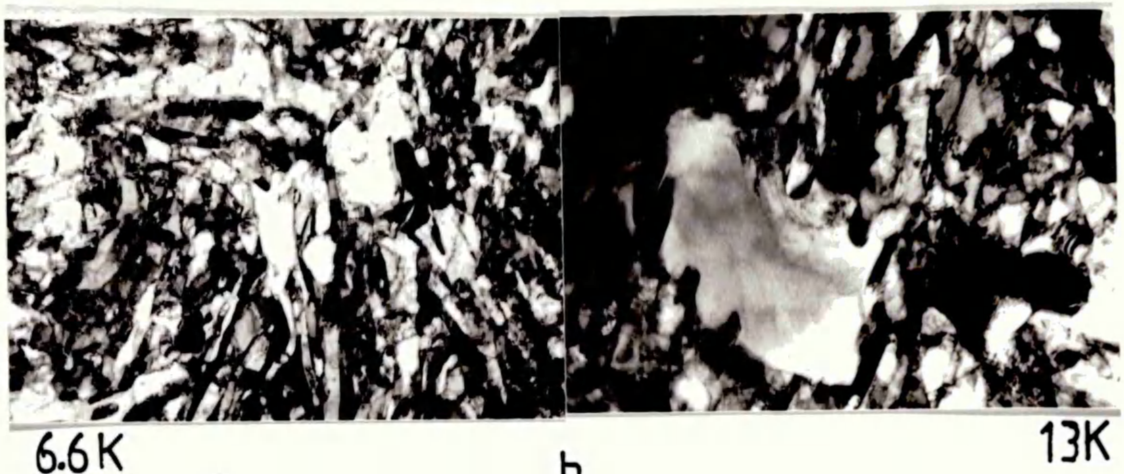

b

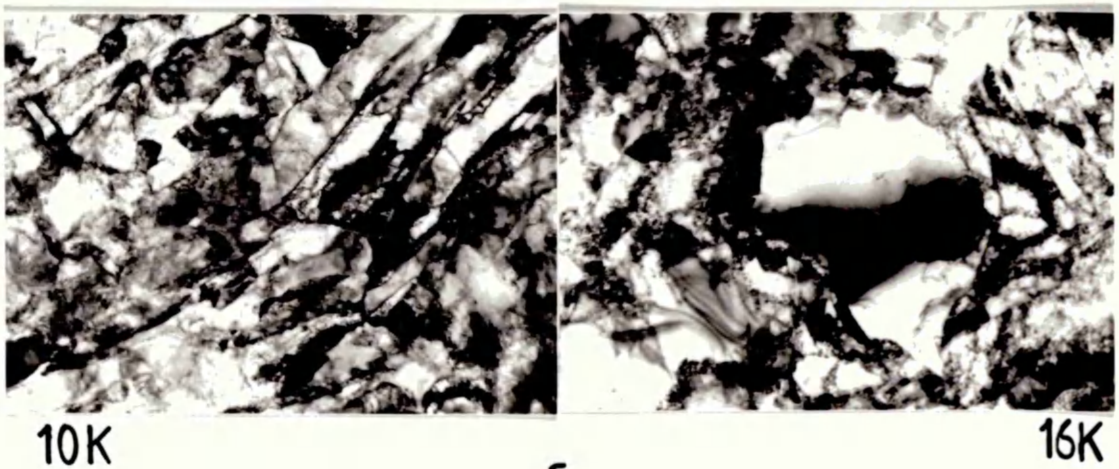

c

Figure 38. Transmission electron micrographs of alloy E(18Cr,7Ni) solution treated for 0.5 hours at 1050°C then aged at:-

(a) 750°C for 1000 hours

(b) 800°C for 1000 hours

An extremely fine distribution of $Cr_{23}C_6$ was observed in the matrix of alloy E at temperatures between 650°C-850°C.

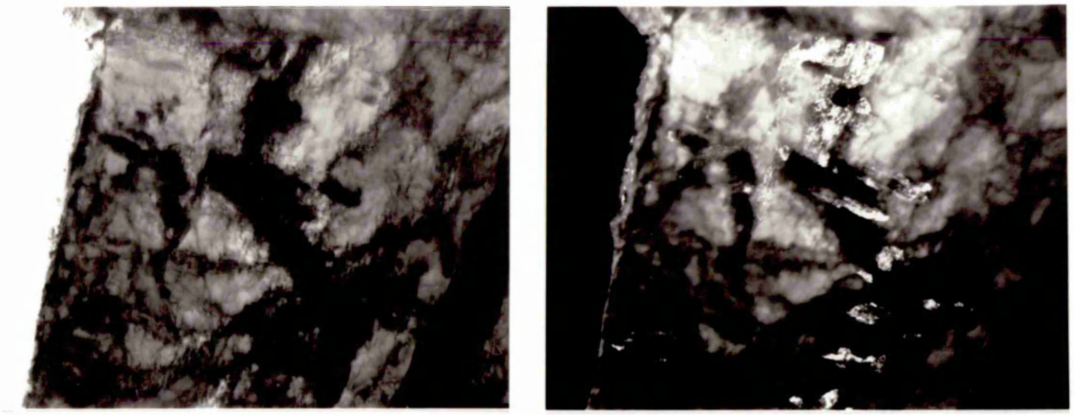

a

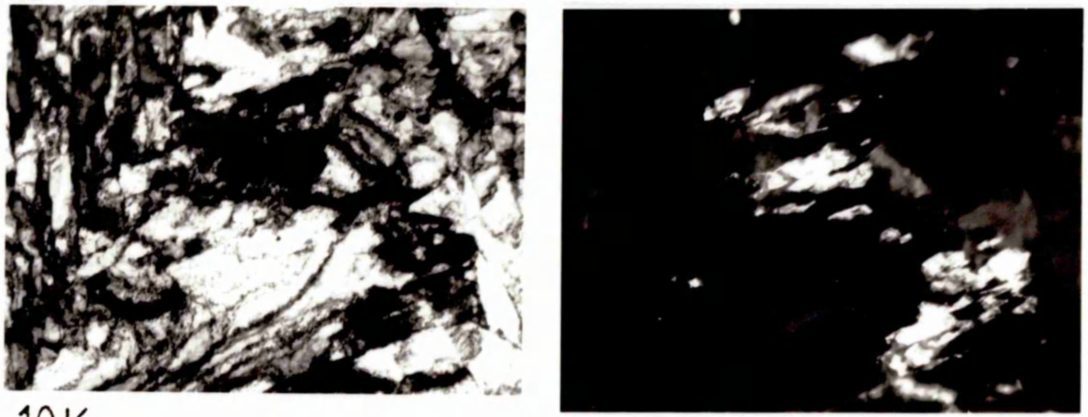

b

Figure 39. Optical micrographs at x200 of alloy E(18Cr,7Ni), solution treated at 1050°C for 0.5 hours then aged at 800°C for 10, 50, 100 and 1000 hours in total. Note the increasing amount of delta ferrite islands present in the matrix with increasing ageing time.

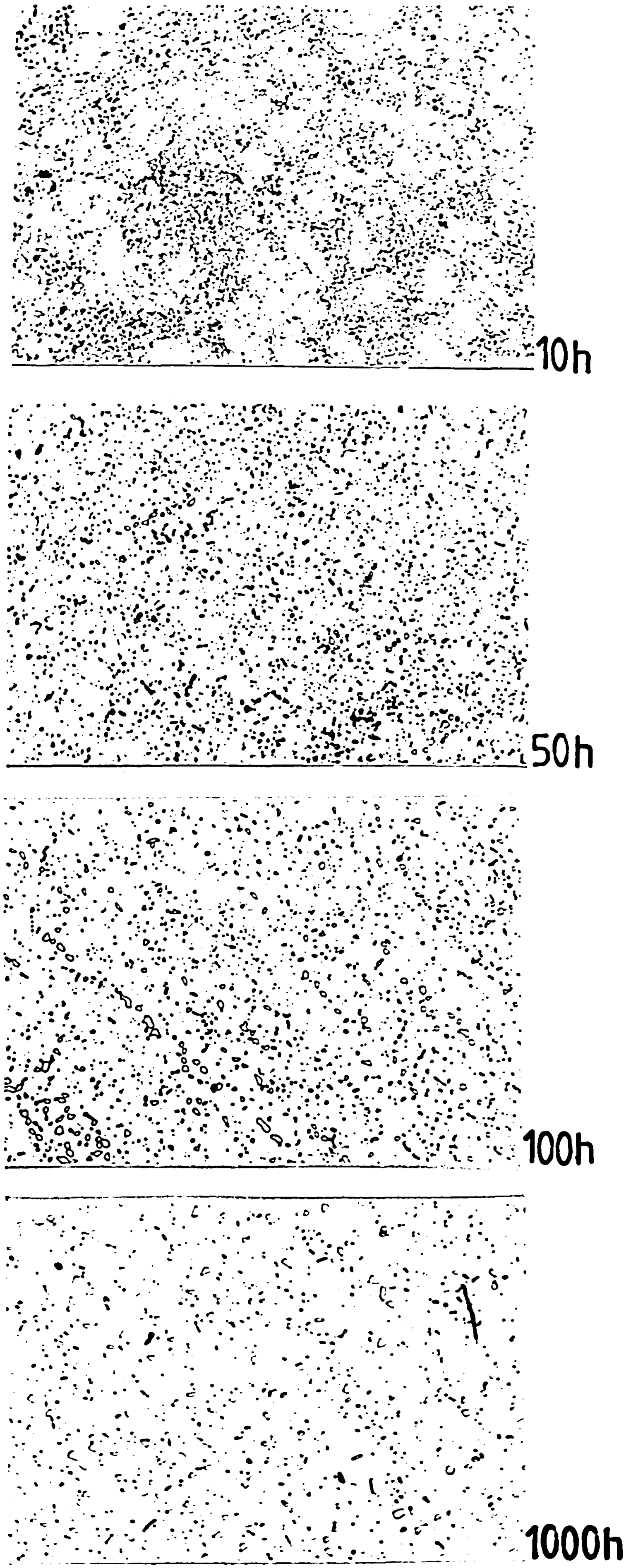
10h
50h
100h
1000h

Figure 40. Hardness versus time curves for alloy F(30Cr,13Ni), solution treated for 0.5 hours at 1050°C then aged at temperatures in the range 400°C-900°C for times of 10-1000 hours.

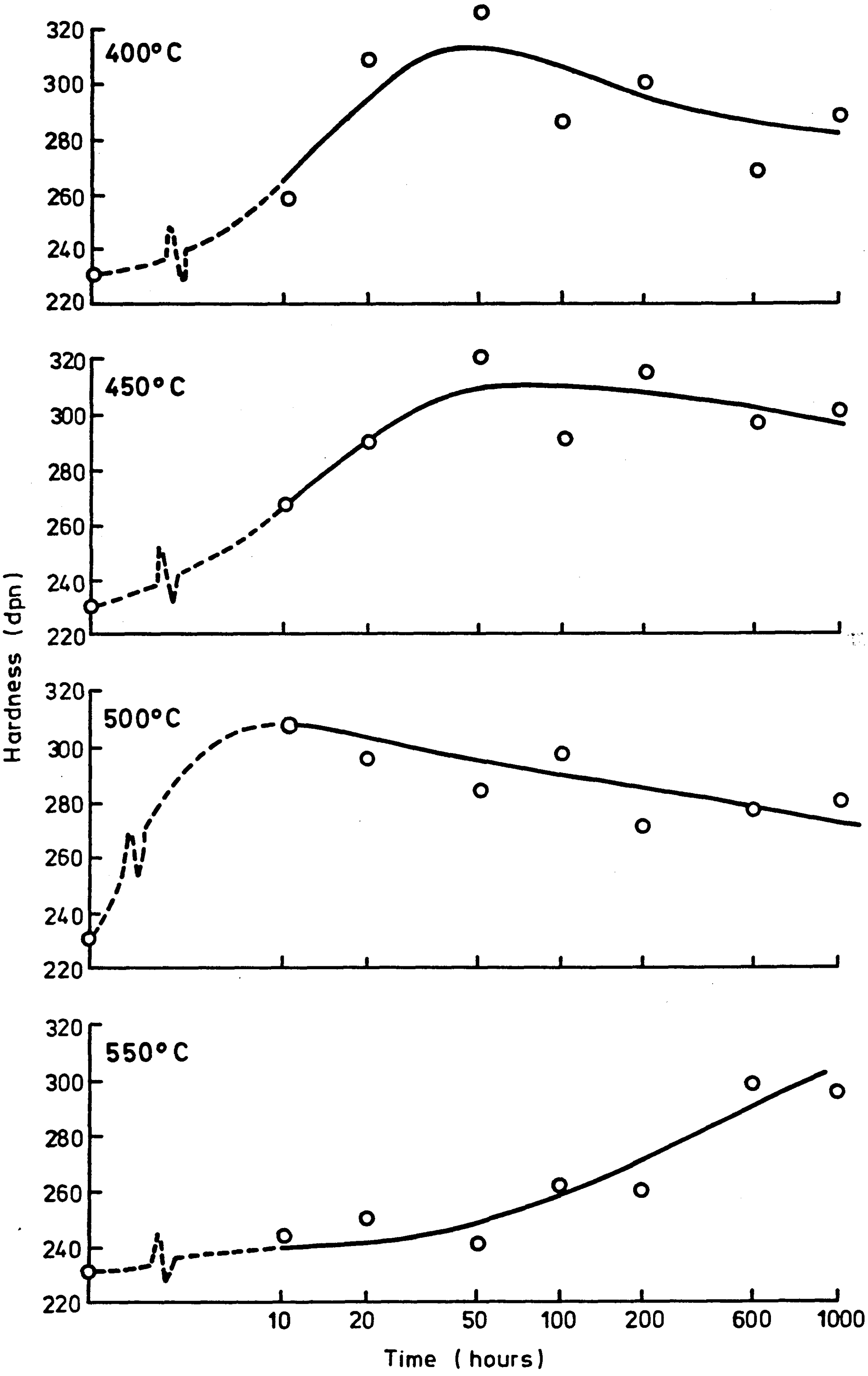
400°C
450°C
500°C
550°C
320
300
280
260
240
220
Hardness (dpn)
10
20
50
100
200
600
1000
Time (hours)

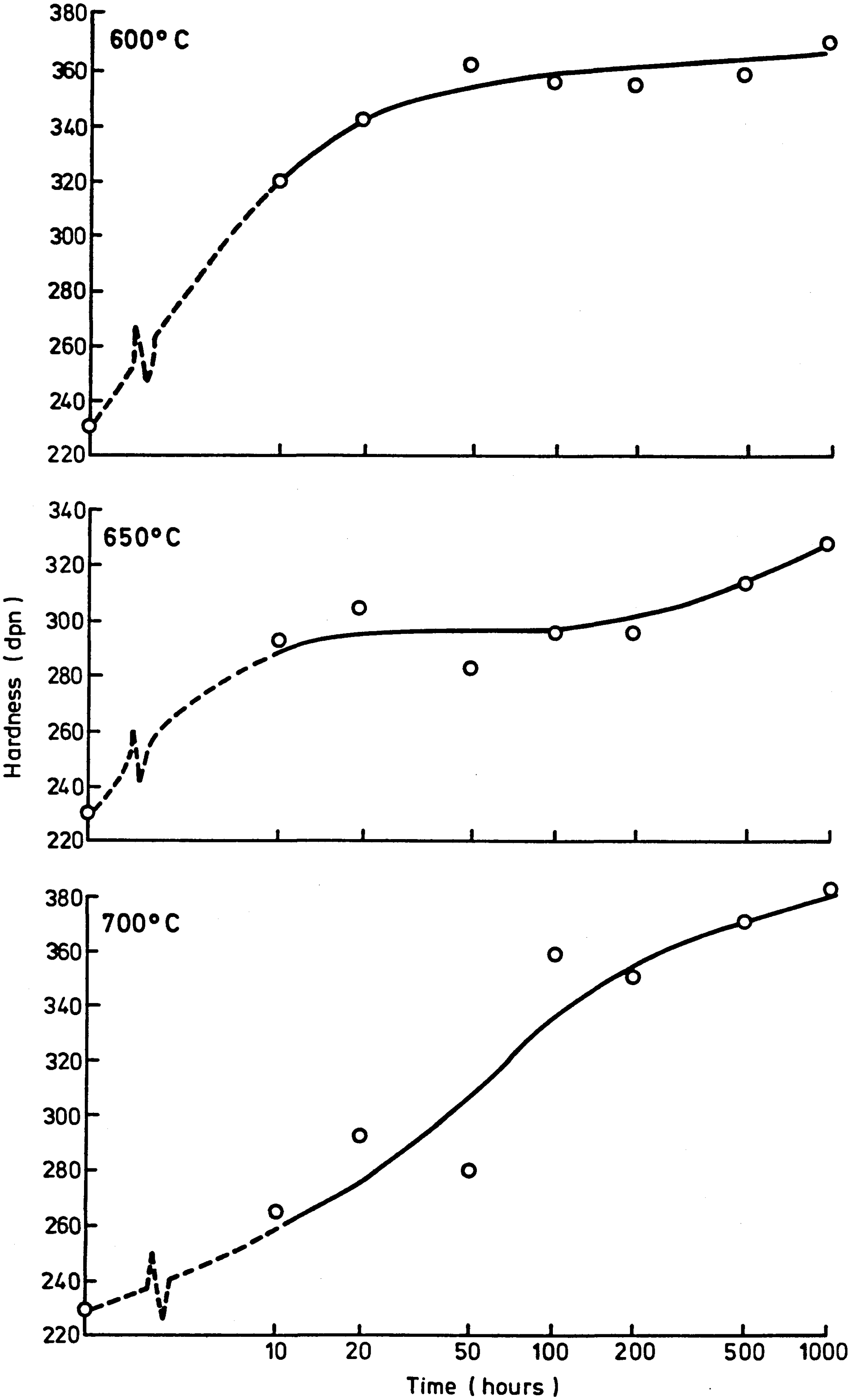
600° C
650° C
700° C
Hardness (dpn)
380
360
340
320
300
280
260
240
220
10
20
50
100
200
500
1000
Time (hours)

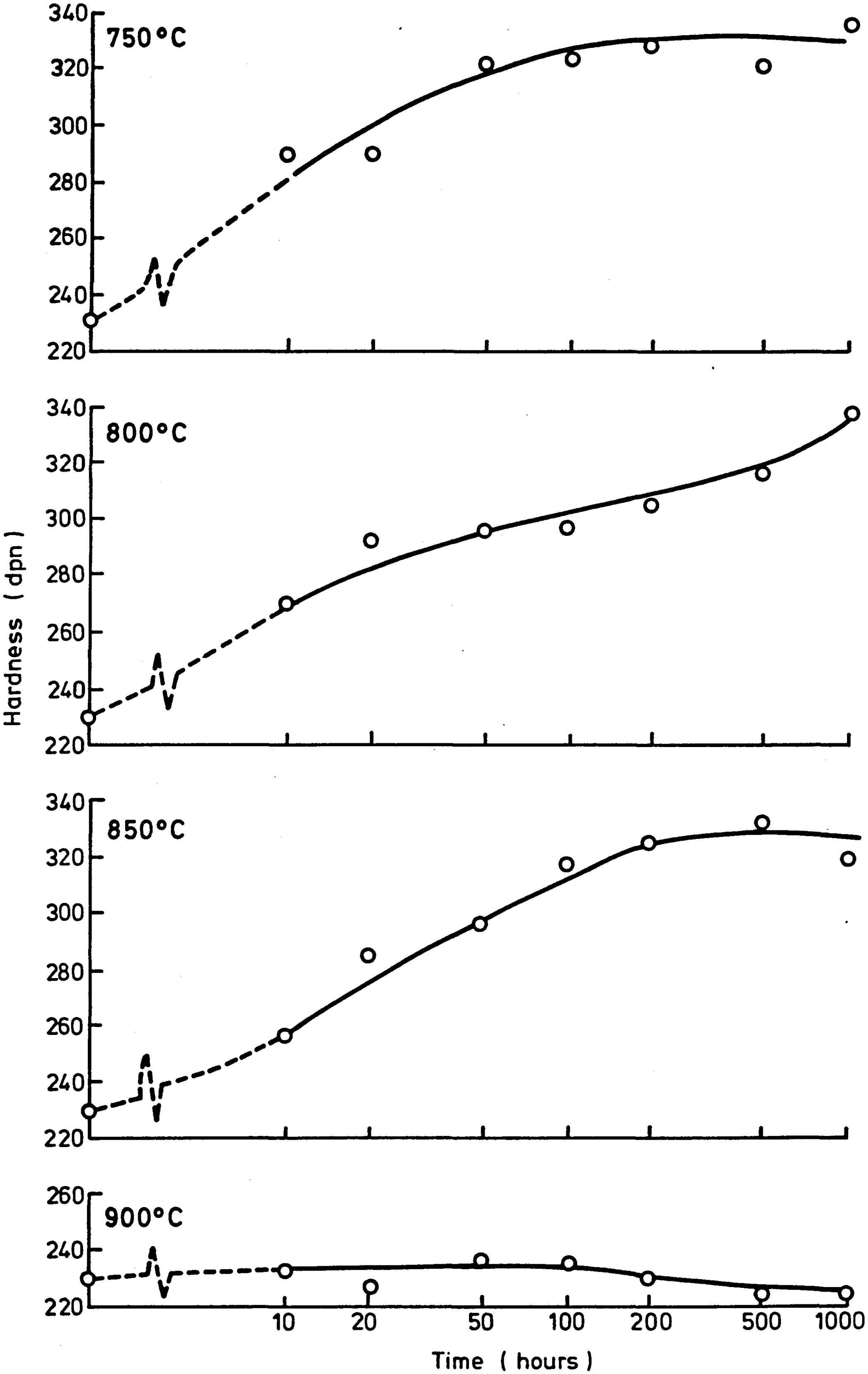
750°C
800°C
850°C
900°C
340
320
300
280
260
240
220
260
Hardness (dpn)
10
20
50
100
200
500
1000
Time (hours)

Figure 41. Transmission electron micrographs of alloy F(30Cr,13Ni), solution treated at 1050°C for 0.5 hours followed by ageing at 500°C:-

(a) shows the microstructure of alloy F after 10 hours at 500°C. Precipitates of $Cr_{23}C_6$ were observed on the grain boundaries with alpha prime precipitates finely distributed within the delta ferrite grains.

(b) shows alloy F after 1000 hours, the $Cr_{23}C_6$ precipitation was increased as was the size of the alpha prime precipitate.

(c) shows the rod like austenite that was also seen precipitating in the delta ferrite grains along with the alpha prime precipitate after ageing alloy F for 1000 hours at 500°C.

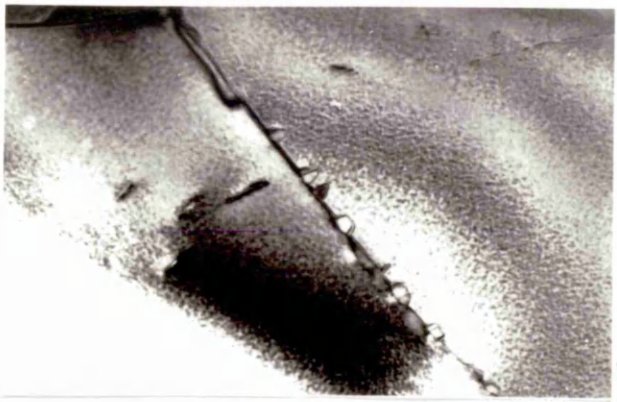

a

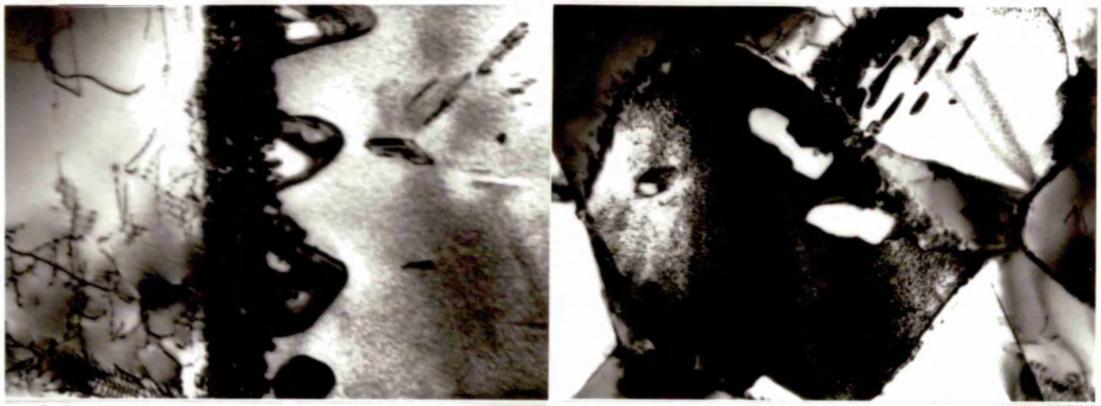

b

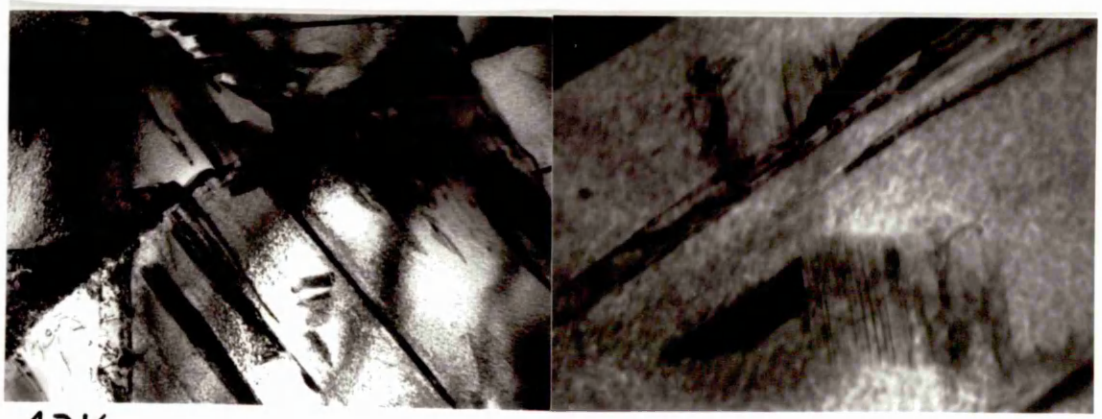

c

Figure 42. Optical micrographs at x480 of alloy F(30Cr,13Ni), solution treated at 1050°C for 0.5 hours followed by ageing at 700°C for 10, 50, 100 and 1000 hours.

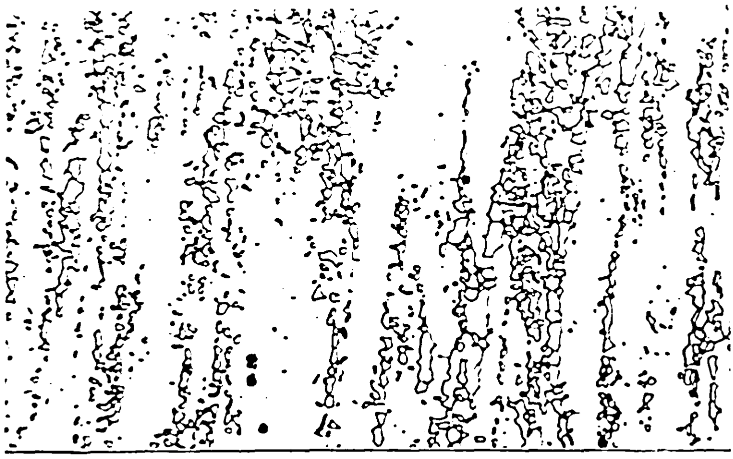

10h

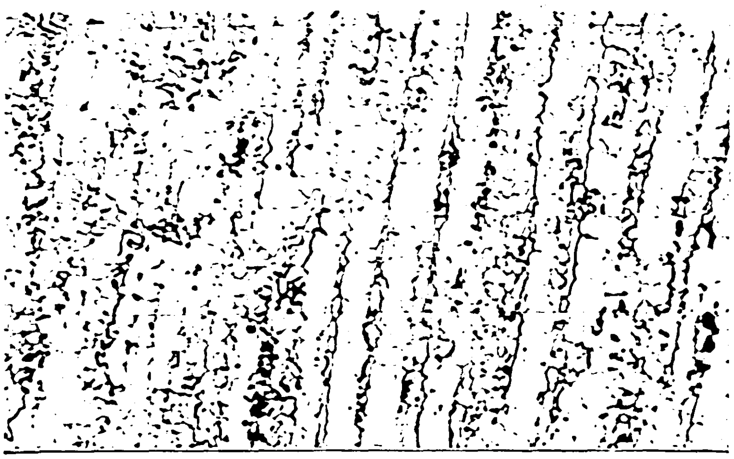

50h

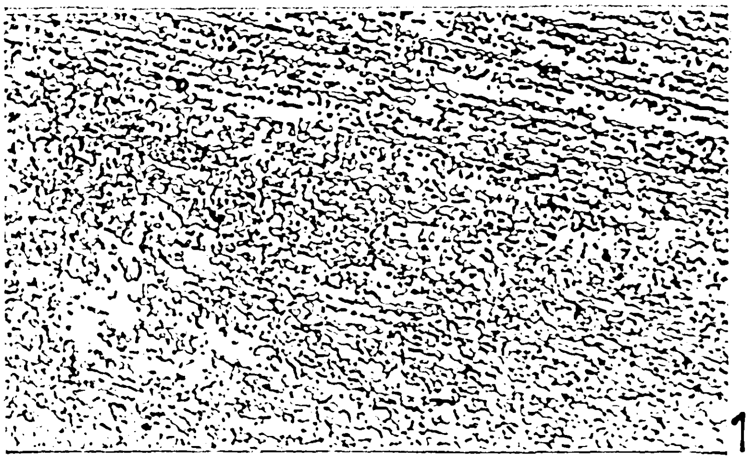

100h

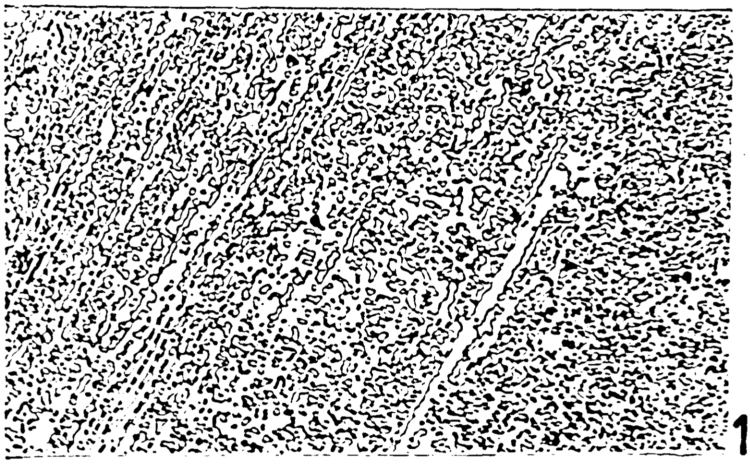

1000h

Figure 43. Transmission electron micrographs of alloy F(30Cr,13Ni), solution treated at 1050°C for 0.5 hours then aged under the following conditions:-

(a) shows alloy F after ageing at 400°C for 10 hours. The darkened grains are delta ferrite.

(b) ageing alloy F at 450°C for 10 hours produced alpha prime precipitation in the delta ferrite grains, along with a cellular precipitation of $Cr_{23}C_6$ on the grain boundaries. Note the alpha prime precipitates in the delta ferrite.

(c) after 1000 hours at 450°C the cellular precipitation of new austenite and $Cr_{23}C_6$ was observed consuming the delta ferrite grains.

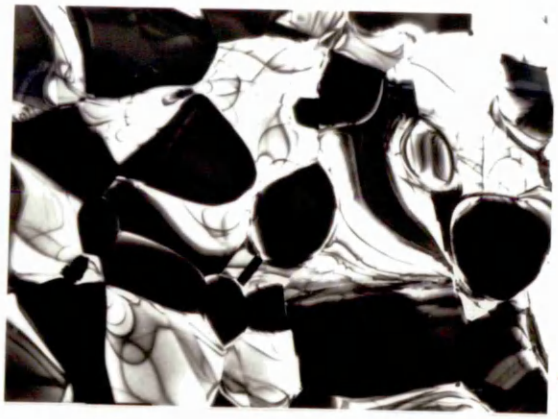

a

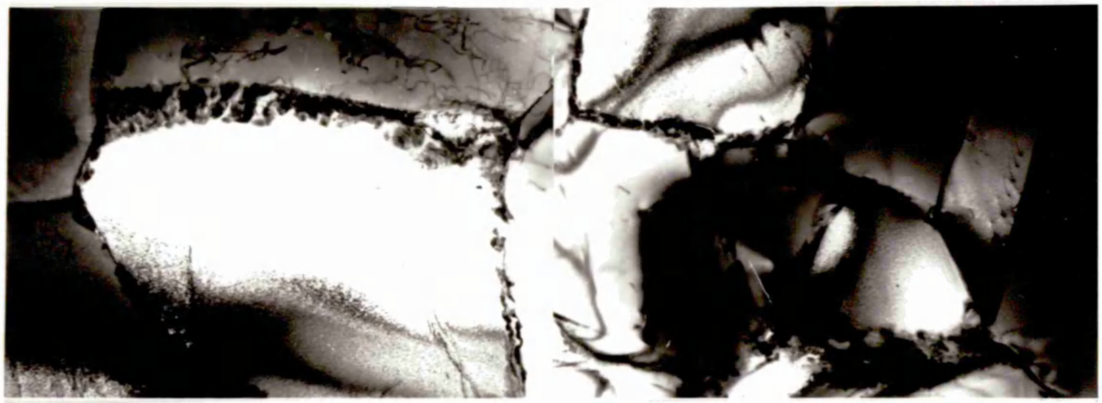

b

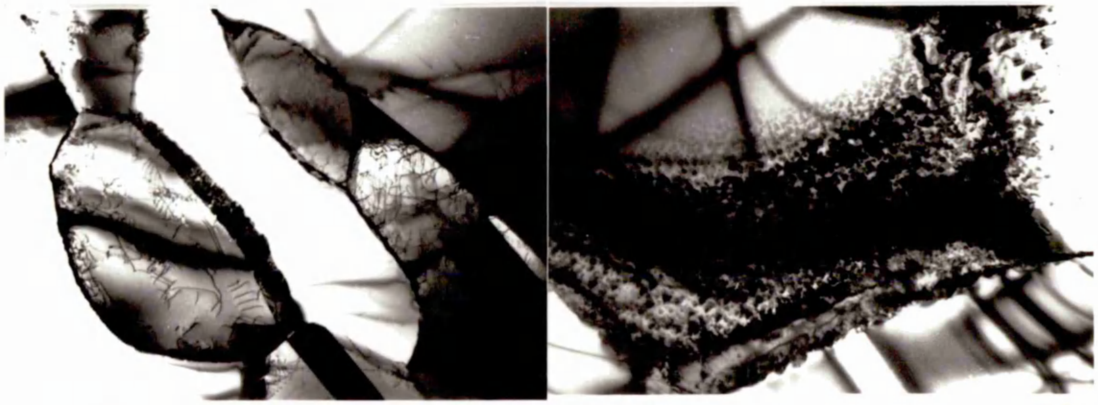

c

Figure 44. Transmission electron micrographs of alloy F(30Cr,13Ni) solution treated at 1050°C for 0.5 hours prior to ageing under the following conditions:-

(a) shows the microstructure of alloy F after ageing for 10 hours at 550°C. A cellular precipitation of $Cr_{23}C_6$ and new austenite was observed on the delta ferrite/austenite grain boundaries. Note the absence of the alpha prime precipitate; 550°C is above the observed maximum temperature for its precipitation.

(b) shows the transformation of the delta ferrite grains, present in alloy F, to sigma phase and new austenite after ageing at 550°C for 200 hours. The transformation that was occurring in some of the delta ferrite grains was unresolvable, yet in some of the grains small pools of the new austenite were clearly observed in the sigma phase.

(c) clearly shows the sigma phase/new austenite transformation front proceeding through the delta ferrite grain in the 550°C, 200 hours aged alloy F. The high magnification micrograph highlights the inability to distinguish the two phases from each other when the transformation was in progress.

(d) shows a series of micrographs taken at a stage when the sigma phase and new austenite could be resolved in the 550°C, 200 hours aged alloy F, allowing electron diffraction of the phases to be carried out.

(i) shows the bright field image.
(ii) shows the dark field image using the sigma reflection.
(iii) shows the dark field image using the austenite reflection.

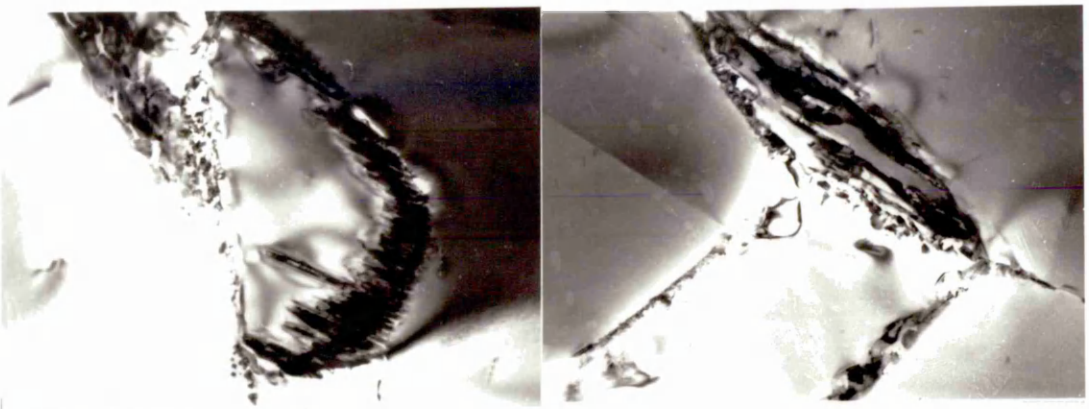

16 K a 20K

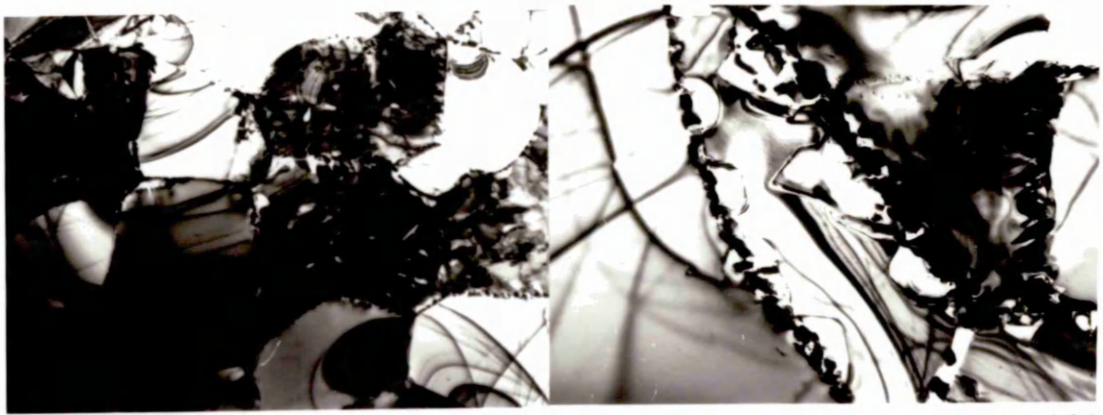

3.3 K 13K

b

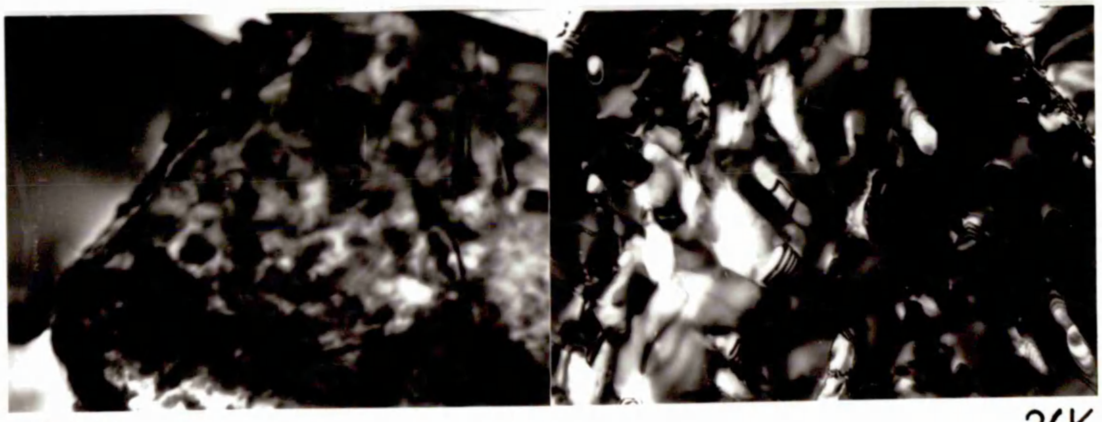

26 K 26K

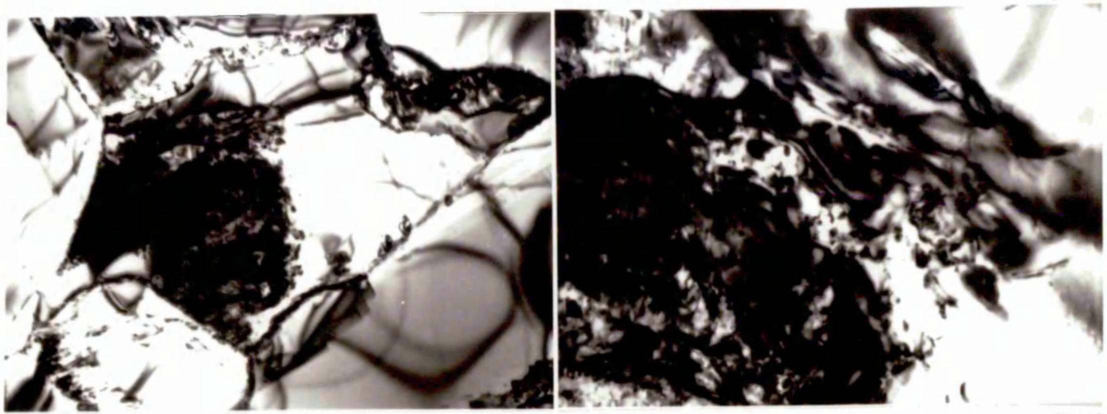

c

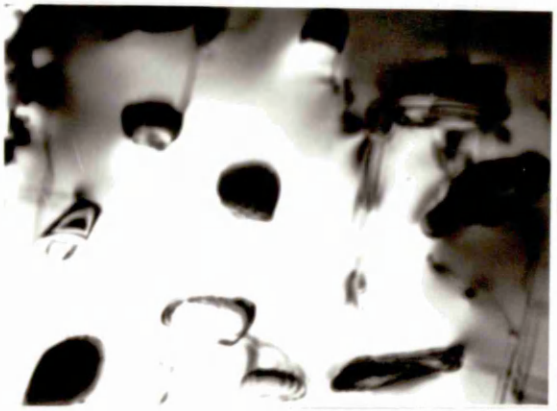

d(i)

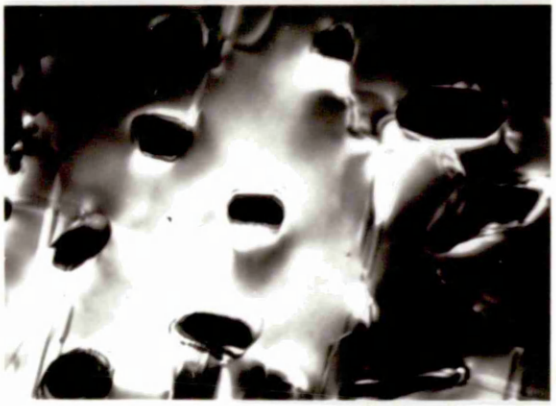

d(ii)

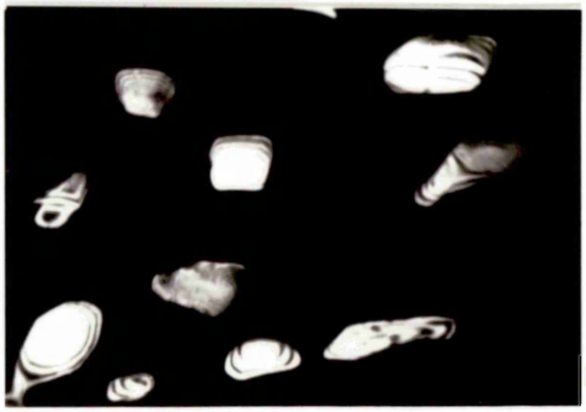

d(iii)

Figure 45. Transmission electron micrographs of alloy F(30Cr,13Ni) after solution treating at 1050°C for 0.5 hours followed by ageing at various temperatures and times. The microstructures produced all consisted of austenite plus sigma phase with some $Cr_{23}C_6$ decorating the grain boundaries.

(a) aged at 550°C for 1000 hours.

(b) aged at 650°C for 10 hours.

(c) aged at 700°C for 10 hours.

(d) aged at 800°C for 10 hours.

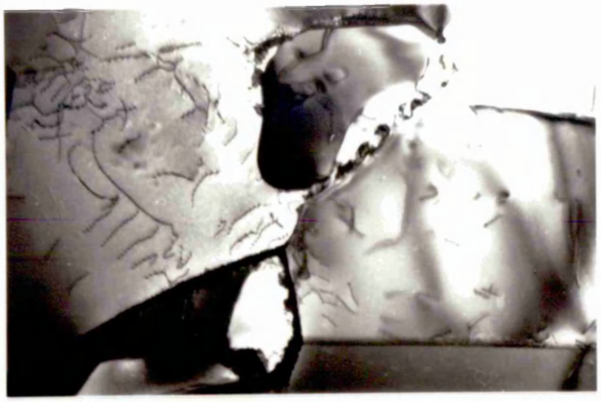
a

13K

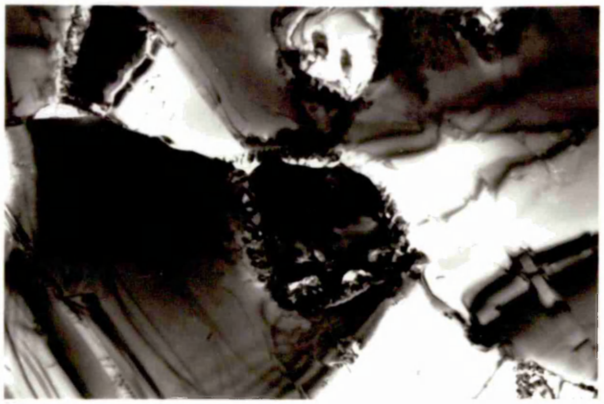
b

6.6K

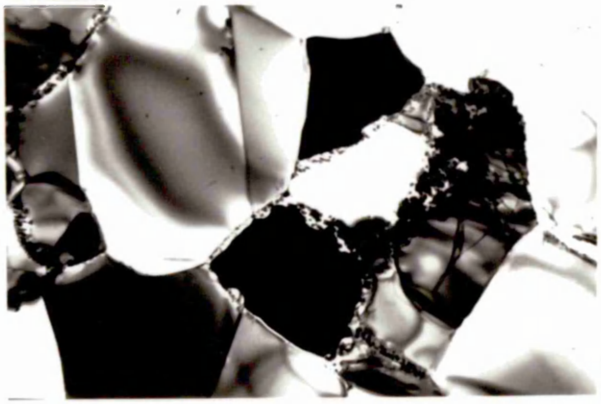
c

5K

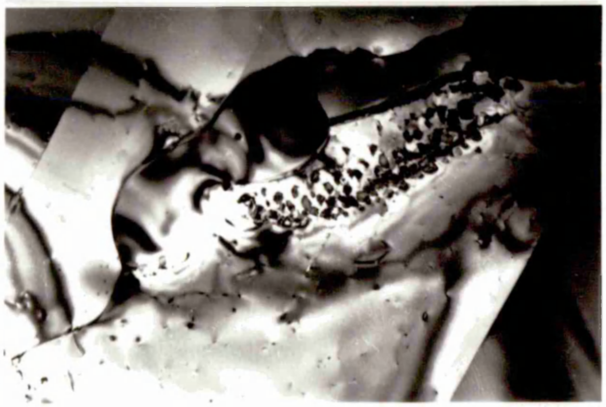
d

10K

Figure 46. Hardness versus time curves for the quaternary alloy 20Cr-23Ni-2Mo. Solution treated for 0.5 hours at 1050°C, then aged at 650°C, 750°C and 850°C for times of 10-1000 hours.

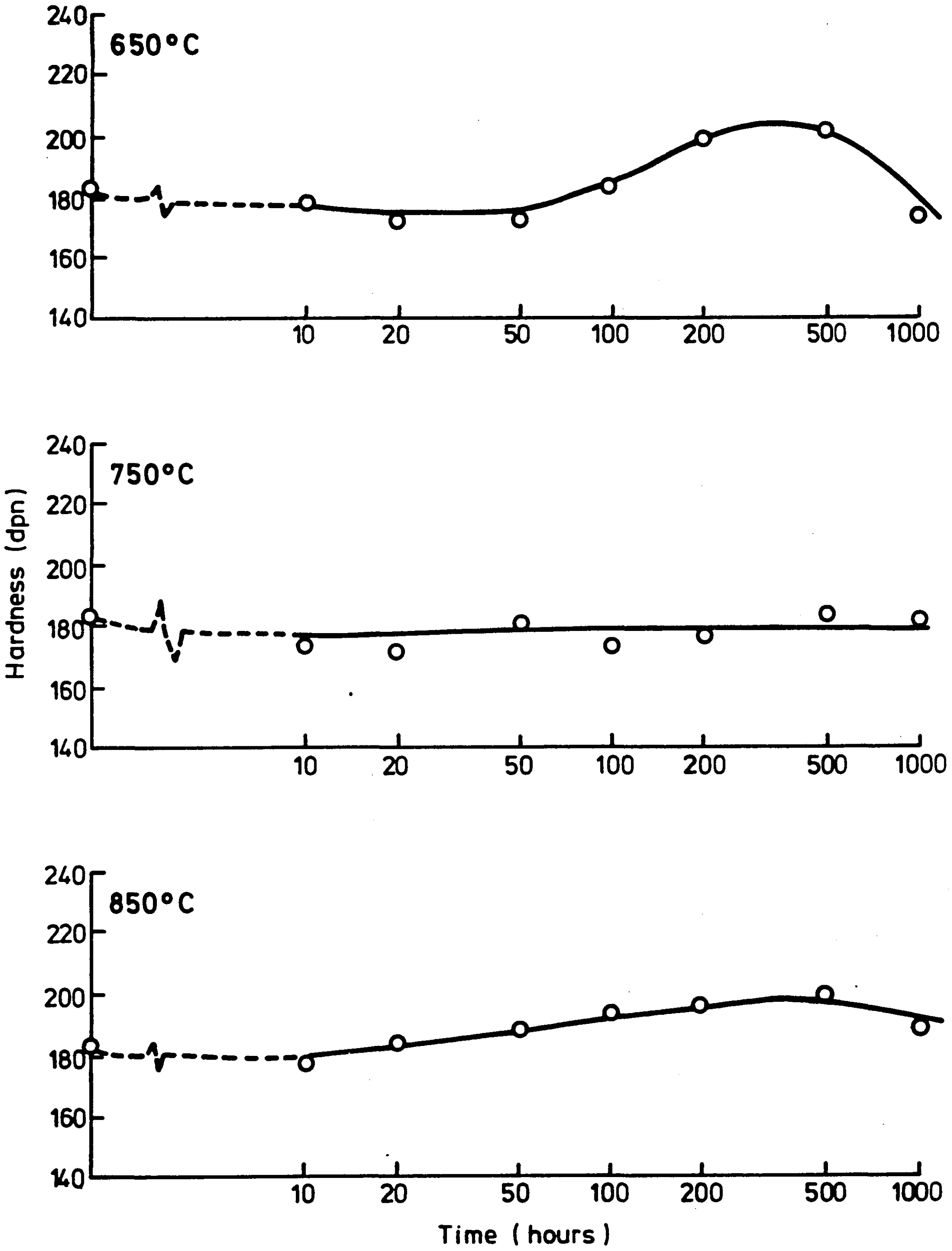
650°C
750°C
850°C
Hardness (dpn)
240
220
200
180
160
140
10
20
50
100
200
500
1000
Time (hours)

Figure 47. Optical micrographs, taken at x480, of the quaternary alloy 20Cr-23Ni-2Mo after solution treating at 1050°C for 0.5 hours then ageing at 750°C for 10, 50, 200 and 1000 hours

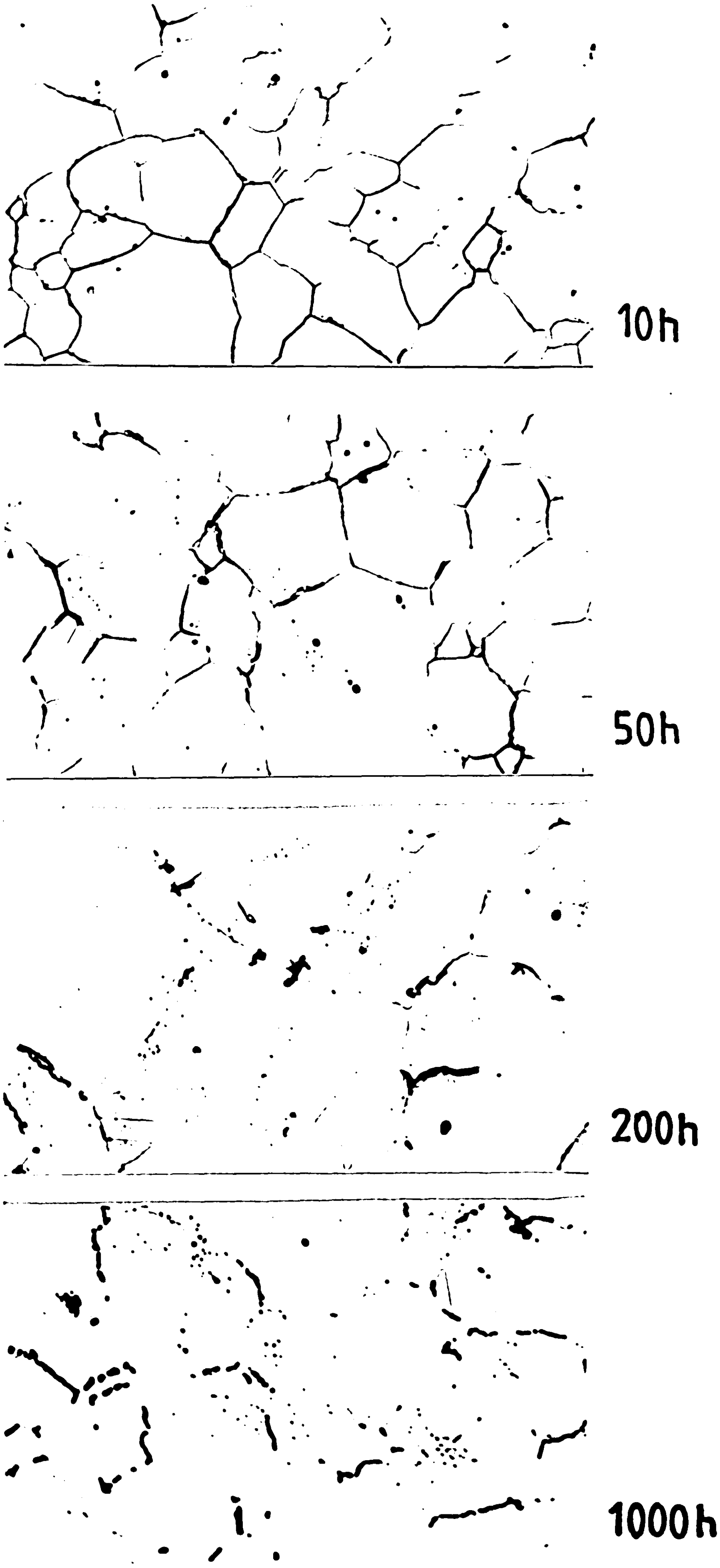
10h
50h
200h
1000h

Figure 48. Hardness versus time curves for the quaternary alloy 20Cr-23Ni-1Nb, which was solution treated at 1050°C for 0.5 hours prior to ageing at 650°C, 750°C and 850°C for 10-1000 hours.

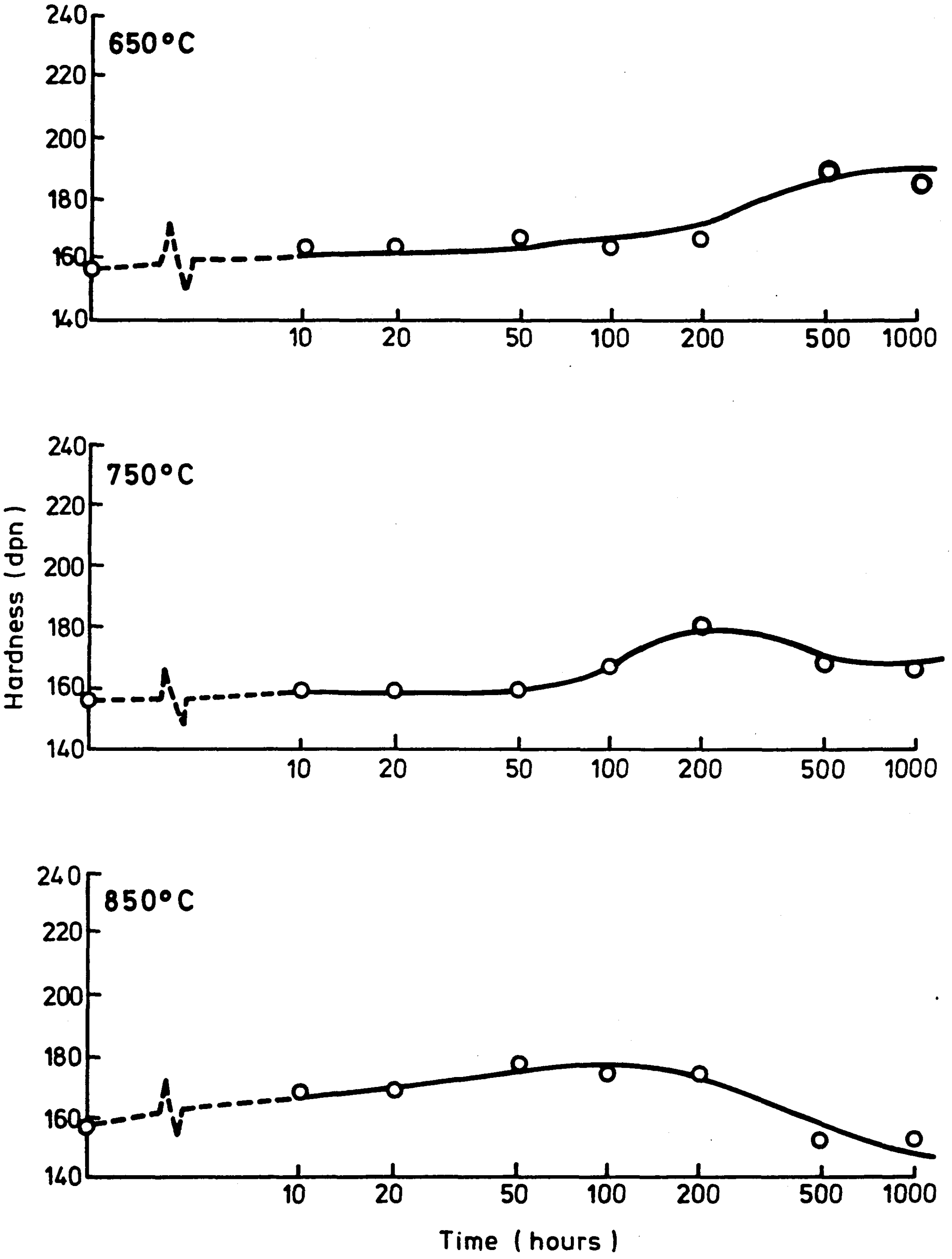
650°C
750°C
850°C
Hardness (dpn)
240
220
200
180
160
140
10
20
50
100
200
500
1000
Time (hours)

Figure 49. Optical micrographs, taken at x480, of the quaternary alloy 20Cr-23Ni-1Nb solution treated at 1050°C for 0.5 hours prior to ageing under the following conditions:-

(a) shows the 750°C aged microstructures obtained after 10, 200 and 1000 hours.

(b) shows the 850°C aged microstructure after 10, 200 and 1000 hours.

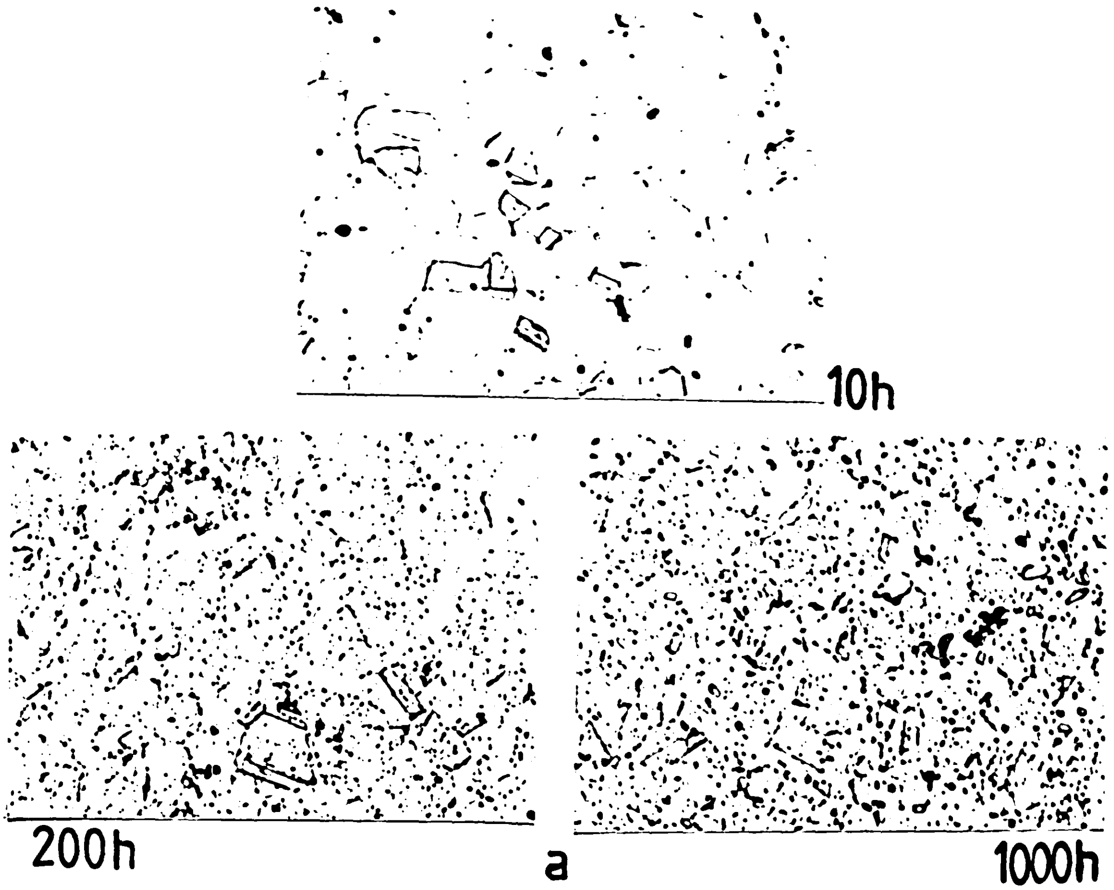
10h
200h
1000h

a

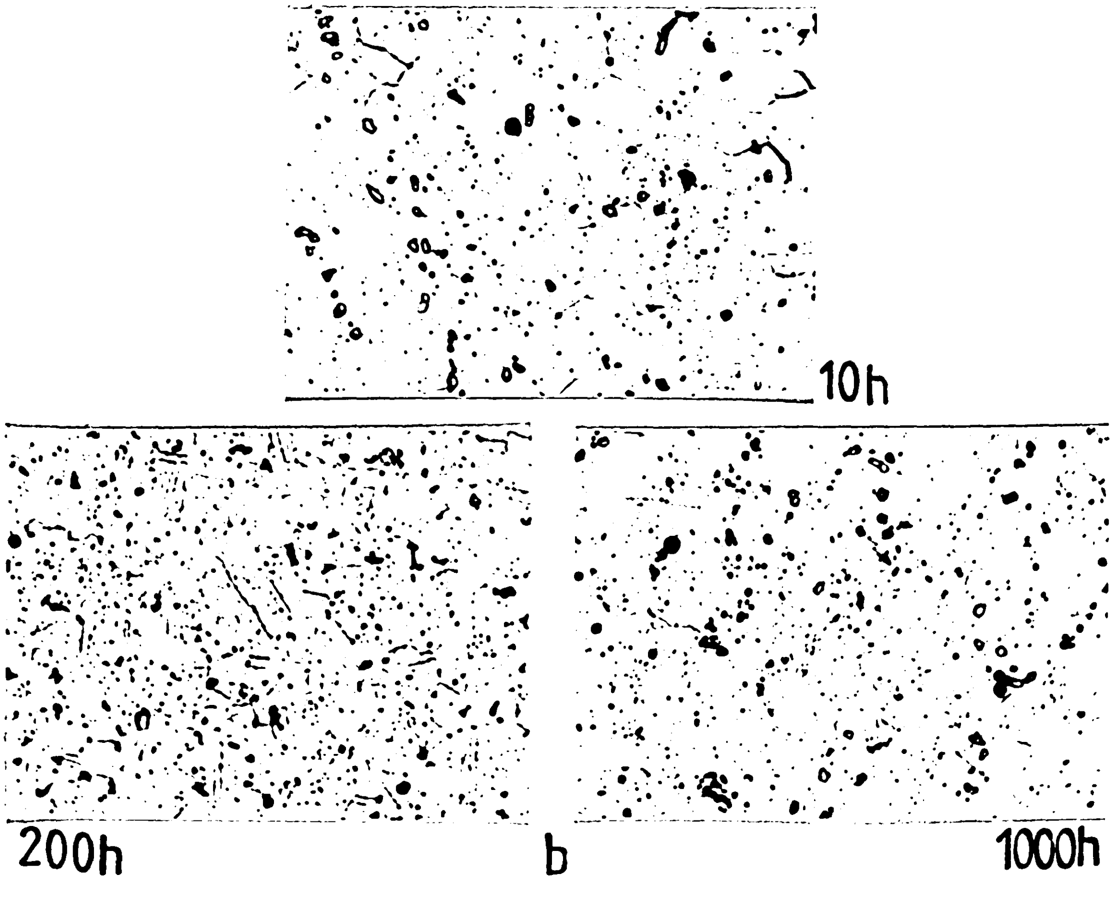
10h
200h
1000h

b

Figure 50. Transmission electron micrographs of the quaternary alloy 20Cr-23Ni-1Nb, after solution treating at 1050°C for 0.5 hours prior to ageing at:-

(a) 750°C for 1000 hours.

(b) 850°C for 1000 hours.

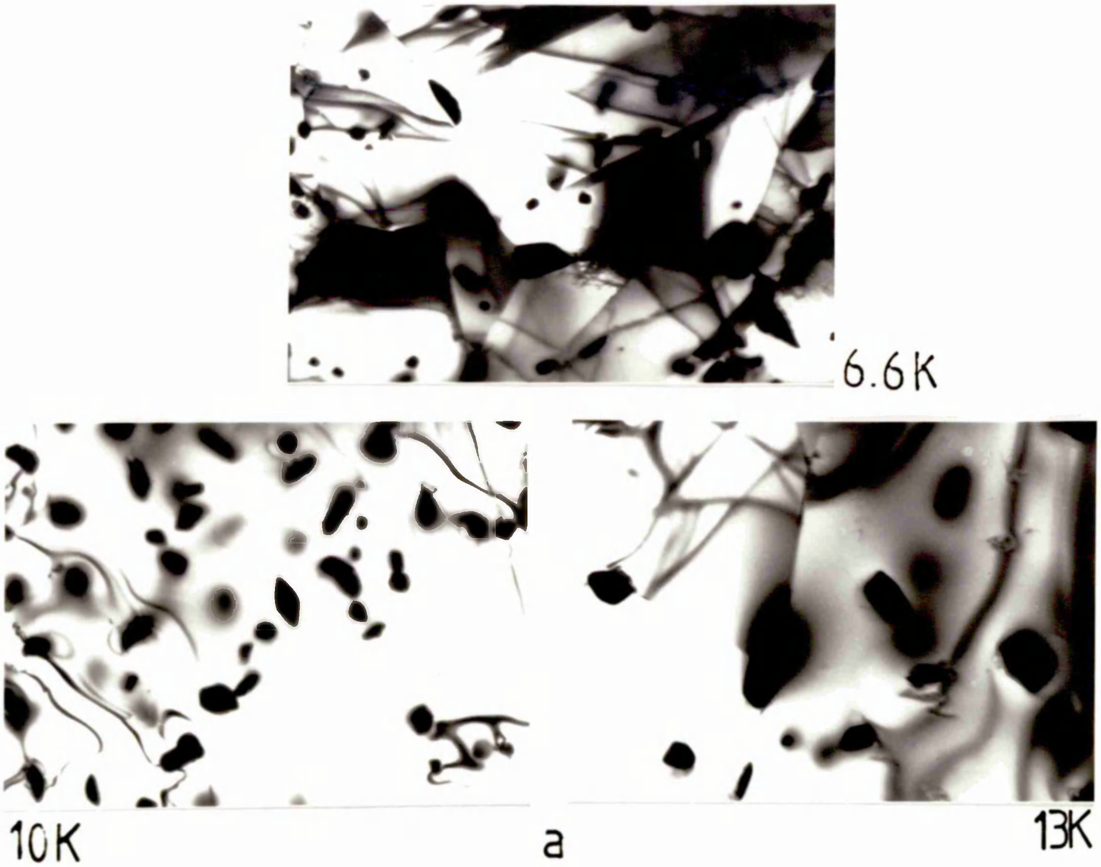

a

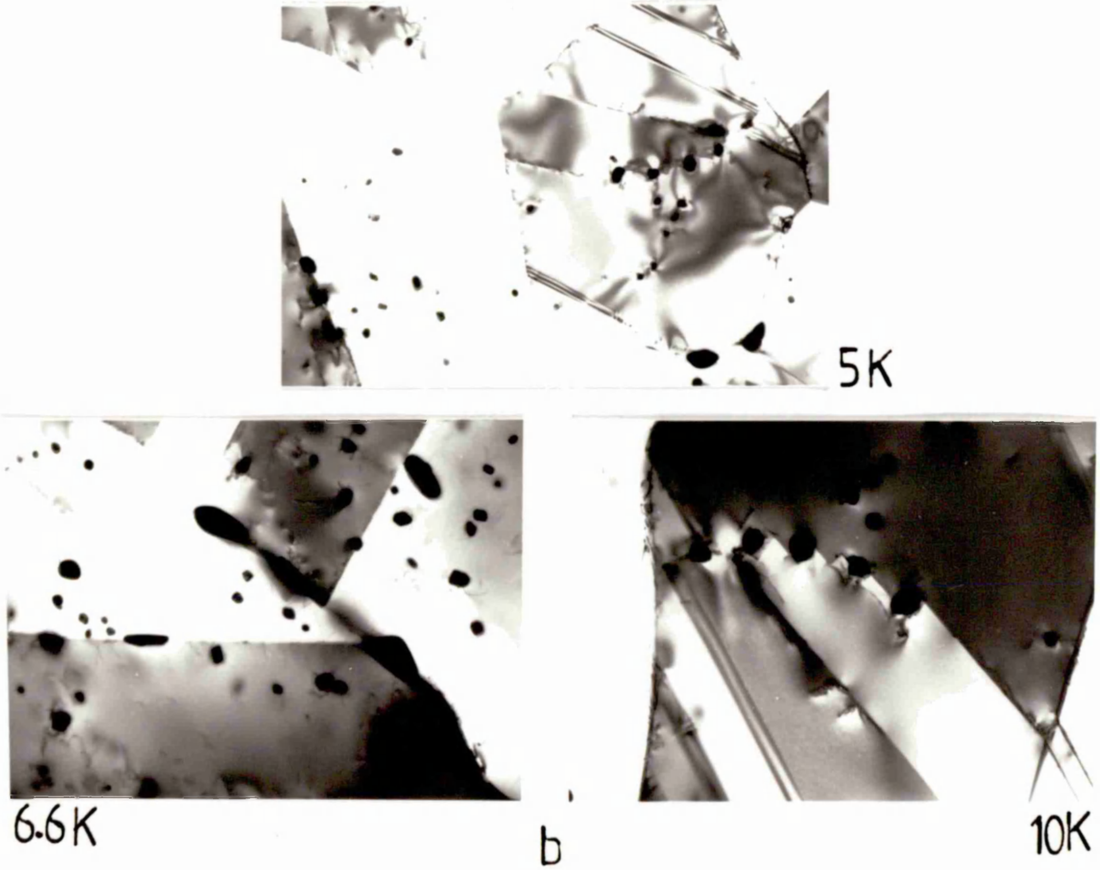

b

Figure 51. Hardness versus time curves for the quaternary alloy 20Cr-23Ni-0.25Ti, which was solution treated at 1050°C for 0.5 hours prior to ageing at 650°C, 750°C and 850°C for times of 10-10000 hours.

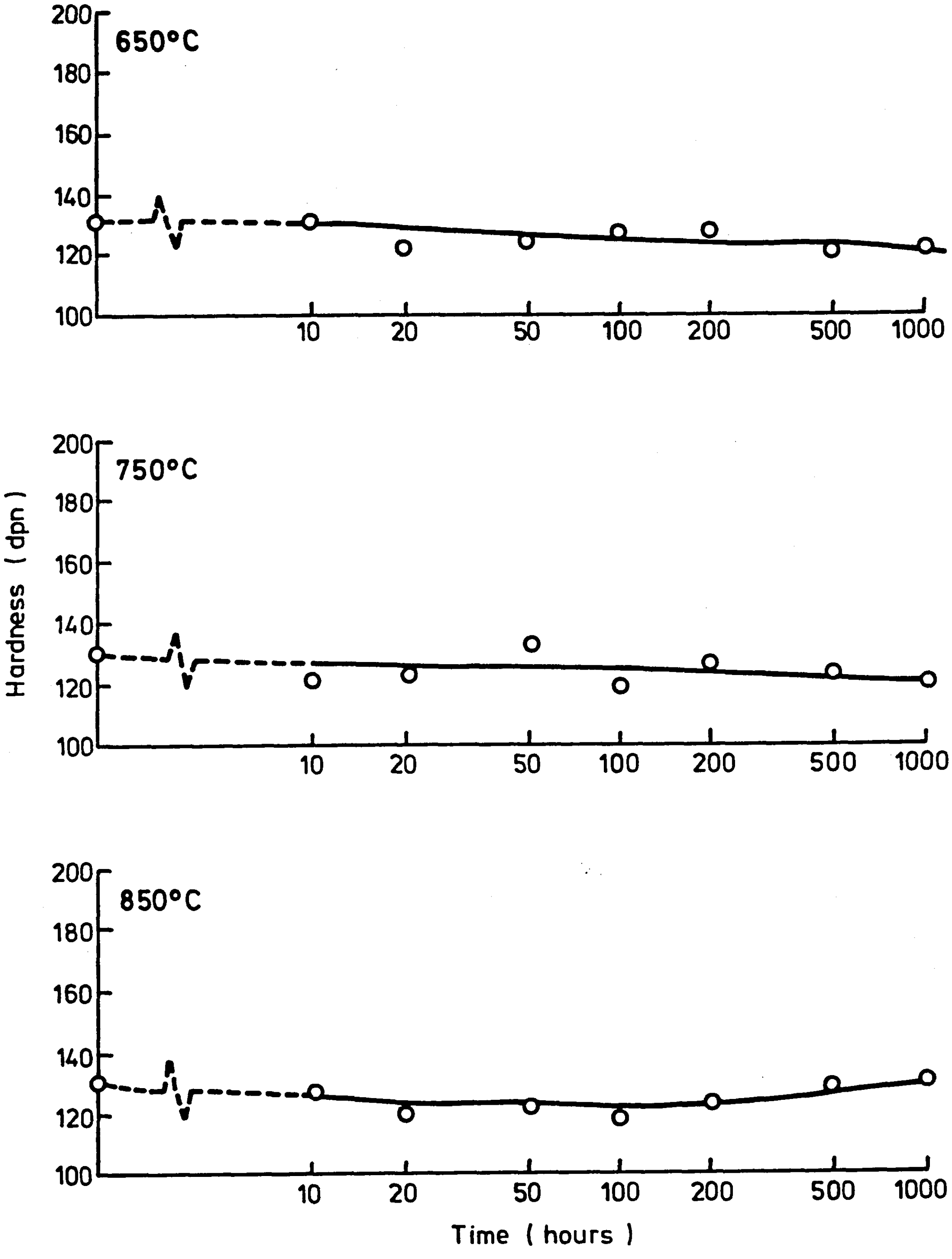
650°C
750°C
850°C
Hardness (dpn)
200
180
160
140
120
100
10
20
50
100
200
500
1000
Time (hours)

Figure 52. Transmission electron micrographs of the quaternary alloy 20Cr-23Ni-0.25Ti, solution treated at 1050°C for 0.5 hours prior to ageing at 850°C for 1000 hours. The precipitate, TiC, was observed on the grain and twin boundaries in this alloy after ageing at 650°C and 750°C and was also observed precipitating on dislocations within the austenite matrix in the 850°C aged alloy.

Figure 53. Hardness versus time curves for the quaternary alloy 20Cr-23Ni-1Si, which was solution treated at 1050°C for 0.5 hours prior to ageing at 650°C, 750°C and 850°C for 10-1000 hours.

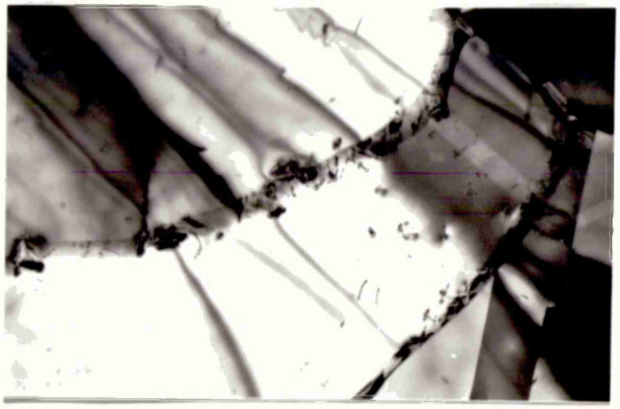

8.3K

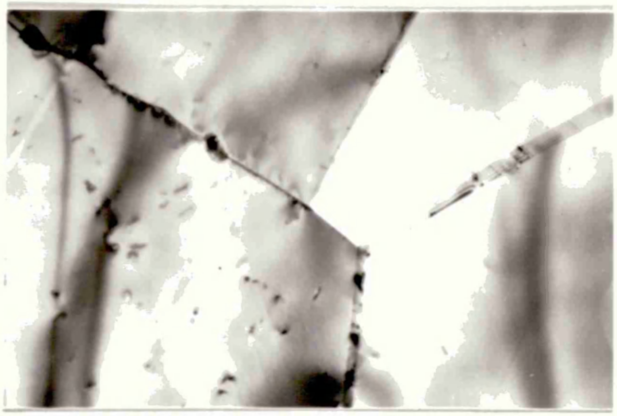

16K

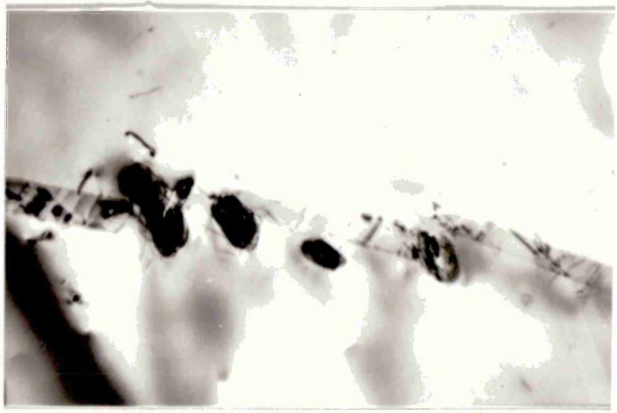

16K

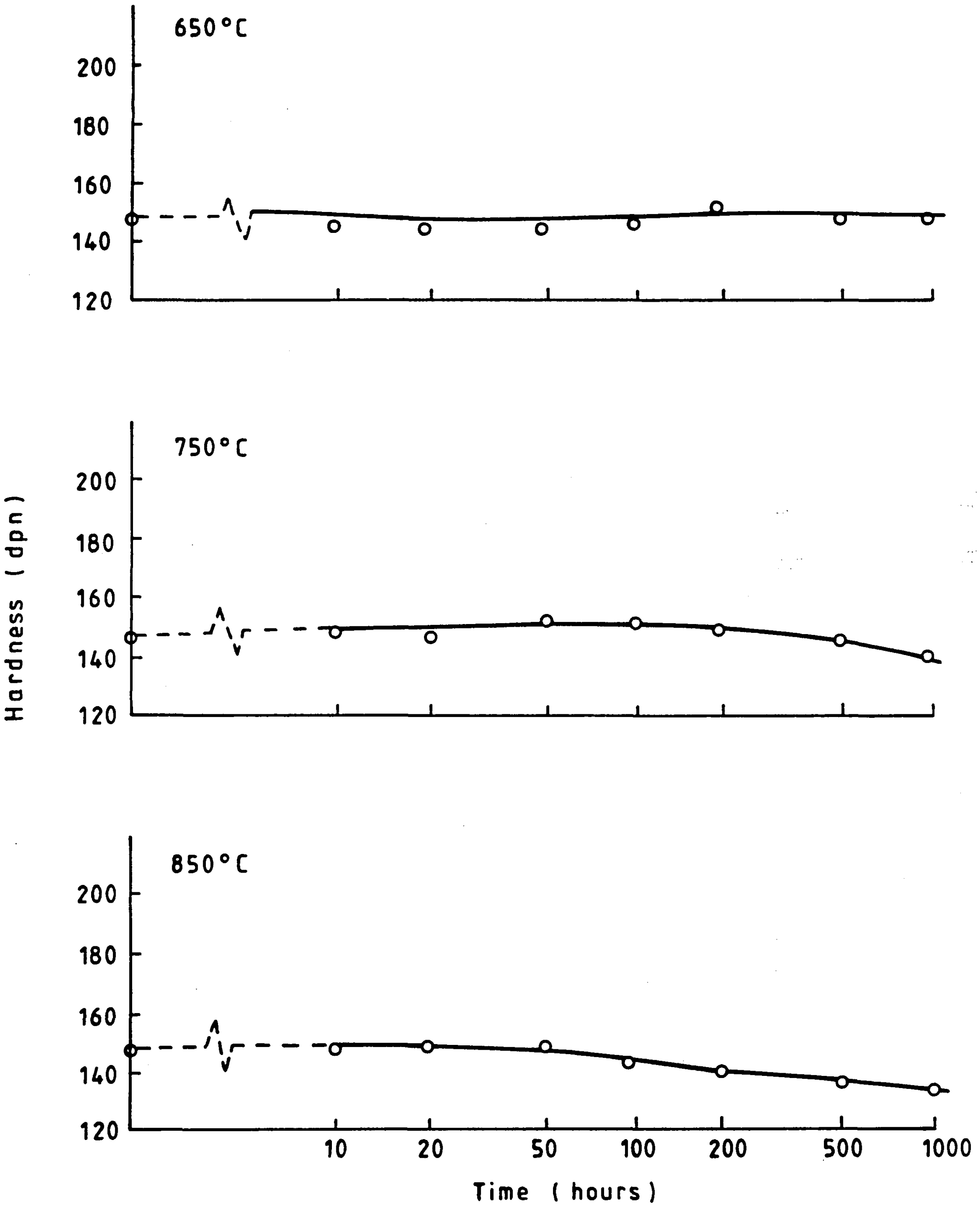

650°C
750°C
850°C
Hardness (dpn)
200
180
160
140
120
10
20
50
100
200
500
1000
Time (hours)

Figure 54. Optical micrographs, taken at x480, of the quaternary alloy 20Cr-23Ni-1Si. The 1%Si quaternary alloy was solution treated at 1050°C for 0.5 hours prior to ageing at 750°C for a total of 10, 50, 200 and 1000 hours.

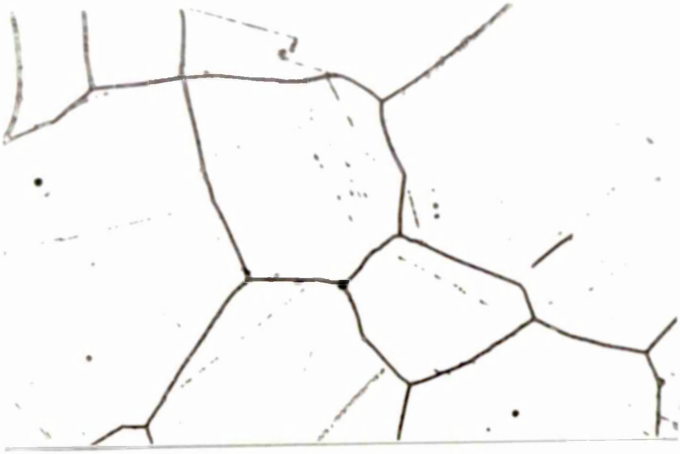

10h

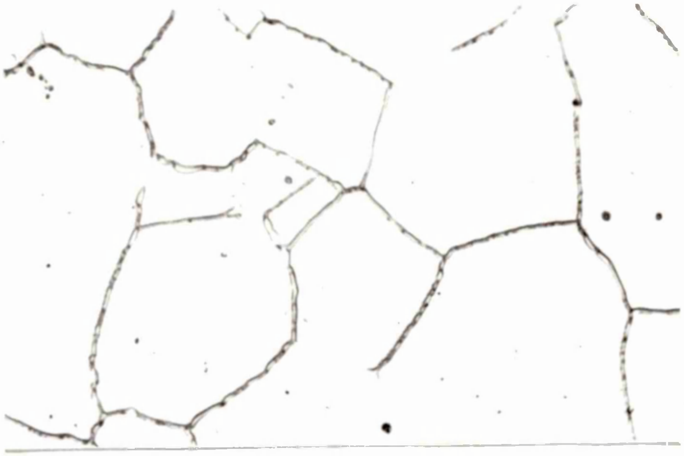

50h

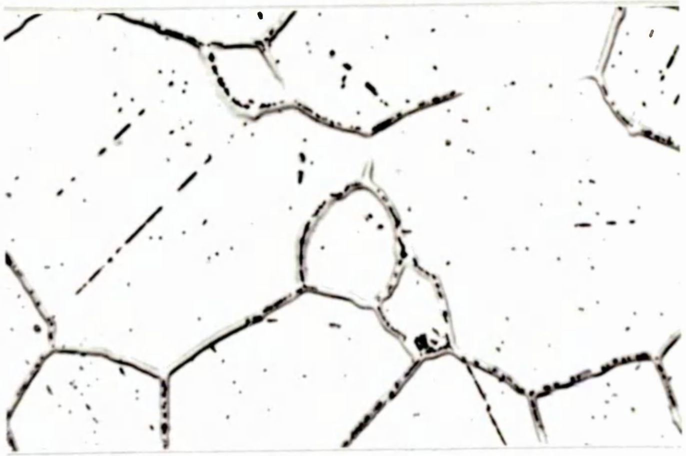

200h

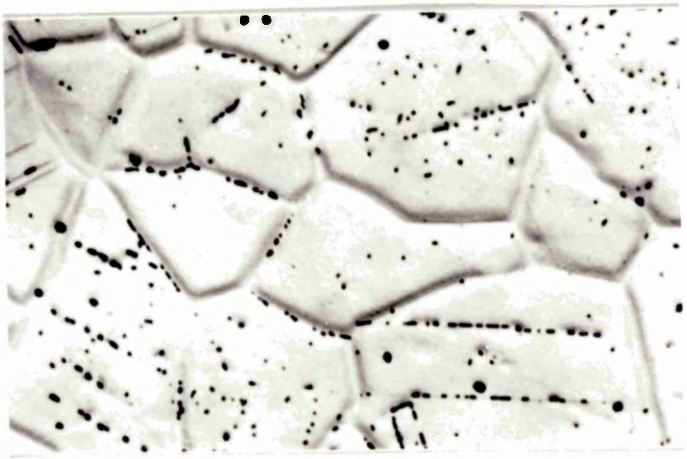

1000h

Figure 55. Hardness versus time curves for the quaternary alloy 20Cr-23Ni-2Si, which was solution treated at 1050°C for 0.5 hours prior to ageing at 650°C, 750°C and 850°C for times of 10-1000 hours.

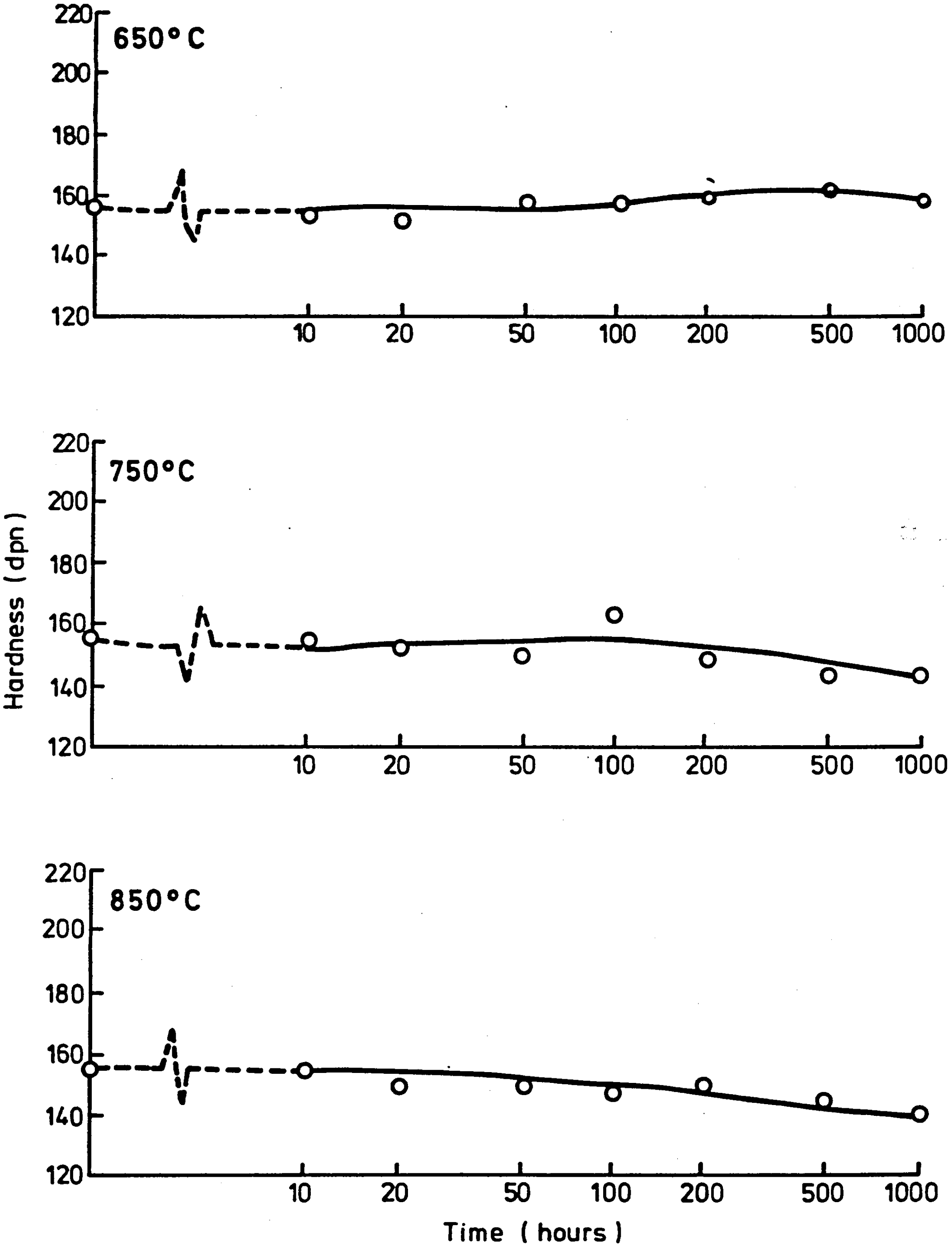
650°C
750°C
850°C
Hardness (dpn)
220
200
180
160
140
120
10
20
50
100
200
500
1000
Time (hours)

Figure 56. Optical micrographs, taken at x480, of the quaternary alloy 20Cr-23Ni-2Si. This 2% Si containing quaternary alloy was solution treated at 1050°C for 0.5 hours prior to aging at 750°C for total of 10, 100, 500 and 1000 hours.

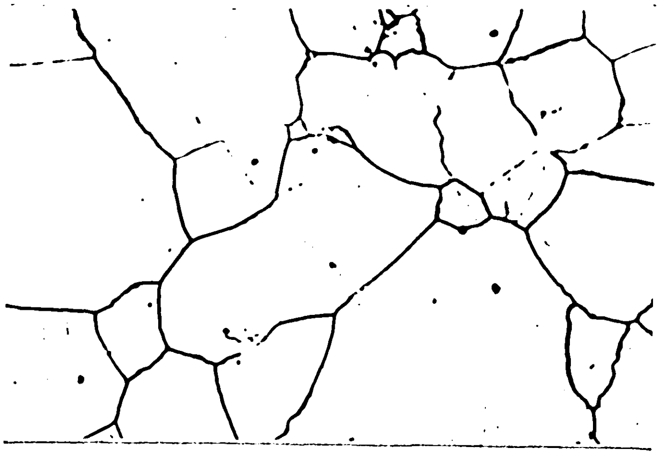

10h

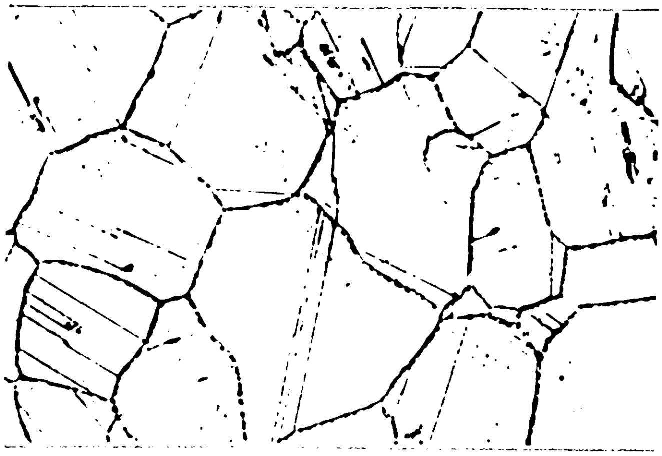

100h

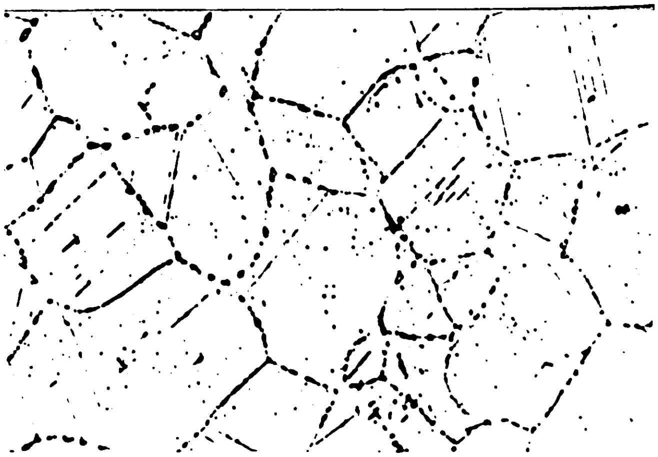

500h

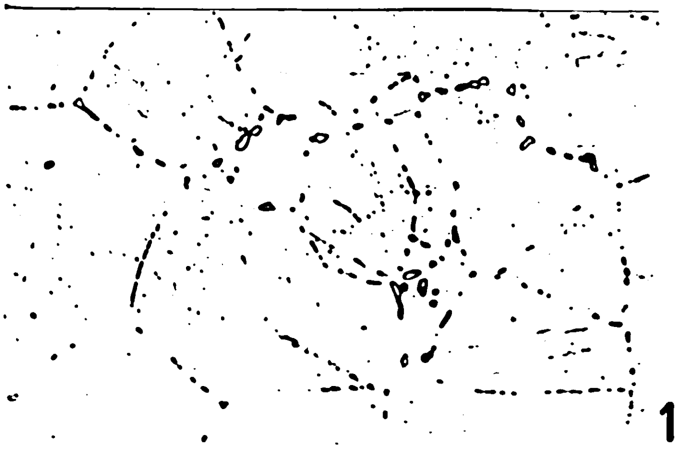

1000h

Figure 57. Transmission electron micrographs taken of the quaternary alloy 20Cr-23Ni-2Si, which was solution treated at 1050°C for 0.5 hours prior to ageing at 750°C for 1000 hours. Si bearing $M_{23}C_6$ precipitates were observed on grain boundaries and on dislocations in the austenite matrix.

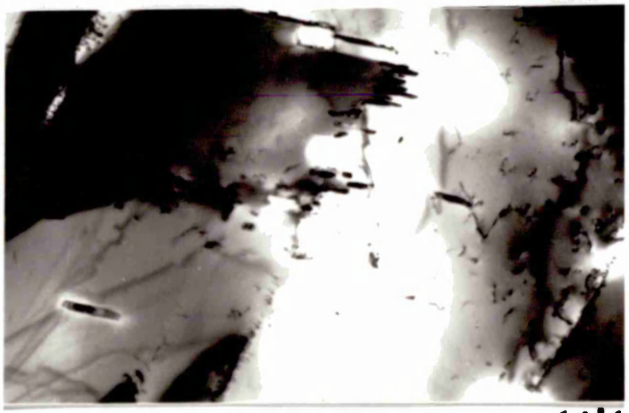

6.6K

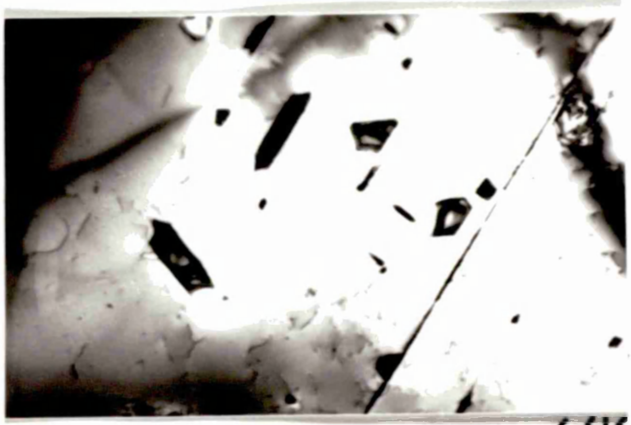

6.6K

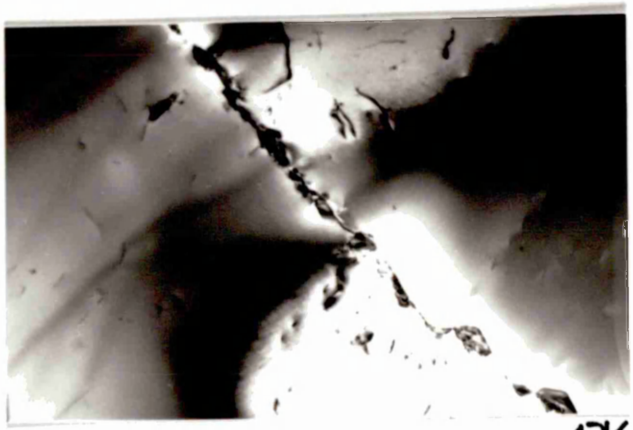

13K

Figure 58. Hardness versus time curves for the quaternary alloy 18Cr-7Ni-2Mo, which was solution treated at 1050°C for 0.5 hours prior to ageing at 650°C, 750°C and 850°C for 10-1000 hours.

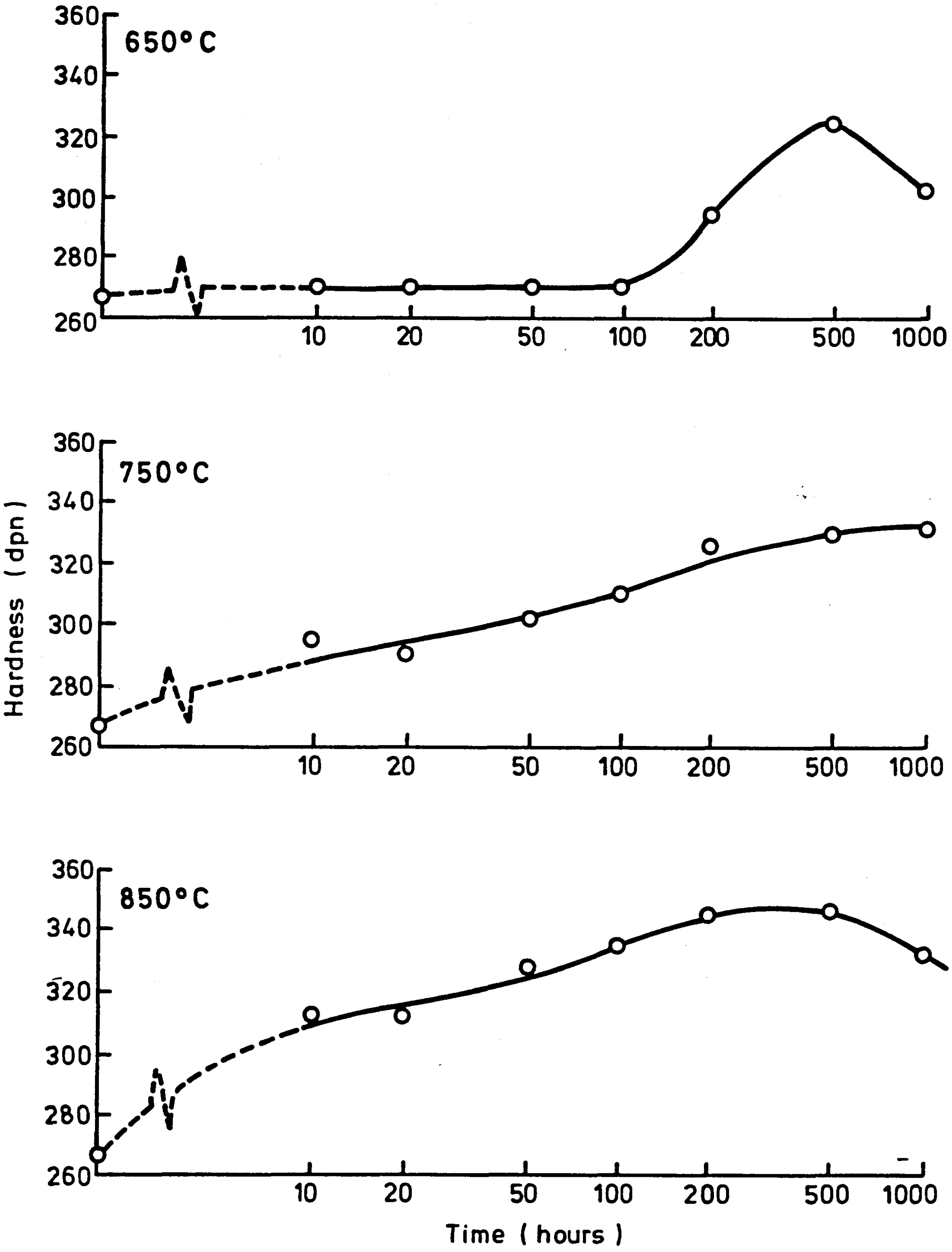
650°C
750°C
850°C
Hardness (dpn)
360
340
320
300
280
260
10
20
50
100
200
500
1000
Time (hours)

Figure 59. Optical micrographs taken at x480 of the quaternary alloy 18Cr-7Ni-2Mo, which was solution treated at 1050°C for 0.5 hours prior to ageing as follows:-

(a) aged at 650°C for 1000 hours.

(b) aged at 750°C for 1000 hours, the transmission electron micrograph shows the sigma phase present in the martensitic matrix.

(c) aged at 850°C for 1000 hours.

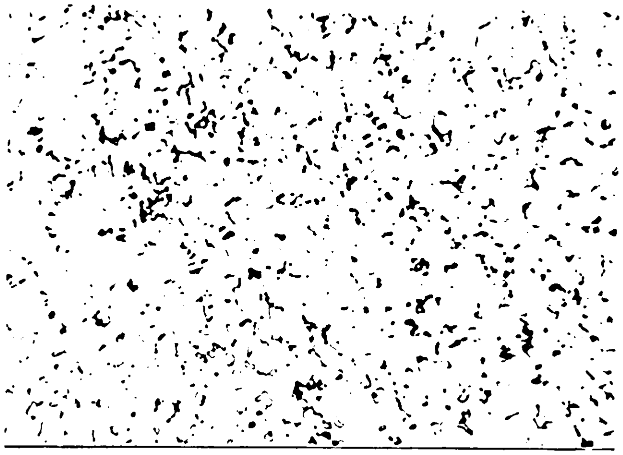

a

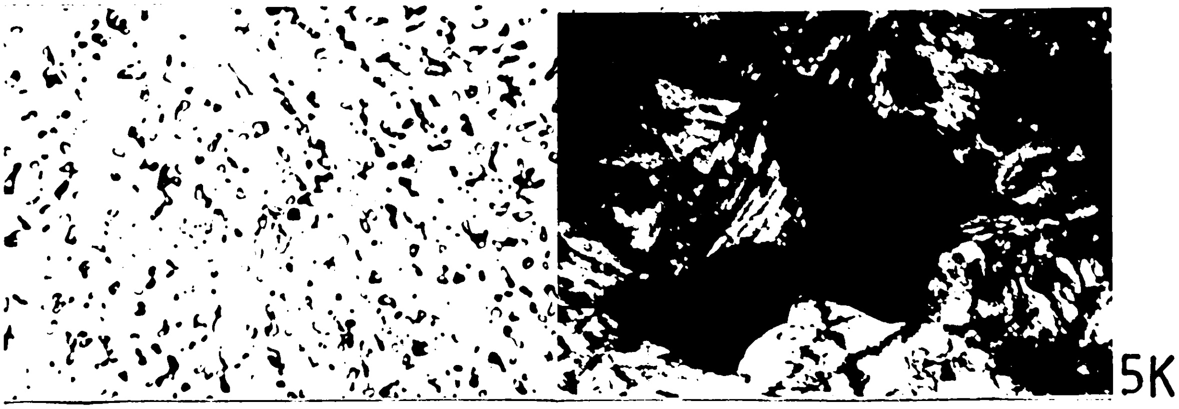

b

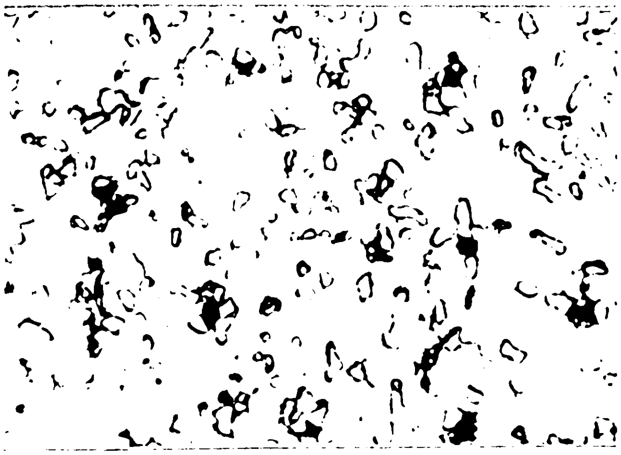

c

Figure 60. Hardness versus time curves for the quaternary alloy 18Cr-7Ni-1Nb, which was solution treated at 1050°C for 0.5 hours prior to ageing at 650°C, 750°C and 850°C for 10-1000 hours.

Figure 61. Transmission electron micrographs of the quaternary alloy 18Cr-7Ni-1Nb, which was solution treated at 1050°C for 0.5 hours prior to ageing at 750°C for 1000 hours.

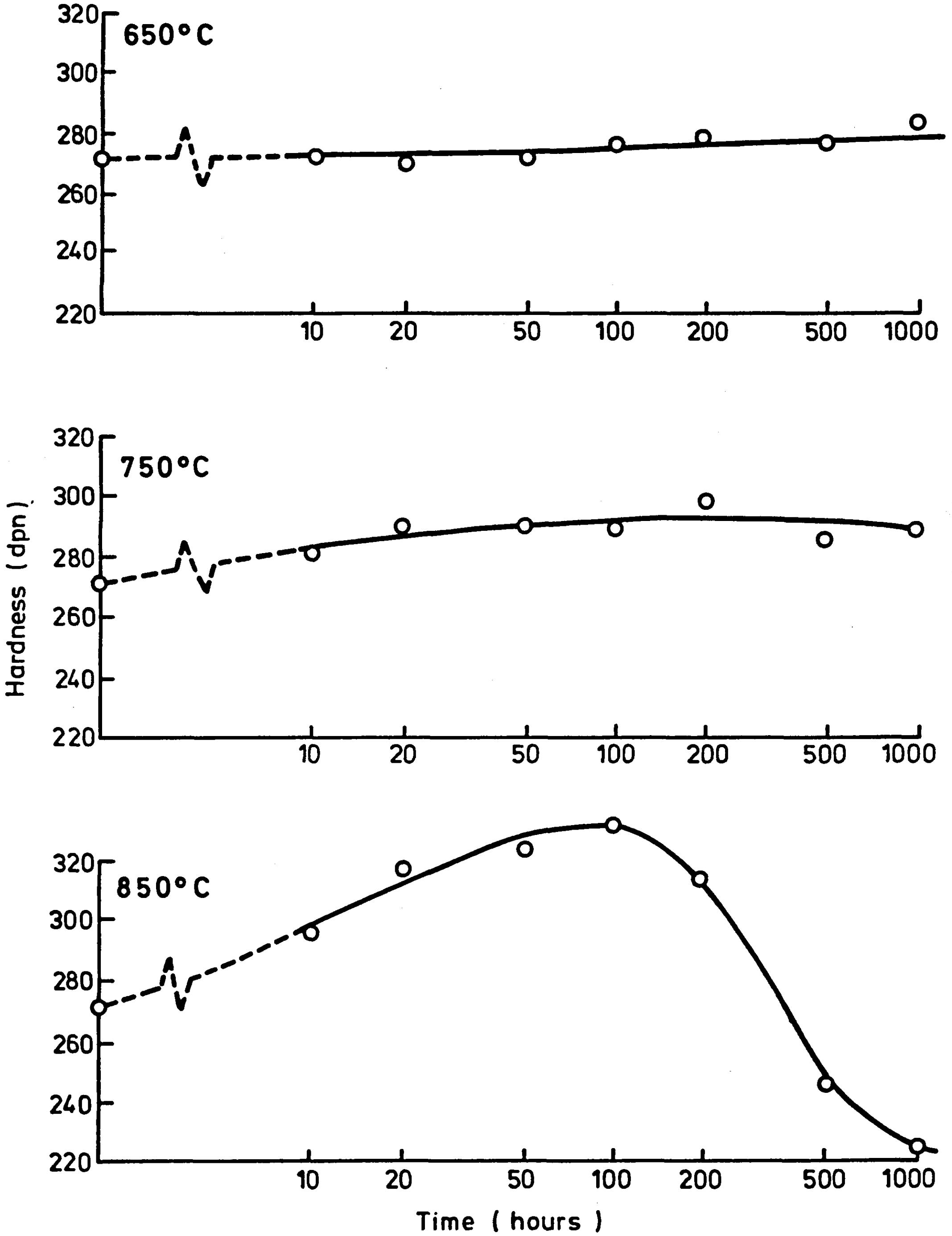
650°C
750°C
850°C
Hardness (dpn)
Time (hours)
220
240
260
280
300
320
10
20
50
100
200
500
1000

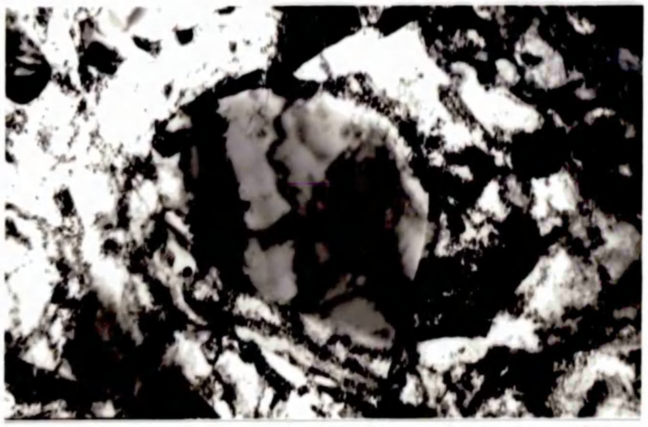

13K

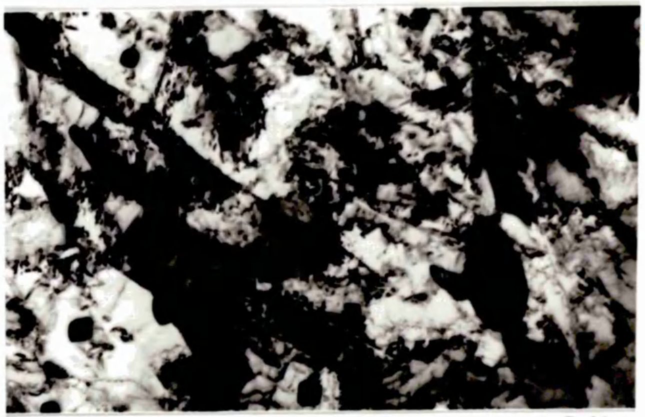

26K

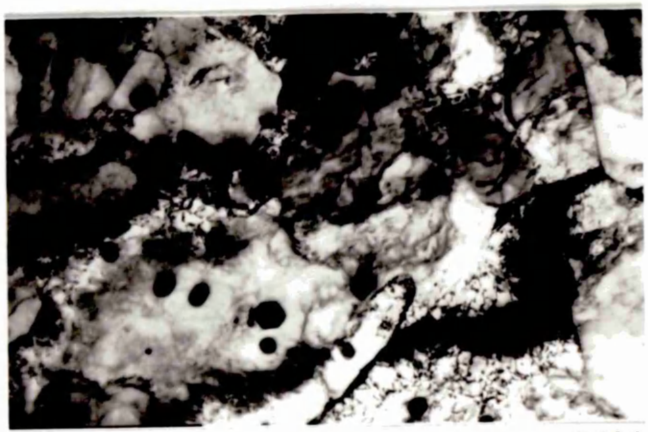

26K

Figure 62. Hardness versus time curves for the quaternary alloy 18Cr-7Ni-0.25Ti, which was solution treated at 1050°C for 0.5 hours prior to ageing at 650°C, 750°C and 850°C for 10-1000 hours.

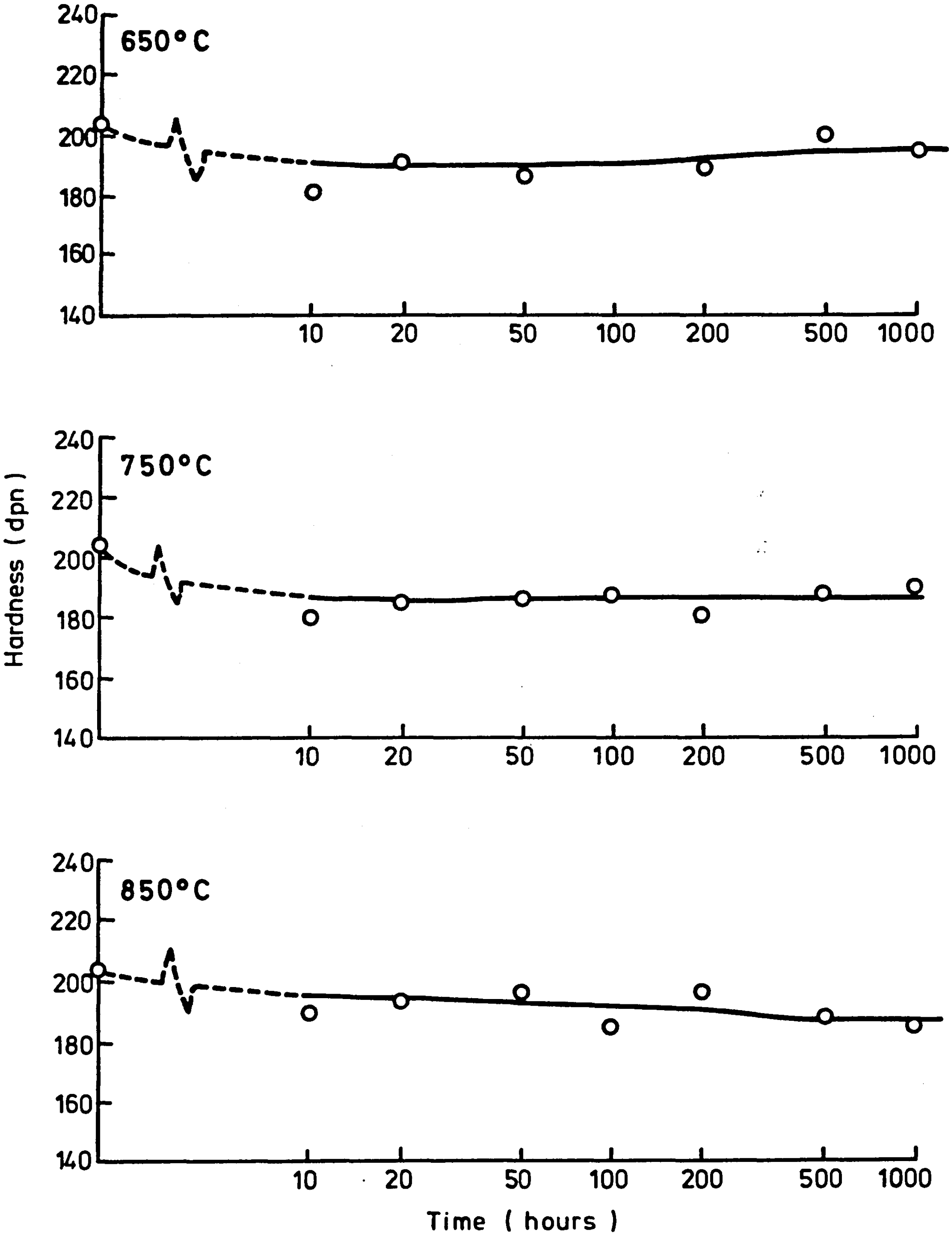
650°C
750°C
850°C
240
220
200
180
160
140
Hardness (dpn)
10
20
50
100
200
500
1000
Time (hours)

Figure 63. Optical micrographs, taken at x480, of the quaternary alloy 18Cr-7Ni-0.25Ti. Unfortunately this alloy missed its specification, the Ni content was too high at 8.21%, whilst the Ti content of the alloy was too low at 0.015%. The alloy therefore, remained fairly stable with respect to the transformation to martensite. The resulting alloy was solution treated at 1050°C for 0.5 hours prior to ageing for:-

(a) 200 hours at 650°C.

(b) 200 hours at 750°C.

(c) 200 hours at 850°C.

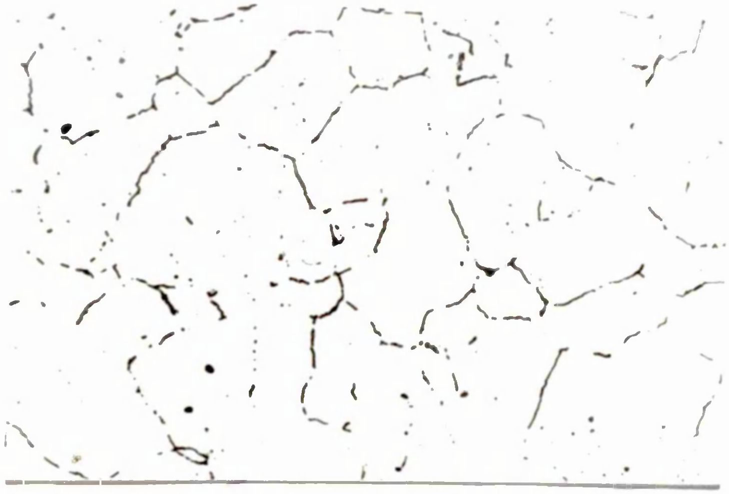

a

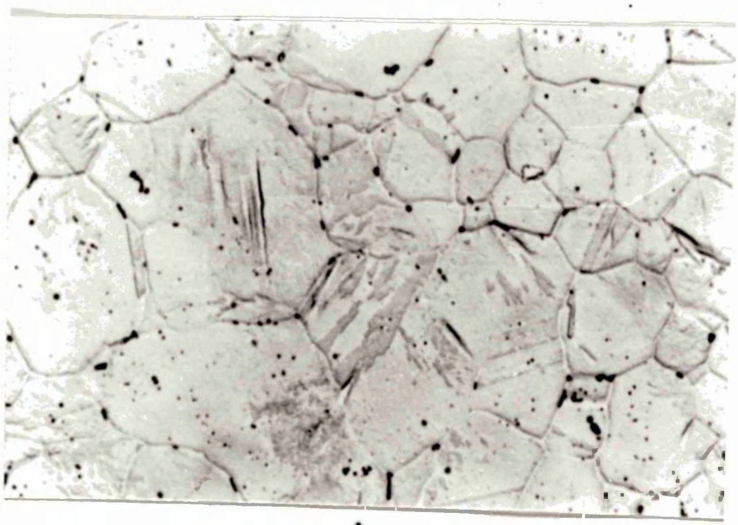

b

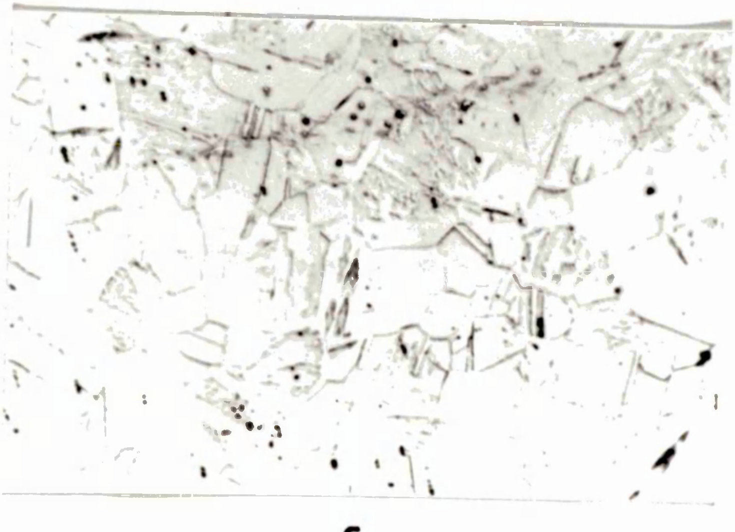

c

Figure 64. Hardness versus time curves for the quaternary alloy 18Cr-7Ni-1Si, which was solution treated at 1050°C for 0.5 hours prior to ageing at 650°C, 750°C and 850°C for 10-1000 hours.

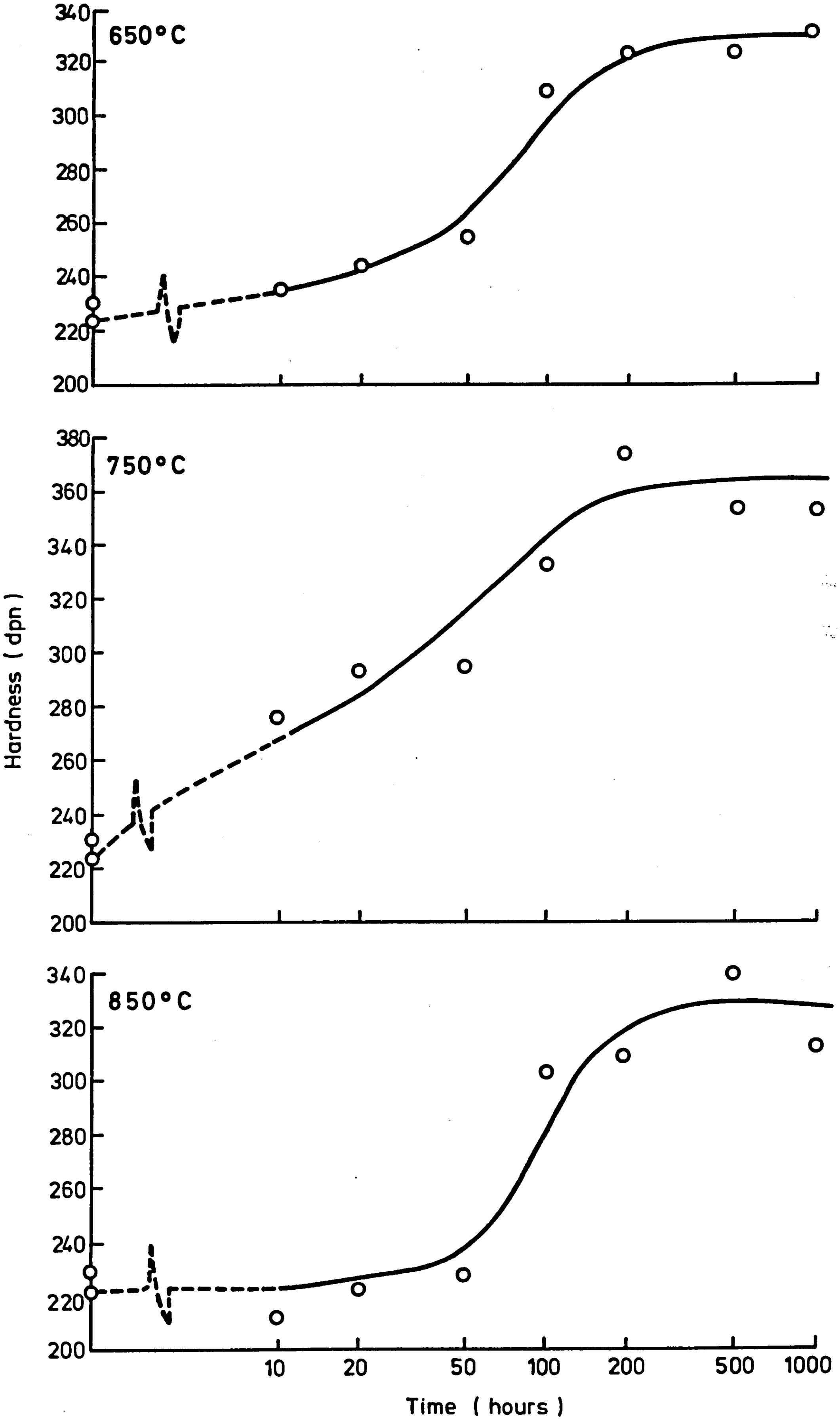

650°C
750°C
850°C
Hardness (dpn)
200
220
240
260
280
300
320
340
360
380
10
20
50
100
200
500
1000
Time (hours)

Figure 65. Optical micrographs, taken at x480, of the quaternary alloy 18Cr-7Ni-1Si, after solution treating at 1050°C for 0.5 hours.

(a) shows the 650°C aged microstructure after 10 and 1000 hours.

(b) shows the 750°C aged microstructure after 10 and 1000 hours.

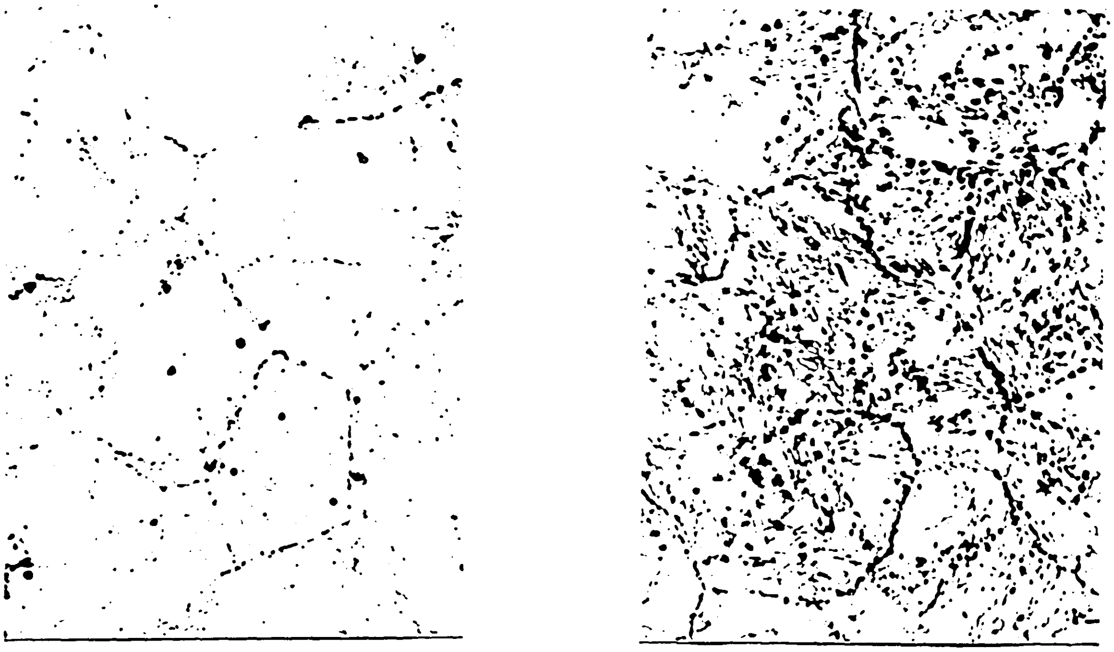

10h a 1000h

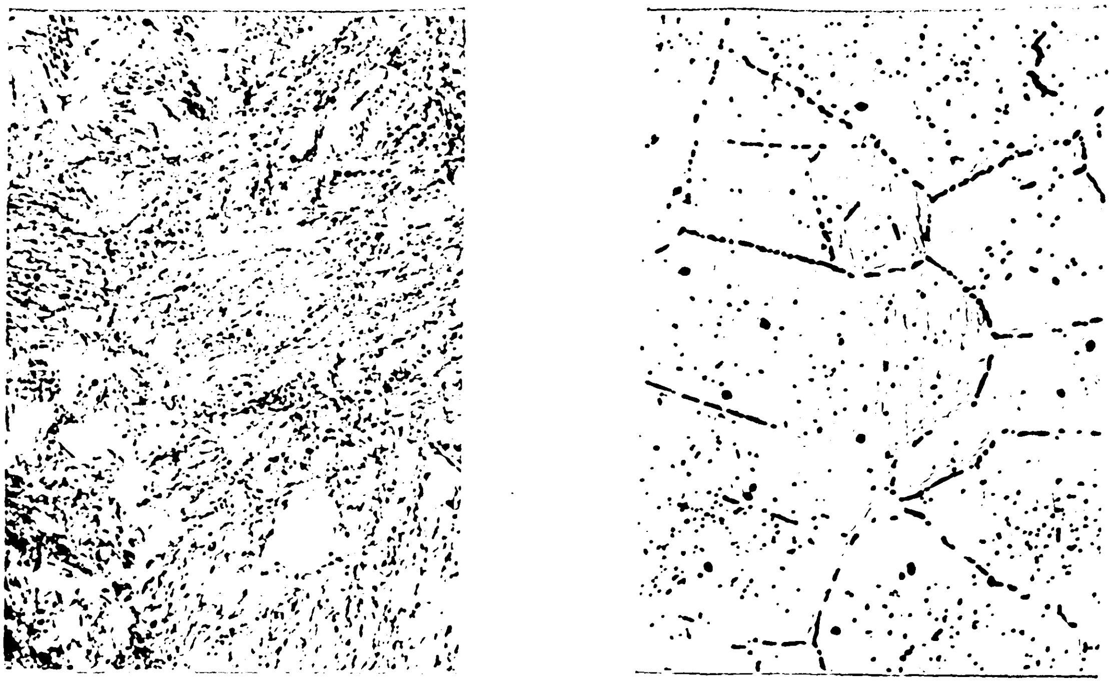

10h b 1000h

Figure 66. Hardness versus time curves for the quaternary alloy 18Cr-7Ni-2Si, which was solution treated at 1050°C for 0.5 hours, followed by ageing at 650°C, 750°C and 850°C for 10-1000 hours.

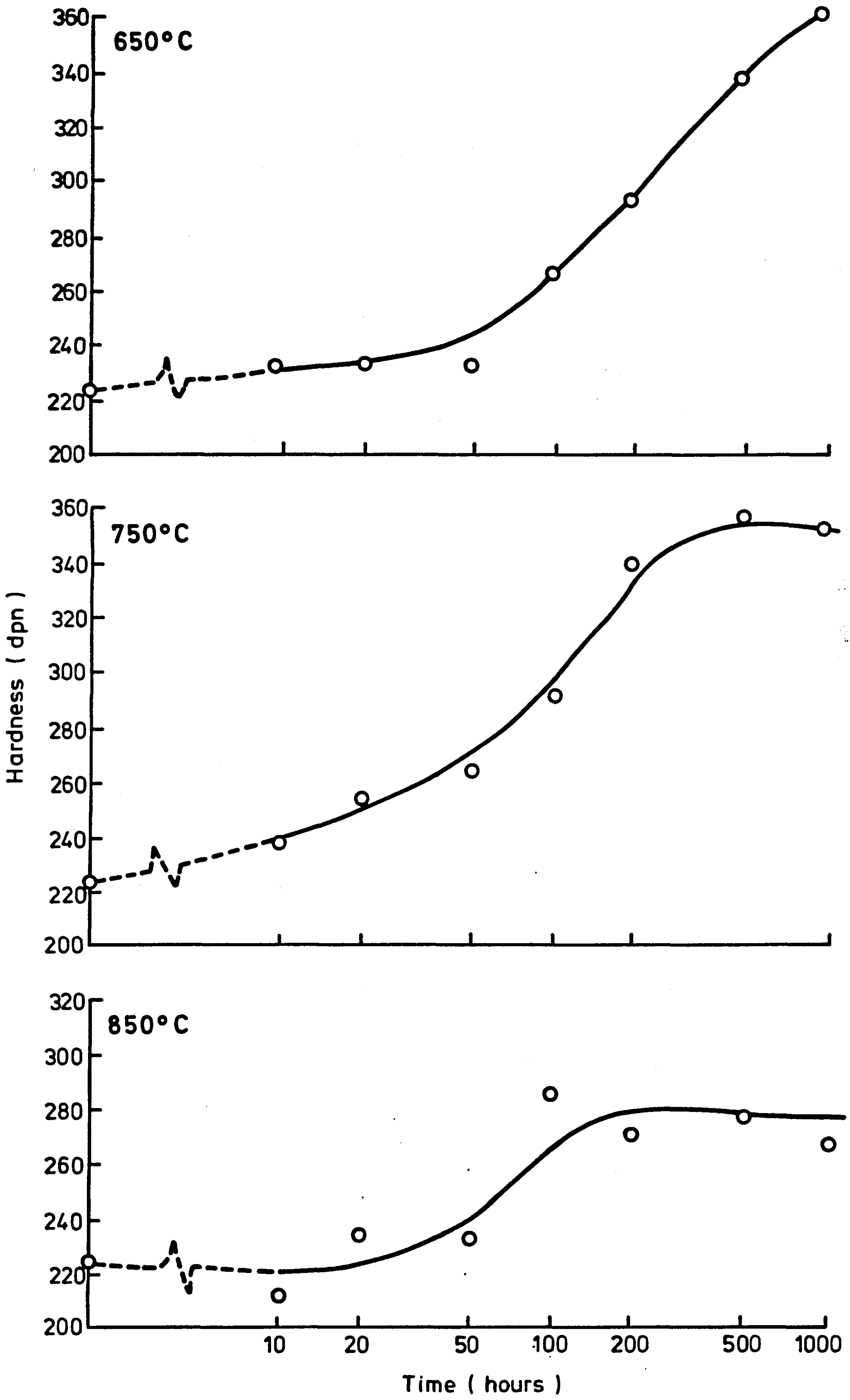
650°C
750°C
850°C
Hardness (dpn)
360
340
320
300
280
260
240
220
200
10
20
50
100
200
500
1000
Time (hours)

Figure 67. Transmission electron micrographs of the quaternary alloys 18Cr-7Ni-1Si and 18Cr-Ni-2Si, both alloys were solution treated at 1050°C for 0.5 hours prior to ageing at 750°C for 1000 hours.

(a) shows the general microstructure of the 1% Si alloy.

(b) shows both bright and dark field micrographs of the 1% Si alloy in which a fine dispersion of the carbide $M_{23}C_6$ was observed.

(c) shows the microstructures of the 2% Si alloy, with laths of austenite and ferrite evident along with the precipitation of $M_{23}C_6$ observed between the laths.

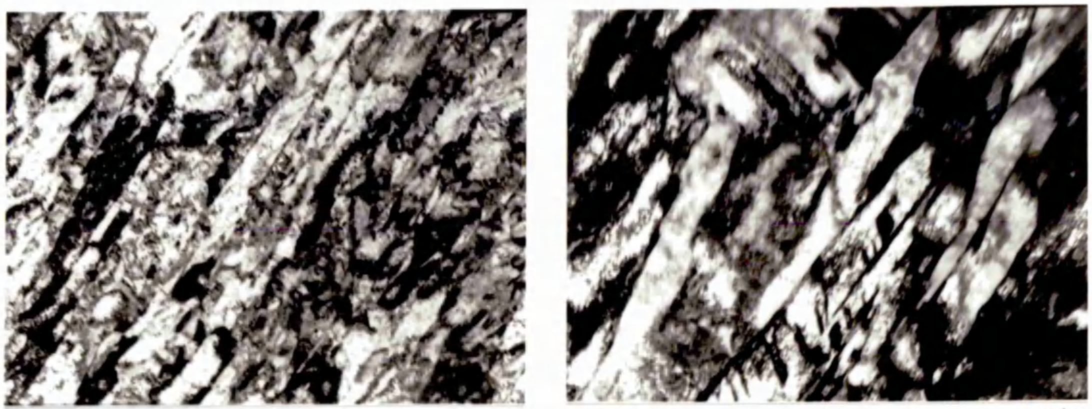

6.6K

20K

a

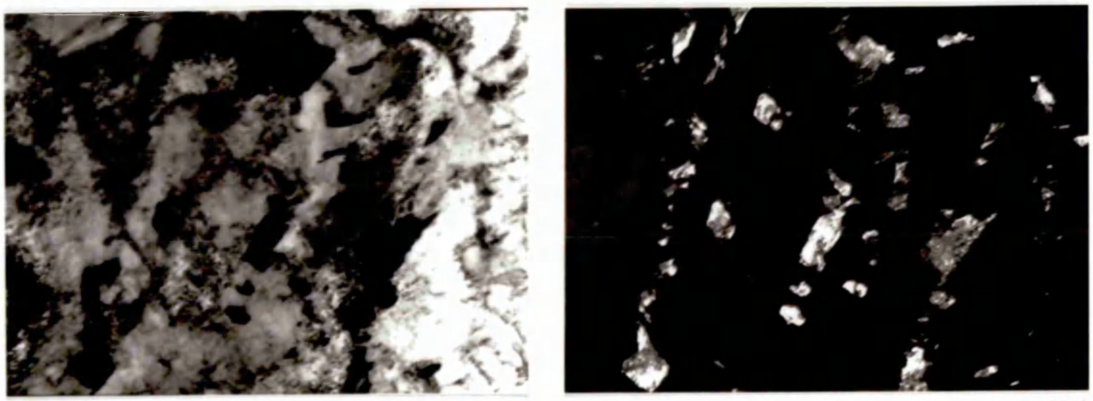

20K

20K

b

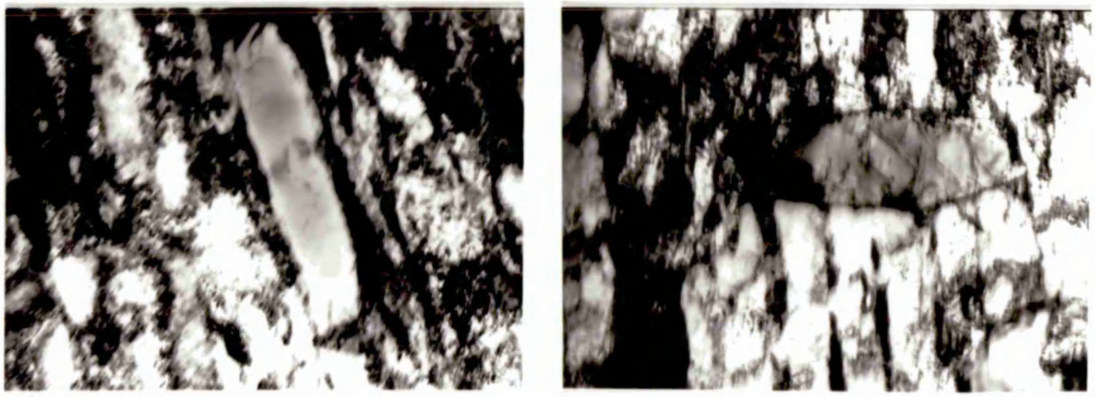

20K

26K

c

Figure 68. Transmission electron micrographs of alloy A(20Cr,23Ni) which was solution treated at 1050°C for 0.5 hours prior to irradiating in the H.V.E.M. at 500°C at a dose rate of 0.5 dpa per minute.

(a) taken after 0.7 dpa shows the dislocation loop build up before the onset of voidage.

(b) taken after 3.0dpa }
showing the voids produced
(c) taken after 15dpa } as a result of the
H.V.E.M. irradiation.
(d) taken after 25dpa }

Figure 69. Graph of percentage void swelling versus dose for alloy A(20Cr,23Ni) irradiated at 500°C and alloy C(30Cr,33Ni) irradiated at 500°C and 600°C. The irradiation was carried out in the H.V.E.M. at a dose rate of 0.5dpa per minute.

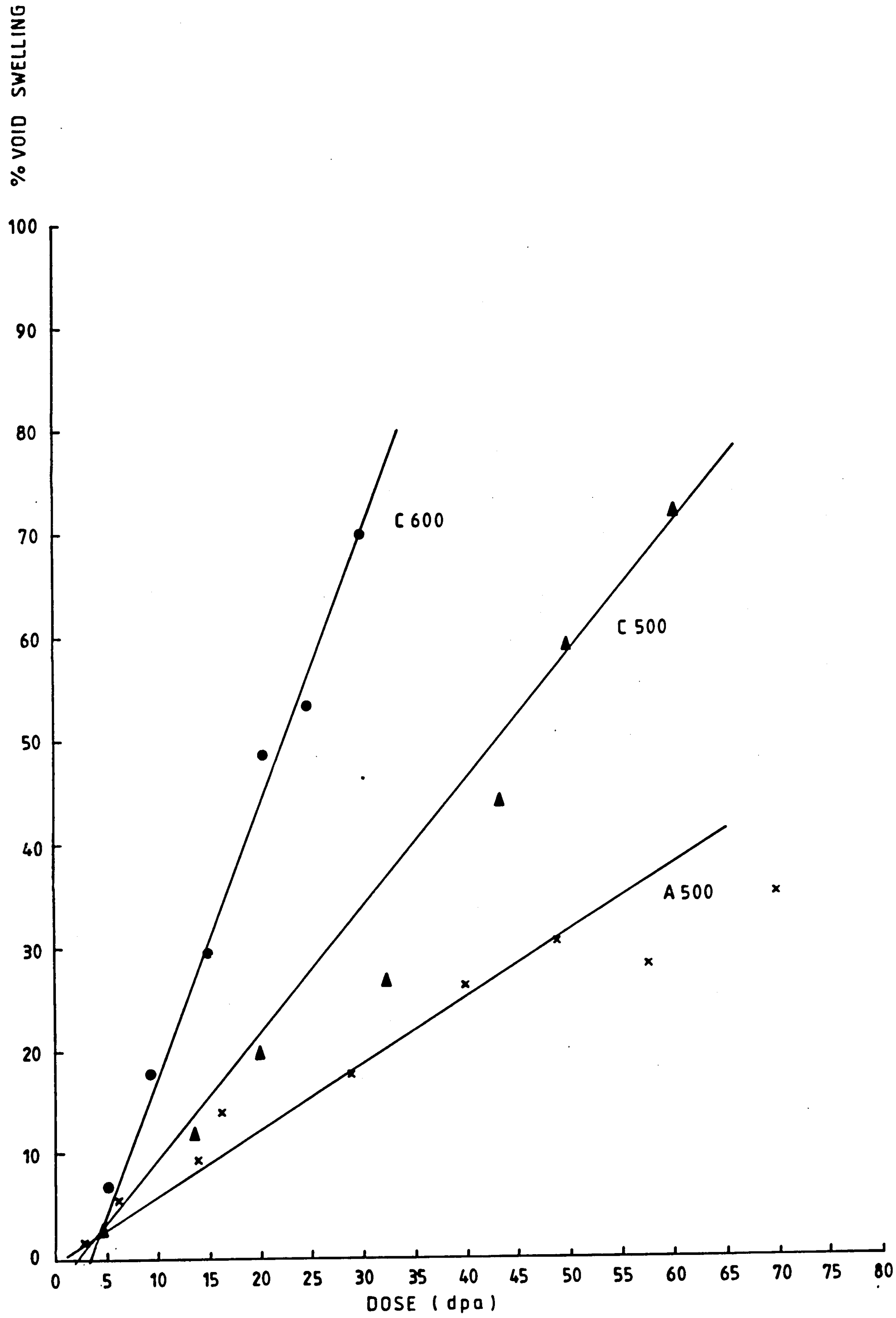

% VOID SWELLING
100
90
80
70
60
50
40
30
20
10
0
0
5
10
15
20
25
30
35
40
45
50
55
60
65
70
75
80
DOSE (dpa)
C 600
C 500
A 500

Figure 70. Transmission electron micrographs of alloy C(30Cr,33Ni) solution treated at 1050°C for 0.5 hours prior to irradiating in the H.V.E.M. at 600°C, with a dose rate of 0.5 dpa per minute.

(a) taken after 3.6 dpa }

(b) taken after 9.3 dpa } showing the voids produced as a result of the H.V.E.M. irradiation.

(c) taken after 15.0 dpa}

(d) taken after 30.2 dpa}

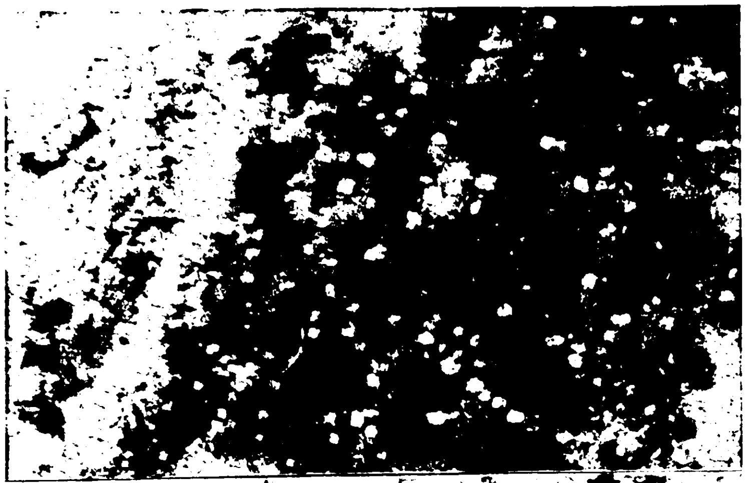
96K

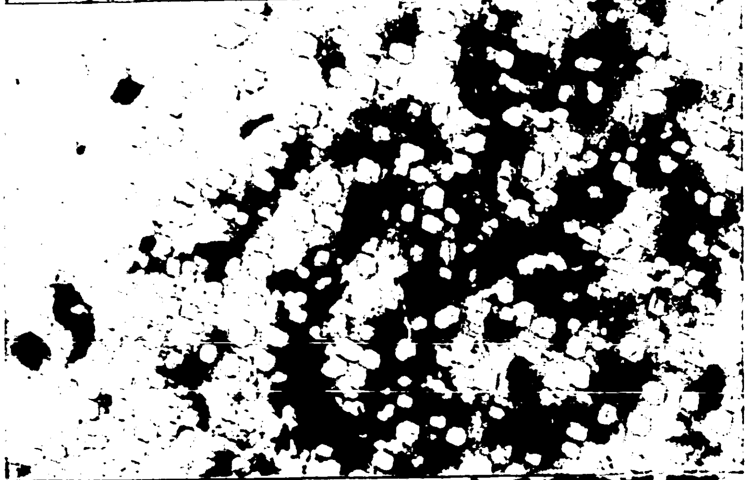
80K

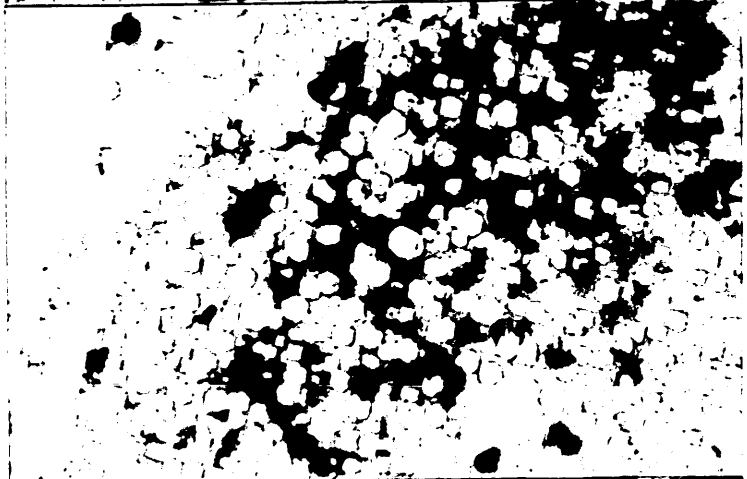
80K

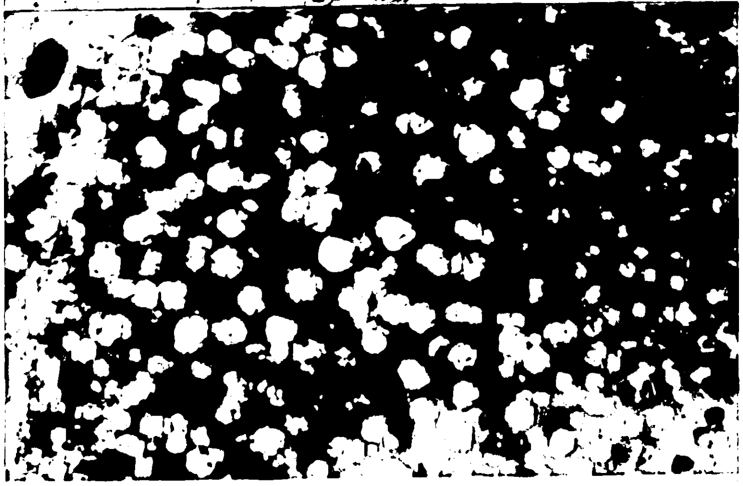
64K

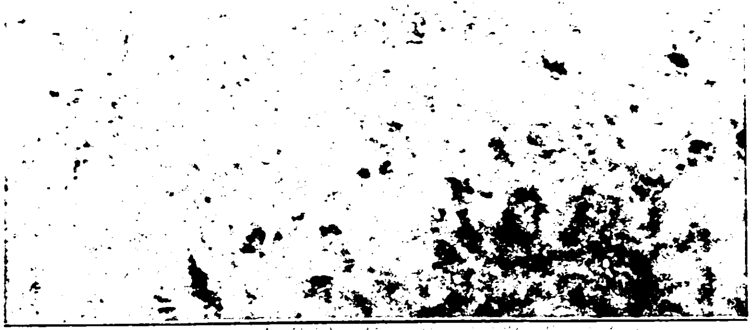
96K

96K

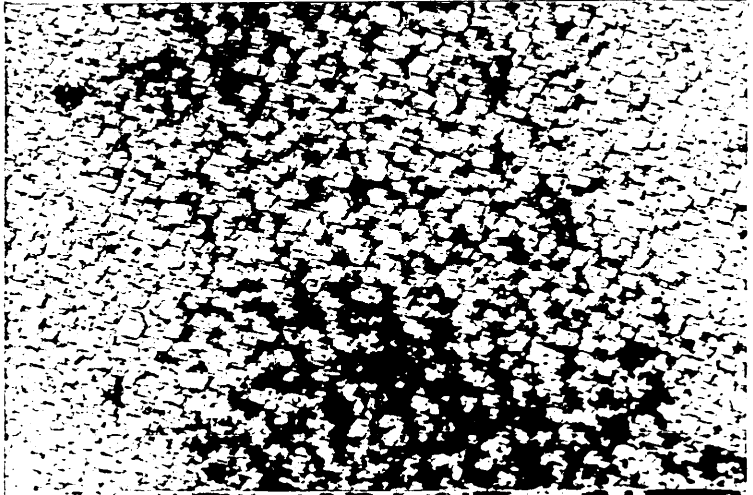
96K

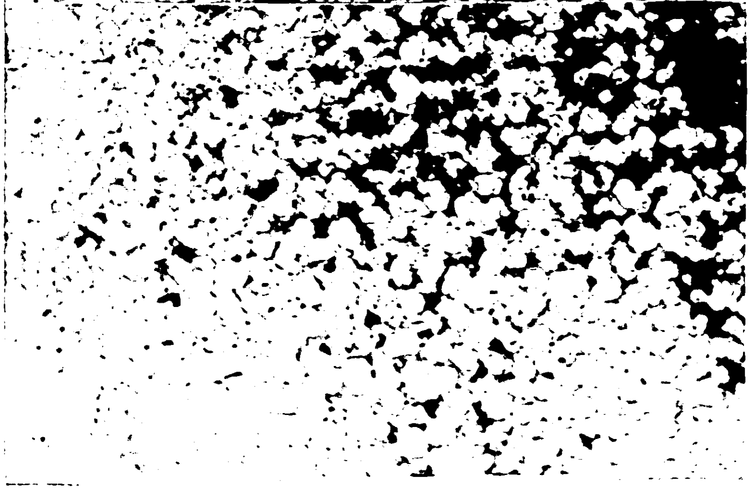
96K

Figure 69. Graph of percentage void swelling versus dose for alloy A(20Cr,23Ni) irradiated at 500°C and alloy C(30Cr,33Ni) irradiated at 500°C and 600°C. The irradiation was carried out in the H.V.E.M. at a dose rate of 0.5dpa per minute.

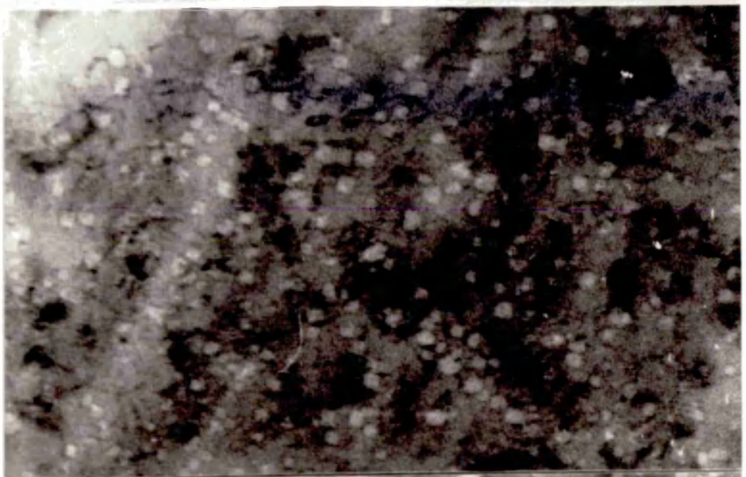

96K

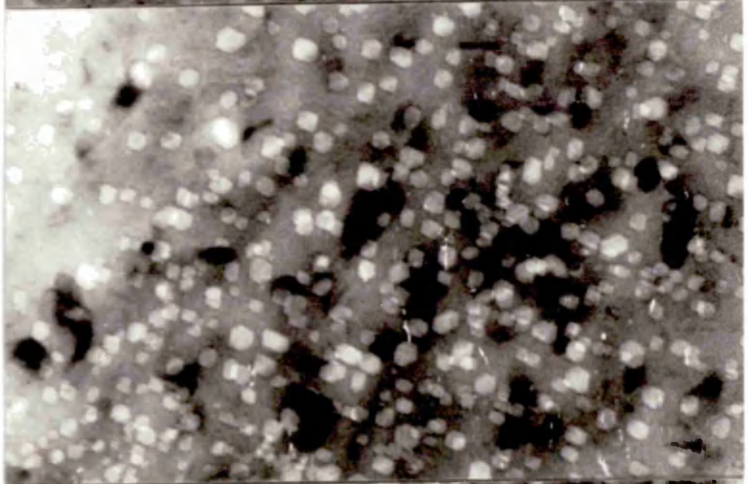

80K

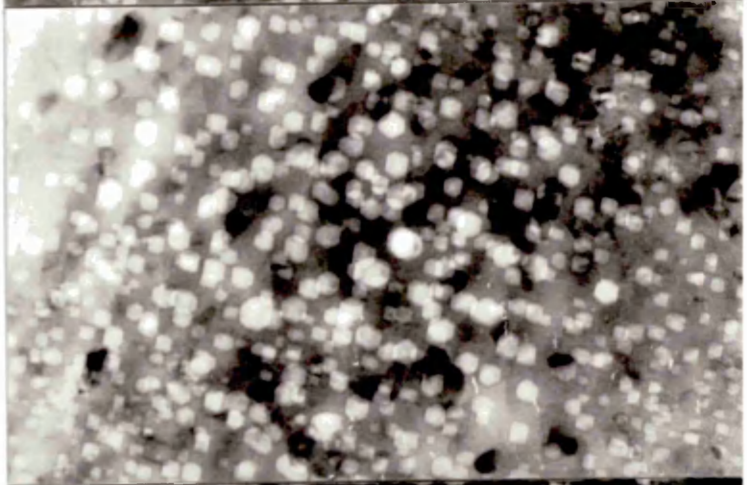

80K

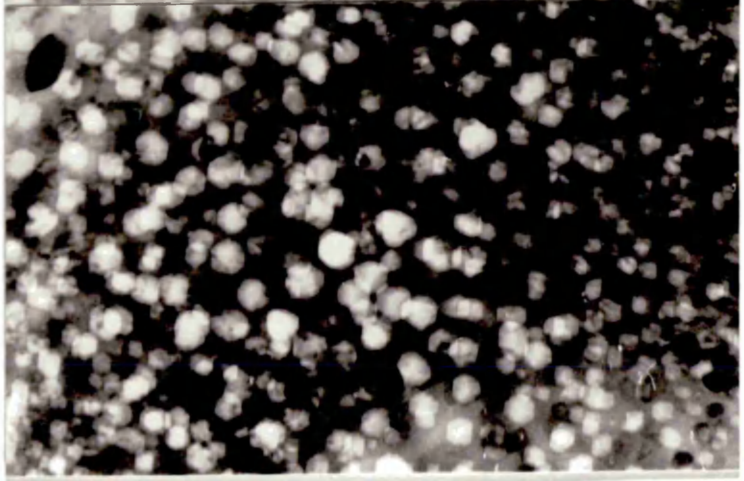

64K

Figure 70. Transmission electron micrographs of alloy C(30Cr,33Ni) solution treated at 1050°C for 0.5 hours prior to irradiating in the H.V.E.M. at 600°C, with a dose rate of 0.5 dpa per minute.

(a) taken after 3.6 dpa }

(b) taken after 9.3 dpa } showing the voids produced
as a result of the
(c) taken after 15.0 dpa} H.V.E.M. irradiation.

(d) taken after 30.2 dpa}

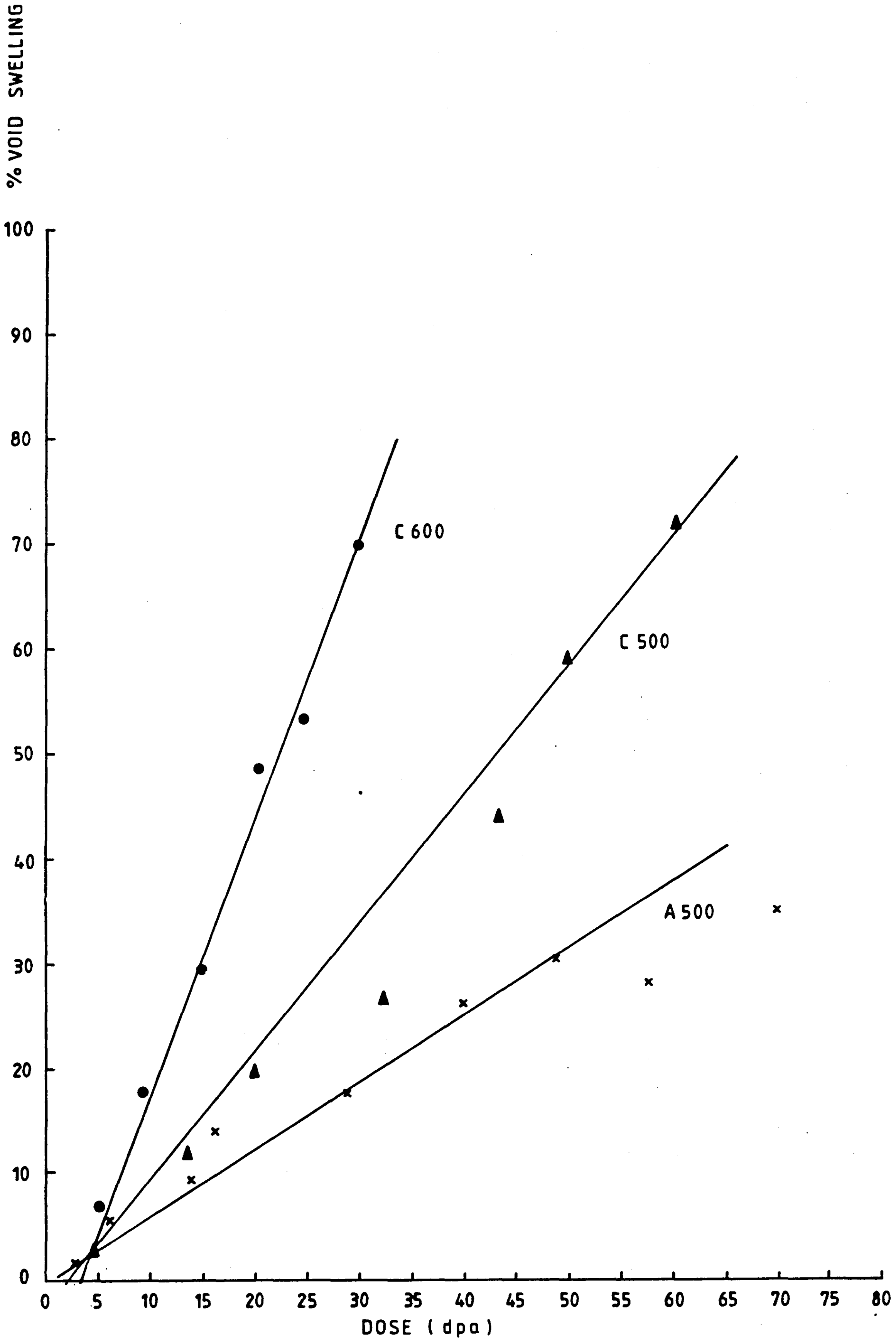

% VOID SWELLING
100
90
80
70
60
50
40
30
20
10
0
0
5
10
15
20
25
30
35
40
45
50
55
60
65
70
75
80
DOSE (dpa)
C 600
C 500
A 500

SECTION 9 - HOUSEHOLD FINANCE

I would like to talk to you now about how you spend your money.

A - IF INTERVIEWEE EMPLOYED

1) Before you returned to work, what arrangements were made for sorting out how your partner's/husband's wages were spent?
(Probe - joint control, allowance system etc.?)

2) How did you feel about this?

3) Now that you have returned to work, what arrangements do you have for sorting out how to spend the money you both bring home?
(Probe - as above)

4) What particular things do you spend YOUR wages on?
(Probe - mortgage/bills, food, clothes for family, personal items, goods for house, holidays?)

5) What things would you have to spend less on or do without, if you were not working?

6) How important is earning a wage to you?

7) What does your husband feel about you earning a wage?

8) Do you tell your partner/husband what you earn?

9) If you can, how much does your partner/husband earn?

B - IF INTERVIEWEE NOT IN PAID WORK

10) What arrangements do you make for sorting out how your partner's/husband's wages are spent?
(Probe - joint control, allowance system, etc?)

11) How do you feel about this?

12) How important to you is earning a wage?

13) What particular things would you spend your wages on?

14) If you can, how much does your partner/husband earn?

APPENDIX C

INTRODUCTORY LETTER TO INTERVIEWEES LIVING IN GREENHILL/BRADWAY

Dear

- I am writing to ask if you can help me. A few months ago, you filled in a questionnaire about your past and present employment. This questionnaire was produced by Sheffield Hallam University and Sheffield City Council, in order to help us gain information about levels of unemployment, employment and skills in Sheffield.

- To find out more about this, especially about the working lives of women in Sheffield, I am talking to women who ARE working or who WOULD LIKE a job in the future. All information gained will be used to help me in my personal studies.

- I would be very grateful if you would agree to talk to me about your experience of work. This would give an important insight into the lives of working women in Sheffield.

- All information is strictly confidential.

- I would be available to talk to you on the dates shown on the attached sheet. Please show the best time for you, and return it to me in the stamped addressed envelope provided. Or if this is not convenient, 'phone the above telephone number to arrange a more suitable time.

- Thank you for reading this, your co-operation is appreciated.

Yvonne Smith

APPENDIX D

STANDARD OCCUPATIONAL CLASSIFICATION (SOC)

1) Managers and administrators

2) Professional occupations

3) Associate professional and technical occupations

4) Clerical and secretarial occupations

5) Craft and related occupations

6) Personal and protective service occupations

7) Sales occupations

8) Plant and machine operatives

9) Other occupations

Figure 71. Transmission electron micrographs of alloy C(30Cr,33Ni) which was solution treated at 1050°C for 0.5 hours prior to irradiating in the H.V.E.M. at 500°C, at a dose rate of 0.5 dpa per minute.

(a) taken after 4.95 dpa }
showing the voids produced
(b) taken after 10.2 dpa }
as a result of the
(c) taken after 20.0 dpa }
H.V.E.M. irradiation.
(d) taken after 30.5 dpa }

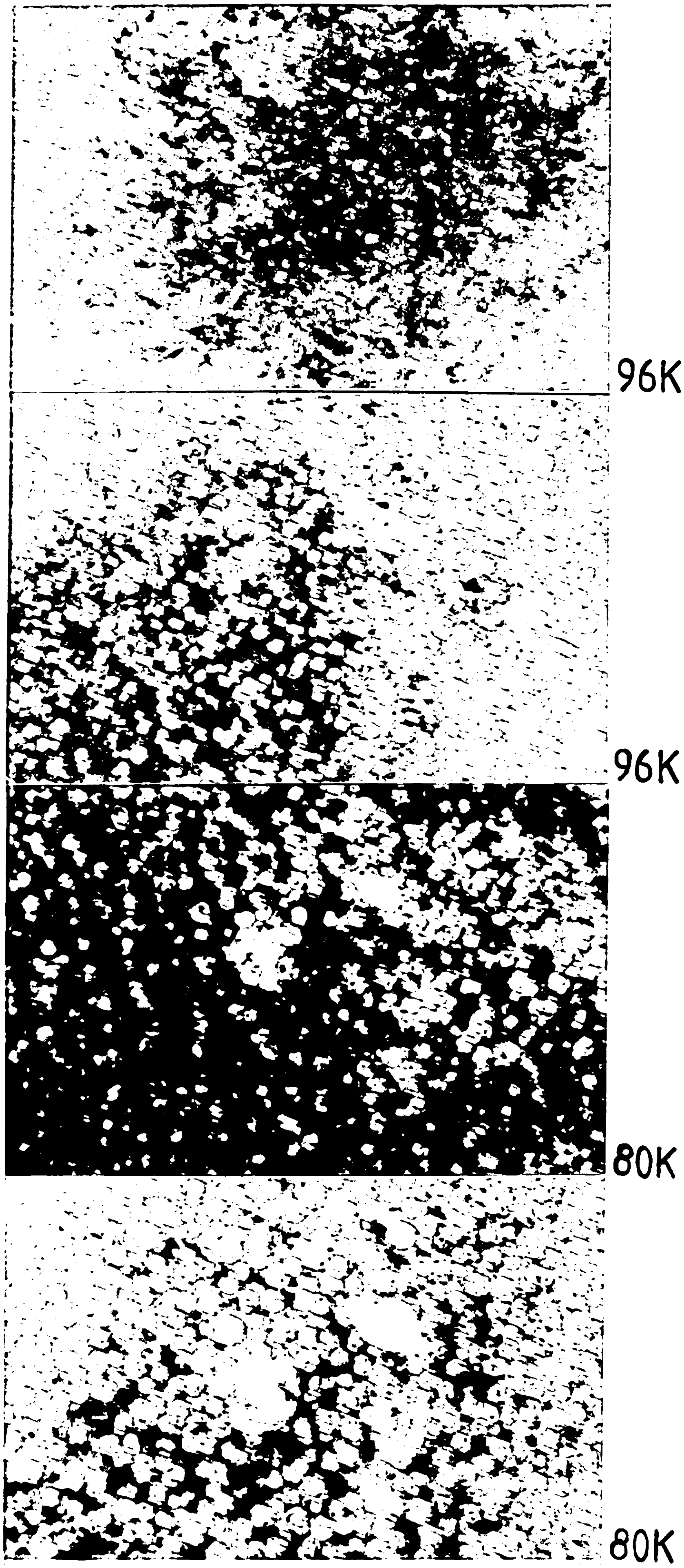
96K
96K
80K
80K

Figure 72. Tranmission electron micrographs of the V.E.C. irradiated alloys. The alloys were irradiated in the V.E.C. a to a total dose of 10 dpa, at a temperature of 550°C.

(a) shows the base ternary alloy A(20Cr,23Ni)× 200k.

(b) shows the quaternary alloy 20Cr-23Ni-2Si× 132k.

(c) shows the quaternary alloy 20Cr-23Ni-2Mo× 200k.

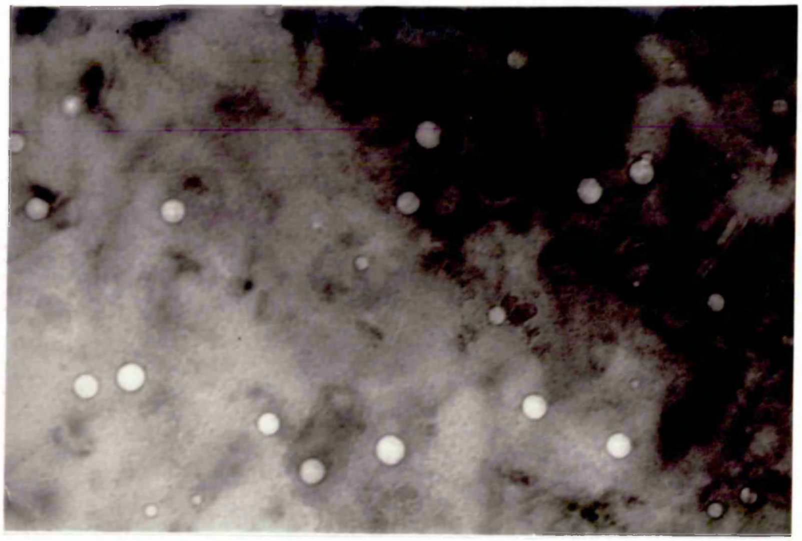

a

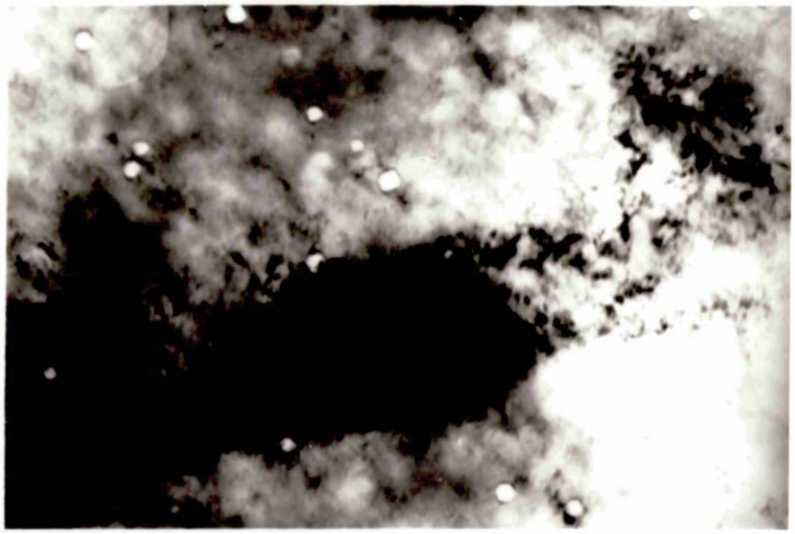

b

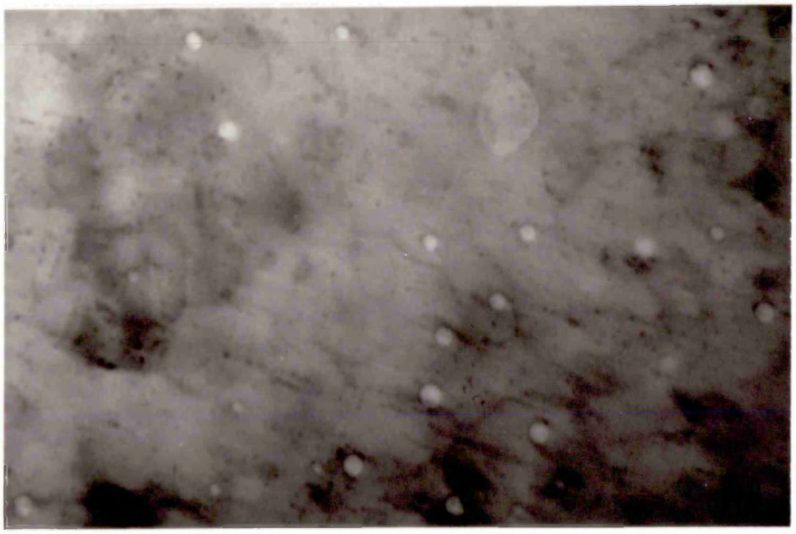

c

Figure 73. Optical micrographs, taken at x480, of the 13000 hours thermally aged N series alloys, based on the composition 12Cr-15Ni with Si additions.

(a) alloy N1(0.14Si) aged at 505°C.

(b) alloy N1(0.14Si) aged at 645°C.

(c) alloy N2(0.49Si) aged at 505°C.

(d) alloy N2(0.49Si) aged at 645°C.

(e) alloy N4(1.42Si) aged at 435°C.

(f) alloy N4(1.42Si) aged at 645°C.

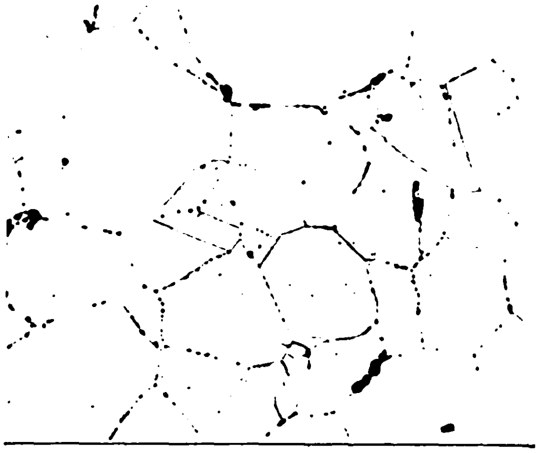

a

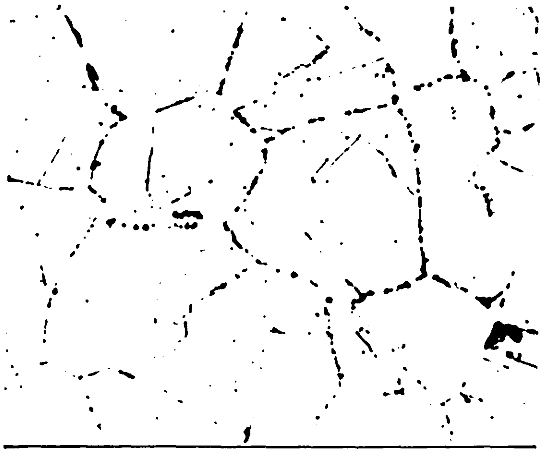

b

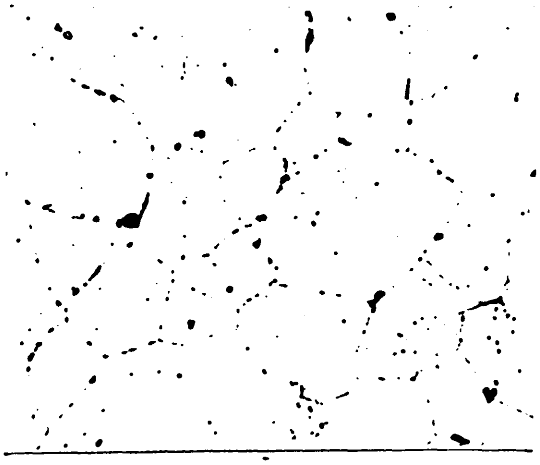

c

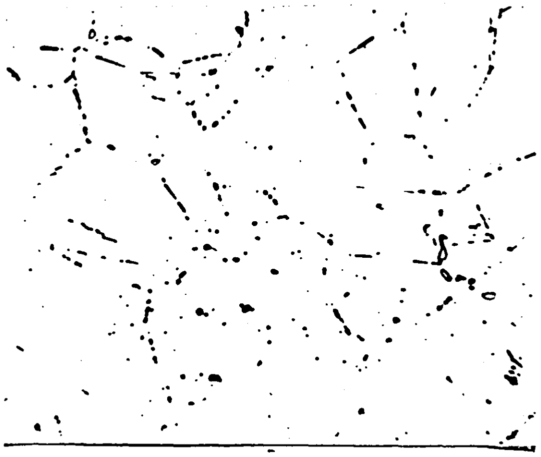

d

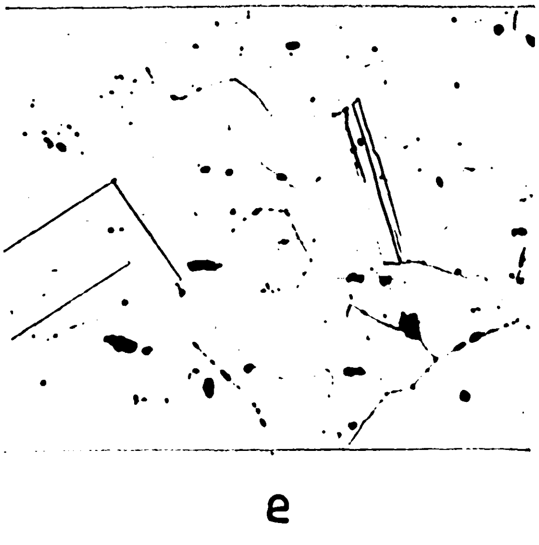

e

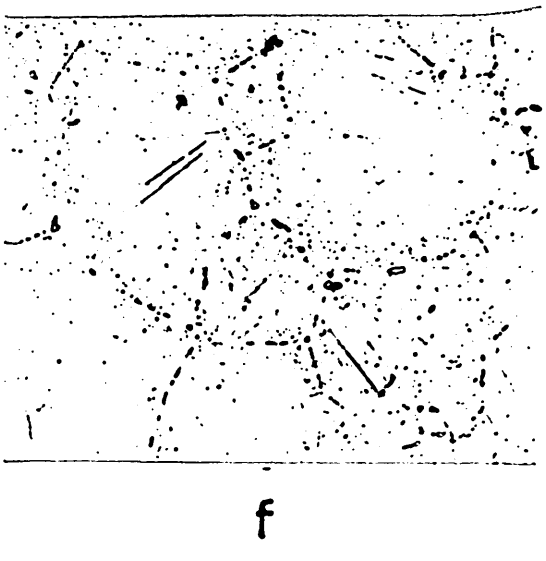

f

Figure 74. Transmission electron micrographs of the N series alloys based on the composition 12Cr-15Ni with silicon additions. These alloys were thermally aged for 13000 hours

(a) shows alloy N1(0.14Si) aged at 435°C.

(b) shows alloy N1(0.14Si) aged at 645°C.

(c) shows alloy N3(0.95Si) aged at 435°C.

(d) shows alloy N3(0.95Si) aged at 575°C.

(e) shows alloy N4(1.49Si) aged at 575°C

a 20K

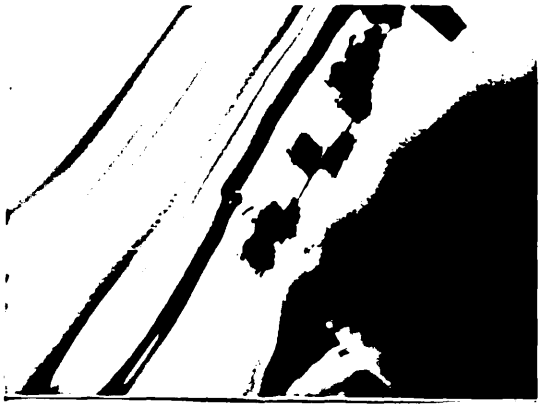

b 13K

c 13K

d 26K

e 10K

e 10K